# Electron Transport through and in Quantum Dot Arrays

Von der Fakultät für Mathematik und Physik
der Gottfried Wilhelm Leibniz Universität Hannover
zur Erlangung des Grades

Doktor der Naturwissenschaften
— Dr. rer. nat. —

genehmigte Dissertation
von

M.Sc. Johannes Christian Bayer

2024

# Abstract

The present thesis investigates serial quantum dot arrays of different sizes, the double quantum dot, the triple quantum dot, and the quadruple quantum dot. The quantum dot device is based on a two-dimensional electron gas formed in a GaAs/AlGaAs heterostructure. A quantum point contact in the vicinity of the quantum dots is utilized as a charge sensor, allowing to detect tunneling of single electrons into or out of the quantum dots as well as between two of the quantum dots. Two qualitatively different regimes are discussed, the transport regime and the isolated regime.

In the transport regime, where the quantum dots are well coupled to electron reservoirs on both sides, electrons can tunnel from one reservoir to the other through the array. Gate voltage dependent measurements are used to characterize the transport properties through the quantum dot arrays and to extract electrostatic properties. For all array sizes, long-range transport across quantum dots in Coulomb blockade is observed for the strong coupling regime.

The isolated regime is reached by increasing the tunnel barriers between reservoirs and the quantum dot array on both sides until tunneling from and into the reservoirs is fully suppressed within the measurement timescales. The number of electrons in an isolated array is fixed, but electrons can still be redistributed inside the array. The charge reconfiguration inside the arrays is tracked using the charge detector. A high level of control over the coupling, and thus the interdot transitions, including long-range transitions between non-neighboring quantum dots, is demonstrated. Time-resolved charge detection was used to investigate the tunneling dynamics of a single, two, and three electrons loaded into a double quantum dot, where the three electron case shows a high sensitivity to environmental parameters.

**Keywords: quadruple quantum dot, single-electron tunneling, charge detection, isolated quantum dots, Coulomb blockade, long-range tunneling**

# Contents

# Symbols

| | |
|---|---|
| $\alpha_{j,i}$ | lever arm of gate *j* with respect to quantum dot *i* |
| B | magnetic field |
| $C_{gate,i}$ | capacitance between *gate* and quantum dot *i* |
| $C_{ij}$ | mutual capacitance between quantum dot *i* and quantum dot *j* |
| $C_m$ | mutual capacitance in a double quantum dot system |
| $C_\Sigma$ | total capacitance of a quantum dot |
| $C_{\Sigma i}$ | total capacitance of quantum dot *i* |
| D | diffusion coefficient |
| $\Delta$ | detuning energy |
| $\Delta_{ij}$ | detuning energy between quantum dot *i* and quantum dot *j* |
| $\Delta E_i$ | energetic shift of the energy levels of quantum dot *i* |
| $\Delta E_{ij}$ | energetic shift of quantum dots *i* and *j* due to the interdot capacitance |
| $\Delta_N$ | detuning of the N-*th* energy level |
| $\Delta t$ | time interval |
| $\Delta V_G$ | gate voltage difference |
| $e$ | elementary charge |
| $E_C$ | charging energy of the quantum dot |
| $E_{Ci}$ | charging energy of quantum dot *i* |
| $E_m$ | mutual charging energy in a double quantum dot |
| $\bar{\epsilon}$ | mean energy |
| $\epsilon_i$ | energy of state *i* |
| $\epsilon_-$ | lower energy (bonding) state of a double quantum dot |
| $\epsilon_+$ | higher energy (antibonding) state of a double quantum dot |
| $\Gamma$ | tunneling rate |
| $\Gamma_l$ | tunneling rate from the right to the left inside a double quantum dot |
| $\Gamma_r$ | tunneling rate from the left to the right inside a double quantum dot |

| | |
|---|---|
| $\Gamma_{ij}$ | tunneling rate between the two elements $i$ and $j$ |
| $\Gamma^*$ | effective tunneling rate |
| $h$ | Planck constant |
| $\hbar$ | reduced Planck constant |
| $I$ | current |
| $I_{avg}$ | average current |
| $I_{dot}$ | current through the quantum dot system |
| $I_{qpc}$ | current through the quantum point contact system |
| $k_B$ | Boltzmann constant |
| $m_i$ | slope of the quantum dot $i$ charging lines |
| $m_{Rij}$ | slope of the reconfiguration line between quantum dot $i$ and quantum dot $j$ |
| $M$ | amount of a substance |
| $\mu_0(N)$ | ground state energy of a quantum dot charged with N electrons. |
| $\mu_e$ | 2DEG electron mobility |
| $\mu_F$ | Fermi level |
| $\mu_S$ | chemical potential of the source reservoir |
| $\mu_D$ | chemical potential of the drain reservoir |
| $\mu_{QDi}$ | chemical potential of the relevant energy level of quantum dot $i$ |
| $n_e$ | 2DEG electron density |
| $N_e$ | number of electrons |
| $N_1$ | number of electrons in quantum dot 1 |
| $N_2$ | number of electrons in quantum dot 2 |
| $N_3$ | number of electrons in quantum dot 3 |
| $N_4$ | number of electrons in quantum dot 4 |
| $N_{TQD}$ | total number of electrons in a triple quantum dot $N_{TQD} = N_1 + N_2 + N_3$ |
| $P$ | power |
| QD1 | quantum dot 1 |
| QD2 | quantum dot 2 |

| | |
|---|---|
| QD3 | quantum dot 3 |
| QD4 | quantum dot 4 |
| $r$ | radius |
| $t$ | time |
| $t_0$ | reference time |
| $t_{int}$ | integration time |
| $\tau$ | time interval between tunneling events |
| $\tau_{ij}$ | residence time ; time interval between a tunneling event into level $i$ and the consecutive tunneling event into level $j$. |
| $\tau_{ii}$ | return time ; time interval between two consecutive events of the same transition |
| $U$ | concentration of substance |
| $V$ | voltage |
| $V_{sd,dot}$ | quantum dot bias voltage |
| $V_{sd,qpc}$ | quantum point contact bias voltage |
| $V_{Bg1}$ | voltage applied to gate Bg1 |
| $V_{Bg2}$ | voltage applied to gate Bg2 |
| $V_{Dg1}$ | voltage applied to gate Dg1 |
| $V_{Dg2}$ | voltage applied to gate Dg2 |
| $V_{Dg3}$ | voltage applied to gate Dg3 |
| $V_{Dg4}$ | voltage applied to gate Dg4 |
| $V_{Tg1}$ | voltage applied to gate Tg1 |
| $V_{Tg2}$ | voltage applied to gate Tg2 |
| $V_{Tg3}$ | voltage applied to gate Tg3 |
| $V_{Tg4}$ | voltage applied to gate Tg4 |
| $V_{Tg5}$ | voltage applied to gate Tg5 |
| $V_{Qg1}$ | voltage applied to gate Qg1 |
| $V_{Qg2}$ | voltage applied to gate Qg2 |
| $V_{th}$ | thermoelectric voltage |
| $V_{QD}$ | voltage applied to a gate capacitively coupled to a quantum dot |
| $V_{QPC}$ | voltage applied to gate capacitively coupled to a quantum point contact |
| $w$ | width |

# **1**

# **Introduction**

Quantum dots are artificially created small objects, in which charge carriers are confined in such a way that they exhibit a discrete energy spectrum. Due to this discrete energy spectrum, quantum dots operate at the level of single charges and single spins. The energy spectrum of the quantum dots can hereby be controlled by, for example, the material basis [1–3], the size [2, 4] and the shape [5, 6] of the quantum dot, as well as by external parameters, such as an applied electric field [7, 8], magnetic field [9, 10], or strain [11, 12]. This combination makes quantum dots versatile building blocks for a variety of quantum technologies. The controllable energy spectrum is, for example, used to fine-tune the optical absorption and emission spectra to improve solar cells [13, 14] or to build high-quality single-photon sources [15, 16] or entangled photon sources [17, 18]. The high level of tunability of quantum dots is also exploited for electronic applications, e.g. to realize accurate single-electron pumps for metrological applications [19, 20] or highly sensitive electrometers [21, 22]. One of the most prominent application of quantum dots is the use of spin states [23–26], charge states [27–31] or hybrids [32, 33] of both to implement qubits for quantum computation by utilizing the high level of control for the initialization, manipulation and read-out procedure.

A variety of quantum technologies, including the qubit application, require the operation of multiple quantum dots. While the use of arrays consisting of multiple quantum dots improves functionality or is even a prerequisite for it, increasing the number of quantum dots simultaneously

increases the parameter space and thus also the tuning complexity. For these technologies, an important task is to achieve the high level of control required for successful operation by implementing efficient and scalable tuning methods for larger arrays of quantum dots.

A detailed understanding of quantum dot arrays is the foundation for implementing such tuning protocols in quantum technologies. Within this thesis, an electrostatically defined quantum dot array with up to four quantum dots in series, based on a GaAs/AlGaAs heterostructure, was investigated. For a double, triple and quadruple quantum dot, electronic transport measurements under variation of gate potentials are used to characterize the quantum dot arrays. With using a sensitive charge detector, the number and distribution of electrons inside the arrays are determined. It is shown, that the quantum dot arrays can be transferred into a regime isolated from the electron reservoirs in a controlled way. In the isolated configuration, the total number of electrons inside the array is fixed, but the electrons can be shuttled between the different quantum dots, which is observable in the charge detector signal. The interdot transitions, including long-range transitions between non-neighboring quantum dots are shown to be robust and highly tunable in the isolated configuration. At the same time, the isolation drastically simplifies the system, especially for small electron numbers. The dynamics of interdot tunneling are discussed based on the statistical analysis on time-resolved single-electron detection in an isolated double quantum dot system.

After this general introduction (**Chapter 1**), the remainder of this thesis is organized as follows:

**Chapter 2 (Fundamentals)** begins with an introduction to the fundamental properties of quantum dots. Furthermore, the coupling mechanisms in multiple quantum dot systems are discussed and finally an introduction to charge detection using a quantum point contact is given.

**Chapter 3 (Experimental basics)** covers the experimental basics. First, the fabrication process for the quadruple quantum dot structure is

explained, followed by a description of the measurement setup. The last part of the chapter introduces the measurement methods on the example of characteristic single quantum dot measurements.

**Chapter 4 (Transport through Quantum Dot Arrays)** focuses on transport measurements through quantum dot arrays with different numbers of quantum dots. The transport properties of a double, triple and a quadruple quantum dot array are discussed. For each array size, the system is characterized based on low bias measurements, followed by bias dependent transport, where the internal level structure greatly influences the transport properties.

**Chapter 5 (Transport in Quantum Dot Arrays)** again investigates the double, triple and quadruple quantum dot arrays, but in the regime isolated from the electron reservoirs. The charge detector is used to track the electrons tunneling inside the quantum dot arrays, from one quantum dot to another. In addition to the experimental data, capacitance model simulations are used to interpret the results. The interdot transitions are shown to be robust and highly tunable, including long range transitions between non-neighboring quantum dots. A controlled procedure for loading a predefined number of electrons into the array is discussed for the triple quantum dot. It is shown, that the complexity of the stability diagrams drastically reduces, when only a single or two electrons are isolated inside the triple quantum dot array.

**Chapter 6 (Time-Resolved Electron Tunneling)** investigates the dynamics of electrons isolated in a double quantum dot based on time-resolved charge detection. First, the digitization procedure is introduced on the example of a single electron loaded into the double quantum dot. Statistical quantities are introduced and discussed in comparison to a single quantum dot coupled to electron reservoirs. With two electrons isolated in the double quantum dot, competing rates emerge due to spin-flips and spin blockade. Finally, the three-electron double quantum dot is investigated. The detector signal here switches between eight different

levels, with most of the transition rates between these levels showing a significant time dependency. This time-dependency is analyzed in detail.

The thesis concludes with summarizing the results in **Chapter 7 (Summary)** and providing complementary data in the **Appendix**.

# 2
# Fundamentals

This chapter provides an introduction into the fundamentals necessary to understand the properties of quantum dots and for the analysis and evaluation of transport through and in quantum dot arrays. The beginning will be an introduction on the basic properties of single quantum dots and their transport characteristics, followed by coupling mechanisms and coupled quantum dots. The chapter concludes with the introduction of the charge detection principle using a quantum point contact.

## 2.1. Quantum Dots

Due to their similarity to real atoms, quantum dots are often called artificial atoms [34–36]. Confinement in all three spatial dimensions leads to a discrete energy spectrum of quantum dots, which allows the quantum dot to bind a defined number of electrons N, similar to a real atom. The confinement potential of a quantum dot however, which defines the energetic spectrum, strongly depends on the size, material, and symmetry of the quantum dot. Quantum dots exist for a wide range of these parameters. From few nanometer sized quantum dots, for example based on phosphorous donors in silicon [37, 38] to hundreds of nanometers using gate defined quantum dots based on a two-dimensional electron gas (2DEG). The latter type is used within the scope of this work and brings the advantage of a large spatial dimension compared to real atoms. This allows the installation of electrical contacts and control gate electrodes

to the quantum dots using standard lithographic techniques [5, 39–42], enabling the electrical investigation of quantum dot systems.
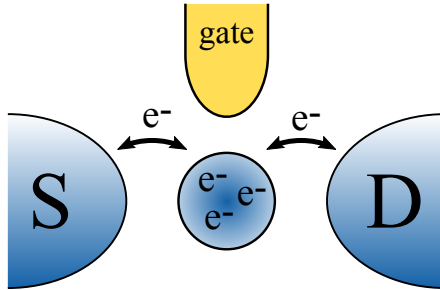


**Figure 2.1.:** Schematic representation of a QD connected to two electron reservoirs source (S) and drain (D) via tunnel barriers. Electrons are exchanged with the electron reservoirs via stochastic tunneling events. A control gate electrode in the vicinity couples capacitively to the quantum dot and allows tuning the number of electrons bound on the QD.

A schematic of a quantum dot, tunnel coupled to two electron reservoirs source (S) and drain (D), is shown in figure 2.1. A control gate electrode in the vicinity acts as an electrostatic tuning mechanism for the quantum dot. Charging and discharging of the quantum dot occurs via tunneling events from or into one of the electron reservoirs. By applying a voltage $V_G$ to the control gate electrode, the discrete energy levels of the quantum dot can be energetically shifted, allowing to manipulate the number of electrons $N$ bound on the quantum dot. At the transition between two different charge states $N$ and $N+1$, energy conserving (elastic) electron tunneling between the electron reservoirs and the quantum dot is possible and the charge of the quantum dot fluctuates between $N$ and $N+1$ electrons.

One of the characteristic parameters of a quantum dot is the charging energy $E_C \approx e^2/C_\Sigma$, where $e$ is the elementary charge and $C_\Sigma$ is the total capacitance of the quantum dot. The charging energy is the additional energy, that has to be provided to load an additional electron into the

quantum dot. The charging energy is the energy scale, which defines the conditions under which single-electron charging and transport phenomena become observable. There are two fundamental criteria to be fulfilled. First, the thermal energy has to be small compared to the charging energy of the quantum dot

$$k_B T \ll E_C, \tag{2.1}$$

where $k_B$ is the Boltzmann constant and $T$ is the temperature. This ensures, that only one energy level of the quantum dot is energetically accessible for elastic tunneling between the quantum dot and the electron reservoirs.

Second, the coupling between quantum dot and electron reservoirs has to be weak, so that the electrons are localized in the quantum dot. For this purpose, the conductance $G_{dot}$ of the quantum dot has to be small compared to the conductance quantum [42–44]

$$G_{dot} \ll \frac{e^2}{h}, \tag{2.2}$$

with elementary charge $e$ and Planck constant $h$. This second criterion can be derived from the time-energy uncertainty relation $\Delta t \Delta E > h$, where $\Delta t = RC_\Sigma$ is the RC-time constant of the quantum dot, i.e., the time it takes to charge or discharge the quantum dot. Resolving the energy difference $\Delta E = E_C \approx e^2/C_\Sigma$, the charging energy of the quantum dot, therefore requires a resistance $R > h/e^2$. Using $G_{dot} = 1/R$ then yields equation 2.2. This implies, that the conductance of a channel coupling a quantum dot to a reservoir has to be well below the ballistic regime i.e., deep in the tunneling regime.

In general, the energy spectrum of a quantum dot consists of two contributions. The *excitation spectrum*, originating from the energy quantization due to the spatial confinement of the electrons, and the *addition spectrum*, which is a result of the Coulomb repulsion between multiple electrons in one quantum dot. Which one of the two contribution domi-

nates, depends on the Fermi-wavelength of the electrons and the size of the quantum dot. Whilst the Coulomb repulsion is typically the dominant energy contribution in metallic quantum dots [45, 46], the confinement energy can become dominant in semiconductor quantum dots.

An approximation of the energy spectrum $\mu_m(N)$ can be given within the constant interaction model. Two important assumptions feed into this model. First, the Coulomb interaction of an electron on the quantum dot is described by a single constant capacitance, the total capacitance $C_\Sigma$. Second, all other interactions except the Coulomb interaction are neglected. The charging energy then writes to [5, 7, 47]

$$E_C \approx \epsilon_{N+1} - \epsilon_N + \frac{e^2}{C_\Sigma},$$

(2.3)

which is only a function of the single particle states $\epsilon_m$ and the total capacitance $C_\Sigma$ of the quantum dot.

### 2.1.1. Excitation Spectrum

The excitation spectrum is the single particle energy spectrum of the quantum dot. It is defined by the confinement potential in all three dimensions and can be obtained by solving the Schrödinger equation. For a gate defined quantum dot based on a 2DEG, the confinement in z-direction is already given by the 2DEG material. The 2DEG typically provides a real two-dimensional system, where only the first subband $E_z^1$ is occupied in z-direction. For gate defined confinement in the remaining two dimensions, an isotropic two-dimensional harmonic potential of the form

$$V(x,y) = \frac{1}{2}m^*\omega_o^2|\vec{r}|^2,$$

(2.4)

with the electron effective mass $m^*$, the radial frequency $\omega_o$, and the radius of the quantum dot $|\vec{r}|^2 = x^2+y^2$, is considered a good approximation [48].

This approximation allows to use the well known Hamilton operator of a two-dimensional harmonic oscillator

$$\mathbf{H} = -\frac{\hbar^2}{2m^*}\nabla^2 + V(\vec{r}). \tag{2.5}$$

with energy eigenvalues

$$\epsilon_{n,l} = (2n + |l| + 1)\hbar\omega_0, \tag{2.6}$$

with radial quantum number $n \in \mathbb{N}_0$, angular momentum quantum number $l = 0, \pm 1, \pm 2, ...$, reduced Planck constant $\hbar$, and radial frequency $\omega_0$. In absence of a magnetic field, which is the $B = 0$ case of the popular Fock-Darwin spectrum [49, 50], the energy spectrum consists of equidistant energy levels, which are separated by $\hbar\omega_0$ in energy. Including a factor of 2 due to spin degeneracy, each of these energy levels consists of a set of $2(n+1)$ degenerate states. In analogy to real atoms, each set of degenerate states can be regarded as an electron shell, where each shell can hold up to $2(n+1)$ electrons, leading to magic numbers $N = 2, 6, 12, 20, ...$ for completely filled shells [10].

For a 2DEG with only one subband occupied, the confinement in z-direction only adds the constant subband energy $E_z^1$ to all states of this single particle spectrum.

### 2.1.2. Addition Spectrum

Whereas the excitation spectrum is a single particle spectrum, the addition spectrum approximates the energy spectrum for multiple electrons in the quantum dot. With more than one electron, interactions between the electrons have to be taken into account. The constant interaction model hereby only takes the Coulomb interaction into account and assumes all other interactions (screening, exchange interaction,...) to be negligible. The quantum dot is described by a total capacitance $C_\Sigma$, which is inde-

pendent of the number of electrons N. When loading electrons into the quantum dot, the electrons successively occupy the single particle states of the excitation spectrum. The ground state energy of a quantum dot loaded with N electrons then becomes

$$E(N) = \sum_{m=1}^{N} \epsilon_m + \sum_{n=1}^{N-1} n \frac{e^2}{C_\Sigma}$$
$$= \sum_{m=1}^{N} \epsilon_m + \frac{1}{2}N(N-1)\frac{e^2}{C_\Sigma}. \qquad (2.7)$$

Each additional electron in the quantum dot increases the total energy of the quantum dot. This increase in total energy for increasing the number of electrons from $N-1$ to N is the chemical potential

$$\mu(N) = E(N) - E(N-1) = \epsilon_N + (N-1)\frac{e^2}{C_\Sigma}. \qquad (2.8)$$

The energy difference between consecutive chemical potentials is then the additional energy, that has to be provided to load an additional electron into the quantum dot, the charging energy

$$E_C = \mu(N+1) - \mu(N) = \epsilon_{N+1} - \epsilon_N + \frac{e^2}{C_\Sigma}. \qquad (2.9)$$

### 2.1.3. Electrostatic Model

The preceding calculations can be extended to an electrostatic model of a quantum dot. The model introduces capacitively coupled elements to describe the environment of the quantum dot and is capable of explaining the observation of Coulomb blockade in electronic transport measurements. Figure 2.2 (a) shows a circuit diagram of a quantum dot, tunnel coupled to two electron reservoirs, and capacitively coupled to a single gate electrode. For this situation, the total capacitance of the quantum
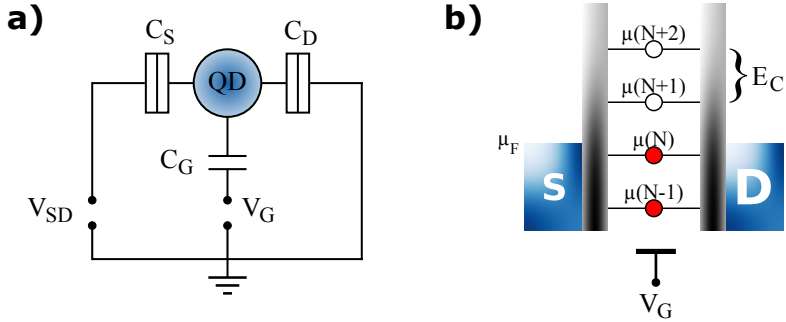
**Figure 2.2.: (a)** Circuit diagram of a QD coupled to two reservoirs and a gate electrode. The total capacitance of the quantum dot $C_\Sigma = C_S + C_D + C_G$ is given by the sum of the source, drain and gate capacitance. **(b)** Schematic energy diagram of a QD. The charging energy $E_C$ is the energy difference between two successive energy levels, i.e. between the ground state chemical potentials of two successive electron numbers. Up to the Fermi energy $\mu_F$, the energy levels of the QD are occupied by electrons, levels above $\mu_F$ are unoccupied. Without an applied bias voltage $V_{SD}$, the electron reservoirs S and D are coequal. A gate voltage $V_G$ acts as an electrostatic tuning mechanism for the states $\mu(N)$ of the quantum dot and thereby allows to control the number of electrons $N$ in the quantum dot.

dot $C_\Sigma$ is given by

$$C_\Sigma = C_S + C_D + C_G. \tag{2.10}$$

In general, the number of capacitances is not limited and a generalized form of equation 2.10 is given by $C_\Sigma = \sum_i C_i$.

This electrostatic model assumes the environmental contributions to be of purely electrostatic nature. The single particle spectrum of the quantum dot is therefore independent of these contributions. In contrast, the electrostatic energy of the quantum dot is affected by the environmental contributions. Being previously defined by the number of charges in the quantum dot, which can only change in integers, the environment now contributes an additional continuous part, which couples capacitively to the quantum dot. For N electrons, the ground state energy of the quantum dot becomes

$$E(N) = \sum_{m=1}^{N} \epsilon_m + \frac{1}{2C_\Sigma} \left( -e(N - N_0) + \sum_i C_i V_i \right)^2, \tag{2.11}$$

where $N_0$ denotes the number of electrons populating the quantum dot without any voltages applied $V_i = 0$, which compensate the background doping. The modified total energy $E(N)$ also affects the electrochemical potential $\mu(N) = E(N) - E(N-1)$. For a set of fixed voltages $V_i$, the electrochemical potential becomes

$$\mu(N) = \epsilon_N + (N - N_0 - \frac{1}{2}) \frac{e^2}{C_\Sigma} - e \sum_i \frac{C_i}{C_\Sigma} V_i. \tag{2.12}$$

In contrast, the characteristic charging energy $E_C = \mu(N+1) - \mu(N) = \epsilon_{N+1} - \epsilon_N + \frac{e^2}{C_\Sigma}$ is of the same form as in the addition spectrum in equation 2.9, where environmental contributions were not explicitly taken into account, but only implicitly as part of $C_\Sigma$. As equation 2.10 shows, the environmental contributions define the total capacitance $C_\Sigma$, which feeds into the charging energy.

Using the electrochemical potentials $\mu(N)$, a schematic energy diagram as shown in figure 2.2 (b) can be set up for the quantum dot. The quantum dot is hereby depicted by the electrochemical potentials for different electron numbers, which will be referred to as energy levels in the following. The two-dimensional electron reservoirs source (S) and drain (D) are occupied by electrons up to the Fermi level $\mu_F$ and separated from the quantum dot by tunneling barriers, which are depicted in grey. The number of electrons $N$ in the quantum dot depends on the electrochemical potentials of the electron reservoirs, which are $\mu_S, \mu_D = \mu_F$ at zero bias voltage. As long as $\mu(N) < \mu_F$, the quantum dot is then charged with electrons.

The last term of equation 2.12 interconnects the internal energies of the quantum dot with externally applied voltages $V_i$. Changing the voltage applied to a gate or an electron reservoir by $\Delta V_i$ shifts all energy levels $\mu(N)$ with respect to the Fermi level $\mu_F$ by

$$\Delta \mu = -e \frac{C_i}{C_\Sigma} \Delta V_i = -e \alpha_i \Delta V_i, \qquad (2.13)$$

where $\alpha_i = C_i/C_\Sigma$ is called the lever arm. This relation can now be utilized to manipulate the number of electrons in the quantum dot. A quantum dot loaded with $N$ electrons will be charged by an additional electron, when $\mu(N + 1) < \mu_F$ or discharged by one electron when $\mu(N) > \mu_F$, which can be achieved by varying an external gate voltage $V_G$.

### 2.1.4. Transport Spectroscopy

Electronic transport experiments are a method for obtaining information about the energy spectrum of a quantum dot and have become a common tool for the investigation of semiconductor quantum dots. In analogy to the optical approach, this approach is called transport spectroscopy [5, 42, 51].

Due to the discrete energy spectrum of quantum dots, energy conserv-

ing (elastic) electron tunneling between a quantum dot and the coupled electron reservoirs can be allowed or blocked, depending on the energetic alignment of the quantum dot energy levels with respect to the reservoir chemical potentials $\mu_S, \mu_D$. Schematic energy diagrams for three different configurations are given in figure 2.3 (a). The first diagram shows a quantum dot charged with N electrons. The energy level $\mu(N)$ lies well below the reservoir chemical potentials $\mu_S, \mu_D$. In this alignment, electrons cannot tunnel out of the quantum dot, since all energetically available states in the reservoirs are occupied. The energy level $\mu(N+1)$ lies well above the reservoir chemical potentials $\mu_S, \mu_D$. Since all occupied states in the reservoirs are lower in energy than $\mu(N + 1)$, no additional electron can tunnel into the quantum dot. This situation, where both, tunneling in and tunneling out processes are forbidden, is called the Coulomb-blockade. From an electrostatic point of view, two approaches can be used to lift this Coulomb-blockade, and drive a tunneling current $I_{dot}$ through the quantum dot.

The first approach utilizes a gate, capacitively coupled to the quantum dot. By variation of the gate voltage $V_G$, the energy levels of the quantum dot are shifted with respect to $\mu_S, \mu_D$, according to equation 2.13. More positive voltage hereby leads to decreasing energy. For example, a gate voltage change of $\Delta V_G = \frac{E_C}{e\alpha_G}$ results in an energy shift of $\Delta\mu = -e\alpha_G\Delta U_G = -E_C$. Beginning from the situation mentioned before, this results in $\mu(N + 1) < \mu_S, \mu_D$, meaning, in equilibrium, the quantum dot is occupied by one additional electron. At the transition point between the two electron numbers, $\mu(N + 1)$ is in resonance with the reservoirs. In this situation, electrons can tunnel into and out of the quantum dot, as depicted in the second energy diagram in figure 2.3 (a). Here, the electron number fluctuates between N and $N + 1$ electrons and already a small bias voltage $V_{sd,dot} \ll E_C$ drives a tunneling current $I_{dot}$ through the quantum dot. The third energy diagram shows a situation similar to the first, where the quantum dot again is in Coulomb-

blockade, but with one additional electron populating the quantum dot.

This cycle repeats for every transition between two electron numbers. Finite conductance $G_{dot}$ is only found close to the resonances between a quantum dot energy level and the reservoirs. As function of a gate voltage $V_{G1}$, this leads to a series of sharp peaks [43, 52, 53] in the quantum dot conductance $G_{dot}$, as schematically depicted in figure 2.3 (b).

The charging energy $E_C$ and the lever arm of the gate $\alpha_{G1}$ hereby define the gate voltage distance $\Delta V_{G1} = \frac{E_C}{e\alpha_{G1}}$ between two conductance peaks. For large quantum dots, where the capacitive contribution to the charging energy dominates ($\epsilon_{N+1} - \epsilon_N \ll \frac{e^2}{C_\Sigma}$), this relation can be used to directly determine the gate capacitance

$$C_{G1} = \frac{e}{\Delta V_{G1}}. \tag{2.14}$$

The shape of a Coulomb peak can be regarded as the evolution of the probability to transfer electrons from one reservoir to the other as function of the energy detuning between the quantum dot energy levels and a reference potential. Thus, the exact lineshape is not only defined by the properties of the quantum dot, but is determined by the interplay between quantum dot and reservoirs. Overall, this leads to a variety of different lineshapes, depending on the conditions of the involved energy scales. For small bias voltages, the most relevant energy scales are given by the charging energy $E_C$, the quantization energy $\Delta E$, the couplings $\widetilde{\Gamma}_S$ and $\widetilde{\Gamma}_D$ between quntum dot and reservoirs, and the thermal energy $E_{th} = k_B T$. Calculated lineshapes for different relations between these quantities can for example be found in Refs. [42, 43, 54]. Experimentally, the peak amplitudes and widths for successive electron numbers in a quantum dot are not expected to be equal or change in a monotonic way. A variety of parameters play a role here, for example the experimentally always present cross-coupling and possibly asymmetric effect of the gate voltage on the tunnel barriers [55], the electron number dependency of degenerate states
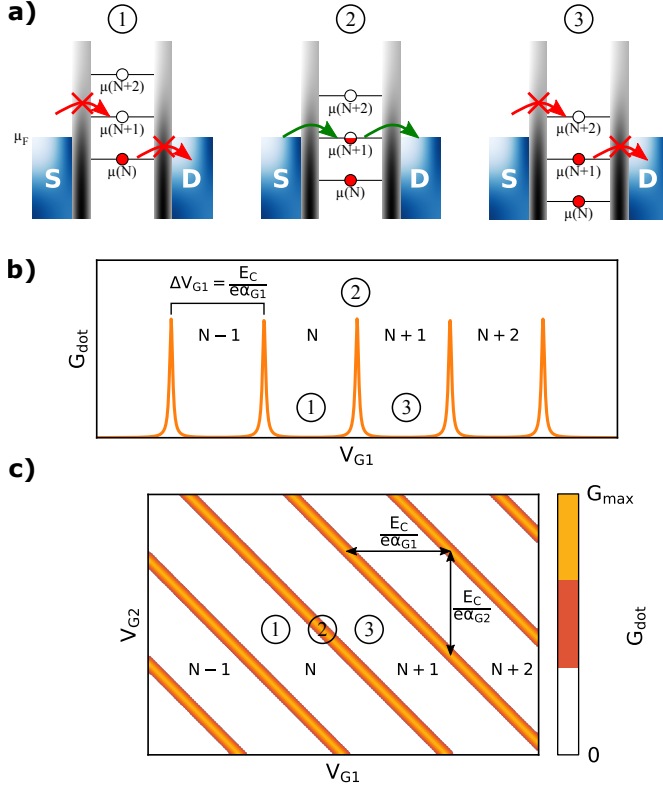
**Figure 2.3.: (a)** A gate voltage $V_{G1}$ can be used to shift the energy levels of a QD. This allows to tune a QD energy level into resonance with the Fermi level $\mu_F$ of the reservoirs. **(b)** The conductance $G_{dot}$ as function of gate voltage $V_{G1}$ then exhibits a series of sharp peaks, where each peak corresponds to a transition between two specific electron numbers N. The distance between two peaks $\Delta V_{G1} = E_C/(e\alpha_{G1})$ is hereby defined by the charging energy $E_C$ and the lever arm of the gate $\alpha_{G1}$. **(c)** As function of two gate voltages $\Delta V_{G1}$ and $\Delta V_{G2}$, a stability diagram is obtained. An energy level shift induced by one gate can be compensated via the other, leading to the occurrence of parallel charging lines. The slope of these charging lines $-\alpha_{G1}/\alpha_{G2}$ is directly given by the lever arm ratio.

available for tunneling in or out of the quantum dot [56], or modified coupling depending on the wave function of the specific state available for tunneling [57, 58].

The second electrostatic approach to lift the Coulomb blockade in quantum dot devices is based on opening a transport window by applying a bias voltage $V_{SD}$. The following assumes the bias voltage to be applied to the source (S) reservoir while the drain (D) reservoir remains at the reference potential. The electrochemical potentials are thus related via $\mu_S = \mu_D - eV_{SD}$. The energy schematics (1)-(3) in figure 2.4 show three simplified energy schemes illustrating the influence of a bias voltage $V_{SD}$. Schematic (1) hereby shows a situation $V_{SD} < 0$, schematic (2) corresponds to $V_{SD} = 0$, and schematic (3) illustrates $V_{SD} > 0$. While (2) again shows a Coulomb blockaded situation, an applied bias voltage opens up an energy window, where occupied states are found in one reservoir while unoccupied states are present in the other reservoir. This energy window is called the transport window. Whenever an energy level $\mu(N)$ of the quantum dot, i.e. the ground state chemical potential for the N-th electron, lies energetically inside this transport window, electrons can tunnel into the quantum dot from one reservoir and tunnel out to the other reservoir, leading to a finite conductance. With one energy level available for transport, the system is in the single electron transport regime, where the sign of the bias voltage dictates the direction of tunneling. For larger bias voltages $|eV_{SD}| \geqslant E_C$, it is possible to have multiple energy levels inside the bias window. Without interactions, each energy level hereby contributes a parallel transport channel. As function of the bias voltage, this leads to a step-like change of the current for each state entering or leaving the transport window, as shown in figure 2.4 (b). On a plateau, the occupation of the quantum dot fluctuates between the annotated numbers of electrons.

In addition to the steps due to ground states entering and leaving the bias window, each excited state $\mu_m(N)$ with $m \geqslant 1$ entering or leaving
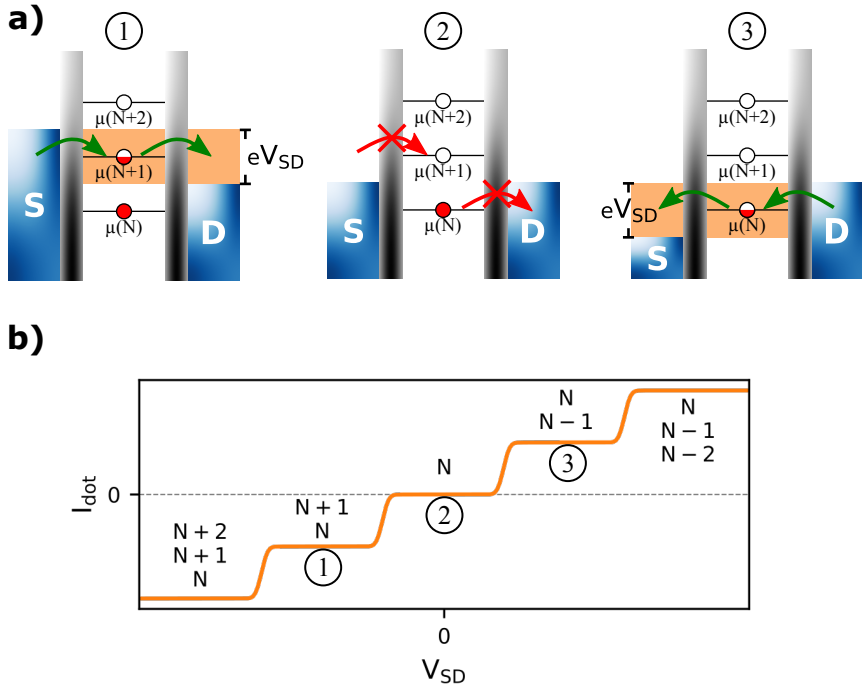
**Figure 2.4.: (a)** Energy level schematics for different bias voltages $V_{SD}$ applied to the source reservoir with (1) $V_{SD} < 0$, (2) $V_{SD} = 0$, and (3) $V_{SD} > 0$. The applied bias voltage opens up a transport window of size $eV_{SD}$. Tunneling through the quantum dot becomes possible, when at least one energy level of the quantum dot lies inside the transport window. The direction of tunneling is defined by the sign of $V_{SD}$. **(b)** Current through the quantum dot as function of the bias voltage $V_{SD}$. An energy level entering (leaving) the transport window adds (removes) one transport channel, leading to steps in the current through the quantum dot. Each level inside the bias window can be either occupied or unoccupied, so that each plateau in the current corresponds to certain numbers of electrons between which the quantum dot fluctuates.

the bias window also provides a parallel channel, but only for tunneling into the quantum dot. As soon as an electron has tunneled into the quantum dot, the electron resides there in a specific state, so that there is no additional channel for tunneling out. Excited states can thus lead to additional but smaller steps in the current $I_{dot}$ as function of the bias voltage $V_{sd,dot}$.

Combining the two parameters, the gate voltage $V_G$ and the bias voltage $V_{SD}$, provides a powerful tool for the spectroscopic investigation of quantum dots. As function of these two parameters, quantum dots show a characteristic pattern, the so called Coulomb diamonds. A schematic of the resulting pattern is shown in figure 2.5. Two sets of parallel lines emerge, one set with positive slopes and a second set with negative slopes, together forming the characteristic diamond shaped pattern. Each individual line hereby corresponds to a unique resonance between a quantum dot state and one of the reservoirs. Since the drain potential is fixed, a resonance between a quantum dot state and the drain reservoir ($\mu_N = \mu_D$) follows $\Delta\mu_N = -e\frac{C_G}{C_\Sigma}V_G - e\frac{C_S}{C_\Sigma}V_{SD} = 0$, where $C_S$ is the source capacitance. A more positive $V_{SD}$ has thus to be compensated by a more negative $V_G$ and vice versa, leading to the negative slope $m_D = -\frac{C_S}{C_G}$. Similarly, a resonance between a quantum dot state and source ($\mu_N = \mu_S = \mu_D - eV_{SD}$) follows $\Delta\mu_N = -e\frac{C_G}{C_\Sigma}V_G - e\frac{C_S}{C_\Sigma}V_{SD} = -eV_{SD}$. According to eq. 2.10, the resulting slope $m_S = \frac{C_\Sigma - C_S}{C_G}$ is always positive, since $C_S$ is an additive component of $C_\Sigma$. Combined with the gate capacitance $C_G$ the two slopes allow to calculate the total capacitance of the quantum dot

$$C_\Sigma = C_G(m_S - m_D). \tag{2.15}$$

A vertical cut through the Coulomb diamonds at $V_{SD} = 0$ crosses several intersections of the source and drain resonances. This results in a series of Coulomb blockade peaks, as has been discussed in the context of figure 2.3. However, additional intersection points are present at finite bias voltages. The two energy schematics (4) and (5) in figure 2.5
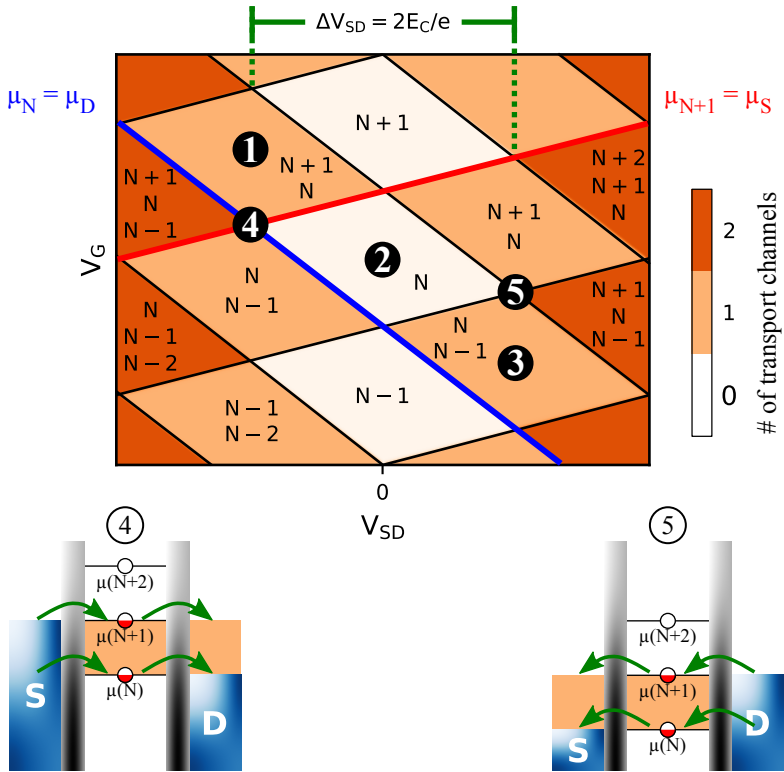
**Figure 2.5.:** Combining the bias voltage $V_{SD}$ dependence and gate voltage $V_G$ dependence results in the so called Coulomb diamonds. Each diamond corresponds to a fixed number of energy levels inside the bias window. For a bias voltage applied at the source reservoir, the boundaries of the diamonds are given by resonances of an energy level with the chemical potentials of source $\mu_S$ (positive slope) and drain $\mu_D$ (negative slope). Numbers (1) - (3) are identical to figure 2.4, (4) and (5) mark special points, where two successive energy levels of the QD ($\mu_N$, $\mu_{N+1}$) are resonant with $\mu_S$ and $\mu_D$, respectively. The charging energy $E_C$ can therefore directly be obtained from the width of the Coulomb diamond.

illustrate the energetic situations at the positions marked by (4) and (5) in the schematic Coulomb diamonds. At position (4), the two resonances $\mu_{N+1} = \mu_S$ and $\mu_N = \mu_D$ intersect. Due to $\mu_S = \mu_D - eV_{SD}$ this provides a direct experimental access to the charging energy $E_C$ of the quantum dot via

$$\mu_S - \mu_D = \mu_{N+1} - \mu_N =: E_C = -eV_{SD}. \tag{2.16}$$

Similarly, the situation (5), where $\mu_S = \mu_N$ and $\mu_D = \mu_{N+1}$ intersect, can be rearranged to

$$\mu_D - \mu_S = \mu_{N+1} - \mu_N =: E_C = eV_{SD}. \tag{2.17}$$

For an experimental determination of the charging energy $E_C$ from Coulomb diamond measurements, it is beneficial to use the relation $\Delta V_{SD} = 2E_C/e$ with $\Delta V_{SD}$ being the width of the diamond in $V_{SD}$-direction. In contrast to using only one corner of the diamond, this method is insensitive to offsets in $V_{SD}$. At the same time, the $\mu_S = \mu_N = \mu_D$ resonances in the Coulomb diamonds allow to determine any experimental offsets in $V_{SD}$.

In combination with the charging energy $E_C$, the height $\Delta V_G$ of the diamond allows to precisely determine the lever arm of the gate $\alpha_G = E_C/(\Delta V_G)$, which interconnects a change of an external parameter with the energy shift of the quantum dot levels.

## 2.2. Coupled Quantum Dots

A system of coupled quantum dots is obtained by bringing two or more quantum dots in close proximity to each other, so that interactions between the quantum dots become important. In addition to the interactions, each quantum dot in a multiple quantum dot system also contributes its own energy scale to the total system. The stability diagram of

a system consisting of $n$ quantum dots thus becomes $n$-dimensional. Independent control over the electron numbers of each quantum dot therefore requires at least one independently tunable parameter per quantum dot in the system. In the following, the basic control and coupling mechanisms will be introduced using the example of a serial double quantum dot, the smallest possible coupled quantum dot system.
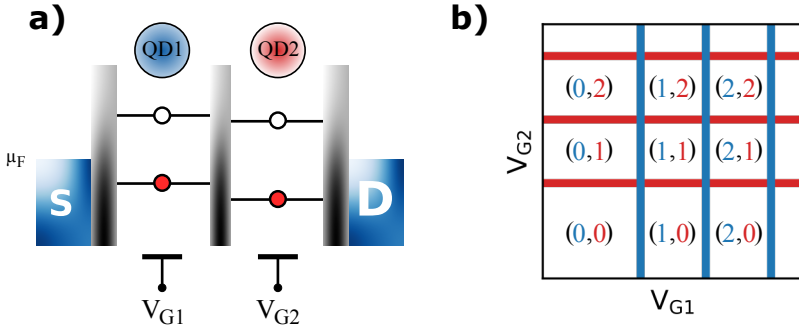


**Figure 2.6.: (a)** Energy level schematic of a serial double quantum dot. The two gate voltages $V_{G1}$ and $V_{G2}$ act as electrostatic tuning parameters for the energy levels of the two quantum dots. **(b)** Schematic charge stability diagram of a in the absence of coupling. The numbers in brackets denote the charge configurations $(N_1, N2)$ in QD1 and QD2. Without cross coupling of the gates, the charging lines are vertical (QD1, blue) and horizontal (QD2, red). The crossing points are quadruple points, which connect for different charge configurations. This situation corresponds to uncoupled quantum dots, far apart from each other.

A simplified energy schematic of a double quantum dot is shown in figure 2.6 (a). The two quantum dots are connected in series between the two electron reservoirs and are separated by a tunnel barrier. In analogy to the single quantum dot, the two quantum dots QD1 and QD2 are depicted by their individual ladder of electrochemical potentials $\mu(N_1)$ and $\mu(N_2)$, where $N_1$ ($N_2$) is the number of electrons in QD1 (QD2). The charging energies $E_{C1}$ of QD1 and $E_{C2}$ of QD2 are thus considered parameters of the individual quantum dots and do not have to be equal. Panel (b) shows,

as a reference, a schematic double quantum dot stability diagram in the absence of interdot coupling. Gate voltage $V_{G1}$ acts as an electrostatic tuning mechanism for QD1 via $\Delta\mu_{QD1} = -e\alpha_{G1,1}V_{G1}$ (equation 2.13), where $\alpha_{j,i}$ is the lever arm of gate $j$ with respect to QD$i$. $V_{G2}$ acts as an electrostatic tuning mechanism for QD2 via $\Delta\mu_{QD2} = -e\alpha_{G2,2}V_{G2}$, respectively. Without any cross-capacitances ($\alpha_{G1,2} = \alpha_{G2,1} = 0$), the double quantum dot stability diagram consists of a series of vertical charging lines (blue) for charging of QD1, combined with a series of horizontal charging lines (red) for charging of QD2. The numbers in brackets $(N_1, N_2)$ denote the number of electrons in QD1, QD2. Each time one of the blue (red) lines is crossed, the charge on QD1 (QD2) changes by one electron. At the intersection points, a state of QD1 is resonant with a state of QD2 and with the Fermi level, $\mu_{QD1}(N_1) = \mu_{QD2}(N_2) = \mu_F$. These intersection points are so-called quadruple points, where four different charge configurations are degenerate. These are the only points in the stability diagram, where non of the quantum dots is in Coulomb-blockade and thus the only points, where current is expected to flow through the serial double quantum dot. However, the situation shown in figure 2.6 (b) is only a good approximation for distant quantum dots, where the interdot coupling and the cross-capacitances of the gates become negligible.

### 2.2.1. Capacitive coupling

For quantum dots in close proximity, both the interdot coupling and the cross-capacitances have to be taken into account. An important interdot coupling mechanism is the capacitive coupling due to the classical Coulomb repulsion. The electrons on the first quantum dot hereby repel other negative charges in their environment and thus increase the energy needed to load electrons into the second quantum dot, and vice versa.

Figure 2.7 (a) shows a circuit diagram of a serial double quantum dot. Each quantum dot is capacitively coupled to a gate electrode. The key new feature is the capacitive coupling between the two quantum dots,

the mutual capacitance $C_m$. Following the constant interaction model and Refs. [22, 42, 59, 60], as well as neglecting all cross-capacitances, the energy of the double quantum dot becomes

$$
\begin{aligned}
E(N, M) = &\sum_{i=1}^{N} \epsilon_i + \frac{E_{C1}}{2} N(N-1) - \frac{N E_{C1} + M E_m}{e} \left( C_{G1} V_{G1} + C_S V_S \right) \\
&+ \sum_{j=1}^{M} \epsilon_j + \frac{E_{C2}}{2} M(M-1) - \frac{M E_{C2} + N E_m}{e} \left( C_{G2} V_{G2} + C_D V_D \right) \\
&+ E_m N M.
\end{aligned}
\tag{2.18}
$$

N and M are hereby the electron numbers on the first and the second quantum dot, respectively, and with $C_{\Sigma 1(2)}$ being the total capacitance of the first (second) single quantum dot, the term

$$
E_m = \frac{e^2}{C_m} \left( \frac{C_{\Sigma 1} C_{\Sigma 2}}{C_m^2} - 1 \right)^{-1}
\tag{2.19}
$$

is the mutual charging energy, the additional energy required to add an electron to one of the quantum dots due to a single electron in the other. $E_{C1}$ and $E_{C2}$ describe the electrostatic part of the individual quantum dot charging energies with

$$
E_{C1(2)} = \frac{e^2}{C_{\Sigma 1(2)}} \left( 1 - \frac{C_m^2}{C_{\Sigma 1} C_{\Sigma 2}} \right)^{-1} .
\tag{2.20}
$$

The mutual capacitance thus leads to a correction factor to the electrostatic energies of the uncoupled quantum dots. This factor is always larger than one due to $C_{\Sigma 1}$ and $C_{\Sigma 2}$ both being sums that include $C_m$. For vanishing $C_m$ the correction factor becomes 1.

With including the capacitive coupling and also including the effect
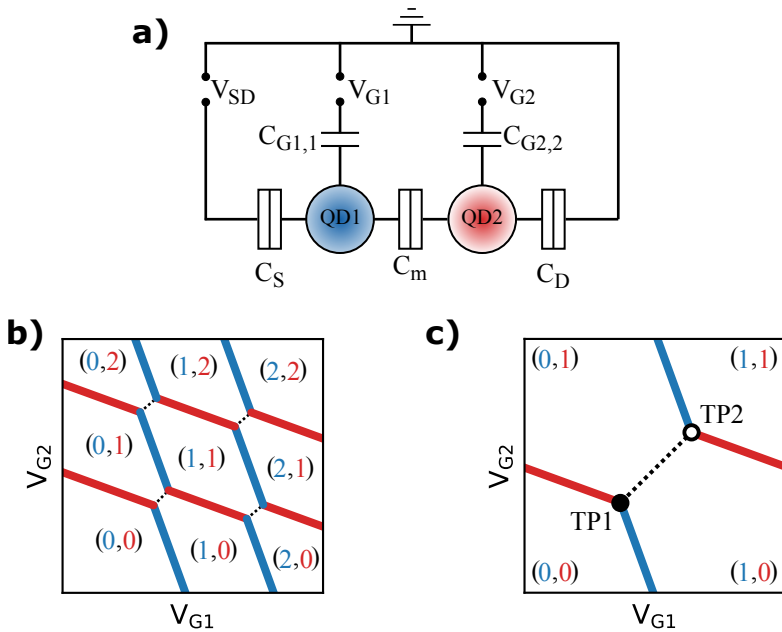
**Figure 2.7.: (a)** Circuit diagram of a serial double quantum dot. Each of the two quantum dots is capacitively coupled to a gate electrode and one of the reservoirs. The mutual capacitance between the two quantum dots is given by $C_m$. The boxes depicting reservoir coupling and interdot coupling consist of resistor and capacitor in parallel. Annotation of the resistances was left out for visual clarity. **(b)** Schematic charge stability diagram of a capacitively coupled double quantum dot with denoted electron numbers $(N_1, N_2)$. Including the more realistic scenario of cross coupling of the gates, the horizontal and vertical lines turn into lines of two different slopes. The mutual charging energy $E_m$ due to the interdot capacitance $C_m$ introduces an energy gap between the $(N_1, N_2)$ and $(N_1 + 1, N_2 + 1)$ states. Each additional electron in one of the quantum dots shifts the charging lines of the other dot. **(c)** Zoom into one of the resonances. The energy gap splits the former quadruple point into two triple points TP1 and TP2. At these triple points, already a small bias voltage drives a tunneling current through the serial double quantum dot.

of cross-capacitances, a schematic stability diagram is shown in figure 2.7 (b). The stable charge configurations $(N_1, N_2)$ are again denoted in brackets. The blue lines correspond to charging lines of QD1, the red lines to those of QD2. As function of gate voltages $V_{G1}$ and $V_{G2}$ the charging lines now have a finite slope due to the cross-capacitances. In addition, the interdot capacitive coupling results in a splitting of the intersection points of the charging lines. The mutual charging energy lifts the degeneracy of the $(N_1, N_2)$ and $(N_1 + 1, N_2 + 1)$ at the intersection points, so that the former quadruple point is separated into two triple points, where three different charge configurations are degenerate.

Including multiple of these split resonances results in the double quantum dot characteristic honeycomb pattern [59]. Figure 2.7 (c) shows a zoom into one of these split resonances with the two marked triple points TP1 and TP2, split by the mutual charging energy $E_m$. For both of these triple points, it is possible to transfer a charge from one reservoir into the other reservoir by cycling through the degenerate charge states. For TP1 (filled circle), beginning in the $(0, 0)$ configuration, an electron can tunnel from the left reservoir into the left QD1, further into the right QD2, and tunnel out into the right reservoir. A small (negative) bias voltage applied to the left reservoir thus allows to drive a current through the double quantum dot via the cycle $(0, 0) - (1, 0) - (0, 1) - (0, 0)$. A similar cycle can be found for TP2 (open circle). For the same bias direction and starting from the double occupied $(1, 1)$ configuration, it is convenient to work in the quasi hole picture, such that a hole enters the right QD2 from the right reservoir, hops further to the left QD1, and finally escapes to the left reservoir. The cycle $(1, 1) - (1, 0) - (0, 1) - (1, 1)$ thus drives a current through the double quantum dot at TP2. Based on this sequential tunneling picture, triple points of type TP1 are also called electron triple points, whereas triple points of the type TP2 are referred to as hole triple points [59, 61].

### 2.2.2. Tunnel Coupling

The second important coupling mechanism for a coupled quantum dot system is the tunnel coupling between the two quantum dots. For two quantum dots in close proximity, the electronic wave functions overlap, so that electrons can tunnel from one quantum dot to the other. In the vicinity of the triple points, where the energy levels of the individual quantum dots are degenerate, a finite tunnel coupling lifts this degeneracy and bonding and antibonding states form, leading to an avoided crossing.

An approximation of the effect of the tunnel coupling can be given by considering only a single electron and one state of each quantum dot. When neglecting interactions to electrons of lower energy, the background electrons can then be treated as an additive term to the total energy $E(N, M)$ according to equation 2.18.

The Hamiltonian of a such a coupled two-level system can be taken as [42, 59]

$$H = \begin{pmatrix} \epsilon_1 & \widetilde{t} \\ \widetilde{t} & \epsilon_2 \end{pmatrix}, \tag{2.21}$$

where $\widetilde{t}$ describes the tunnel coupling and $\epsilon_{1/2}$ are the energy levels of the two quantum dots for the uncoupled case $\widetilde{t} = 0$.

The corresponding single-electron energy eigenvalues are

$$\epsilon_\pm = \frac{\epsilon_1 + \epsilon_2}{2} \pm \frac{1}{2} \sqrt{(\epsilon_1 - \epsilon_2)^2 + 4\widetilde{t}^2}. \tag{2.22}$$

The lower energy state $\epsilon_-$ (bonding state) becomes the ground state for the single electron, with the higher energy state $\epsilon_+$ (antibonding state) being an excited state. With introducing relative coordinates for the two quantum dots, the mean energy $\bar{\epsilon} = (\epsilon_1 + \epsilon_2)/2$ and the detuning $\Delta_{12} = \epsilon_1 - \epsilon_2$, equation 2.22 can be rewritten to

$$\epsilon_{\pm} = \bar{\epsilon} \pm \frac{1}{2}\sqrt{\Delta_{12}^2 + 4\widetilde{t}^2}. \tag{2.23}$$

As function of the two parameters $\bar{\epsilon}$ and $\Delta_{12}$, the solid lines in figure 2.8 (a) show the lower energy bonding state $\epsilon_-$ and the higher energy antibonding state $\epsilon_+$. The energy difference between the ground and the excited state

$$\Delta E = \epsilon_+ - \epsilon_- = \sqrt{\Delta_{12}^2 + 4\widetilde{t}^2}, \tag{2.24}$$

becomes minimal at zero detuning between the quantum dots, with $\Delta E(\Delta_{12} = 0) = 2|\widetilde{t}|$.
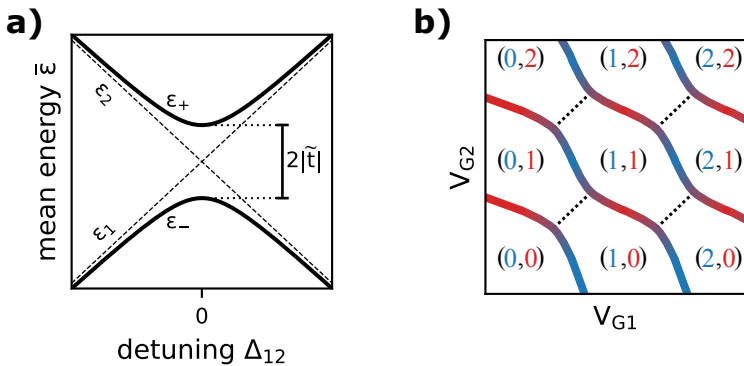


**Figure 2.8.: (a)** Effect of a finite tunnel coupling on a single electron in a double quantum dot. The two individual states $\epsilon_1$ and $\epsilon_2$ (dotted lines) of the two quantum dots hybridize and form a bonding $\epsilon_-$ and antibonding $\epsilon_+$ state, showing an avoided crossing as function of the detuning $\Delta_{12}$. **(b)** Schematic stability diagram of a tunnel coupled double quantum dot. The double quantum dot characteristic honeycomb pattern is defined by the Coulomb repulsion. Close to the resonances, the tunnel coupling leads to the formation of the $\epsilon_{\pm}$ states, resulting in the characteristic bending of the charging lines and an additional splitting of $2|\widetilde{t}|$.

The dashed lines show the energies $\epsilon_1$ and $\epsilon_2$ of the individual quantum dots for zero tunnel coupling. For large detuning $\Delta_{12}$ between the quantum dot levels, the double quantum dot states $\epsilon_{\pm}$ converge to the states

of the individual quantum dots. When following the ground state $\epsilon_-$ as function of the detuning, the electron is localized in one quantum dot in the beginning and transferred to being localized in the other quantum dot in a smooth way.

With neglecting all interactions except for the Coulomb interaction and the tunnel coupling, the single electron double quantum dot states $\epsilon_\pm$ can be used to approximate the behavior of a multi electron double quantum dot. Figure 2.8 (b) shows a schematic stability diagram for such a system as function of two gate voltages $V_{G1}$ and $V_{G2}$. Due to the Coulomb interaction, the overall behavior follows the honeycomb pattern of a capacitively coupled double quantum dot (see figure 2.7 (b)). QD1 charging lines are again colored in blue, QD2 charging lines are colored in red. Close to the double quantum dot resonances (triple points), the individual quantum dot states $\epsilon_{i/j}$ hybridize and form bonding and antibonding states $\epsilon_\pm$, leading to an additional splitting of $2|\widetilde{t}|$. A color gradient from blue to red is used to symbolize the smooth transition regions. The black dotted lines are again reconfiguration lines, where one electron moves from one quantum dot to the other. The mean energy axis of panel (a) is parallel to the reconfiguration lines, the detuning axis is perpendicular to the reconfiguration lines.

Each resonance consists of four charge configurations $(N, M)$, $(N + 1, M)$, $(N, M + 1)$, and $(N + 1, M + 1)$, with the total change in charge being two electrons. For each resonance, the effect of the tunnel coupling is approximated by the formation of the double quantum dot states $\epsilon\pm$ on top of a background charge configuration. The first electron with respect to this background charge configuration then occupies the lower energy state $\epsilon_-$, whereas the second electron occupies the higher energy $\epsilon_+$ state.

## 2.3. Charge Detection

To complement the transport spectroscopy, a charge detector can be installed to the quantum dot system, granting access to the exact number and distribution of the electrons in the quantum dot system. Since all charging events in quantum dots are based on single electrons, a reliable charge detector has to be highly sensitive to local potential changes.

Charge detectors for quantum dot systems are typically based on the use of a parallel circuit in which a capacitively coupled sensor element is located in the vicinity of the quantum dot system under investigation. Commonly used charge sensor types are based on using a quantum dot [22, 62–64] or quantum point contact [31, 65–67] as the capacitively coupled sensor element. The high sensitivity due to the sharp Coulomb blockade peaks and the relative ease of fabrication and integration made especially metallic single-electron transistors (SETs) attractive in the early stages of single charge detection [21, 68, 69] and of highly sensitive electrometers in general [70–72].

In this work, the charge detector is implemented in form of a quantum point contact (QPC). One advantage of the QPC is the simplicity of the design in comparison to a quantum dot. Typically, a QPC detector can be implemented with only one additional gate, whereas good control over a quantum dot detector would require at least three additional gates, a plunger gate and one gate for controlling each of the two tunnel barriers. Additionally, the high sensitivity of the sharp Coulomb peaks comes with the downside of the necessity to readjust the detector gate voltages often for constantly being in a sensitive regime. These readjustments, as well as the localized charge on the detector dot lead to electrostatic backaction onto the system under investigation. A QPC on the other hand does not contain localized charges and typically needs less adjustment of the gate voltage, thus providing the benefit of only small electrostatic backaction. However, QPC detectors also need to be carefully tuned, since

biased QPCs emit phonons, which also interact with the system under investigation [73–75].
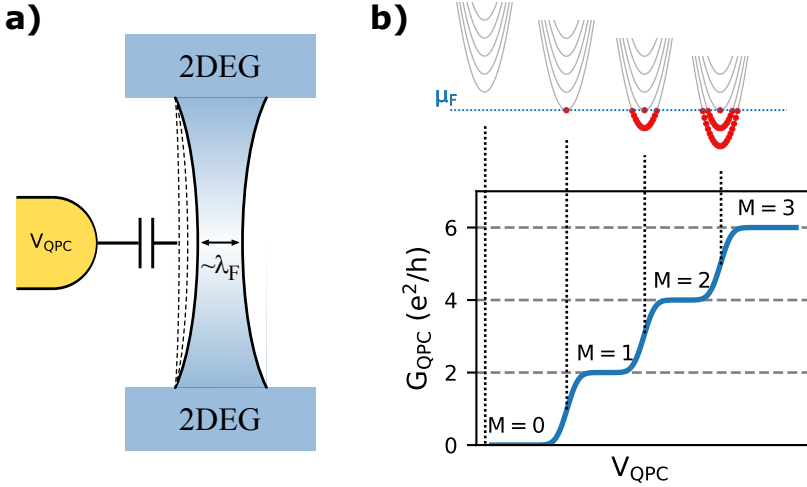


**Figure 2.9.: (a)** Schematic of a quantum point contact. A gate electrode is used to form a narrow channel within the 2DEG with a width comparable to the Fermi wavelength $\lambda_F$. Electronic transport through this one-dimensional channel is ballistic, for channels that are short compared to the mean free path of the electrons. **(b)** Conductance $G_{QPC}$ as function of the QPC gate voltage $V_{QPC}$. Each one-dimensional subband crossing the Fermi level $\mu_F$ contributes $2e^2/\hbar$ to the total conductance of the QPC, resulting in the characteristic conductance plateaus of one-dimensional conductor.

A QPC is a one-dimensional transport channel. Forming a QPC requires confinement to the order of the Fermi wavelength $\lambda_F$ in two spatial dimensions. In a 2DEG, this can for example be achieved using electrostatic potentials applied to gate electrodes, as schematically depicted in figure 2.9 (a). While the confinement leads to energy quantization in two dimensions, electrons can freely move in channel direction. Energetically separated one-dimensional sub-bands form, where each sub-band is an individual transport mode. As long as the channel length is small com-

pared to the mean free path $l_{mfp}$ of the electrons, transport through these modes is ballistic. Each single mode crossing the Fermi level $\mu_F$ then contributes the conductance quantum $G_0 = 2e^2/h$ to the total conductance of the QPC [42, 76–78]

$$G_{QPC} = s \cdot \frac{e^2}{h} \cdot M_{QPC}. \tag{2.25}$$

$M_{QPC}$ hereby denotes the number of modes crossing the Fermi level $\mu_F$, s is the degeneracy factor of the modes. For electrons in absence of a magnetic field $s = 2$ due to the spin degeneracy. The spin degeneracy can be lifted by applying an external magnetic field [39, 77, 79].

A gate voltage $V_{QPC}$ can be used to manipulate the constriction. The gate voltage hereby changes the width and potential landscape of the QPC constriction, both defining the energy configuration of the one-dimensional sub-bands. More negative voltages $V_{QPC}$ decrease the width of the constriction, thereby increasing the ground state energy and energy spacing of the sub-bands. As function of the gate voltage $V_{QPC}$, the conductance of a quantum point contact therefore exhibits a series of steps, as shown in figure 2.9 (b). As depicted by the energy band schematics on top, a step occurs each time a sub-band crosses the Fermi level $\mu_F$. The step height is hereby given by the conductance quantum. The width of each plateau depends on the energy spacing of the one-dimensional subbands and therefore strongly depends on the exact potential landscape. Equidistant steps are observed for a saddle-point constriction [80], a commonly used approximation for a QPC in a 2DEG.

Similar to changing a gate voltage $V_{QPC}$, changing the charge on a quantum dot in the vicinity of the QPC has an influence on the potential landscape of the QPC constriction. Each additional electron on the quantum dot slightly decreases the width of the constriction, as schematically depicted in figure 2.10 (a). In the $V_{QPC}$-space, each additional charge on the quantum dot slightly shifts the detector curve toward more posi-
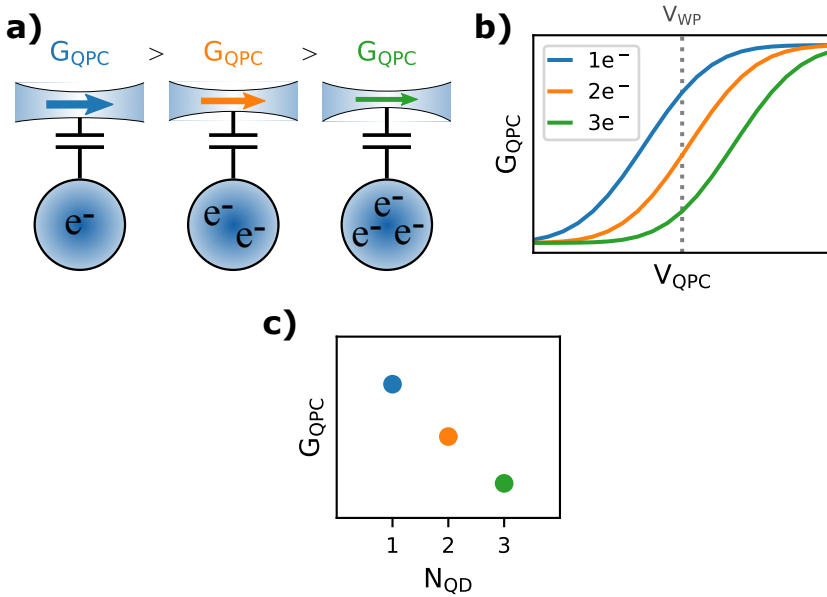
**Figure 2.10.: (a)** Schematic of a narrow QPC channel capacitively coupled to a quantum dot. Each additional electron on the quantum dot slightly decreases the width of the QPC channel. **(b)** Conductance of the QPC $G_{QPC}$ as function of the gate voltage $V_{QPC}$. The negative potential of each additional electron in the quantum dot shifts the QPC curve toward more positive potential in the $V_{QPC}$-space. **(c)** Operating the QPC at a fixed gate voltage $V_{WP}$, the QPC conductance becomes sensitive to the number of electrons $N_{QD}$ in the quantum dot.

tive $V_{QPC}$. For one (blue), two (orange), and three (green) electrons, this is schematically depicted in figure 2.10 (b). With fixing a working point $V_{QPC} = V_{WP}$ (grey dotted line) for the QPC on a transition between two plateaus, the conductance $G_{QPC}$ becomes sensitive to the number of electrons on the quantum dot. Panel (c) illustrates $G_{QPC}$ at the working point $V_{WP}$ for the three different electron numbers. As long as the uncertainty in the measurement of $G_{QPC}$ is small compared to the conductance change for adding or removing an electron on the quantum dot, this allows to monitor changes of the electron number $N_{QD}$ on the quantum dot by monitoring the conductance $G_{QPC}$.

Even though the exact gate voltage dependency of a QPC sensitively depends on a variety of parameters including geometry [80, 81], temperature [77, 81], magnetic field [77, 79], and bias [82, 83], or might show additional substructures, for example the '0.7 anomaly' [84, 85], this detection scheme is very robust, since it only depends on the coupling strength between QPC and quantum dot. The sensitivity for the charge detection is then determined by the conductance change $\Delta G_{QPC}$ as function of potential, which can be approximated by $dG_{QPC}/dV_{QPC}$, the slope of the QPC conductance as function of gate voltage.

Figure 2.11 illustrates how a QPC charge detector responds on charging events in a quantum dot in the vicinity. A schematic of a simple configuration of a quantum dot, capacitively coupled to a QPC, is shown in (a). The quantum dot is connected to the QD source and QD drain reservoirs, the QPC is connected to the QPC source and QPC drain reservoirs. A gate electrode in the vicinity of the quantum dot allows to control the energy of the quantum dot levels $\mu_N$ by applying a gate voltage $V_{QD}$. The voltage applied to the QPC gate electrode is chosen to $V_{QPC} = V_{WP}$ (compare figure 2.10 (b)), so that the QPC is in the transition region between two plateaus and is sensitive to potential changes.

As function of $V_{QD}$, the quantum dot shows Coulomb blockade oscillations, as discussed in 2.1.4. The number of electrons on the quantum
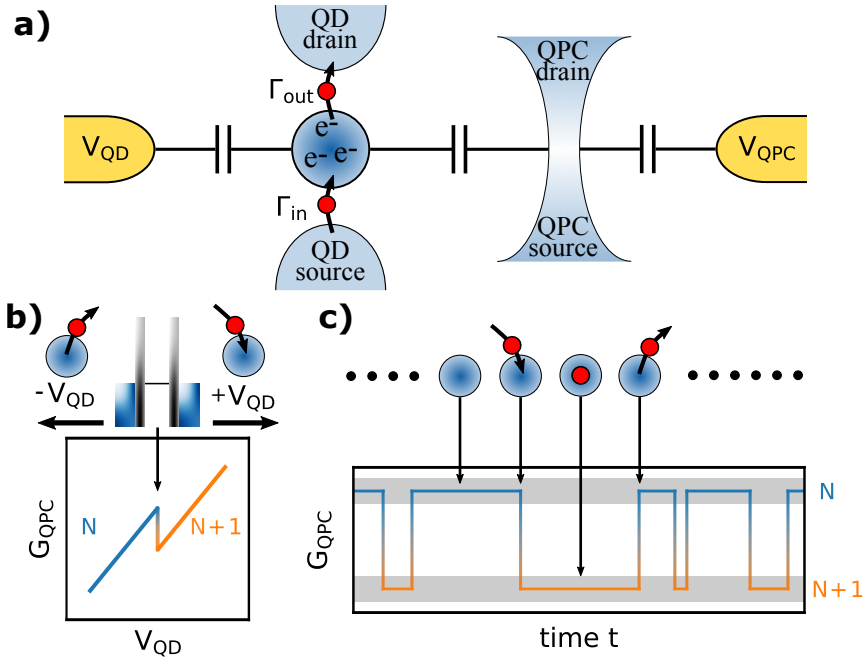
**Figure 2.11.:** Illustration of the detection of charging events in a quantum dot using a quantum point contact. **(a)** Schematic of a quantum dot capacitively coupled to a QPC. The quantum dot and the QPC can be controlled with gate voltages $V_{QD}$ and $V_{QPC}$, respectively. The quantum dot is coupled to two electron reservoirs source and drain, so that electrons can tunnel into and out of the quantum dot with tunneling rates $\Gamma_{in}$ and $\Gamma_{out}$. **(b)** Conductance of the QPC $G_{QPC}$ with changing $V_{QD}$. The voltage $V_{QD}$ cross couples to the QPC, leading to a finite slope. Changing the electron number of the quantum dot leads to a step in $G_{QPC}$. Depending on the direction of the $V_{QD}$ change, the step can be due to adding (positive direction) or removing (negative direction) an electron. **(c)** At the transition, the quantum dot switches between $N$ and $N + 1$ electron. As function of time $G_{QPC}$ switches to a low conductance state, whenever an electron tunnels into the quantum dot and back to the high conductance state, when the electron tunnels out again. Due to the stochastic nature of tunneling, the times between the switching events fluctuate.

dot always changes by one, when crossing one of the Coulomb blockade peaks. When simultaneously monitoring the QPC conductance, a step-like behavior is observed, as depicted in figure 2.11 (b). Changing the electron number of the quantum dot leads to a potential change and thus slightly shifts the QPC curve with respect to the fixed working point $V_{QPC} = V_{WP}$. Since the working point of the QPC does not change, this shift is observed as a step in the QPC conductance. The steps in the QPC conductance $G_{QPC}$ and the Coulomb blockade peaks in the $G_{QD}$ are therefore observed at the same voltages $V_{QD}$. A finite slope of $G_{QPC}$ away from the resonance occurs in the presence of cross-coupling of the gate voltage $V_{QD}$ on the QPC channel. This cross coupling is expected, since the quantum dot and the QPC are required to be in close proximity for the charge detection to be sensitive.

As long as tunneling into and out of the quantum dot is fast compared to the timescale of the measurement, the charge detector shows the equilibrium charge configuration of the quantum dot. In this case, the QPC conductance $G_{QPC}$ does not depend on the direction of the measurement, i.e., the QPC conductance $G_{QPC}$ is the same for sweeping $V_{QD}$ from more positive to more negative voltages compared to sweep $V_{QD}$ from more negative to more positive voltages. However, as sketched on top of figure 2.11 (b), the underlying process differs. For sweeping toward more negative $V_{QD}$, the observed step corresponds to an electron leaving the quantum dot, while toward more positive voltages, the step comes as a result of loading an additional electron onto the quantum dot.

At the position of the step, the quantum dot is bistable. A level of the quantum dot is in resonance with the reservoirs and the number of electrons on the quantum dot stochastically fluctuates between N and N + 1 electrons. Therefore, also the QPC conductance $G_{QPC}$ fluctuates, as shown in figure 2.11 (c). As long as there are N electrons on the quantum dot, the QPC conductance is stable. As soon as an additional electron tunnels into the quantum dot, the QPC conductance drops to a lower level,

corresponding to $N+1$ electrons in the quantum dot. After a certain time the electron then tunnels out again and the QPC conductance returns to the original value for $N$ electrons. The timescale of the fluctuations is determined by the tunneling rates $\Gamma_{in}$ and $\Gamma_{out}$ into and out of the quantum dot. With a sufficiently high detector bandwidth $\Gamma_{det} > \Gamma_{in}, \Gamma_{out}$ these fluctuations become resolvable, allowing to detect single-electron charging events in a time-resolved manner [86–88]. Time resolved detection of single-electron tunneling is for example used as a readout procedure for quantunm dot based spin qubits [89, 90] and provides an error detection method for single electron pumps [91, 92].

# 3

# Experimental Basics

This chapter will give an introduction into the experimental techniques used within the scope of this work. Beginning with the heterostructure, the fabrication methods for the quadruple quantum dot device are discussed. An introduction into the measurement setup will be given, and the chapter concludes with the introduction of characteristic transport measurements on a single quantum dot.

## 3.1. Heterostructure

The quantum dot device investigated within the scope of this work, is based on a two-dimensional electron gas (2DEG). This 2DEG is formed in a $GaAs/AlGaAs$ heterostructure [93, 94], which was grown by E. P. Rugeramigabo via molecular beam epitaxy (MBE) [95, 96]. The layer structure according to the growth protocol is shown in figure 3.1a. At the $GaAs/AlGaAs$ interface at $110\,nm$ below the surface, which is marked in blue, the 2DEG is formed.

Growing $GaAs$ and $AlGaAs$ on top of each other leads to strainless and atomically flat interfaces, since the $Al$-content in $Al_xGa_{1-x}As$ has a vanishing effect on the lattice constant. The band gap on the other hand is modulated by the $Al$-content and can be tuned between the $GaAs$ ($\sim 1.4\,eV$) and $AlAs$ ($\sim 2.1\,eV$). By bringing the two different materials in contact, the Fermi level $\mu_F$ aligns, which leads to a deformation of the energy bands in the interface region. A triangular shaped potential well is
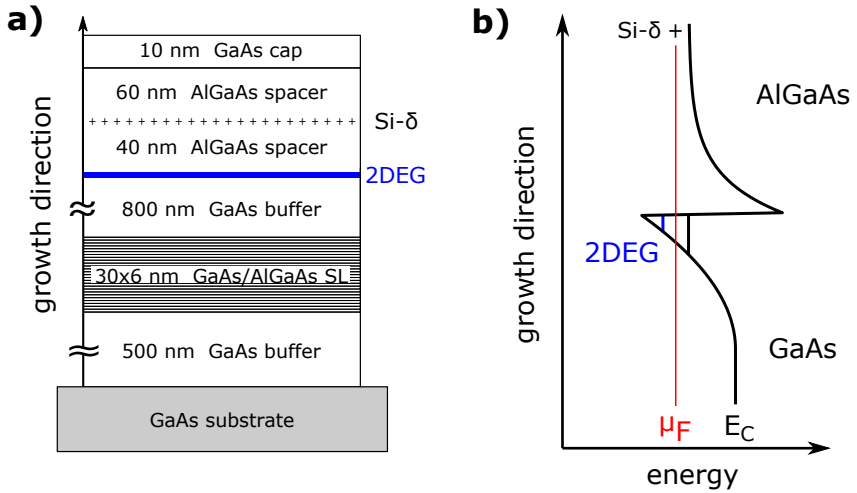
**Figure 3.1.: (a)** Schematic of the material layer order of the used heterostructure. A two-dimensional electron gas (2DEG) forms at the interface between $GaAs$ and $AlGaAs$ (blue). **(b)** Schematic conduction band edge diagram close to the $GaAs/AlGaAs$ interface. A dip in the conduction band emerges in growth direction in the $GaAs$ and forms a triangular shaped quantum well. The Fermi level $\mu_F$ allows only the lowest energy subband to be occupied by electrons. In this subband, electrons can only move perpendicular to the growth direction.

formed inside the $GaAs$, as schematically depicted in figure 3.1b. In this confinement region, two-dimensional energy subbands are formed. By appropriate $Si$-doping, the Fermi level $\mu_F$ is tuned into the gap between the lowest two subbands, so that at low temperatures only the lowest subband is occupied by electrons. Since electrons confined in this subband can only move perpendicular to the growth direction, this system is called two-dimensional electron gas.

By magnetotransport measurements on a Hall-bar, characteristic electronic properties of a 2DEG are obtained. For the heterostructure used, the charge carrier density $n_e = 2.4 \times 10^{11} \, cm^{-2}$ and charge carrier mobility $\mu_e = 5.1 \times 10^5 \, cm^2 \, V^{-1} \, s^{-1}$ were determined. These values allow the calculation of the Fermi wavelength $\lambda_F = \sqrt{2\pi/n_e} \approx 51 \, nm$ and the electron mean free path $l_{mfp} = h\mu_e/(e\lambda_F) \approx 4 \, \mu m$, which are characteristic length scales of the 2DEG. To see quantization effects or ballistic transport, the device dimensions have to be in this regime.

## 3.2. Lithography

To realize an electrically contacted quantum dot device in a two-dimensional electron gas, the heterostructure is processed by optical lithography and electron beam lithography. Within the scope of this thesis, the optical lithography was maintained and the electron beam lithography was optimized in terms of structure sizes and reproducibility. The quantum dot device used within this thesis was fabricated in the preceding master thesis, where the fabrication and process parameters are documented in detail [97]. The individual fabrication steps are therefore only outlined in this context.

As a first step, a sample of $4.5 \times 4.5 \, mm^2$ is cut out of the heterostructure. The sample surface is then cleaned using Acetone/Isopropanol in an ultrasonic bath. After this cleaning, the sample is prepared for lithographic processing. The processing steps of the optical lithography are

sketched in figure 3.2 (a), figure 3.2 (b) shows the steps for the electron beam lithography.
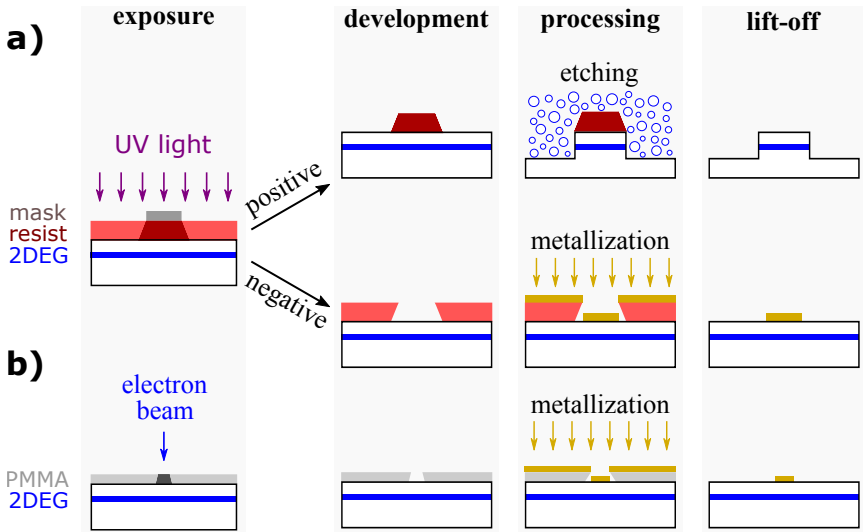


**Figure 3.2.: (a)** Processing steps of the optical lithography. Positive photoresist is used to produce protective masks for etching procedures. Negative photoresist is used for metallization steps, where an *undercut* profile of the resist is required for a successful *lift-off* procedure. **(b)** Processing steps of the electron beam lithography used to fabricate nanoscale structures. An *undercut* profile emerges in the resist after development due to scattering of the electrons.

For the optical lithography, a thin film of UV-sensitive photoresist is spin coated onto the sample. An optical mask, consisting of transparent fused silica with opaque Chromium patterns is then brought into contact with the resist coated sample. In this configuration and under UV-illumination, exclusively the parts which are not covered by Chromium are exposed. Depending on the type of photoresist, either the exposed areas (positive photoresist Shipley S1805; developer Microposit MF319) or the unexposed areas (negative photoresist AZ 5214E; developer AZ 726)

can now be removed in a wet chemical development process. The mask pattern is thus transferred into the resist and the uncovered heterostructure surface is prepared for further processing, while the remaining resist protects the covered areas.

In the first step, an isolated region where the 2DEG is preserved, a so called mesa, is created. By using a $H_2O : H_2O_2 : H_3PO_4$ etching solution, the uncovered parts of the heterostructure are dissolved with a certain etching rate. The 2DEG is hereby destroyed. After a given time (etching depth = etching rate $\times$ time), the etching process is stopped by dipping the sample into water. After removing the remaining resist with Acetone, the mesa etching process is completed. A microscope image of a mesa is shown in figure 3.3 (a).

The second step aims toward electrically contacting the 2DEG. Metallization ($Au/Ge$) is hereby thermally evaporated onto the sample in a vacuum chamber. A negative photoresist is used for this step, as it provides the necessary *undercut* profile. In the following *lift-off* procedure, Acetone is used to remove the resist. Due to the *undercut* profile, the metallization on the heterostructure surface is not connected to the metallization on top of the resist and therefore remains on the surface. By annealing this metallization, the ohmic contacts to the 2DEG are formed. Figure 3.3 (b) shows the sample after the anneling. In addition to the contacts, bondpads are produced in this step.

In a third step, the gate leads are fabricated. The gate leads are connected to bondpads and reach over the etching edge on top of the mesa. The procedure is similar to the fabrication of the ohmic contacts but with a $Cr/Au$ metallization and without annealing. A microscope image of the sample after the evaporation of the gate leads is shown in figure 3.3 (c). These gate leads include markers, which enable the alignment between optical and electron beam lithography.

The final lithographic step, where the gate structure defining the quantum dots is fabricated is done using electron beam lithography. In the
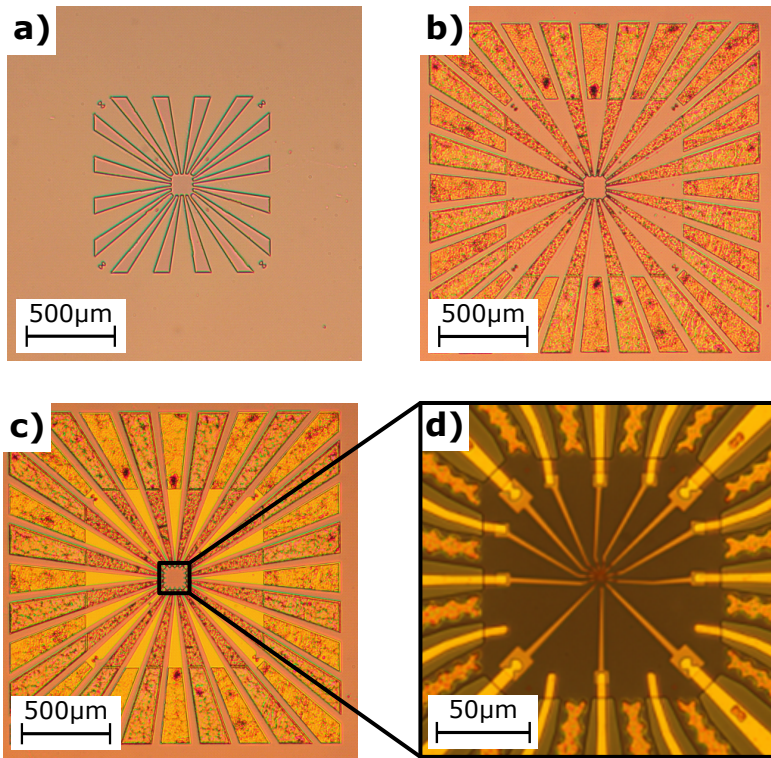
**Figure 3.3.:** Optical microscopy images of the fabrication steps for a gate de-
fined quantum dot device based on a 2DEG material. **(a)** A defined mesa is
created using a wet chemical etching procedure. **(b)** Metal evaporation on
the sidearms of the mesa and subsequent annealing forms Ohmic contacts to
the 2DEG. Additional bond pads for the following gate leads are placed aside
of the mesa. **(c)** A second metallization but without annealing is used to de-
fine gate leads. **(d)** Zoom into the central area of the mesa. The nanoscale
gate structure is patterned via electron beam lithography and connected to
the gate leads fabricated before via optical lithography.

beginning, an electron sensitive resist (PMMA 950K 3% Anisol) is spin coated onto the sample. In a direct write process, the focused electron beam of a scanning electron microscope (SEM) is guided over the predefined areas. The exposed areas can then be removed using a developer (MIBK). Forward scattering of the electrons in the resist results in an *undercut* profile, which again enables the metallization and following *lift-off*. At this point, the device fabrication is completed, a microscope image of a finalized device is shown in figure 3.3 (d).

## 3.3. Measurement Setup

To begin with, the gap between the device contact size ($\sim 100\,\mu m$ diameter) and the measurement instruments contacts ($\sim 1\,cm$ diameter) size has to be bridged. The first step into this direction is done by contacting the sample to a chip carrier with 20 contacts. The sample is glued into the chip carrier and the chip carrier contacts are bonded to the device bondpads with thin gold wires. The chip carrier can then be plugged into a sample holder, which allows the connection of the measurement instruments.

To fulfill the condition $k_B T \ll E_C$, which is a requirement for the observation of single electron transport, the sample has to be cooled to low temperatures. To achieve these low temperatures, the sample holder is put into a cryostat. The cryostat used here is an Oxford Instruments $^3$He-$^4$He dilution refrigerator. The main components of this dilution refrigerator are the so called 1K-pot, the dilution chamber and the still. The 1K pot is used to precool and condense the $^3$He. Via a needle valve, the 1K-pot is filled with liquid $^4$He from the main bath. By pumping on the $^4$He gas phase, the vapor pressure and thereby the temperature of the 1K-pot is reduced to $\sim 1.5\,K$. After precooling the $^3$He/$^4$He mixture with the 1K-pot, the mixture is further cooled by several counterflow heat exchangers, using the cold $^3$He, which is coming from the mixing chamber.

After these heat exchangers, the mixture enters the mixing chamber. At a critical temperature of around $0.86\,\mathrm{K}$, the ${}^3\mathrm{He}/{}^4\mathrm{He}$ mixture separates into two phases. One phase is a ${}^3\mathrm{He}$-rich (concentrated) and the other a ${}^3\mathrm{He}$-poor (dilute) phase. The ${}^3\mathrm{He}$ is diluted as it flows from the concentrated into the diluted phase across the phase boundary. This crossing of the phase boundary is an endothermic process, which therefore removes heat from the mixing chamber environment. To maintain a steady flow of ${}^3\mathrm{He}$, the diluted phase is connected to the still, which is held at low pressure by pumping on the gas phase. Due to the much higher partial pressure of ${}^3\mathrm{He}$ compared to ${}^4\mathrm{He}$ at the still temperature, the pumped gas is almost pure ${}^3\mathrm{He}$, which is then fed back into the system, resulting in a ${}^3\mathrm{He}$ circulation. Additionally, heat is supplied to the still to further increase the ${}^3\mathrm{He}$ flow. This way, base temperatures of $\sim 10\,\mathrm{mK}$ can be achieved. More detailed information about the dilution refrigerator operating principle can be found in [98].

With the sample holder in the cryostat, the device contacts can now be connected to measurement instruments. An SEM image of the device with schematic wiring is shown in figure 3.4. All DC voltages are applied using AD5791 20 bit DACs (digital-to-analog converter). For the quantum dot source voltage $V_{\mathrm{sd,dot}}$ and the QPC source voltage $V_{\mathrm{sd,qpc}}$, a voltage divider or an AC/DC voltage adder with integrated voltage divider is used to increase the minimal voltage step size.

The currents are measured using transimpedance amplifiers, which convert the current in a proportional voltage. For both currents, $I_{\mathrm{dot}}$ and $I_{\mathrm{qpc}}$, ITHACO 1211 current preamplifiers with tunable amplification factor have been used. Typical amplification factors for the measured device range from $10^6\,\mathrm{V\,A^{-1}}$ to $10^9\,\mathrm{V\,A^{-1}}$.

The instruments for measuring the output voltages vary depending on the measurement session. In most cases, the output voltage was digitized using an analog input module (16/18 bit ADC, analog-to-digital converter) of an ADwin-Pro II. The ADwin-Pro II is a freely programmable real-
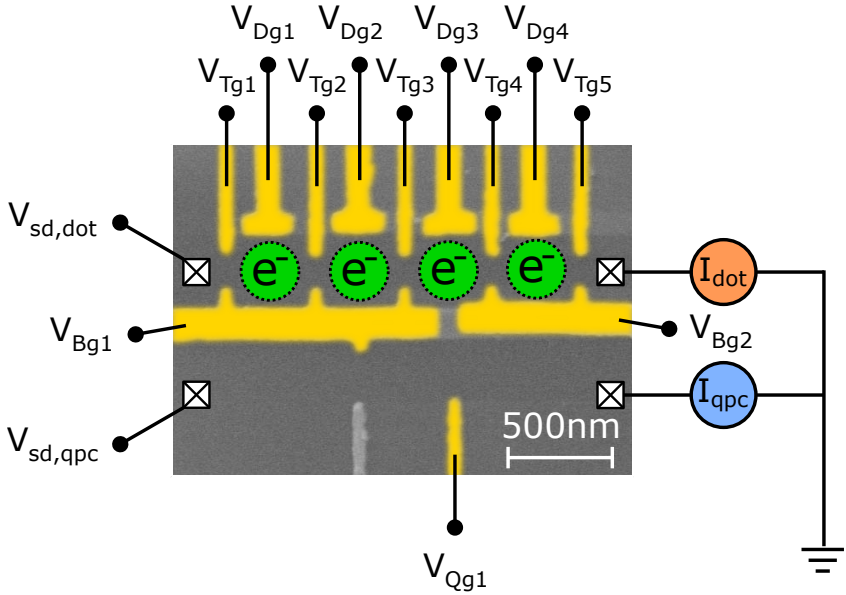
**Figure 3.4.:** Colored SEM image of the quadruple quantum dot device. The device consists of a total of 13 gate electrodes, of which 12 (colored in gold) were used to define quantum dot systems from single to quadruple dots. By applying negative voltages $V_{Bg1}$ and $V_{Bg2}$, the 2DEG is split in two galvanically isolated part, the quantum dot part on the top side, the QPC charge detector part on the lower side. The quantum dots, depicted as green circles, are formed electrostatically in the 2DEG by applying negative voltages to the respective gates. Each of the quantum dots is defined by two tunnel barrier gate voltages $V_{Tgi}$ and a plunger gate voltage $V_{Dgi}$.

time controller with a sampling rate of up to $500\,\mathrm{kHz}$. Alternatively, the output voltages were measured via Keithley 2000 multimeter. In some cases, additional AC measurements have been performed by connecting a lock-in amplifier (EG&G 7260 DSP Lock-In Amplifier / Ametek 7270 General Purpose DSP Lock-In Amplifier) to the source voltage via the AC/DC voltage adder and on the output of the transimpedance amplifier.

All measurement instruments were controlled by a measurement computer via Python and PyMeasure. A detailed documentation about PyMeasure can be found in the dissertation of T. Wagner [99]. Within the scope of this thesis, several instrument drivers and functionalities have been implemented and revised.

## 3.4. Quantum Dot Characterization

This section describes the basic measurement techniques for the characterization and investigation of quantum dot systems using the example of a single quantum dot. Linear and non-linear transport experiments are presented, the charge detection is introduced and the opportunities of virtual gates are discussed. A more detailed characterization of the device is given in [97].

When applying negative voltages to the gates, the resulting negative potential repels the electrons in the 2DEG underneath, which leads to the depletion of the 2DEG. In a first step, the two current paths $I_{dot}$ and $I_{qpc}$ are galvanically isolated from each other by applying sufficiently negative voltages $V_{Bg1}$ and $V_{Bg1}$ to the central gates. The small gap between both gates is hereby electrostatically closed, but increases the capacitive coupling between both current paths.

A quantum dot can now be formed using a plunger gate and two tunnel barrier gates. By applying negative voltages $V_{Dg3}$, $V_{Tg3}$ and $V_{Tg4}$, the third quantum dot (QD3) is formed. The quantum dot is coupled to the electron reservoirs via two tunnel barriers, which are formed between the

center gates $V_{Bg1}$, $V_{Bg1}$ and the tunnel barrier gates $V_{Tg3}$, $V_{Tg4}$. Additionally, a QPC charge detector is formed via $V_{Qg1}$.
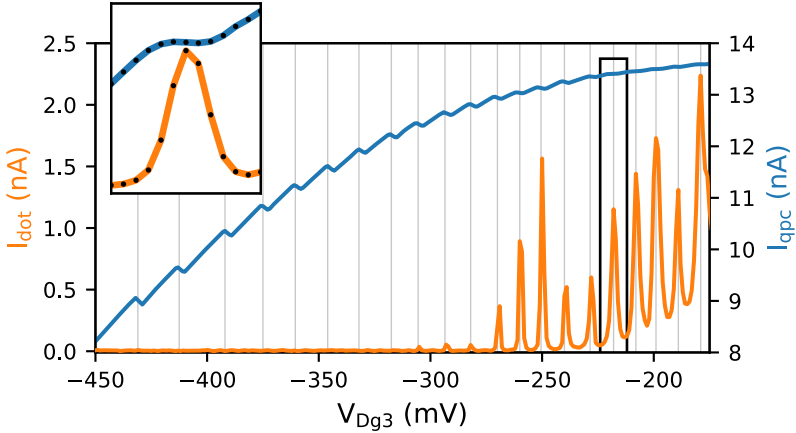


**Figure 3.5.:** Current $I_{dot}$ (orange) and $I_{qpc}$ (blue) as function of the plunger gate voltage $V_{Dg3}$. The current $I_{dot}$ shows clear Coulomb blockade oscillations, the characteristic behavior of a single quantum dot. For each peak crossed toward more negative $V_{Dg3}$, the quantum dot is depopulated by one electron. Electrons removed from the quantum dot hereby change the potential at the QPC charge detector and thus the conductance of the QPC. Each step in the detector current $I_{qpc}$ corresponds to the occupation of the quantum dot changing by one electron. When the tunneling rates become small toward more negative voltages, the measured current $I_{dot}$ drops below the noise floor. The charge detector however still responds to changes in the quantum dot occupation. The inset shows $I_{dot}$ and $I_{qpc}$ in different scale for the peak marked by the black rectangle. The time averaged detector signal resolves the average occupation of the quantum dot, leading to a smooth step of the same width as the Coulomb blockade peak.

To perform a current measurement, a small bias voltage of $V_{sd,dot} \approx 100\,\mu V$ is applied to drive a current through the quantum dot. The gate voltages $V_{Dg3}$, $V_{Tg3}$ and $V_{Tg4}$ are adjusted to deplete the 2DEG. Via $V_{Tg3}$, the coupling to the left reservoir can be tuned and via $V_{Tg4}$, the

coupling to the right reservoir, respectively. The charge detector is tuned onto a steep flank as function of the gate voltage $V_{Qg1}$, to obtain a high sensitivity to potential changes. The detector bias voltage is chosen to $V_{sd,qpc} = 1\,\mathrm{mV}$, to ensure such a steep flank. Figure 3.5 shows the dot current $I_{dot}$ and the detector current $I_{qpc}$ as function of the plunger gate voltage $V_{Dg3}$. The dot current $I_{dot}$ shows a peak, whenever one of the energy levels of the QD passes through the transport window, where tunneling of electrons from source to dot and from dot to drain is energetically possible. Toward more negative $V_{Dg3}$, the number of electrons on the QD is hereby reduced by one for each peak observed. Up to $V_{Dg3} \approx 300\,\mathrm{mV}$ these quantum dot characteristic Coulomb blockade oscillations are observable. For more negative $V_{Dg3}$, the current through the quantum dot drops below the noise floor is is not resolvable any more.

The detector current $I_{qpc}$ shows a decreasing behavior toward more negative $V_{Dg3}$, due to the more negative potential which narrows the QPC channel. At the positions of the Coulomb resonances however, a step like increase of $I_{qpc}$ is observed. This increasing current comes as a result of the decreasing electron number in the quantum dot, which decreases the negative potential and therefore widens the QPC channel. These steps occur for every change in the electron number of the quantum dot. However, the steps are not perfectly sharp but show a broadening, which follows the peak width of the Coulomb blockade oscillations. This is due to the signal integration over one power line cycle (PLC), which corresponds to the integration time $t_{int} = 20\,\mathrm{ms}$. Within this timescale, many electrons tunnel into and out of the quantum dot and the resulting detector signal resolves the average charge on the quantum dot. The steps therefore probe the occupation probability of the quantum dot. With more negative $V_{Dg3}$, both tunnel barriers become less transparent and the tunneling current $I_{dot}$ at some point drops below the resolution limit. The detector current $I_{qpc}$ on the other hand still shows distinct steps due to the charging events of the quantum dot. The detector therefore does

not only provide additional information but at the same time increases the measurement range.

By measuring as function of two gate voltages, a stability diagram is obtained. Such a stability diagram of QD2 as function of the two tunnel barrier gates $V_{Tg2}$ and $V_{Tg3}$ is shown in figure 3.6. The current $I_{dot}$ is shown in (a), the corresponding differential detector signal $\Delta I_{qpc}/\Delta V_{Tg2}$ in (b). Each of the visible charging lines correspond to an energy level of the quantum dot being in resonance with the leads. From the slope of the charging lines, the gate capacitance ratio $C_{Tg2}/C_{Tg3} \approx 1.1$ can be estimated. For the most positive gate voltages $-0.3\,\mathrm{V} \geqslant V_{Tg2}, V_{Tg3} \geqslant -0.35\,\mathrm{V}$, the Coulomb blockade oscillations are only barely visible. Here, the tunnel barriers are not yet well defined. For more negative voltages on both gates in the regime $-0.35\,\mathrm{V} \geqslant V_{Tg2}, V_{Tg3} \geqslant -0.4\,\mathrm{V}$ the charging lines develop but the current between two resonances does not drop to zero. In this region, the tunnel barriers are already defined, so that a quantum dot is formed. The coupling of the quantum dot to both reservoirs is very strong in this region, so that neighboring resonances overlap, preventing a total Coulomb blockade. For more negative $V_{Tg2}, V_{Tg3} \leqslant -0.4\,\mathrm{V}$, the barriers are well defined and total Coulomb blockade is observed. At $V_{Tg2} \approx -0.45\,\mathrm{V}$ for the left barrier, and at $V_{Tg3} \approx -0.45\,\mathrm{V}$ for the right barrier, the threshold, where the current $I_{dot}$ drops below the resolution limit, is reached. For more negative voltages, no current is observed.

The differential detector signal $\Delta I_{qpc}/\Delta V_{Tg2}$ shows the opposite behavior. For more positive voltages, the charging lines are only vaguely visible. Here, the broadening of the charging lines due to the large coupling leads to a slowly changing average occupation of the quantum dot, which consequently leads to small changes in the detector current between two gate voltage steps. In the regime of the total Coulomb blockade however, the charging lines become clearly visible and even more pronounced, where the current $I_{dot}$ is already below the resolution limit.
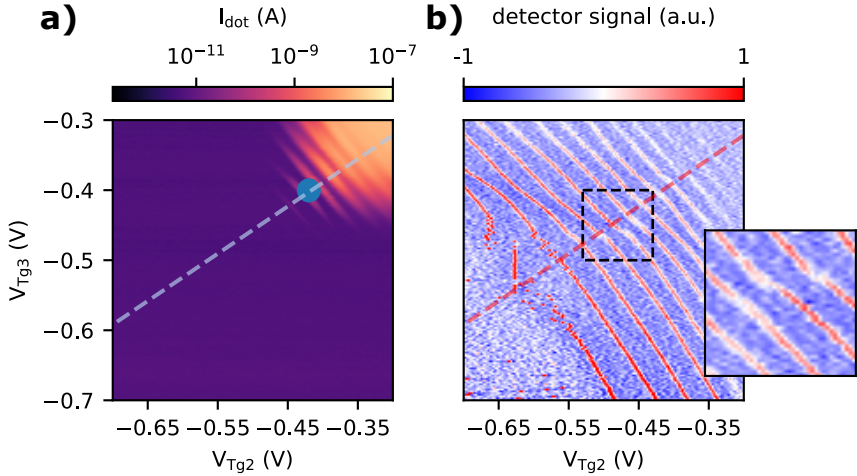
**Figure 3.6.:** Two-dimensional measurement as function of both tunnel barrier gate voltages $V_{Tg2}$ and $V_{Tg3}$ at an applied bias voltage $V_{sd,dot} = 0.5\,\mathrm{mV}$. **(a)** Current $I_{dot}$ through the quantum dot. Different regimes of coupling occur in the stability diagram. Finite current is only observed when both barriers are transparent, i. e. for the most positive gate voltages $V_{Tg2}$ and $V_{Tg3}$ (top right). The parallel lines are the single quantum dot characteristic Coulomb blockade oscillations. More negative $V_{Tg2}$ ($V_{Tg3}$) reduce the coupling to the left (right) reservoir and thereby eventually suppress the current. **(b)** Corresponding charge detector signal. Charging lines are visible over a much larger range of gate voltages. Moving along a charging line tunes the asymmetry of the coupling to the reservoirs. The inset shows a zoom into the box, where the visible charging lines experience a small shift around the symmetric coupling configuration. Dashed lines in (a) and (b) approximately follow the coupling symmetry.

For the most negative $V_{Tg2}, V_{Tg3} \leqslant -0.5\,\text{V}$, the charging lines start to appear noisy. This is due to tunneling rates of the order of the integration time. In this regime, the detector signal does not integrate over many tunneling events, but single events and their stochastic nature becomes dominant. By further decreasing the tunneling rates via more negative gate voltages, the measurement timescale becomes too short for the system to relax to its ground state and occupied energy levels are lifted above the Fermi energy. This effect leads to the gap, which is visible in the last charging line of the stability diagram.

The charge stability diagrams in figure 3.6 were taken with an applied bias $V_{sd,dot} = 0.5\,\text{mV}$. For the Coulomb blockade resonances in the dot current $I_{dot}$, this additionally broadens the charging lines. Since the detector signal is only sensitive to changes in the average occupation of the QD, this does not hold for the detector signal. When moving along one charging line, the energetic shift of a more negative voltage on one gate is compensated by a more positive voltage on the other gate. As function of the two tunnel barrier gates, this means the coupling symmetry to the reservoirs is tuned when moving along the charging line. The most positive $V_{Tg2}$ on a given charging line correspond to the most negative $V_{Tg3}$ on this line. This results in a large tunneling rate $\Gamma_S$ between source and dot and a small tunneling rate $\Gamma_D$ between drain and dot. Therefore $\Gamma_S \gg \Gamma_D$ and with a positive bias $V_{sd,dot} = 0.5\,\text{mV}$ applied on the source contact, the QD energy level is on average unoccupied as soon as the energy level comes into the bias window. In this configuration, the detector shows the resonance between drain and the energy level. For the most negative $V_{Tg2}$ on the same charging line $\Gamma_S \ll \Gamma_D$. Here, the energy level is on average occupied and the detector shows the resonance between source and energy level. Due to the bias voltage, both resonances are at different energies and therefore also shifted in the stability diagram. In a small region, where $\Gamma_S \approx \Gamma_D$, a transition between these visible resonances occurs. It is not a sharp transition however, but gradually and with

a lower contrast in the detector signal. The lower contrast results from the fact that in this region the average occupation changes over the full bias window, leading to a broadening of the charging line in the detector signal. These transitions are found close to the diagonal perpendicular to the charging lines. The inset of figure 3.6 (b) shows a zoom into the marked area, where four of these transitions are found. With a higher measurement resolution, these transitions might show the excited states spectrum [100]. The position of the $\Gamma_S \approx \Gamma_D$ symmetry points on the different charging lines fluctuate with respect to dashed line, which is a linear fit to 7 symmetry points. The different charging lines correspond to different quantum mechanical states of the QD, which couple differently to the reservoirs.

This linear fit can now be used to couple both tunnel barrier gates. This can be described as a virtual gate, which influences the coupling to both reservoirs at the same time. A stability diagram as function of the coupled tunnel barrier gates $V_{Tg2,Tg3}$ and the plunger gate $V_{Dg2}$ is shown in figure 3.7 (a). The slope of the charging lines show that the capacitive coupling of the plunger gate is approximately twice as large as the combined capacitance of both tunnel barrier gates. It is clearly visible, that the pinch off, where the current $I_{dot}$ drops to zero shifts toward more negative $V_{Dg2}$ for more positive $V_{Tg2,Tg3}$. This dependency can now be used to define another virtual gate, which consists of $V_{Tg2}$, $V_{Tg3}$ and $V_{Dg2}$. Along the blue line in the graph, the tunnel barrier voltages approximately compensate the influence of the plunger gate $V_{Dg2}$ on the tunnel barriers.

This can now be used for Coulomb diamond measurements, which provide information about the energy scales of the quantum dot. Figure 3.7 (b) shows the differential conductance $\Delta I_{dot}/\Delta V_{sd,dot}$ as function of $V_{sd,dot}$ and the plunger gate voltage $V_{Dg2}$ and (c) as function of $V_{sd,dot}$ and the virtual gate $V_{Dg2,Tg2,Tg3}$ along the blue line in (a). For both, (b) and (c), the variation range of the plunger gate voltage $V_{Dg2}$ is identical.
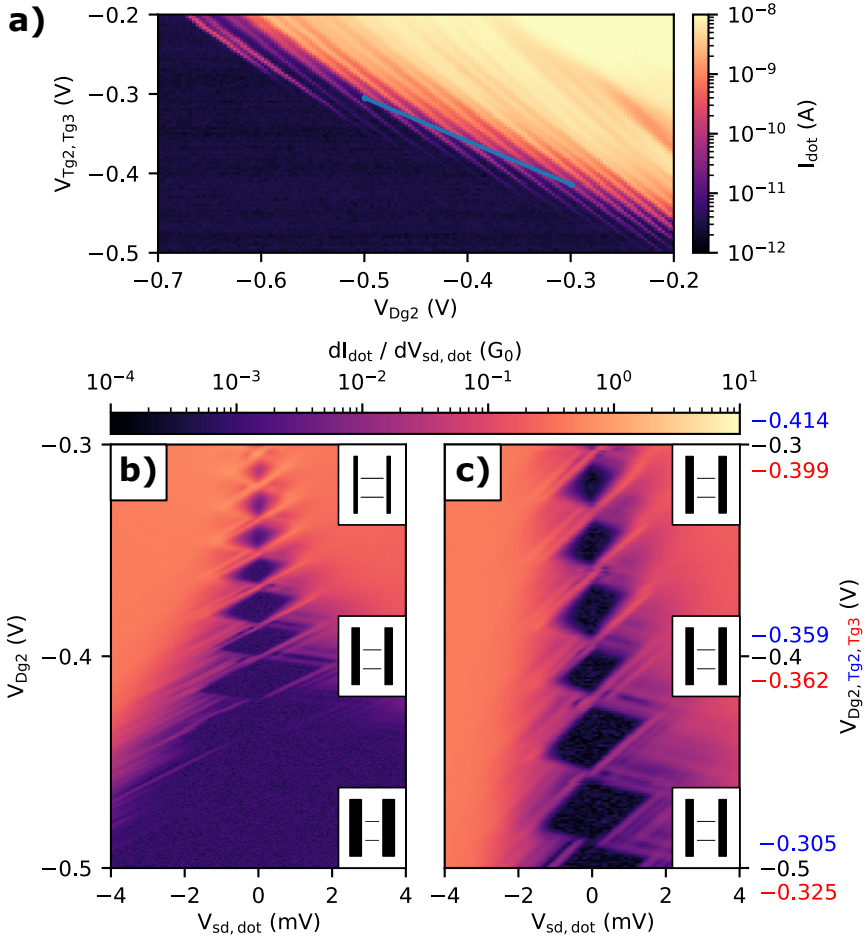
**Figure 3.7.: (a)** Current $I_{dot}$ as function of plunger gate voltage $V_{Dg2}$ and the coupled gate voltage $V_{Tg2,Tg3}$ along the coupling symmetry line. Lines of approximately constant coupling can be approximated as lines parallel to the pinch-off. **(b)** Coulomb diamonds as function of $V_{Dg2}$ for $V_{Tg2,Tg3} = -0.4\,\text{V}$ and **(c)** along the blue line in (a). The coupled gate voltage $V_{Dg2,Tg2,Tg3}$ keeps the coupling nearly constant, resulting in homogeneous Coulomb diamonds.

Some differences between the two plots directly catch the eye. With using only $V_{Dg2}$ in (b), the overall conductance is high for the most positive values and below the resolution limit for the most negative $V_{Dg2}$. This comes as a result of the cross-coupling of the plunger gate on the tunnel barriers. The barriers are narrow for the most positive voltages, intermediate for intermediate voltages and become large for the most negative voltages, as sketched in the insets. In contrast, the overall conductance and appearance of the diamonds is almost homogeneous using the virtual gate $V_{Dg2,Tg2,Tg3}$ in (c). Here, the barrier increasing effect of more negative $V_{Dg2}$ is compensated by more positive values applied to the tunnel barrier gates $V_{Tg2}$ and $V_{Tg3}$, resulting in the barriers being almost constant along the y-axis. However, even assuming perfect compensation of the tunnel barriers, the observed Coulomb diamonds are not perfectly identical. Each feature corresponds to a specific state of the quantum dot, which can couple quite differently, as can be seen in the lowest diamond of figure 3.7 (c). The lower resonance of the diamond shows a blockade phenomenon around $V_{sd,dot} = 0$. Since the diamond is fully resolved for bias voltages $|V_{sd,dot}| \gtrsim 0.2\,\mathrm{mV}$, it is clear that a state of the quantum dot is resonant with the reservoirs, but no significant differential conductance is observed. Even though the mechanism behind this blockade cannot be determined from the available data, the presence of the blockade underlines the sensitivity of the transport properties on the exact configuration.

Another major difference when comparing the single gate to the virtual gate Coulomb diamonds lies in the shape of the diamonds. The width to height ratio of the diamonds is clearly smaller for the diamonds as function of the virtual gate voltage $V_{Dg2,Tg2,Tg3}$. As shown in section 2.1.4, this ratio is determined by the lever arm of the gate. With the charging energy $E_C = e\Delta V_{sd,dot}/2$, where $\Delta V_{sd,dot}$ is the full width of a diamond, and the height $\Delta V_{gate}$ of the same diamond, the conversion factor from gate voltage to energy, the lever arm $\alpha_{gate} = E_C/\Delta V_{gate}$,

can be determined. However, especially for the single gate diamonds in (b), the width $\Delta V_{sd,dot}$ of the diamonds, and therefore the charging energy, is not constant but tends to increase toward smaller electron numbers. Due to this dependency, characterization measurements should always be performed in a configuration as close as possible to the actual working point of the device. Extracting the lever arms from all visible diamonds of the $V_{Dg2}$ measurement yields $\alpha_{Dg2} = -0.106(\pm 0.030)$, and thus $\Delta\mu_{Dg2} = -0.106(\pm 0.030)eV_{Dg2}$ (mean $\pm$ standard deviation) for the energy level shift as function of $V_{Dg2}$. For the virtual gate the conversion becomes $\Delta\mu_{Dg2,Tg2,Tg3} = -0.058(\pm 0.010)eV_{Dg2,Tg2,Tg3}$. The beneficial effect of constant tunnel barriers therefore comes at the cost of an approximate factor of two smaller lever arm of the virtual gate. In addition to the larger range of $V_{Dg2}$ needed for the same energetic shift, two additional gate voltages are changed using the virtual gate, resulting in an overall greater influence on the potential landscape in the vicinity. Therefore, both options, using single gates or combining gates into a virtual gate come with there own benefits and downsides and the optimal choice depends on the task.

For the investigation of effects, which depend sensitively on the coupling or the coupling symmetry, as for example the Kondo effect in quantum dots [101, 102], it can be beneficial to implement a virtual gate consisting of the two tunnel barrier gates. Coupling the two tunnel barrier gates in parallel to the charging lines, approximately perpendicular to the virtual gate discussed earlier (dashed line in figure 3.6), results in a tuning parameter for the coupling symmetry without shifting the energy levels of the quantum dot.

# 4

# Transport through Quantum Dot Arrays

This chapter provides an overview over the transport properties of arrays consisting of multiple quantum dots. Based on using gate electrodes to manipulate the energy level alignment in the quantum dot array, a combination of current signals and charge detection signals will be presented and discussed. The first part will hereby be about the smallest possible array, the double quantum dot, followed by the extensions to the triple and quadruple quantum dot array.

## 4.1. Double Quantum Dot

A double quantum dot (DQD) is the smallest implementation of a multi quantum dot device. As such, it provides an excellent platform to study interdot coupling phenomena and their influence on the transport properties of multi quantum dot devices. Both, parallel and serial configurations are versatile platforms for research and applications. The parallel arrangement of two quantum dots for example allows to use one quantum dot as a charge detector for the other [103, 104] or to split Cooper pairs [105, 106]. Serial double quantum dots are frequently used as a basis to form spin qubits [23–26], and charge qubits [27–31], as well as hybrid qubits [32, 33]. Interestingly, both, the parallel [107, 108] and the serial [109, 110] configuration are candidates for thermoelectric devices.

In this work, the gate layout defines a serial configuration of QDs. The DQD presented here consists of the two central QDs of the device, QD2 and QD3. The DQD is defined by the gate voltages $V_{Bg1}$ and $V_{Bg2}$ from the lower side, and the plunger gate voltages $V_{Dg2}$ and $V_{Dg3}$ from the upper side. Via tunnel barrier gate voltages $V_{Tg2}$ and $V_{Tg4}$, the coupling between the DQD and both reservoirs is controlled, $V_{Tg3}$ is used to tune the interdot tunnel coupling. Both QDs contribute their individual energy scale to the overall system, which results in a two-dimensional energy space of the DQD. Additionally, the interdot coupling and the interaction between both QDs become crucial parameters for the properties and characteristics of the DQD system.

By measuring the transport through the DQD as function of both plunger gate voltages $V_{Dg2}$ and $V_{Dg3}$, the two-dimensional energy space of the DQD is probed. The current $I_{dot}$ through the DQD is given in figure 4.1 (a). The inset shows a colored SEM image of the device. The coloring of the gates relates to the gate voltages. Gray gates are grounded, golden gates are at finite voltages and red gates are measurement parameters. Similar to the SQD measurements, a bias voltage $V_{sd,dot} \approx 300\,\mu V$ is applied to predefine a transport direction. The constant gate voltages are $V_{Bg1} = V_{Bg2} = -0.4\,V$, $V_{Tg2} = -0.35\,V$, $V_{Tg3} = -0.25\,V$, and $V_{Tg4} = -0.47\,V$.

Two different slopes of charging lines are visible in the DQD current. These can be attributed to the two QDs by making reasonable assumptions for the relevant lever arms $\alpha_{j,i}$ of gate $j$ with respect to QD$i$ based on the gate layout. Due to the symmetric gate layout, $\alpha_{Dg2,2} \approx \alpha_{Dg3,3}$ and $\alpha_{Dg2,3} \approx \alpha_{Dg3,2}$. Additionally, the different distances allow the assumptions $\alpha_{Dg2,2} > \alpha_{Dg2,3}$ and $\alpha_{Dg3,3} > \alpha_{Dg3,2}$. With this, the two different slopes of charging lines can be clearly assigned to the two QDs. For the almost vertical charging lines, the influence of $V_{Dg2}$ on the energy levels is much larger than the influence of $V_{Dg3}$. These charging lines therefore correspond to energy levels of QD2. The charging lines
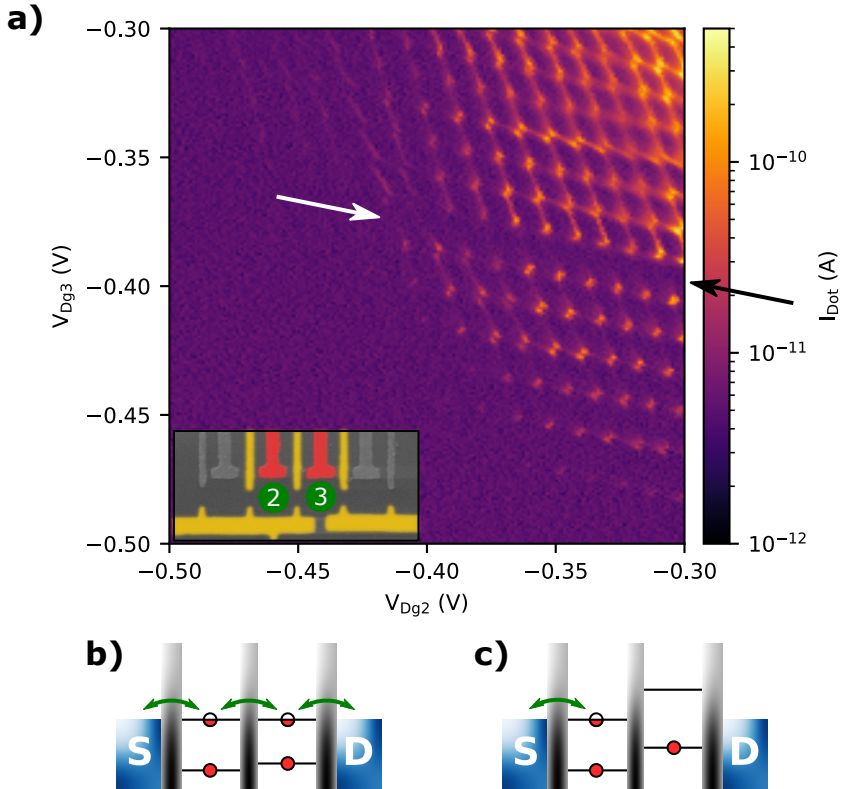
**Figure 4.1.: (a)** DQD Current $I_{dot}$ as function of the plunger gate voltages $V_{Dg2}$ and $V_{Dg3}$. Markers show the points, where the co-tunneling current is taken for figure 4.3. The arrows highlight a particular electron number of QD3, where the co-tunneling current is suppressed. Inset: Colored SEM image of the device. Gray gates are grounded, golden gates are kept at fixed voltages, and red gates are measurement parameters. **(b)** Energy level scheme of a DQD resonance. **(c)** Energy level scheme corresponding to the marked positions in the stability diagram, where QD2 is in resonance with Source, while QD3 is in Coulomb blockade.

with the smaller slope correspond to energy levels of QD3, respectively.

Whenever two of the charging lines approach each other, they anticross due to the interdot coupling, as described in section 2.2. This splits every DQD resonance into two energetically separated triple points and leads to the formation of the characteristic DQD honeycomb pattern [59]. At these triple points, exchange of electrons between the QDs and the reservoirs is energetically allowed, as depicted by the energy level schematic in figure 4.1 (b). From the capacitive model, current through the DQD is only expected to flow at these triple points, where three charge states are degenerate.

In the gate voltage region $-0.375\,\mathrm{V} \lesssim V_{Dg2} \lesssim -0.325\,\mathrm{V}$ and $-0.45\,\mathrm{V} \lesssim V_{Dg3} \lesssim -0.4\,\mathrm{V}$ in figure 4.1 (a), this behavior is well reproduced and the off-resonant current is strongly suppressed due to the Coulomb blockade. However, especially for the most positive gate voltages $V_{Dg2}$, $V_{Dg3} > -0.35\,\mathrm{V}$, finite current is not only observed at the triple points, but additionally in configurations where only one of the QDs is in resonance with the reservoirs, while the other QD is in Coulomb blockade, as schematically depicted in figure 4.1 (c). In this region, the honeycomb pattern is fully resolved in the DQD current $I_{dot}$. This can be explained when taking co-tunneling into account, where the off-resonant QD is only virtually occupied. For the most negative voltages $V_{Dg2}, V_{Dg3} \lesssim -0.4\,\mathrm{V}$, the current vanishes. In this regime, the tunneling rates are too small to resolve the current. Overall, both the resonant and the off-resonant current decrease from more positive to more negative voltages. This is a consequence of the capacitive influence of the gates on the neighboring tunnel barriers and therefore on the tunnel couplings $t_{S2}$ (between source and QD2), $t_{3D}$ (between QD3 and drain), and $t_{23}$ (between QD2 and QD3).

However, neither the resonant nor the off-resonant current decreases monotonously, but they fluctuate as function of the electron numbers in the QDs, with an overall decreasing trend. Especially at one particular

electron number $N_3$ in QD3, which is highlighted by the two arrows in figure 4.1 (a), the off-resonant current is fully suppressed, while finite values are found for more and less electrons in QD3. The current through the DQD is thus not only a function of the tunnel barriers but also dependent on the electron configuration. For more detailed insight, it is therefore necessary to determine the electron numbers on the QDs.

The detector signal corresponding to this measurement is shown in figure 4.2 (a) and complements the information of the current measurement. The charging lines of both QDs are visible over the entire voltage range, so that the regions of stable charge can clearly be identified. However, direct access to the electron numbers in the QDs is prevented due to the fact that the QDs were not fully depopulated within this measurement. In a more indirect way, the electron numbers can nevertheless be determined via the charging energies. The charging energies for the successive electron numbers can be determined by extracting the gate voltage differences $\Delta V_{\text{D}g2}$ between successive QD2 charging lines and $\Delta V_{\text{D}g3}$ between successive QD3 charging lines, respectively. The charging energy is then given by $E_C = -\alpha_{\text{G},i} \cdot e\Delta V_G$ (equation 2.13), where $\alpha_{\text{G},i}$ is the lever arm of gate $G$ with respect to QD$i$, $e$ the elementary charge and $\Delta V_G$ the gate voltage difference. The same procedure is then used on a reference measurement, where both QDs were fully depopulated. By comparing the evolution of the charging energies it is then possible to determine the electron number.

To account for fluctuations within the measurements, the gate voltage difference $\Delta V_G$ for each electron number was taken at six different positions in the stability diagram and the mean of these values was used to calculate the charging energies. The lever arms $\alpha_{\text{D}g2,2} = 0.097$ and $\alpha_{\text{D}g3,3} = 0.098$ used for the gate voltage to energy conversion have been determined by Coulomb diamond measurements. Figure 4.2 (b) exemplarily shows the charging energies for QD3 as function of the electron number, for the reference measurement (blue) and extracted from (a) (red).
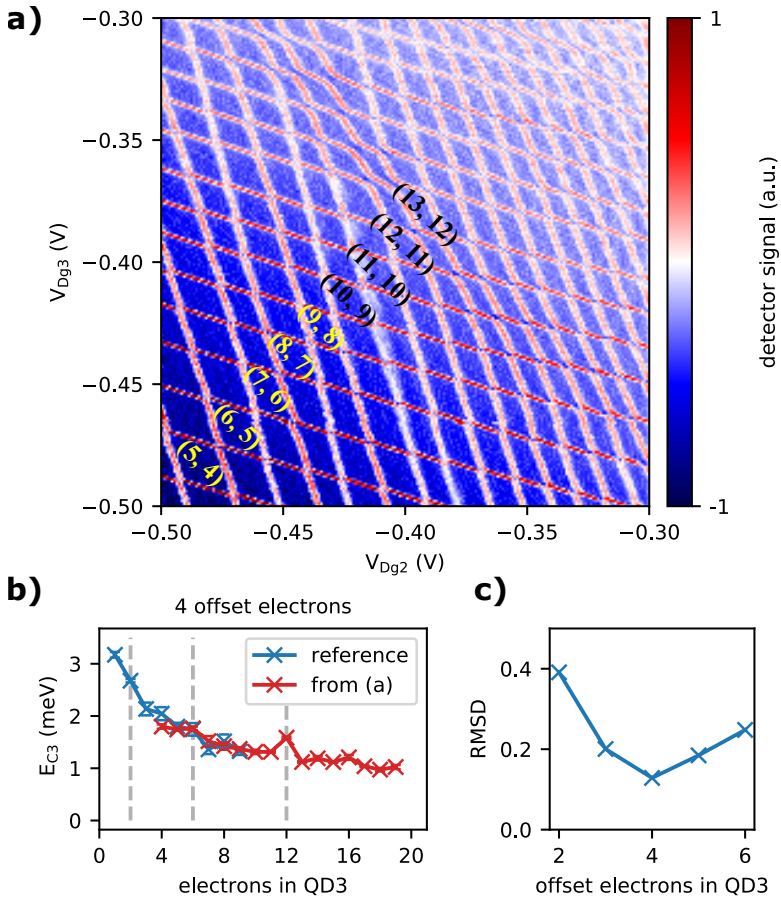
**Figure 4.2.: (a)** Detector signal corresponding to figure 4.1 (a). The charging lines of both QDs are visible over the full range of the stability diagram. **(b)** Evolution of the charging energies $E_{C3}$ of reference data with known electron numbers (blue) and data from (a) (red) with an offset of four electrons in QD3. The gray dashed lines indicate "magic numbers". **(c)** RMSD for different offset electrons in QD3. The clear minimum at four offset electrons determines the number of electrons in QD3. The identical procedure for QD2 is given in the appendix A.1 and results in five offset electrons in QD2. With these offsets, the charge states $(N_2, N3)$ of QD2 and QD3 are given in (a).

The red curve is offset by four electrons, so that in the overlapping region, the charging energies match best. As function of the number of offset electrons, the deviation from the reference curve increases. For different offset numbers, the root-mean-squared deviation

$$\text{RMSD} = \sqrt{\frac{\sum_{n=1}^{m}(E_{n,ref} - E_n)^2}{m}}$$

of the overlapping region was calculated, where $m$ is the number of overlapping points. $E_{n,ref}$ is the charging energy of the $n$-*th* electron from the reference measurement, $E_n$ the charging energie of the $n$-*th* electron extracted from figure 4.2 (a), with $n$ including the offset.

For two to six offset electrons in QD3, the RMSD is shown in figure 4.2 (c). It shows a clear minimum at four offset electrons, which allows to assign the QD3 electron numbers. The same procedure for QD2 results in five offset electrons and is found in the appendix A.1. The numbers $(N_2, N_3)$ in brackets in figure 4.2 (a) are the electron numbers in QD2 and QD3, based on these determined offset values.

This can now be used to investigate the co-tunneling through the DQD as function of the electron number $N_3$ in QD3. Figure 4.3 (a) shows again the measured current $I_{dot}$ as function of gate voltages $V_{Dg2}$ and $V_{Dg3}$. The colored dots mark positions on different charging lines of QD2 with QD3 being off-resonant. Each color hereby corresponds to one charging line of QD2. The positions are chosen, so that the detunings of the N-*th* and (N+1)-*st* energy level of QD3 with respect to the resonant level of QD2 are approximately equal, $\Delta_N \approx \Delta_{N+1}$. This situation is depicted in the energy level scheme in figure 4.3 (b). The current for these points is shown in figure 4.3 (c) in logarithmic scale and as function of the electron number in QD3. The lines are colored according to the dots in (a). For the number of electrons in QD2, 20 means the 20-*th* charging line of QD2 is in resonance with the reservoirs.

Lower electron numbers in the QDs correspond to more negative gate
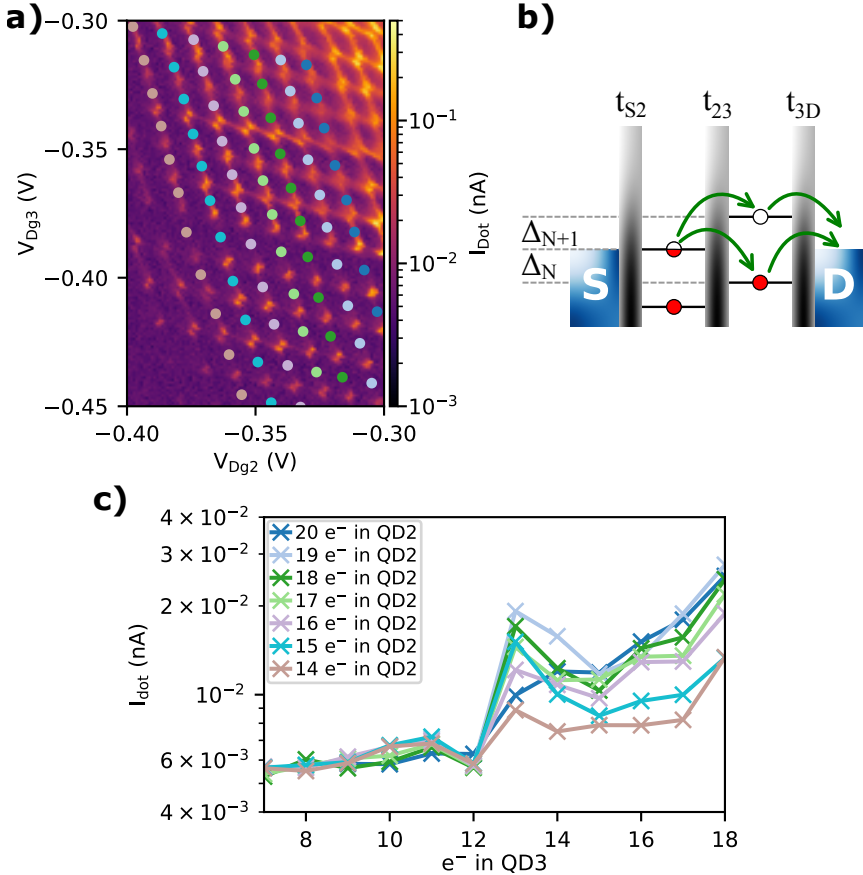
**Figure 4.3.: (a)** Transport regime of figure 4.1 (a) Colored points mark positions on a charging line of QD2 while QD3 is off-resonant. **(b)** Energy level schematic for the marked positions. The two closest energy levels of QD3 are approximately equally detuned with respect to QD2 $\Delta_N \approx \Delta_{N+1}$. **(c)** Co-tunneling current through QD3 as function of the number of electrons in QD3. Different lines represent different electron numbers in QD2 and are colored according to the markers in (a). The co-tunneling current is suppressed for the 'magic number' of $N_3 = 12$ electrons in QD3 whereas enhanced for $N_3 = 13$.

voltages. The lowest currents are therefore found for low electron numbers, where for $N_3 \leqslant 7$ the co-tunneling current is not resolvable any more and the spreading of the values is given by the noise floor. Up to $N_3 = 11$ the co-tunneling current then slightly increases and drops to a level below the noise floor at $N_3 = 12$, followed by a significant peak at $N_3 = 13$. From $N_3 = 15$ onward, the co-tunneling current again increases. This trend is observable for different electron numbers in QD2 while only the magnitude of the co-tunneling current is modulated. This indicates a mechanism, which is mainly dependent on QD3.

The situation of finite current with QD2 being resonant with the source reservoir and QD3 being off-resonant is comparable to co-tunneling through a SQD (QD3), with QD2 acting as reservoir. In lowest order, the co-tunneling coupling between QD2 and the non-neighboring drain reservoir is given by [42]

$$t_{co} = \frac{t_{23}t_{3D}}{\Delta_N} + \frac{t'_{23}t'_{3D}}{\Delta_{N+1}} \qquad , \qquad (4.1)$$

where $t_{23}$ is the coupling between QD2 and the N-*th* energy level of QD3, $t_{3D}$ the coupling between the N-*th* energy level of QD3 and drain and $\Delta_N$ is the detuning of the energy level with respect to the resonant QD2 and $\mu_D$. $t'_{23}$, $t'_{3D}$ and $\Delta_{N+1}$ refer to the (N+1)-*st* energy level of QD3, respectively.

The coupling quantities are directly affected by the gate voltages due to their capacitive influence on the tunnel barriers. In terms of gate voltage, the x-axis scale of figure 4.3 (a) is not linear, but monotonic. Smaller $N_3$ correspond to more negative $V_{Dg3}$, and at the same time to slightly more positive $V_{Dg2}$ (following the slope of the QD2 charging lines). Due to the monotonic changes in gate voltages, the capacitive influence on the coupling quantities is also expected to be monotonic, which therefore cannot explain the behavior as function of $N_3$. On the other hand, the evolution of the charging energies, which is given in 4.2 (b), is not strictly

monotonic and defines the detuning energies via $\Delta_N \approx \Delta_{N+1} \approx E_C/2$.

Especially at $N_3 = 12$, an increased charging energy is found, meaning the charging of the $13th$ electron needs additional energy compared to neighboring electron numbers. The charging energies for $N_3 = 11, 12, 13$ are

$$E_C = \begin{cases} 1.31\,\text{meV} & N_3 = 11 \\ 1.58\,\text{meV} & N_3 = 12 \\ 1.12\,\text{meV} & N_3 = 13 \end{cases} .$$

The vanishing co-tunneling current at $N_3 = 12$ is connected to this larger charging energy and the therefore larger detuning. The increasing co-tunneling current for $N_3 < 12$ also agrees with the decreasing charging energies. However, the behavior for $N_3 > 12$ does not follow the evolution of the charging energy. The increased charging energy for $N_3 = 12$ hints toward orbital shell effects. In two dimensions, $N = 12$ is a 'magic number' of a completely filled shell [10]. In a simplified picture of a symmetric potential without Hund's rules, the quantum mechanical states within an orbital shell are degenerate and the charging energy reduces to the classical Coulomb repulsion. Only when loading the first electron onto a new shell, the quantum mechanical contribution to the charging energy becomes relevant, leading to a peak in the charging energy.

The findings of a suppressed co-tunneling current for $N_3 = 12$ and a pronounced peak at $N_3 = 13$ shows evidence for the influence of shell effects on the coupling strength. When comparing the behavior to real atoms, the reactivity shows a similar behavior. Noble gases with a completely filled outer shell are chemically inert, while alkali metals with a single valence electron in the outer shell are highly reactive.

**Bias effects on a Double Quantum Dot**

A bias voltage $V_{sd,dot}$, as applied in the previous sections, is used to predefine a transport direction. However, as clearly visible in Coulomb diamond measurements, a transport window defined by a bias voltage can affect the transport properties of QD systems drastically. In the following, the transport properties of a DQD under applied bias are discussed.

For bias voltages $-0.5\,\text{mV} \leqslant V_{sd,dot} \leqslant 0.5\,\text{mV}$, a representation of the measured current $I_{dot}$ through the DQD as function of the plunger gate voltages $V_{Dg2}$ and $V_{Dg3}$ is shown in figure 4.4. The respective bias voltages are given in the upper left corner of each graph. For better comparability, $-I_{dot}$ is shown for the bias range $-0.5\,\text{mV} \leqslant V_{sd,dot} \leqslant -0.1\,\text{mV}$, where the measured current is negative. Additionally, a positive offset $I_{off} = 110\,\text{pA}$ was added for all bias voltages, so that also negative values can be visualized in the logarithmic scale. The fixed gate voltages are $V_{Bg1} = V_{Bg2} = -0.55\,\text{V}$, $V_{Tg2} = -0.5\,\text{V}$, $V_{Tg3} = -0.55\,\text{V}$, and $V_{Tg4} = -0.75\,\text{V}$. To achieve well defined tunnel barriers between the DQD and the reservoirs, voltages $V_{Dg1} = -0.35\,\text{V}$ and $V_{Dg4} = -0.275\,\text{V}$ are applied to the two outer plunger gates, so that the 2DEG is depleted, but QD1 and QD4 are not yet formed. The differences in gate voltages compared to the previously discussed DQD measurement are due to a different cooldown cycle of the device, which always leads to changes, especially regarding the electron density of the 2DEG.

The $V_{sd,dot}$ values are the voltage source values, which are applied to the right reservoir. The effective bias voltage differs from these values due to a thermoelectric voltage contribution. The sign change in the current happens between $V_{sd,dot} = 0\,\text{mV}$ and $V_{sd,dot} = -0.1\,\text{mV}$, which allocates the thermoelectric voltage $V_{th}$ in the interval $0\,\text{mV} \leqslant V_{th} \leqslant 0.1\,\text{mV}$. The black spots close to the resonances, which are only present for the two bias voltages close to the effective zero bias, can be explained by current rectification effects [111] of frequency noise. The overall current increases when increasing the bias window by increasing $|V_{sd,dot}|$.
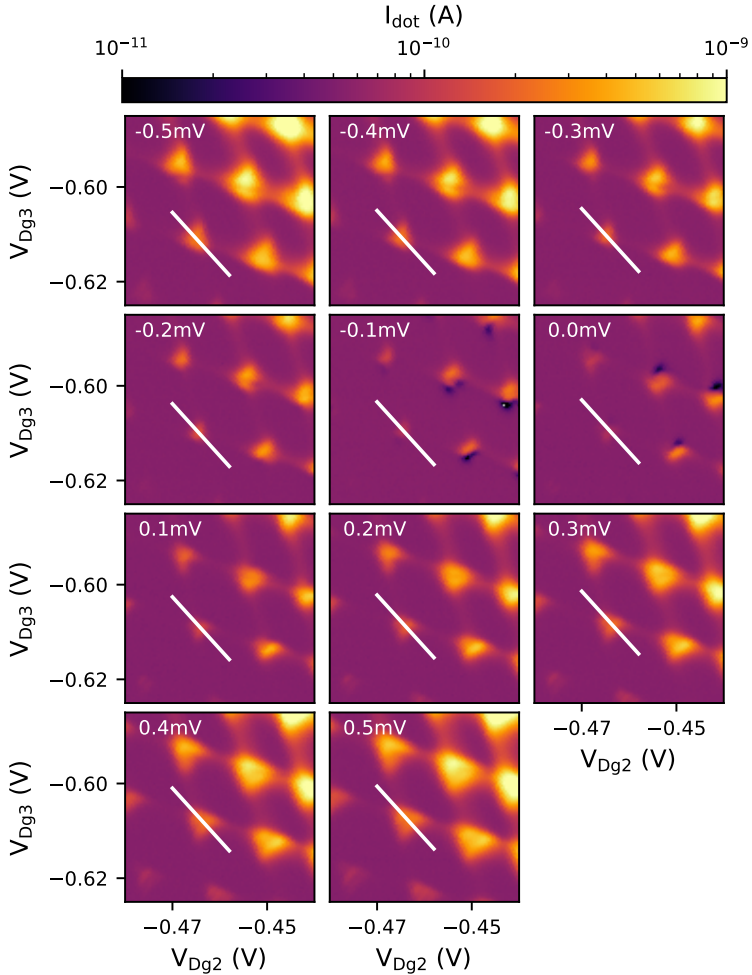
**Figure 4.4.:** DQD current $I_{dot}$ as function of the plunger gate voltages $V_{Dg2}$ and $V_{Dg3}$ for different $V_{sd,dot}$. $V_{sd,dot}$ is hereby applied to the drain reservoir, which is next to QD3.

The main differences are found close to the resonances, where regions of finite current are emerging. Additionally, the charging lines, where only one of the QDs has an energy level inside the bias window, are only barely visible for $|V_{sd,dot}| \leqslant -0.1\,\mathrm{mV}$ and become more and more pronounced with increasing bias voltage.

The emerging regions of finite current close to the resonances grow with increasing absolute bias voltage $|V_{sd,dot}|$. Depending on the sign of the bias voltage the sign of the current $I_{dot}$ and the direction of the triangular shaped finite current region is inverted. These triangular regions are typical for coupled DQDs under an applied bias with one bias triangle emerging for each of the two triple points of a resonance [59].

Figure 4.5 shows the $V_{sd,dot} = 0.5\,\mathrm{mV}$ data, where the triangular regions of finite current are well pronounced. In (a), the current $I_{dot}$ is shown, the corresponding detector signal is given in (b). An overlay of both is shown in (c). The detector signal shows clearly the charging lines of both QDs, where again the larger slope corresponds to QD2 and the smaller slope to QD3, allowing to identify the charge stability regions. Relative to the configuration $(N_2, N_3) = (0, 0)$, four charge states around a single resonance are given in figure 4.5 (a) and (b). The four configurations are the relevant charge configurations for this specific resonance. Contributions of other configurations can be neglected due to the charging energies of both QDs being of the order of $E_C \approx 1.3\,\mathrm{meV}$, which exceeds the transport window opened up by the applied bias by a factor of approximately 2.5.

From the overlay (c), where both the finite current regions and the charging lines are visible, it is clear that only one triangle per resonance is visible. This comes as a result of a small interdot capacitance as well as weak interdot coupling. There is only a small energy gap between the two triple points, so that the two triangles strongly overlap and appear as a single triangular region of finite current. For one of the resonances, the three corners of the triangle are marked by green circles and labeled as a,
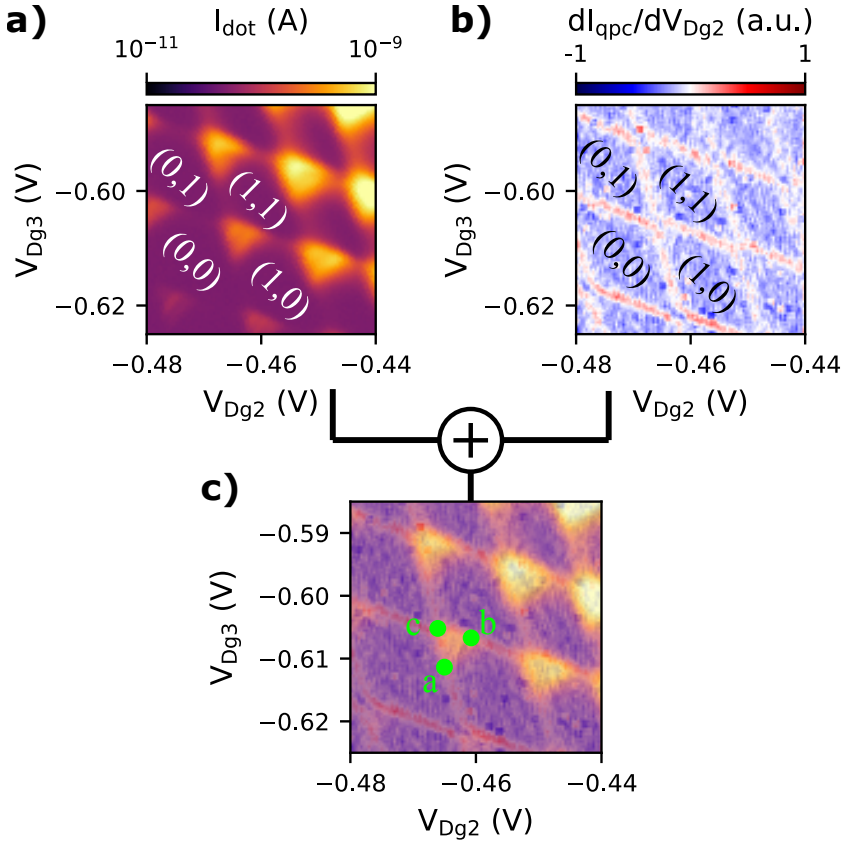
**Figure 4.5.: (a)** DQD current $I_{dot}$ as function of the plunger gate voltages $V_{Dg2}$ and $V_{Dg3}$ for $V_{sd,dot} = 0.5\,\mathrm{mV}$. The numbers in brackets in (a) and (b) are the electron numbers $(N_2, N_3)$ relative to $(0, 0)$. **(b)** Corresponding charge detector signal. The charging lines of both quantum dots are clearly visible and allow the assignment of the stable charge regions. **(c)** Overlay of (a) and (b), where both, the current through the DQD and the charging lines of the two QDs are visible. Due to the small interdot capacitance, the bias triangles of the two triple points strongly overlap, so that only a single bias triangle is visible per resonance. The three corners of a bias triangle are marked by a, b, and c.

b, and c.

The line connecting the two points a and b is parallel to the charge reconfiguration lines, interconnecting the triple points of the DQD resonances. In this direction, the detuning between the two QDs is kept constant, but the total energy is changed. Vice versa, perpendicular to the reconfiguration line, the detuning between the two QDs changes, while the total energy is kept constant. Due to the applied bias, which opens up a transport window of size $eV_{sd,dot}$, the line between points a and b can be identified as the resonance between the two QDs. As long as the two QDs are in resonance and inside the transport window, electrons can tunnel through the DQD.

Beginning from this resonance line, the triangle reaches out into the region, where the $(0, 1)$ configuration is energetically most favorable. Point c in figure 4.5 (c) marks the third corner of the triangle, the maximum detuning between the energy levels of the two QDs, for which current through the system is observed. As function of the detuning $\Delta$ relative to this point, cuts along the lines marked in figure 4.4 are shown in figure 4.6 (a) for different bias voltages. Point c is taken as the reference value here, since, with including the charge detector signal, position c can be determined more accurately than positions a and b. The detuning is calculated via equation 2.13 with lever arms $\alpha_{Dg2,2} = 0.1$ and $\alpha_{Dg3,3} = 0.1$. The cross lever arms, calculated via the slopes of the charging lines, are $\alpha_{Dg3,2} = \alpha_{Dg2,2}/2.8$ and $\alpha_{Dg2,3} = \alpha_{Dg3,3}/2.27$. The values $\alpha_{Dg2,2}$ and $\alpha_{Dg3,3}$ are rounded values. The values extracted from Coulomb diamond measurements are within 5 % of the rounded value, which is of the order of the readout uncertainty for the given Coulomb diamonds.

The current as function of detuning strongly depends on the applied bias voltage $V_{sd,dot}$. With more positive $V_{sd,dot}$, the peak position shifts toward more positive detuning energies, where the involved QD2 energy level becomes energetically more favorable. At the same time, the magnitude of the current $|I_{dot}|$ and the peak width increase with increasing
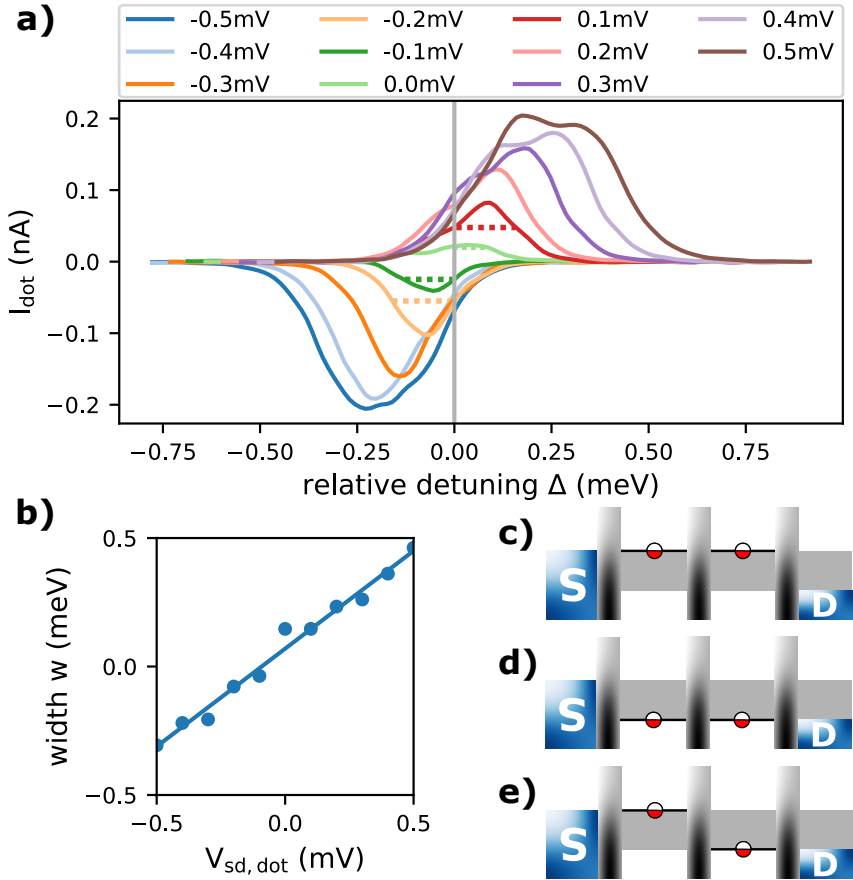
**Figure 4.6.: (a)** Cuts along the lines marked in 4.4. The current $I_{dot}$ is shown as function of the relative detuning between both QDs. $\Delta = 0$ corresponds to point c in figure 4.5. For positive detuning the involved QD2 energy level is energetically more positive. **(b)** The width (in energy detuning) of the current peak as function of the bias voltage $V_{sd,dot}$. The dotted lines in (a) illustrate, how the width is determined. The peak width follows the bias voltage linearly with approximately $w \approx eV_{sd,dot}$. **(c)**, **(d)**, and **(e)** show energy level schematics for the endpoints of the bias triangle, marked by a, b, and c in figure 4.5, respectively.

the absolute value of the bias voltage $|V_{sd,dot}|$. Figure 4.6 (b) shows the peak width $w$ as function of the bias voltage. The peak width $w$ is hereby taken at $I_{dot} = I_{dot}(\Delta = 0)$ in (a), which is illustrated by the dotted lines for some bias voltages.

The solid line shows a linear fit to the determined peak width, yielding $w \propto (0.89 \pm 0.13) \cdot eV_{sd,dot}$. Note here, that the small errors in the determination of $\Delta = 0$ have a large impact on the proportional constant. The determination of the $\Delta = 0$ positions was done by using the detector signal but due to the measurement resolution, the precision is limited. The given error originates from multiple fits for reasonable $\Delta = 0$ positions.

Within this uncertainty, the detuning at point c, the maximum detuning for which current through the DQD is observed, is defined by the transport window $\Delta \approx eV_{sd,dot}$. With this, the extent of the triangular structures is fully determined. For the case of a positive bias voltage, figure 4.6 (c), (d), and (e) show energy level schematics of the three corners of the bias triangle, corresponding to positions a, b, and c in figure 4.5 (c), respectively. Due to the positive bias voltage being applied to the drain reservoir, the drain chemical potential is smaller than the source chemical potential, so that electrons tunnel through the DQD from source to drain. Points a and b correspond to the two QDs being resonant. Since point a is located at more negative voltages, it is higher in energy than point b. Point a can thus be identified as the resonance of both QDs with source. The lower energy point b corresponds to the resonance of both QDs with drain. Toward point c, the detuning becomes more negative, so that the QD3 energy level becomes energetically more favorable. Eventually, at point c, the energy detuning matches the transport window. Here, the QD2 energy level is in resonance with source, the QD3 energy level is in resonance with drain.

In summary, this part discussed electronic transport through a DQD system. Charge stability diagrams as function of two gate voltages showed the DQD typical honeycomb pattern. In the weak coupling

regime, current was only present close to the triple points, as expected for a serial DQD system. For stronger coupling however, current was also observed in situations where only one of the QDs had an energy level within the bias window while the other QD was in Coulomb blockade. The co-tunneling current through the DQD (QD2 and QD3) with a QD2 energy level inside the bias window and QD3 being off-resonant, showed a significant dependency on the number of electrons $N_3$ in QD3. A suppression of the co-tunneling current was observed for the 'magic number' $N_3 = 12$ of a completely filled two-dimensional electronic shell, followed by a significant peak for one additional electron. The observed effect of the shell filing on the co-tunneling reminds of the reactivity of atoms, where completely filled shells (noble gases) provide stable configurations and alkali metals with one valence electron are highly reactive. Under an applied bias, the transport through the DQD showed triangular regions of finite current, the characteristic bias triangles. The boundaries of the bias triangles were discussed and the energetic extent was verified based on detuning dependent transport.

## 4.2. Triple Quantum Dot

A triple quantum dot (TQD) is the natural sequel of a DQD in terms of the investigation of multi quantum dots. By integrating a third quantum dot into the system, a variety of new possibilities and phenomena arises. TQDs are charging rectifiers [112, 113], and show quantum cellular automata processes [114–116]. A TQD qubit is expected to allow for additional functionality and tools for quantum computation compared to the DQD qubit [117–119]. But already the device design brings new opportunities. Where the DQD is limited to serial and parallel configurations, a TQD can be arranged in a triangular geometry [120–123], where each of the QDs can be tunnel coupled to both others. But also in the serial configuration discussed here, the third QD changes the system in a qualitative way. The serial TQD is the smallest possible QD chain, in which the central QD is not directly coupled to an electron reservoir and therefore can only be charged or discharged involving a second QD. The third QD also introduces a third, independent energy scale, the energy space of the TQD thus becomes three-dimensional [116, 124–126].

The overall complexity and flexibility of the system rises not only due to the additional energy scale. The additional QD compared to the DQD system also brings two additional tunnel coupling parameters. With three energy dimensions, four tunnel couplings and a bias voltage, the parameter space is quite large and a single measurement only provides insight into a small piece of the whole picture.

Even though a two-dimensional stability diagram does not provide all system information, it can for example be used to classify the parameter regime inside the parameter space. Such a stability diagram as function of the outer plunger gate voltages $V_{Dg1}$ and $V_{Dg3}$ is shown in figure 4.7. The current through the TQD $I_{dot}$ is presented in (a), the corresponding charge detector signal in (b). The constant gate voltages are $V_{Bg1} = V_{Bg2} = -0.55\,\text{V}$, $V_{Tg1} = -0.6\,\text{V}$, $V_{Tg2} = -0.37\,\text{V}$,

$V_{Tg3} = -0.52\,V$, $V_{Tg4} = -0.55\,V$, and $V_{Dg2} = -0.525\,V$. A bias voltage $V_{sd,dot} = 75\,\mu V$ was applied to predefine the transport direction. An offset of $I_{off} = 5.9 \times 10^{-11}\,A$ is added to $I_{dot}$ for the color plot in (a), so that negative currents due to rectification effects at $V_{Dg1} \approx -0.54\,V$, $V_{Dg3} \approx -0.62\,V$ have positive values and can thus be shown in logarithmic scale.

The current $I_{dot}$ shows structures of finite values in the regime $V_{Dg1} \gtrsim -0.6\,V$ and $V_{Dg3} \gtrsim -0.66\,V$. For more negative gate voltages, the current drops below the resolution limit of the measurement setup. In a serial configuration, the current through the device gets more and more suppressed with increasing the number of QDs. Therefore, the charge detection becomes more relevant, since it shows all charging events, which allows to identify the charge states contributing to the current flow. A comparison between current and detector signal allows the identification of two charging lines of the center QD2 in the transport regime, which are marked by arrows in figure 4.7 (a) and (b). The charging line marked as $N_2$ is almost entirely visible in the current, indicating strong coupling of the center QD2 to the neighboring QDs. For the $N_2 - 1$ charging line, the suppression of the current due to Coulomb blockade of QD1 or QD3 is significantly larger and finite current is mainly found close to the TQD resonances.

This trend of decreasing coupling strength of the center QD2 for more negative gate voltages is also clearly visible in the detector signal. The $N_2$ charging line is only vaguely visible in the detector signal. On the one hand, this is due to the hybridization with the neighboring QDs, which leads to a bending of the QD2 charging line close to the resonances. One the other hand, a large coupling broadens the charging lines. With the fixed detector response amplitude of a single charge being removed from the QD, this decreases the contrast in the given differential detector signal. For the $N_2 - 1$ charging line, the bending due to hybridization is also observed, but only for the most positive $V_{Dg3} \gtrsim -0.62\,V$. The broad-
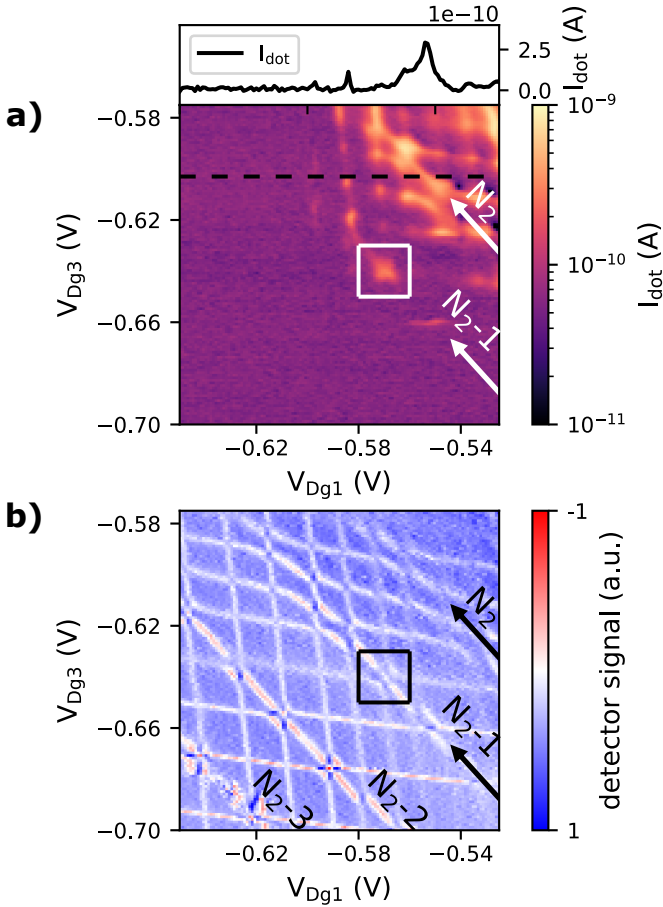
**Figure 4.7.: (a)** TQD current $I_{dot}$ as function of the outer plunger gate voltages $V_{Dg1}$ and $V_{Dg3}$. The panel on top shows a cut along the dashed line. Two charging lines of the center QD are marked by arrows. **(b)** The corresponding detector signal clearly shows three different slopes of charging lines, attributed to the three QDs. The charging lines of the center QD are nicely visible and almost diagonal. Loading and unloading does not rely on resonances with the outer QDs. The box marks a TQD resonance, visible in both, current $I_{dot}$ and detector signal.

ening of the charging line is smaller compared to the $N_2$ charging line, which in turn leads to the better contrast. Along the $N_2 - 2$ charging line, no features are visible in the current $I_{dot}$. In the detector signal however, the charging line is well resolved and the bending of the charging lines close to the resonances with the outer QDs, a signature of strongly tunnel coupled QDs, almost completely disappeared. The $N_2 - 3$ charging line, found at the most negative gate voltages $V_{Dg1}$ and $V_{Dg3}$, is not clearly visible any more. The charging line does not appear as a straight line, but is noisy, especially in the center of the honeycomb pattern span by QD1 and QD3. This is an indication for the tunneling times being of the order of the integration time $t_{int} = 20\,ms$. In contrast to before, the detector here does not integrate over many tunneling events, but instead reacts on single tunneling events, which reveals the stochastic nature of the tunneling. The highest tunneling rate for charging QD2 dominates this process.

A line cut along the horizontal dashed line in figure 4.7 (a) is shown on top of the color plot. The main peak in $I_{dot}$ corresponds to a resonance of QD2 with the reservoirs, while QD1 and QD3 are off-resonant. This peak lies in the center of the honeycomb cells span by QD1 and QD3 energy levels, where the detuning of the energy levels is maximal. The peak current is $I_{max} = 0.29\,nA$, which converts via $\Gamma^* = I/e$ to the effective tunneling rate $\Gamma^* = 1.83\,GHz$. A full transport cycle contributing to the current hereby consists of a loading event from the source reservoir to QD2 with rate $\Gamma_{S2}$ and an unloading event from QD2 into the drain reservoir with rate $\Gamma_{2D}$. Since the effective tunneling rate $\Gamma^* = \frac{\Gamma_{S2}\Gamma_{2D}}{\Gamma_{S2}+\Gamma_{2D}}$ is always smaller than the contributing individual tunneling rates, $\Gamma^*$ is a lower bound for the individual tunneling rates $\Gamma_{S2}$ and $\Gamma_{2D}$, which are co-tunneling rates. Within the shown gate voltage range of $125\,mV$ per gate, the change in co-tunneling rates between QD2 and the reservoirs can therefore be estimated to vary from the GHz-regime for the most positive gate voltages to the order of $50\,Hz (= 1/t_{int})$ for the most neg-

ative gate voltages.

Similar to the off-resonant current in the DQD, finite current through the TQD is not only found for situations, where all three QDs are resonant. Especially resonances of both outer QDs with the center QD2 being off-resonant are pronounced features in the current in 4.7 (a). In this situation, the current is also co-tunneling mediated, but in contrast to before, the co-tunneling interconnects QD1 and QD3 via virtual occupation of QD2 [127, 128]. For different peaks, the peak currents $I_{max}$ for this type of resonances close to the maximal detuning of the center QD2 are of the order of $I_{max} \approx 0.2\,\mathrm{nA}$ (1.2 GHz) and therefore slightly smaller than the previous process, where two co-tunneling transitions are involved. This might be due to the fact, that the leads and therefore multiple states are involved in these processes, whereas co-tunneling between QD1 and QD3 is between two discrete QD states.

Additionally, there is an asymmetry visible in the QD1-QD3 resonances. In $V_{Dg1}$-direction, the resonances are visible until the current drops below the resolution limit. In $V_{Dg3}$-direction, the resonances are only pronounced features for $V_{Dg3} \gtrsim -0.63\,\mathrm{V}$. This indicates a coupling asymmetry, where either $t_{23}$ or $t_{3D}$ are small compared to the other couplings and therefore the suppression of the off resonant current is more efficient. The detector signal gives additional information concerning these couplings. The charging lines of QD1 (almost vertical) are broadened and have a low contrast in the transport regime. Since this is also the case for QD2 and QD3 being off-resonant, the dominant process for charging and discharging QD1 is tunneling between source and QD1. This indicates a strong coupling $t_{S1}$ between source and QD1. The QD3 charging lines (almost horizontal) are less broadened and have higher contrast in the transport regime. The asymmetry in the QD1-QD3 resonances is thus most likely due to $t_{3D} < t_{S1}$.

A resonance between all three QDs is marked by boxes in figure 4.7 (a) and (b). For three center plunger gate voltages $V_{Dg2}$, a zoom onto this

resonance is shown in figure 4.8. (a-c) show the current $I_{dot}$, (d-f) the corresponding charge detector signal, and (g-i) show schematic stability diagrams with denoted electron configurations ($N_1$,$N_2$,$N_3$). Zero hereby refers to the background electron configuration. The fixed gate voltages are identical to figure 4.7.

In general, a TQD resonance is a three-dimensional object, where six quadruple points, each connecting four different charge configurations, are located within the three-dimensional energy space. These quadruple points are the TQD analogue to the triple points in DQDs, where the system is conductive even in the absence of a bias voltage. A two-dimensional measurement can therefore only provide partial information about the resonance and the quadruple points. The maximum number of quadruple points, that can be visible in a single two-dimensional measurement is four. However, in general, the plane in which four quadruple points are visible, is tilted against the two measurement axes, which reduces the amount of quadruple points visible in a single two-dimensional cut. The two remaining quadruple points are generally not visible in a two-dimensional cut, since the fourth configuration touches a visible triple point from the third dimension [116].

The center column (b, e, h) of figure 4.8 corresponds to $V_{Dg2} = -524.8\,\mathrm{mV}$ and shows a TQD resonance, close to a situation, where four quadruple points are expected simultaneously. The left (a, d, g) and right (c, f, i) column are taken at $2\,\mathrm{mV}$ more positive and more negative $V_{Dg2}$ values, respectively. The current $I_{dot}$ in the resonant case (b) shows finite values within the full plane enclosed by the four quadruple points. In (e), the detector signal shows the relevant charging lines for this resonance. An idealized schematic stability diagram, where the four quadruple points are highlighted by red dots is given in (h). As a first step, the lever arms are calculated to get insight into the relevant energy scales of this resonance.

From Coulomb diamond measurements (see appendix, figure A.2), the lever arms $\alpha_{Dg1,1} = -0.091e\Delta V_{Dg1}$, $\alpha_{Dg2,2} = -0.071e\Delta V_{Dg2}$, and
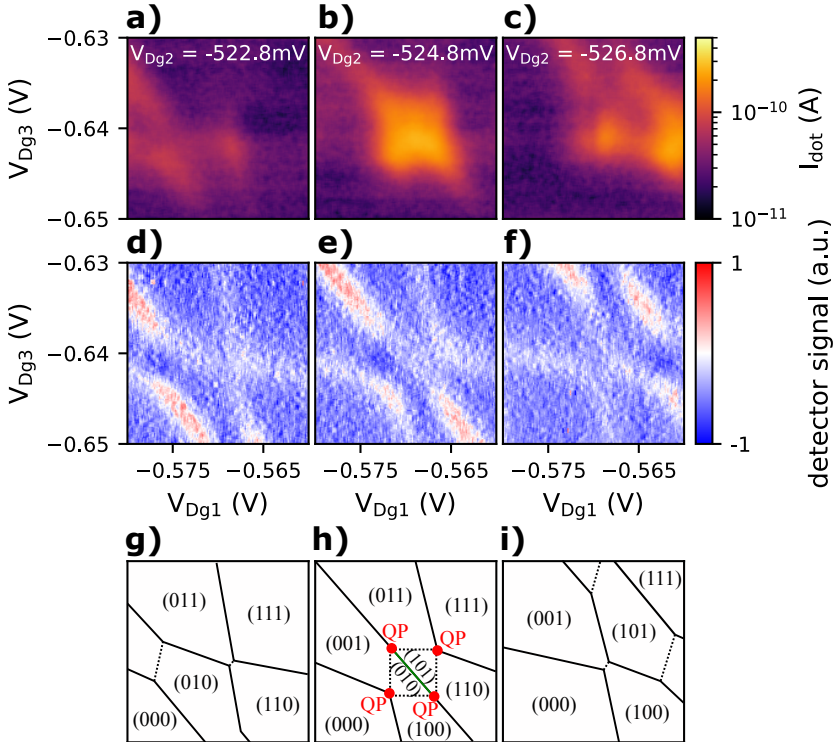
**Figure 4.8.:** Triple quantum dot resonance as function of the outer plunger gate voltages $V_{Dg1}$ and $V_{Dg3}$ for three values of the center gate $V_{Dg2}$. **(a-c)** The current $I_{dot}$ shows finite values not only at the resonances but also in the **(d-f)** corresponding detector signal, **(g-i)** schematic stability diagram with denoted charge configurations $(N_1, N_2, N_3)$, which refer to the background charge configuration.

$\alpha_{Dg3,3} = -0.077e\Delta V_{Dg3}$ have been determined for this cooldown cycle. The gate voltage difference $\Delta V_{Dg2} = -4\,\text{mV}$ thus converts into an energy difference of $\Delta E_2 = 284\,\mu eV$. Simultaneously, the gate voltage difference $\Delta V_{Dg2} = -4\,\text{mV}$ shifts the QD1 energy levels in $V_{Dg1}$-direction by $\Delta V_{Dg1} = 1.4\,\text{mV}$. This converts into an energetic shift of $\Delta E_1 = 128\,\mu eV$, yielding a lever arm $\alpha_{Dg2,1} = -0.032e\Delta V_{Dg2}$. Following the same procedure for QD3, the gate voltage difference $\Delta V_{Dg3} = 1.0\,\text{mV}$ converts into $\Delta E_3 = 77\,\mu eV$, yielding $\alpha_{Dg2,3} = -0.019e\Delta V_{Dg2}$. To compensate the energy level shift of QD2 $\Delta E_2 = 284\,\mu eV$ via $V_{Dg1}$, $\Delta V_{Dg1} = 8.4\,\text{mV}$ are needed. This results in $\alpha_{Dg1,2} = -0.034e\Delta V_{Dg1}$. The slope of the QD2 charging line in the $V_{Dg1}$-$V_{Dg3}$-space is $m = -1.07$, which allows to calculate $\alpha_{Dg3,2} = \alpha_{Dg1,2}/1.07 = -0.032e\Delta V_{Dg1}$. Finally, the lever arms $\alpha_{Dg1,3} = -0.0097e V_{Dg1}$ and $\alpha_{Dg3,1} = -0.0093e V_{Dg1}$ can be determined via the slopes of the QD1 and QD3 charging lines. These lever arms are summarized in tabular 4.1.

|       | $V_{Dg1}$ | $V_{Dg2}$ | $V_{Dg3}$ |
|-------|-----------|-----------|-----------|
| **QD1** | 0.091   | 0.032   | 0.0093  |
| **QD2** | 0.034   | 0.071   | 0.032   |
| **QD3** | 0.0097  | 0.019   | 0.077   |

**Table 4.1.:** Lever arms between gate voltages $V_{Dg1}$, $V_{Dg2}$, $V_{Dg3}$ and QD1, QD2, QD3.

With the lever arms it is now possible to calculate the energetic shift of the energy levels due to the interdot capacitances. These are the relevant energies for a TQD resonance, which define the extent of the resonance in the three-dimensional energy space. The bending of the charging lines due to hybridization does not allow exact extractions of the $\Delta V_G$ values in the given gate voltage range. However, good estimations can be derived for the QD2-QD3 resonance from the left hand resonance in figure 4.8 (d) and for the QD1-QD2 resonance from the top resonance in (f).

For the QD2-QD3 resonance, the energetic shift of the QD3 energy level is $\Delta V_{Dg3} \approx 2\,\text{mV}$, which converts into $\Delta E_{23} = -e\alpha_{Dg3,3}\Delta V_{Dg3} \approx 150\,\mu eV$. The shift of the QD1 energy level due to charging QD2 is also $\Delta V_{Dg1} \approx 2\,\text{mV}$, which converts into $\Delta E_{12} \approx 180\,\mu eV$. Both, (d) and (f) allow to extract the $\Delta V_{Dg1}$ and $\Delta V_{Dg3}$ values for the QD1-QD3 resonance, which lies in the center of both graphs. Due to the large distance the interdot capacitance $C_{13}$ between the two QDs is small, and therefore the shift $\Delta V_{Dg1} \approx 800\,\mu V$ as well. The shift is in this case smaller than the linewidths of the charging lines. Converting into energy yields $\Delta E_{13} \approx 70\,\mu eV$.

On the one hand, these energetic shifts due to the capacitive coupling between the QDs show, that the voltage range $\Delta V_{Dg2} = \pm 2\,\text{mV}$ compared to the resonant situation already present off-resonant situations. Nevertheless, in both cases (a) and (c), finite current is observed. This can be explained by the strong tunnel coupling between the QDs in combination with the proximity to the TQD resonance. Additionally, a QPC bias of $V_{sd,qpc} = 0.5\,\text{mV}$ was applied for the charge detection, which can act as a source of phonons and therefore enables inelastic tunneling [73–75]. Another source of energy is given by the dot bias $V_{sd,dot} = 75\,\mu V$, which is similar to the energetic shift $\Delta E_{13}$. The bias voltage in combination with the strong coupling, which further broadens the charging lines leads to an overlap and therefore the coexistence of all four possible charge configurations for the QD1-QD3 resonances. Effectively, the small interdot capacitance $C_{13}$ leads to a relatively flat three-dimensional TQD resonance. In combination with the availability of energy, this explains the observation of current in the full plane defined by the quadruple points in figure 4.8 (b).

## Bias effects on a Triple Quantum Dot

In the following, the effects of an applied bias on a TQD system will be discussed. A bias voltage does not only predefine a transport direction but

at the same time acts as a source of energy and therefore enables transport via excited configurations.

Similar to the DQD system discussed in section 4.1, gate dependent transport through the TQD under varying bias voltages $V_{sd,dot}$ will be discussed. Figure 4.9 shows an overview of the current $I_{dot}$ through the TQD as function of the outer plunger gate voltages $V_{Dg1}$ and $V_{Dg3}$ for different bias voltages $-2\,\mathrm{mV} \leqslant V_{sd,dot} \leqslant 2\,\mathrm{mV}$. As for the DQD case, an offset $I_{off} = 1.5 \times 10^{-11}\,\mathrm{A}$ is added to also allow negative current values to be plotted in logarithmic scale. For negative bias values the absolute current $|I_{dot} - I_{off}|$ is shown. The given bias values are the values applied to the drain (right) reservoir. Due to thermal voltages, the effective bias voltage differs from these values. The constant gate voltages are $V_{Bg1} = V_{Bg2} = -0.55\,\mathrm{V}$, $V_{Tg1} = -0.61\,\mathrm{V}$, $V_{Tg2} = -0.365\,\mathrm{V}$, $V_{Tg3} = -0.525\,\mathrm{V}$, $V_{Tg4} = -0.64\,\mathrm{V}$, and $V_{Dg2} = -0.547\,\mathrm{V}$.

Beginning from $V_{sd,dot} = 0\,\mathrm{V}$ toward more negative values, the overall current strongly increases. Up to $V_{sd,dot} = -0.8\,\mathrm{mV}$, the charging lines of QD1 (almost vertical) and QD3 (almost horizontal) are visible over the full transport range. The QD2 charging lines however, which are expected with an almost diagonal slope, can not clearly be identified. Only the rectification effects for $V_{sd,dot} = 0\,\mathrm{V}$ and $V_{sd,dot} = 0.4\,\mathrm{mV}$ and increased current values along a diagonal through $V_{Dg1} \approx -0.525\,\mathrm{V}$ and $V_{Dg3} \approx -0.55\,\mathrm{V}$ for $V_{sd,dot} = -0.4\,\mathrm{mV}$ hint toward quantized energy levels of QD2 taking part in the transport. In the corresponding detector signals (appendix A.3), the almost diagonal QD2 charging lines are however clearly visible.

For more negative $V_{sd,dot} \leqslant -0.8\,\mathrm{mV}$ and for the most positive gate voltages $V_{Dg1}$ and $V_{Dg3}$ the current strongly increases. For $V_{sd,dot} = -1.6\,\mathrm{mV}$ and $V_{sd,dot} = -2.0\,\mathrm{mV}$ the charging lines, the characteristic feature of single electron tunneling, are not resolvable due to the high background current in the regime $V_{Dg1} \geqslant -0.525\,\mathrm{V}$, $V_{Dg3} \geqslant -0.55\,\mathrm{V}$. The disappearance of the charging lines in this regime is also observed in
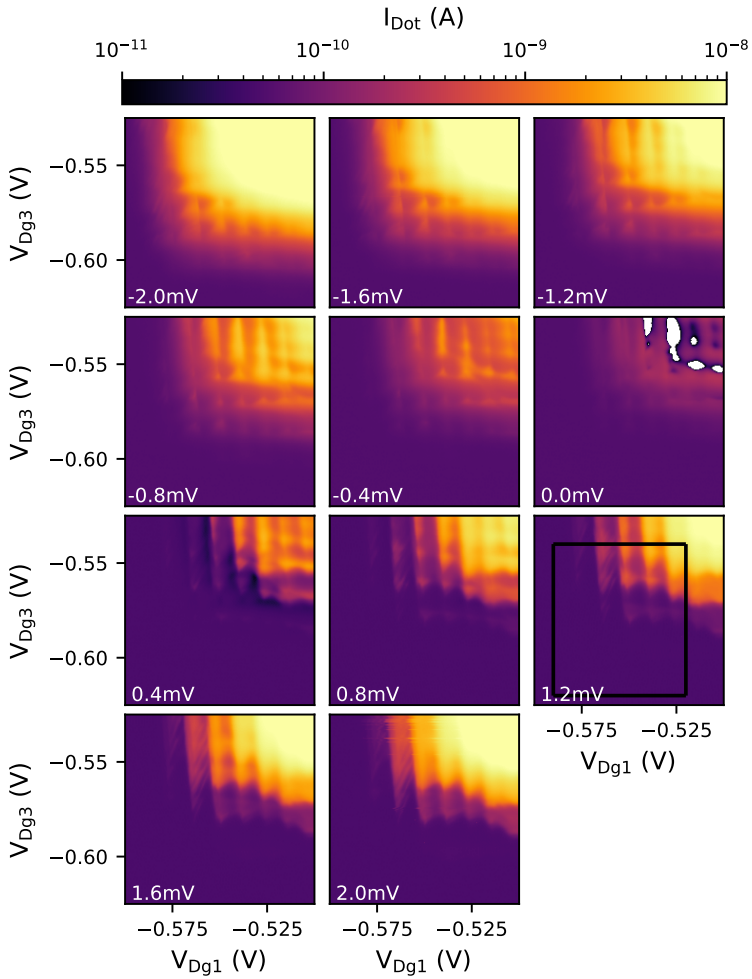
**Figure 4.9.:** TQD current $I_{dot}$ as function of the outer plunger gate voltages $V_{Dg1}$ and $V_{Dg3}$ for different $V_{sd,dot}$ in logarithmic color scale. For $V_{sd,dot} = 0\,V$, strong rectifying effects lead to negative currents (white spots), which can not be plotted in logarithmic scale.

the detector signals (appendix A.3). Most likely, this is a consequence of the electrostatic effect of the bias voltage. The applied bias voltage tilts the electrostatics of the total system and thereby also affects the tunneling barriers with respect to the reference potentials $\mu_S$ and $\mu_D$. Combined with the already small tunnel barriers in the regime of the most positive gate voltages, this can lead to a situation, where the QDs are not well defined any more.

In the regime of more defined tunneling barriers, $V_{Dg1} \leqslant -0.55\,V$ and $V_{Dg3} \leqslant -0.575\,V$, the $V_{sd,dot} \leqslant -0.8\,mV$ data shows triangular/trapezoid structures at the QD1-QD3 resonances, which remind of the DQD under applied bias discussed in section 4.1. In positive bias direction, beginning at $V_{sd,dot} = 0.4\,mV$, similar triangles evolve. In contrast to the negative bias direction, the positive bias direction shows additional substructures with increasing bias voltage. These substructures evolve with a positive slope in gate space, which reminds of the reconfiguration lines, where two QD states are degenerate. In a typical, unbiased stability diagram, these reconfiguration lines are the only lines with a positive slope.

The transport in this regime is thus again a function of the detuning between two QDs. However, in a TQD system three different detunings $\Delta_{12}$ between QD1 and QD2, $\Delta_{23}$ between QD2 and QD3, and $\Delta_{13}$ between QD1 and QD3 are present. So as a first step, a comparison of the different slopes in the stability diagram is used to identify the relevant detuning energy. Figure 4.10 panel (a) and (b) show a zoom into the $V_{sd,dot} = 1.2\,mV$ data, in the range marked by the box in figure 4.9.

The triangular shaped regions of finite off-resonant current are emerging from the QD1-QD3 resonances. For $V_{Dg1} \geqslant -0.555\,V$, no substructures are visible in the off-resonant current areas. Toward more negative $V_{Dg1}$ values, the substructures become prominent features in $I_{dot}$. Interestingly, the detector signal in (b) shows these structures as well, indicating changes in the average occupation or distribution of electrons in the TQD due to the underlying process. From the detector signal, the differ-
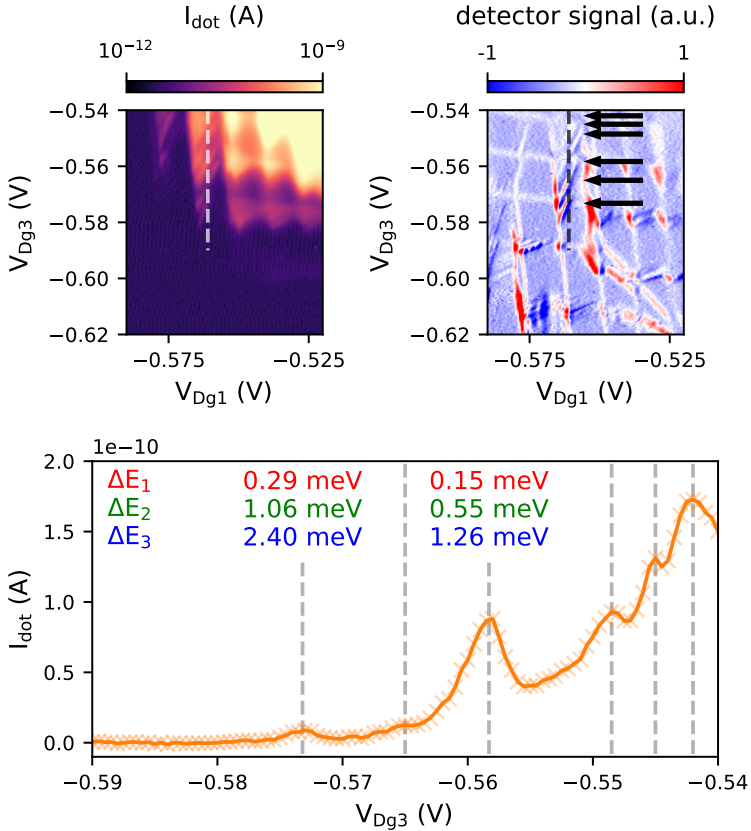
**Figure 4.10.:** (a) Current through the TQD as function of $V_{Dg1}$ and $V_{Dg3}$ for $V_{sd,dot} = 1.2\,\mathrm{mV}$ in the area marked by the box in figure 4.9. (b) Corresponding detector signal. Charging lines of all three QDs are visible, as well as reconfiguration lines, which coincide with the substructures present in the $I_{dot}$. Arrows mark the peak positions in the current along the dashed line. (c) Cut along the vertical dashed line in (a) and (b). The energy shifts $\Delta E_1$, $\Delta E_2$, and $\Delta E_3$ are given with respect to the rightmost peak, which coincides with a QD3 charging line. The two peaks, where the energy shifts are given, are two successive charging lines of QD3.

ent slopes of the charging and reconfiguration lines can be determined. The slope of the QD1 charging lines is $m_1 = -9.67$, the slope of the QD2 charging lines can be determined to $m_2 = -1.06$, and the slope of the QD3 charging lines is $m_3 = -0.13$. Two reconfiguration line slopes can be read out as well. In the lower part of the stability diagram, reconfiguration lines with slope $m_{R1} = 0.48$ are found, the slope of the substructures is $m_{R2} = 2.41$. All slopes are defined by the gate lever arms ratios. For the charging lines, the slopes are $m_i = -\alpha_{Dg1,i}/\alpha_{Dg3,i}$. Using the values of table 4.1, the slopes calculate to $m_1 = -9.78$, $m_2 = -1.06$, and $m_3 = -0.12$, matching well with the extracted charging line slopes.

For the reconfiguration lines, the relation between lever arms and reconfiguration line slope is [129]

$$m_{Rij} = \frac{\alpha_{Dg1,i} - \alpha_{Dg1,j}}{\alpha_{Dg3,j} - \alpha_{Dg3,i}} \qquad . \tag{4.2}$$

The calculated values are $m_{R12} = 2.51$, $m_{R23} = 0.54$, and $m_{R13} = 1.20$. Comparing the extracted and the calculated slopes allows to assign the slope $m_{R1}$ to the QD2-QD3 reconfiguration and the slope of the substructures $m_{R2}$ to the QD1-QD2 reconfiguration. Increased conductivity within the areas of off-resonant current is therefore found for specific detuning values $\Delta_{12}$ between QD1 and QD2. Figure 4.10 (c) shows a vertical cut through (a). $V_{Dg1} = -0.561\,\text{V}$ was chosen, so that the cut lies between two QD1 charging lines, meaning QD1 is off-resonant over the $V_{Dg3}$ range shown. The cut shows a series of peaks with varying distances, which are marked by the gray dashed lines. The positions of the peaks are additionally marked by arrows in the detector signal in (b). The detector signal allows to assign charging events to the peaks. The first peak on the right coincides with a QD3 charging line in the detector signal. For the two peaks at $V_{Dg3} = -0.558\,\text{V}$ and $V_{Dg3} = -0.573\,\text{V}$, the energetic shift values of the QDs $\Delta E_1$, $\Delta E_2$, and $\Delta E_3$ with respect to the first peak are given. From the stability diagram and from the $\Delta E_3$ val-

ues, these peaks can clearly be assigned to charging lines of QD3. With $\Delta E_C(N_3) = 1.26\,\text{meV}$ and $\Delta E_C(N_3 - 1) = 2.40\,\text{meV} - 1.26\,\text{meV} = 1.14\,\text{meV}$, the charging energies are typical values for this device in the many electron regime [97].

The smaller peaks in-between are due to the substructures, which are parallel to the QD1-QD2 reconfiguration line in the stability diagram. Each of these peaks therefore corresponds to a fixed detuning value between QD1 and QD2. In the detector signal, these peaks coincide with the dark blue lines, which correspond to a more negative potential in the vicinity of the detector. This can either be achieved by adding an electron to the system or by moving an electron into the direction of the detector. The energetic shift $\Delta E_i$ for each individual QD and all detunings between different QDs are given in table 4.2. All values are with respect to the peak at $V_{Dg3} = -0.542\,\text{V}$, the rightmost peak in figure 4.10 (c).

| $V_{Dg3}$ (V) | -0.542 | -0.545 | -0.549 | -0.558 | -0.565 | -0.573 |
|---|---|---|---|---|---|---|
| $\Delta E_1$ (meV) | 0 | 0.03 | 0.06 | 0.15 | 0.21 | 0.29 |
| $\Delta E_2$ (meV) | 0 | 0.10 | 0.22 | 0.55 | 0.78 | 1.06 |
| $\Delta E_3$ (meV) | 0 | 0.23 | 0.50 | 1.26 | 1.77 | 2.40 |
| $\Delta_{12}$ (meV) | 0 | 0.07 | 0.16 | 0.40 | 0.57 | 0.77 |
| $\Delta_{23}$ (meV) | 0 | 0.13 | 0.28 | 0.71 | 0.99 | 1.34 |
| $\Delta_{13}$ (meV) | 0 | 0.20 | 0.46 | 1.11 | 1.56 | 2.11 |

**Table 4.2.:** Energetic shift and detuning values for the peaks marked in figure 4.10.

Using the detuning values $\Delta_{12}$ between QD1 and QD2 the energy scale of the process behind the substructures can be deduced. While $\Delta_{12} = 0.07\,\text{meV}$ for the $V_{Dg3} = -0.545\,\text{V}$ peak does not provide an energy scale, due to the definition of $\Delta_{12} = 0$, where the energy level alignment of QD1 and QD2 is not known, the detuning difference between two successive substructure peaks is a meaningful value. When starting at the

$V_{Dg3} = -0.545\,\text{V}$ peak and going to the $V_{Dg3} = -0.549\,\text{V}$ peak, the detuning between QD1 and QD2 changes by $\Delta_{12} = 0.16\,\text{meV} - 0.07\,\text{meV} = 0.09\,\text{meV}$.

The detector signal shows, that the two leftmost peaks in figure 4.10 (c) coincide with the substructures. In detuning between QD1 and QD2, this means $\Delta_{12} = 0.77\,\text{meV} - 0.57\,\text{meV} = 0.20\,\text{meV}$, providing an additional meaningful value for the underlying process. The energy scale between successive substructure peaks extractable here is therefore in the range of $90\,\mu\text{eV} \leqslant \Delta_{12} \leqslant 200\,\mu\text{eV}$, which is the energy scale of excited states of the individual QDs in the many electron regime [97]. It is thus very likely, that the underlying processes of the substructures are based on excited state interdot transitions between QD1 and QD2.

However, since these substructures are not visible over the full transport range, the presence of excited states is not the only condition to be satisfied. Additional information about the boundary conditions is relevant for understanding the underlying process. Referring to this, figure 4.11 shows Coulomb diamonds in this range, which inherently provide additional information about the bias dependency and allow deeper insight into the energy level alignment. However, the Coulomb diamonds were not obtained in the typical way by directly measuring $I_{dot}$ or $dI_{dot}/dV_{sd,dot}$ as function of $V_{sd,dot}$ and stepping the gate voltage. The Coulomb diamond data presented here was reconstructed from the three-dimensional data set already used for figure 4.9. In this case, the transport $I_{dot}$ was measured as a sequence of two-dimensional stability diagrams with sweep gate voltage $V_{Dg1}$ and stepping the gate voltage $V_{Dg3}$ after each $V_{Dg1}$-line. Only after completion of the two-dimensional measurement, the bias voltage $V_{sd,dot}$ was stepped. The differential conductance $dI_{dot}/dV_{sd,dot}$ was then obtained by taking the numerical derivative of $I_{dot}$. Due to the three-dimensionality of the original measurement, the $V_{sd,dot}$ resolution of $133\,\mu\text{V}$ is low compared to typical Coulomb diamond measurements.
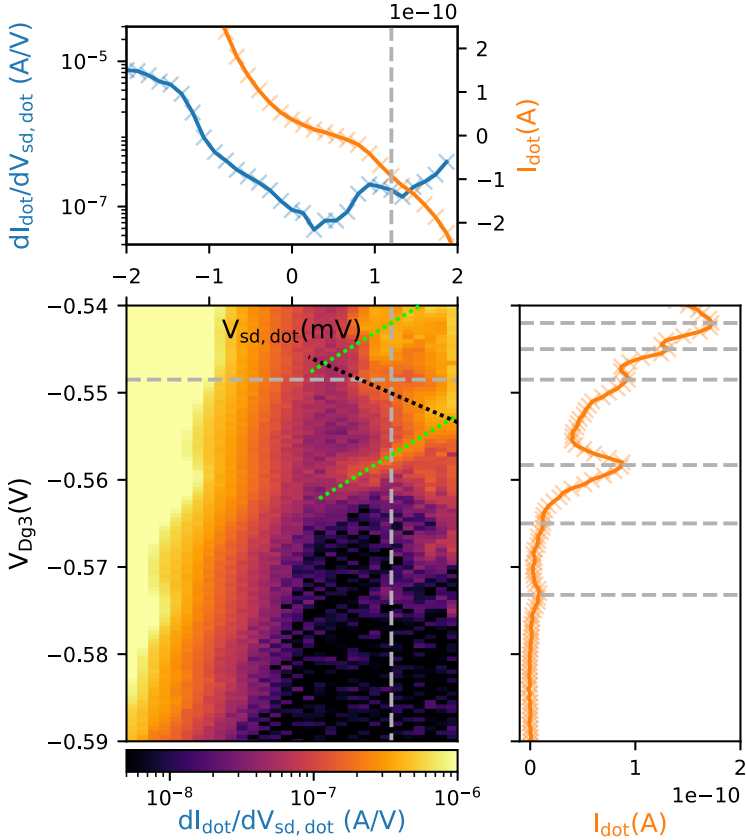
**Figure 4.11.:** TQD Coulomb diamonds as function of $V_{Dg3}$ reconstructed from the three-dimensional data presented in figure 4.9. The $dI_{dot}/dV_{sd,dot}$ data was obtained by taking the numerical derivative of $I_{dot}$. The color plot shows the Coulomb diamonds. Dotted lines are guides to the eyes. The top panel shows a horizontal cut, the right panel a vertical cut along the dashed lines. Orange lines present $I_{dot}$, the blue line in the top panel shows $dI_{dot}/dV_{sd,dot}$. The crossing point of both cuts is the $V_{Dg3} = -0.549\,V$ substructure peak in figure 4.10 and table 4.2. The vertical cut in the right panel is identical to figure 4.10 (c).

103

Nevertheless, due to the stability of the device, some of the typical features of Coulomb diamonds can be recognized in the color plot. No perfect Coulomb blockade is observed, where the current drops below the resolution limit, as soon as one QD is in blockade, but some of the source and drain resonances can be identified. The horizontal and vertical dashed line mark the cuts presented in the top and right panel, respectively. The data in the right panel is hereby only the current $I_{dot}$ and identical to figure 4.10 (c). Both cuts intersect at the $V_{Dg3} = -0.549\,V$ substructure peak discussed before.

First of all, the asymmetry regarding positive and negative $V_{sd,dot}$ catches the eye. Toward negative $V_{sd,dot}$, the absolute current $|I_{dot}|$ increases substantially faster than toward positive $V_{sd,dot}$. This is probably due to the electrostatic effect of the bias voltage, which tilts the potential of the 2DEG. By applying negative potentials, the tunneling barriers are therefore reduced with respect to the 2DEG potential, which results in higher currents. Applying positive potentials has the reversed effect of increasing tunneling barriers, which reduces the current.

For positive $V_{sd,dot}$, where the substructures are found, the tunnel barrier configuration allows the observation of several resonances. As described in 2.1.4, positive slopes in Coulomb diamonds correspond to resonances with the reservoir, where the potential is applied (here: right, drain), negative slopes correspond to resonances with the grounded reservoir (here: left, source). The most prominent feature in the Coulomb diamonds is the resonance, which corresponds to the $V_{Dg3} = -0.558\,V$ peak in the vertical cut in the right panel. It is marked by the lower green dotted line. In the previous discussion, the detector signal was used to identify this peak as a QD3 charging line. Due to the positive slope, which identifies a resonance with the right reservoir, the dominant process for charging QD3 can therefore be deduced to be charging via the neighboring drain reservoir.

Beginning from this resonance and going toward more positive

$V_{Dg3}$, a faintly visible resonance with a negative slope is found in $dI_{dot}/dV_{sd,dot}$ along the black dotted line. At $V_{Dg3} = -0.55\,V$ this resonance intersects with the vertical cut. This value is close to the $V_{Dg3} = -0.549\,V$ substructure peaks in $I_{dot}$. The small offset $V_{Dg3}$ can be understood by taking the background current into account. The background current increases toward more positive $V_{Dg3}$, so that a peak on top of the background becomes asymmetric and is shifted toward more positive $V_{Dg3}$. A detailed analysis of a peak structure on a background current thus requires the subtraction of the background current [130].

Since the absolute values of the positive and negative slope are similar, the negative slope resonance can also be assigned to QD3. With the topmost peak in the vertical cut at $V_{Dg3} = -0.542\,V$ also being known as a QD3 resonance, the upper green dotted line can be constructed in parallel to the lower one, which should coincide with the QD3 resonance. From this half diamond, the bias offset can be read to $V_{sd,off} \approx 350\,\mu V$. The right corner of the half diamond lies at $V_{sd,dot} \approx 1.9\,mV$, the gate voltage difference between the two QD3 resonances is $\Delta V_{Dg3} \approx 15\,mV$. The charging energy can therefore be estimated to $E_C \approx 1.55\,meV$, yielding a lever arm of $\alpha_{Dg3,3} = -0.103\,e\Delta U_{Dg3}$. This is significantly larger than the earlier found value of $\alpha_{Dg3,3} = -0.77\,e\Delta U_{Dg3}$, which can be explained by the large uncertainties in the determination of the slopes due to the long timescales between the individual data points.

In the horizontal $dI_{dot}/dV_{sd,dot}$ cut in the top panel, the position of the substructure (gray dashed line) does not show a pronounced feature. The substructure is located at $V_{sd,dot} = 1.2\,mV$ directly behind the visible peak at $V_{sd,dot} = 1\,mV$, which comes from the QD3-source resonance. This might be due to the low resolution and relative noise due to the reconstruction, but can as well be a signature, that the conductance of the substructures does not show a significant bias dependency.

The available information about the situation, in which the substructures in the gate voltage dependent transport and under applied bias are

present, can now be combined to discuss a probable underlying process. Referring to this, figure 4.12 (a) shows the charge detector signal, which was already shown in figure 4.10 for $V_{sd,dot} = 1.2\,mV$ and (b) shows a schematic energy level diagram based on the information gathered within this section.



**a)** detector signal (a.u.)   **b)**
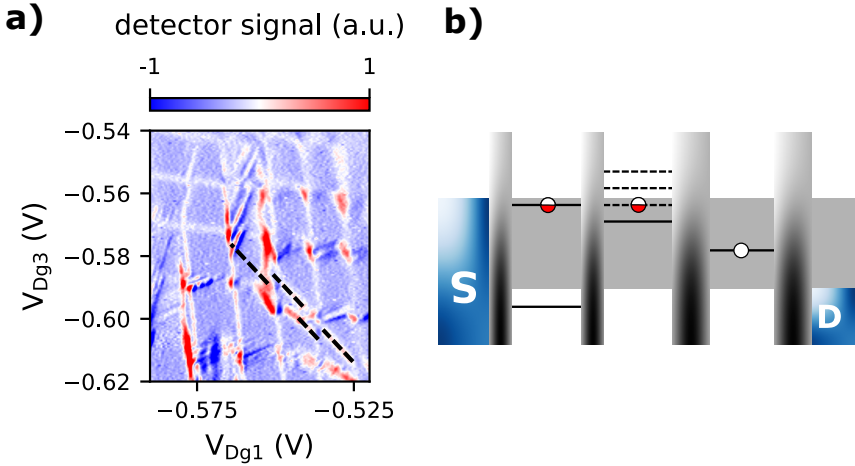
**Figure 4.12.:** (a) Charge detector signal of the $V_{sd,dot} = 1.2\,mV$ data, as already shown in figure 4.10. The dashed lines mark a QD2 charging line where the gaps are shifts due to the interdot coupling. (b) Schematic energy level diagram illustrating the process, which leads to the substructures in the linear transport under applied bias. The ground or any excited state of QD2 is loaded from source via the resonant QD1 ground state. Followed by higher order tunneling via QD3 to drain this allows a contribution to the current $I_{dot}$.

The presence of substructures was observed in the transport regime for the most negative $V_{Dg1}$ and in parallel to the QD1-QD2 charge reconfiguration lines. The most negative voltages $V_{Dg1}$ correspond to the largest tunneling barriers between source and QD1 as well as between QD1 and QD2. In the detector signal, the substructures are visible as a charging events, which increase the negative potential in the vicinity of the de-

tector. Between two of the substructure lines, the negative potential is reduced (white/red lines), i.e. an electron is removed from the vicinity of the detector. Since this occurs in parallel to the QD1-QD2 reconfiguration lines, the process behind the substructures increases the occupation probability of QD2 via electron transfer from QD1. At the same time, the visibility in the detector signal means, that the loading process of QD2 via source and QD1 is more efficient than the unloading process via QD3 to drain. As a consequence, the ground state charging lines of QD1 and QD2 in the detector signal have to be resonances with source. From the Coulomb diamonds it is known, that the dominant process for discharging QD3 is the drain resonance. In combination, this can be explained by the tunnel barriers to the left of QD2 being more transparent than the tunnel barriers to the right of QD2.

The substructure lines are connected to a QD1 charging line. They are evolving into positive gate voltage direction, meaning toward lower energies compared to the resonance at which QD1 is discharged. Including the shifts due to the interdot coupling, a continuation of the QD2 charging line, which is almost diagonal and enters the stability diagram from the bottom right is given by the dashed lines in figure 4.12 (a). Similar to the QD1 situation, the substructures are only found at energies lower than the ground state discharging of QD2. Since the substructure lines merge with the QD1 charging line, the contribution of the excited states comes from QD2.

The process behind the substructures is therefore a transition between the QD1 ground state and QD2. Different substructure lines are due to resonances between either the ground state or an excited state of QD2, where each line corresponds to a different QD2 state. To complete the charge transfer from source to drain, which is necessary for these structures to be visible in the current $I_{dot}$, there have to be transitions from QD2 via QD3 to the drain reservoir. An exemplary energy level diagram for the case of the resonance between QD1 and the first excited state of

QD2 is shown in figure 4.12 (b). Since the substructures are also present for off-resonant QD3, the QD3 level is chosen off-resonant in the diagram. Two possible charge transfer mechanisms from QD2 to drain while QD3 is off-resonant are higher order tunneling or inelastic tunneling, for example by emission of a phonon. Based on the previously derived configuration of the tunnel barriers with larger barriers around QD3, inelastic tunneling hereby is the more probable process.

Starting from the resonance condition sketched in figure 4.12 (b) and changing the detuning $\Delta_{12}$ between QD1 and QD2 breaks the resonance, where elastic tunneling is allowed. As a consequence, the efficiency of the loading process for QD2 goes down and thus the average occupation of QD2 as well, which is resolved in the detector signal.

For $V_{D\,g3} \geqslant -0.58\,\mathrm{V}$, QD2-QD3 reconfiguration lines become visible as dark blue lines. This is a sign for the right tunnel barrier to become even less transparent, which allows charging processes from the source via QD2 to change the average occupation of QD3 within the integration time. This shows how a coupling asymmetry in a TQD device can have critical impact on the transport characteristics under the availability of energy.

In this part, electronic transport measurements through a TQD system were presented and discussed. A short introduction about the serial TQD system was given based on a two-dimensional stability diagram as function of the two outer plunger gate voltages. Different coupling regimes of the center QD, which is not directly coupled to a reservoir, were shown. Ranging from strongly coupled with the neighboring QDs, so that finite current was observed along the full charging line, over the intermediate regime, where current is only observed close to a TQD resonance down to a regime, where the charging line becomes noisy in the charge detection signal due to tunneling rates of the order of the measurement frequency. In the regime of intermediate coupling, the three-dimensional energy space of a TQD resonance was discussed. The charge detector

signal was used to identify the extent of the TQD resonance in the three-dimensional energy space. With a bias voltage larger than one of the energy dimensions, finite current was observed in the full volume of the resonance. The bias dependency of transport through a TQD was discussed. With applying larger bias voltages, triangular shaped structures of finite current formed, similar to the DQD case. In several of the triangular structures, additional substructures were present. Based on the coupling asymmetry, the energy scales and the energetic situation for which the substructures are observed, a plausible mechanism for the occurrence of the substructures was deduced.

## 4.3. **Quadruple Quantum Dot**

Quadruple quantum dots (QQDs) can be seen as a crucial step toward the implementation of QD based applications. Serial arrangements naturally inherit all functionality of a serial TQD while the additional QD provides additional functionality, as for example the possibility to operate the system as a coupled two qubit system, with each qubit consisting of a DQD [26, 131, 132]. Similar to the extention from two to three QDs, the extention to four QDs also provides new possibilities in terms of the arrangement of the QDs. A QQD can be arranged in a 2x2 QD array, the smallest possible implementation of a QD matrix [58, 133].

The quadruple quantum dot (QQD) uses the potential of the device to its fullest. All gates are used to define four QDs in series. In a serial QQD, two of the QDs are not directly coupled to a reservoir, but only indirectly via another QD. Due to this indirect coupling, the energy level alignment of QD2 and QD3 and their coupling parameters are expected to have a large impact on the transport properties. However, with a four-dimensional energy space and five coupling parameters, the parameter space is even larger than for the TQD. A two-dimensional stability diagram therefore only reveals a small part of the full picture.

Such a stability diagram as function of the outer plunger gate voltages $V_{Dg1}$ and $V_{Dg4}$ is shown in figure 4.13. The QQD current $I_{dot}$ is given in (a) in logarithmic scale, the corresponding detector signal is shown (b). The constant gate voltages are $V_{Bg1} = V_{Bg2} = -0.575\,\text{V}$, $V_{Tg1} = -0.525\,\text{V}$, $V_{Tg2} = -0.335\,\text{V}$, $V_{Tg3} = -0.40\,\text{V}$, $V_{Tg4} = -0.525\,\text{V}$, $V_{Tg5} = -0.60\,\text{V}$, and $V_{Dg2} = V_{Dg3} = -0.59\,\text{V}$. A bias voltage of $V_{sd,dot} = 100\,\mu\text{V}$ was applied to predefine the transport direction. A two-dimensional uniform filter was used to smooth the detector signal. The vertical red line in the detector signal at $V_{Dg1} \approx -0.47\,\text{V}$ corresponds to a jump in $I_{qpc}$, most likely induced by a charge trap in the vicinity.

The symmetry of the device can again be used to assign the charging lines of different slopes to the four QDs. In the given serial configuration, the current $I_{dot}$ depends strongly on resonances between the QDs, so that the identification of the charging lines of the individual QDs can be difficult. The detector signal however shows the charging events of the individual QDs also away from resonances. The almost vertical charging lines with the small spacing of $\Delta V_{Dg1} \approx 10\,\text{mV}$ can be assigned to QD1. The second largest (negative) slope with the spacing of $\Delta V_{Dg1} \approx 50\,\text{mV}$ corresponds to QD2 charging lines. The small (negative) slope stems from QD3 charging lines. QD4 charging lines are only barely visible in the detector signal on this scale. This is a result of $V_{Dg1}$ being the sweep gate and the derivation in $V_{Dg1}$-direction. In combination with the slope of the QD4 charging lines being expected to be almost horizontal, the contrast in the detector signal is drastically reduced, especially for strong coupling, where the contrast of the charging lines is already small due to the broadening.

In this two dimensional cut, the current $I_{dot}$ in 4.13 (a) shows dominantly a honeycomb pattern defined by the charging lines of the two central QDs, QD2 and QD3. In the most positive gate voltage range $V_{Dg1} \geqslant -0.475\,\text{V}$ and $V_{Dg4} \geqslant -0.525\,\text{V}$ finite current is present along the entire charging lines of QD2 and QD3, an indication for strong coupling, where co-tunneling mediated transport is possible. Where the QD2 and QD3 charging lines intersect, broad and pronounced peaks in the current $I_{dot}$ occur. The charging lines of QD1 and QD4 are mainly observed as an additional modulation pattern on top of the main honeycomb pattern defined by QD2 and QD3. The panel on top of the color plot shows in linear scale a cut along the horizontal dashed line. A large and broad peak develops at the QD2-QD3 resonance. The oscillation on top of the peak has a periodicity of $\Delta V_{Dg1} \approx 10\,\text{mV}$, corresponding to the charging lines of QD1. Similarly, the double peak structure in the vertical cut on the right shows a spacing of $\Delta V_{Dg4} \approx 10\,\text{mV}$ and can therefore be

attributed to QD4.

Toward more negative gate voltages the current $I_{dot}$ does not fully resolve the QD2-QD3 honeycomb structure anymore. For $V_{Dg1} \lesssim -0.475$ V, the finite current along the QD3 charging lines for off-resonant QD2 drops below the noise floor. For $V_{Dg4} \lesssim -0.525$ V, the finite current along the charging lines of QD2 with QD3 being off-resonant becomes unresolvable. Both indicates a decrease in coupling from more positive to more negative voltages. Interestingly, for both, the QD2 and the QD3 charging lines, the more relevant gate in this case is the one further away from the respective QD. From the electrostatic point of view, the main influence of a more negative $V_{Dg1}$ on the coupling is on the tunnel barriers between source and QD1, as well as QD1 and QD2, whereas tunneling into and out of QD3 involves the tunnel barriers between QD2 and QD3, as well as between QD3 and QD4. Vice versa, $V_{Dg4}$ has the strongest influence on the barriers between QD3 and QD4 as well as between QD4 and drain, but tunneling into and out of QD2 involves the tunneling barriers between QD1 and QD2 as well as between QD2 and QD3. The detector signal in figure 4.13 (b) resolves the expected effect on the tunnel barriers in terms of the broadening of the respective charging lines. The charging lines of QD2 are less broadened for more negative $V_{Dg1}$ due to the decreasing coupling strength. The charging lines of QD3 are less broadened toward more negative $V_{Dg4}$, respectively. In the current $I_{dot}$, this effect is pronounced as decreasing width and amplitude of the current features. On the other hand, the detector signal does not show significant influence of the $V_{Dg1}$ on the width of the QD3 charging lines or of $V_{Dg4}$ on the width of the QD2 charging lines. The mechanism behind the suppression in this situation is therefore not likely to be due to the influence of the gate voltages on the tunneling barriers.

In the current $I_{dot}$, the charging lines of QD2 show finite current for $N_3 + 1$ electrons in QD3 and is suppressed after the transition to $N_3$ electrons in QD3. Equivalently, the finite current along the charging lines of
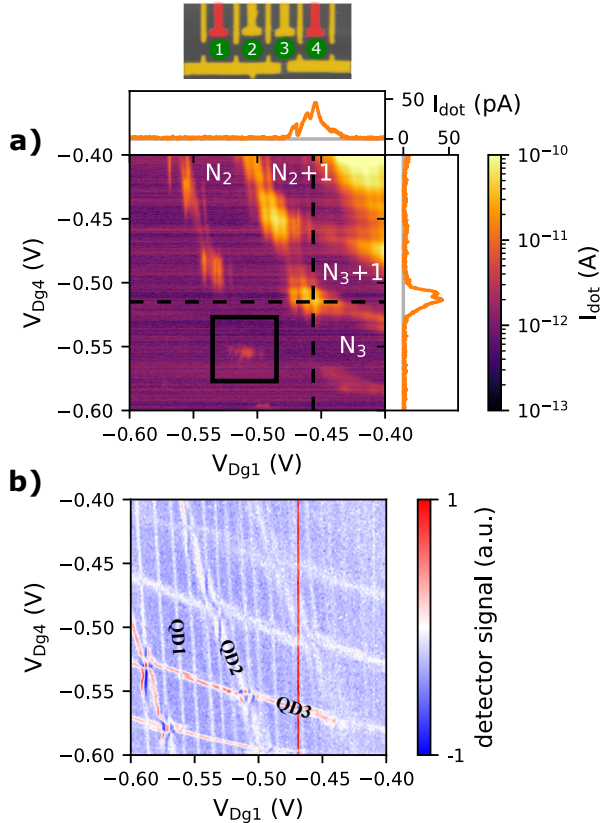
**Figure 4.13.:** (a) QQD current $I_{dot}$ as function of the outer plunger gate voltages $V_{Dg1}$ and $V_{Dg4}$. Finite current is only found for at least one of the center QDs being in resonance with the reservoirs. Resonances between QD2 and QD3 are found as broad peaks, which extend over several energy levels of QD1 and QD4. The black box marks a resonances in the regime, where the off-resonant current is strongly suppressed. (b) Corresponding charge detector signal. Charging lines of QD1, QD2, and QD3 can be identified. One charging line of each QD is labeled accordingly. The charging lines of QD4 are not visible in this configuration due to the charging lines being almost horizontal, which in combination with sweep gate voltage $V_{Dg1}$ and numerical derivation in $V_{Dg1}$-direction drastically reduces the contrast of the charging lines.

QD3 ís suppressed after the transition from $N_2 + 1$ to $N_2$ electrons in QD2. This reminds of the DQD 4.1, where co-tunneling was shown to be a function of the electron number and therefore the states involved. A decreasing coupling strength due to the changes in the electron numbers is therefore a likely explanation for the observed suppression of the off-resonant current.

The following will discuss the configuration and conditions around the resonance at $V_{D\,g1} \approx -0.5\,\text{V}$ and $V_{D\,g4} \approx -0.55\,\text{V}$ in figure 4.13, where finite current is still observed around the resonance but off-resonant current is already strongly suppressed. Figure 4.14 (a) shows a zoom into the lower part of the stability diagram, allowing to identify contributions of QD4. A single charging line of QD4 is faintly visible for the most negative $V_{D\,g4}$, where the cross coupling on the tunnel barriers results in the weakest coupling strength for QD4. The charging line is almost horizontal and marked by the lowest green arrow on the right side of the graph. For the rest of the stability diagram, no more charging lines of QD4 can be clearly identified.

However, at several positions, marked by the black arrows, features in the QD3 charging lines indicate the presence of further charging lines of QD4. The mutual charging energies due to the capacitive coupling lead to a shift of the charging lines, whenever another QD is (dis-)charged, i.e. at each crossing of two charging lines, the behavior of a coupled DQD is observed. For non-neighboring QDs however, this shift does not exceed the linewidth of the charging lines. Resonances between neighboring QDs on the other hand show a larger splitting and the characteristic charge reconfiguration lines connecting the two triple points. In the given measurement configuration with gate voltage $V_{D\,g1}$ being swept from more positive to more negative voltages, these charge reconfigurations occur from the left to the right of the array. The sequential charge reconfigurations from QD1 to QD2, and from QD2 to QD3 hereby transfer an electron closer to the charge detector, located below QD3, resulting in a more neg-
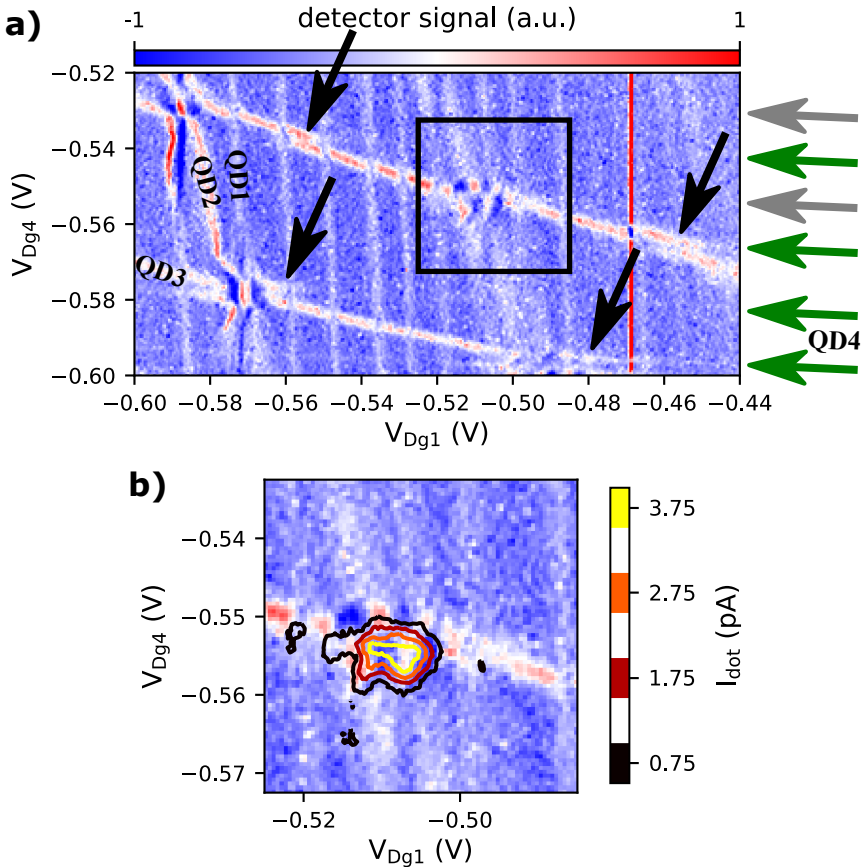
**Figure 4.14.: (a)** Zoom into the charge detector signal of figure 4.13. Black arrows mark features in the QD3 charging lines, fitting to the behavior expected for QD3-QD4 resonances. The green arrows on the right mark the positions of the QD4 charging lines based on these features. A faint signal is observed for the lowest QD4 charging line. Gray arrows mark probable positions for additional QD4 charging lines, based on the spacing between the green arrows. **(b)** Zoom into the resonance area, marked by the box in (a). The detector signals is overlaid by contour lines of the current $I_{dot}$. The highest $I_{dot}$ values are located asymmetrically with respect to the QD2-QD3 resonance. Combined with the larger extent of the resonance current in $V_{Dg1}$-direction this indicates the presence of a QD4 charging line and thus a QQD resonance.

ative potential and thus dark blue color in the detector signal color plot. The charge reconfiguration from QD3 to QD4 on the other hand removes an electron from the vicinity of the detector, so that white/red color is observed.

By calculating the lever arms of the two gates, an estimate for the slopes of the sequential reconfiguration lines can be given. The lever arms $\alpha_{Dg1,1} = 0.091$ and $\alpha_{Dg4,4} = 0.078$ are obtained directly from Coulomb diamond measurements (see appendix, figure A.2). With the cross lever arms $\alpha_{Dg1,2}$ and $\alpha_{Dg1,3}$ already calculated for the TQD (table 4.1) and the slopes $m_i = -\frac{\alpha_{Dg1,i}}{\alpha_{Dg4,i}}$ of the QD$i$ charging lines, the remaining lever arms can be calculated. The slopes $m_i$ obtained from figure 4.14 (a) are $m_1 = -18$, $m_2 = -5.0$, $m_3 = -0.21$, and $m_4 = -0.059$. The resulting lever arms of the two gate voltages $V_{Dg1}$ and $V_{Dg4}$ to all four QDs are given in table 4.3.

|  | QD1 | QD2 | QD3 | QD4 |
|---|---|---|---|---|
| $\alpha_{Dg1}$ | 0.091 | 0.032 | 0.0093 | 0.0046 |
| $\alpha_{Dg4}$ | 0.0051 | 0.0064 | 0.044 | 0.078 |

**Table 4.3.:** Lever arms between the plunger gate voltages $V_{Dg1}$ and $V_{Dg4}$ and all four quantum dots.

Using the lever arms, the reconfiguration line slopes can then again be calculated according to equation 4.2. The calculated slopes $m_{Rij}$ for the charge reconfiguration lines from QD$i$ to QD$j$ become $m_{R12} = 43.9$, $m_{R23} = 0.60$, and $m_{R34} = 0.14$. Thus, the QD3-QD4 charge reconfiguration lines are almost horizontal and of white/red color in the charge detector signal. In combination with the contrast of the QD4 charging lines being very small due to the almost horizontal charging lines, the main visible feature of resonances between QD3 and QD4 is an almost horizontal shift of the QD3 charging lines. Situations, where such a shift occurs are marked by black arrows in figure 4.14 (a). For the resonance marked by

the topmost black arrow, the shift in $V_{Dg1}$-direction hereby is of the order of the $V_{Dg1}$ spacing of the QD1 charging lines. With $\alpha_{Dg1,1}/\alpha_{Dg1,3} \approx 10$, the mutual charging energy between QD3 and QD4 can be estimated to $E_{m34} \approx E_{C1}/10$. For typical charging energies of the device in the many electron regime being $1\,meV \lesssim E_{C1} \lesssim 1.5\,meV$, the mutual charging energy is of the order $100\,\mu eV \lesssim E_{m34} \lesssim 150\,\mu eV$, fitting well to the values obtained for the TQD resonance.

The green arrows on the right side of figure 4.14 (a) mark the approximate positions of the QD4 charging lines based on the QD3-QD4 resonances marked by the black arrows. For the lowest green arrow, the QD4 charging line is faintly visible, so that the slope of the charging lines is known and also used for the estimate of the positions. Based on the spacing between the green arrows, there are most likely two additional QD4 charging lines present in the graph, since the level spacing of the charging lines in the many electron regime is typically almost equidistant. The approximate position of these two QD4 charging lines is marked by the gray arrows. However, in contrast to the charging lines marked in green, there are no shifts in any QD3 charging line present, that can clearly be attributed to resonances with these two QD4 charging lines.

In proximity to resonances with additional QDs however, the energetic situation is much more complex than with only two QDs involved, so that the simple expectation of only an almost horizontal shift does not necessarily remain upheld. Moving an electron from QD3 to QD4 also lowers the levels of QD1 and QD2, since $E_{m14} < E_{m13}$ and $E_{m24} < E_{m23}$, which in turn can lead to charge reconfiguration or even an additional electron being loaded onto one of the QDs.

In the center of the box in figure 4.14 (a) (and in the current $I_{dot}$ in figure 4.13 (a)), an extended resonance between QD1, QD2, and QD3 is visible. Additionally, the lower gray arrow, where a charging line of QD4 is expected, points to this resonance. Over the extent of the resonance, several dark blue areas indicate charge reconfigurations and the

detailed path of the individual charging lines can not be followed in the two-dimensional gate space due to the four-dimensional energy space of the QQD. The complexity of the resonance structure in combination with the expected QD4 charging line indicates the presence a QQD resonance.

Panel (b) in figure 4.14 shows a zoom into the detector signal around the resonance marked by the box in (a). In addition, the detector signal is overlaid with contour lines of the current $I_{dot}$. The current $I_{dot}$ hereby is $I_{dot} \geqslant 0.75\,\text{pA}$ ($1.75\,\text{pA}, 2.75\,\text{pA}, 3.75\,\text{pA}$) within the areas enclosed by black (dark-red, orange, yellow) lines. Interestingly, even though the honeycomb pattern observed in the current $I_{dot}$ in figure 4.13 (a) was predominantly defined by the QD2 and QD3 charging lines, the contour lines show a clear asymmetry with respect to the QD2-QD3 resonance. However, for the black contour line, which can be interpreted as the onset of the current peak, the QD2-QD3 resonance appears to be a boundary. In the upper part, the black contour line follows the QD3 charging line, while the QD2 charging line provides a rough boundary on the left side. Only the bulge at $V_{Dg4} \approx -0.555\,\text{V}$ noticeably crosses the QD2 charging line.

Combined with the shape of the yellow contour line, corresponding to the highest current values, this bulge is a strong indicator for a QD4 charging line crossing the resonance. The upper part of the yellow contour line is close to horizontal with a very small negative slope and directly points to the bulge in the black contour line. Since a very small negative slope is exactly what is expected for the QD4 charging lines, the shape of the current peak confirms the presence of an additional QD4 charging line at the position marked by the lower gray arrow in figure 4.14 (a).

The presence of a QD4 charging line crossing the resonance can explain both, an asymmetry of the shape of the current peak, as well as an asymmetry with respect to the QD2-QD3 resonance. Additionally, however, the charging lines of QD2 and QD3 appear to be boundaries for the observed current, very similar to the DQD under applied bias discussed

in section 4.1. The bias voltage dependency of the transport through a QQD will be discussed in the following.

## Bias effects on a Quadruple Quantum Dot

This part analyzes the influence of an applied bias voltage on the transport properties of a QQD system. Similar to the DQD and TQD, the main focus will hereby be on qualitative changes in the stability diagrams, which are an indicator for transport mechanisms only occurring in the presence of a bias voltage $V_{sd,dot}$.

Figure 4.15 (a) shows the current $I_{dot}$ through the serial QQD array in linear scale as function of the outer plunger gate voltages $V_{Dg1}$ and $V_{Dg4}$. The applied bias voltage $V_{sd,dot} = -0.05\,\mathrm{mV}$ is annotated at the bottom of the graph. As indicated by the sample schematic on the right, the bias voltage is applied to the right reservoir. While the transport is blocked for the most negative voltages, several features are observed in the current for more positive voltages, again mainly resolving the honeycomb pattern defined by the two center QDs, QD2 and QD3. However, there is no clearly defined transport direction. The yellow areas are positive currents, whereas the black areas show negative current. Positive current hereby means electrons tunneling from the left reservoir to the right reservoir. There are regions in the stability diagram clearly favoring the positive transport direction, whereas other regions favor negative transport direction. Since the distribution of the positive and negative current regions does not follow a clear systematic, a likely explanation are rectification effects with a dependency on the coupling parameters. A zoom into the green box of figure 4.15 (a) is shown on the right, showing a cross of negative current, surrounded by dots of positive current, following an almost horizontal line, as well as an almost vertical line. The pattern of the dots of positive current is therefore most likely defined by resonances between QD1 and QD4, whereas the cross of negative current is defined by a specific electron numbers in QD1 and a specific electron

number in QD4. Similar to the DQD, discussed in section 4.1, the transport properties of the QQD are strongly influenced by the exact electron configuration.

Due to thermoelectric voltage contributions, the bias voltage effectively applied between the reservoirs is not equal to the voltage $V_{sd,dot}$, which is the voltage applied by the voltage source. For small bias voltages, both, positive as well as negative currents are observed in the stability diagrams, so that determining the effective zero bias voltage is not possible. However, a method for determining a reasonable reference point is given by the following procedure. First, the measured current is corrected for offsets by subtracting the average value of the current measured in the regime $V_{Dg1}, V_{Dg4} < -0.64\,\text{V}$, where the current is expected to be zero. After the offset correction, the average value $I_{avg}$ of the entire stability diagram becomes a measure for the balance between positive and negative currents. For the situation of the applied bias voltage $V_{sd,dot} = -0.05\,\text{mV}$, shown in figure 4.15 (a), this average value is $I_{avg} \approx 1\,\text{pA}$. For all bias voltages measured over the same gate voltage range, this value is the closest to zero, and is used as a reference point. For the remainder of this section, the values $V_{sd,dot}$ will be given with respect to this reference point, i.e. $V_{sd,dot} = V_{applied} + 0.05\,\text{mV}$.

For bias voltages $V_{sd,dot} = \pm 0.3\,\text{mV}, \pm 0.9\,\text{mV}, \pm 1.5\,\text{mV}$ with respect to this reference point, a representation of the current $I_{dot}$ is shown in logarithmic color scale in figure 4.15 (b) for the same gate voltage range as in (a). The representation of the current, $I_{dot}$ multiplied by the sign of the bias voltage, is chosen over the conductivity due to the uncertainty in the determination of the absolute value of the bias voltage. Additionally, a small offset $I_{off} = 5\,\text{pA}$ is added, so that the noise around $I_{dot} = 0$ does not produce negative values which can not be plotted in logarithmic scale. With these adjustments, the current for positive and negative bias direction can be plotted on the same scale.

The left column shows $V_{sd,dot} = -0.3\,\text{mV}$ (top) and $V_{sd,dot} =$
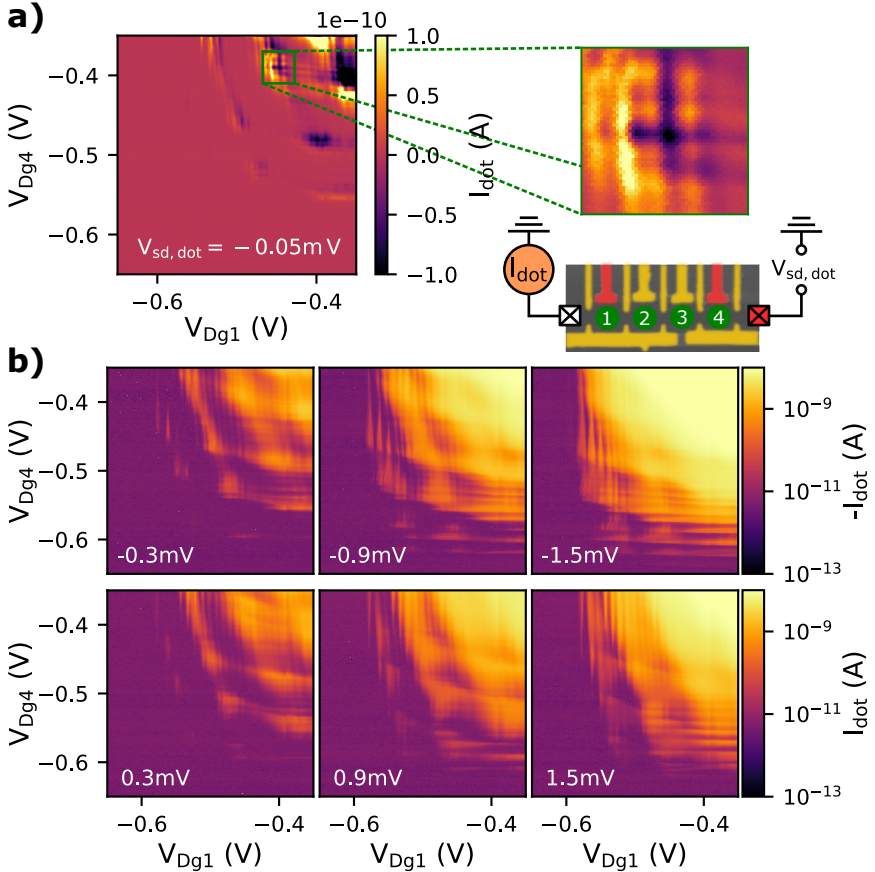
**Figure 4.15.: (a)** QQD current $I_{dot}$ in linear scale and as function of the outer plunger gate voltages $V_{Dg1}$ and $V_{Dg4}$ for bias voltage $V_{sd,dot} = -0.05\,\text{mV}$. The sample scheme clarifies the circuit configuration. The current is not directed, showing both, regimes of positive (yellow) and negative (black) values. The zoom shows a cross of negative current defined by specific electron numbers in QD1 and QD4, indicating a strong dependency on the coupling configuration. **(b)** QQD current $\pm I_{dot}$ in logarithmic scale for different bias voltages $V_{sd,dot} = \pm 0.3\,\text{V}, \pm 0.9\,\text{V}, \pm 1.5\,\text{V}$. The transport is clearly directed already for $V_{sd,dot} = \pm 0.3\,\text{V}$. Triangular regions emerge around the QD2-QD3 resonances with increasing size for increasing $|V_{sd,dot}|$ and opposite direction for opposite sign of $V_{sd,dot}$.

121

0.3 mV (bottom). Both bias directions do not show values significantly smaller than the fluctuations around the applied offset, showing that the transport direction is fully determined by the bias direction. Apart from the opposite direction of the current and a small electrostatic shift, the two stability diagrams are similar. Both show finite current in the full range $V_{Dg1}, V_{Dg4} \geqslant -0.45\,V$ with peaks along the charging lines of QD2 and QD3, growing into larger peaks at the resonances of the two QDs. For slightly more negative voltages, a honeycomb pattern of finite current along the charging lines of QD2 and QD3 with suppression in the center of the cells is observed. Going to even more negative voltages $V_{Dg1} \approx -0.55\,V$, well separated features of finite current are only observed close to resonances between QD2 and QD3. These features are dominated by almost vertical components, indicating an increasing importance of QD1 on the transport properties. This can be understood from the cross coupling of $V_{Dg1}$ on the two tunnel barriers of QD1. The increasing tunnel barriers decrease the coupling of QD1 to both sides, so that co-tunneling via QD1 becomes much less likely and thus the Coulomb blockade between the levels of QD1 is observed. Similarly, around $V_{Dg4} \approx -0.6\,V$ faintly visible and almost horizontal structures occur, indicating an increasing importance of QD4 on the transport properties.

Compared to the reference measurement in figure 4.15 (a), for both bias values $V_{sd,dot} = \pm 0.3\,mV$ the pinch-off, where the current drops below the noise floor is shifted toward more negative voltages, both, in $V_{Dg1}$ and $V_{DG4}$-direction. Additionally, the current is clearly directed and comparable features occur broadened.
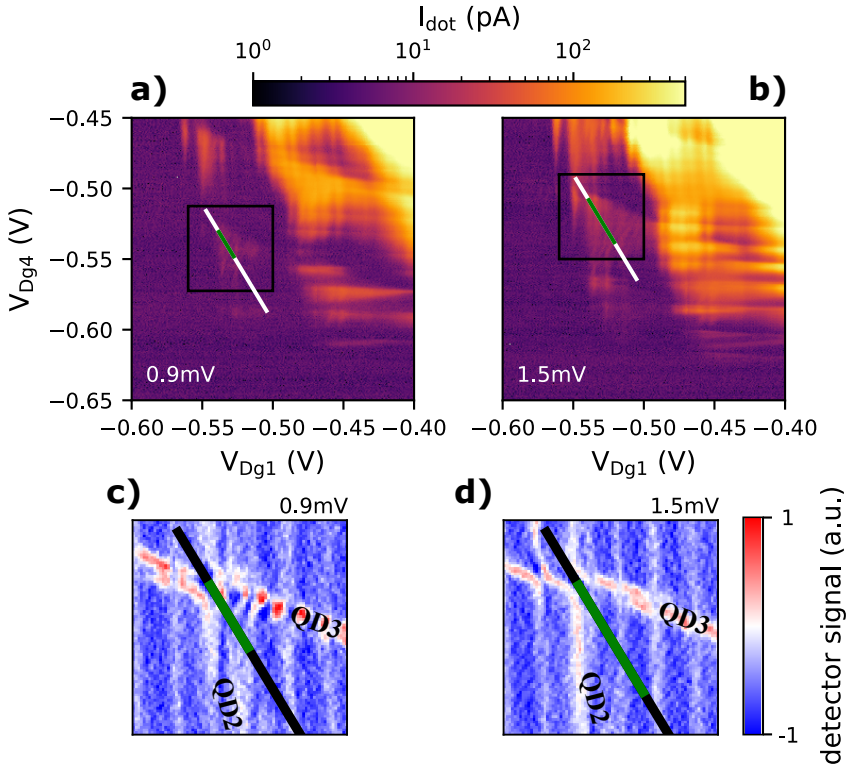
With increasing the bias voltages to $V_{sd,dot} = \pm 0.9\,mV$, shown in the center column of figure 4.15 (b), the broadening of the features further increases, so that the regime, where finite current is present also in the center of the honeycomb cells defined by QD2 and QD3, shifts to more negative voltages compared to the $V_{sd,dot} = \pm 0.3\,mV$ cases. At the

same time, the almost vertical (QD1) and almost horizontal (QD4) features close to the pinch-off become much more pronounced. The most significant change, however, is given by the formation of triangular structures of finite current. The triangles emerge from the intersections of the QD2 and QD3 charging lines, and the direction of the triangles is inverted by changing the sign of the bias voltage.

The observed trends continue when the bias voltage is further increased to $V_{sd,dot} = \pm 1.5\,\text{mV}$, shown in the right column of figure 4.15 (b). The broadening and hence overlap of the current features continues to increase, and the almost vertical QD1 charging lines, as well as the almost horizontal QD4 charging lines become even more pronounced near the pinch-off region. Additionally, the size of the triangular structures increases. This behavior is very similar to the DQD under applied bias described in section 4.1, where finite current was observed up to a maximum detuning $\Delta_{23} \approx eV_{sd,dot}$.

To compare the DQD and the QQD case, a zoom into the area of the triangular current features is shown in figure 4.16 for bias voltages (a) $V_{sd,dot} = 0.9\,\text{mV}$ and (b) $V_{sd,dot} = 1.5\,\text{mV}$. For the triangular structure showing the smallest overlap with other features, a line cutting the QD2-QD3 reconfiguration line perpendicularly, i.e. along the detuning axis, is shown in the graphs. The slope of the line is calculated from the reconfiguration line slope $m_{\Delta_{23}} = -1/m_{R23}$ with $m_{R23} = 0.6$ calculated from the lever arms given in tabular 4.3. Panels (c) and (d) in figure 4.16 show the charge detector signals corresponding to the boxes in (a) and (b), respectively. The charge detector signal shows clearly the charging lines of QD2 and QD3 and was used in order to determine the center of the QD2-QD3 resonance defined by these charging lines as accurately as possible.

However, an absolutely accurate determination is not possible because the QD2-QD3 resonances do not occur as isolated features in the QQD system, but both QDs also interact with QD1 and QD4. Resonances be-

**Figure 4.16.:** Zoom into the current $I_{dot}$ for **(a)** $V_{sd,dot} = 0.9\,\mathrm{mV}$ and **(b)** $V_{sd,dot} = 1.5\,\mathrm{mV}$ in the area where pronounced triangular structures occur. The size of the triangular structures increases with increasing bias voltage. The lines cut through the QD2-QD3 reconfiguration line along the $\Delta_{23}$ detuning axis. **(c)** and **(d)** show the detector signals corresponding to the boxes in (a) and (b), respectively. To achieve high accuracy, the reference value for the detuning $\Delta_{23} = 0$ is taken as the center of the reconfiguration line from the charge detector signal. The green part of the cut lines in all panels represents the QD2-QD3 detuning interval $0 \leqslant \Delta_{23} \leqslant eV_{sd,dot}$.

tween QD1 and QD3 for the $0.9\,\text{mV}$ case in (c), for example, lead to a frag-
mented appearance of the QD3 charging line. Within this uncertainty,
the green part of the cut lines in all four panels represent the interval
$0 \leqslant \Delta_{23} \leqslant eV_{sd,dot}$. As in the DQD case, the reference value $\Delta_{23} = 0$ is
taken as the center of the QD2-QD3 charge reconfiguration line observed
in the detector signal. The detuning is calculated from the lever arms
given in table 4.3.

A further zoom into the into the triangular shaped regions of fi-
nite current is shown in figure 4.17 for (a) $V_{sd,dot} = 0.9\,\text{mV}$ and (b)
$V_{sd,dot} = 1.5\,\text{mV}$ in linear scale. The white arrows represent the $\Delta_{23}$
detuning axis with the green parts again highlighting the detuning inter-
val $0 \leqslant \Delta_{23} \leqslant eV_{sd,dot}$. The current along the arrows is shown in figure
4.17 (c) as function of the detuning $\Delta_{23}$ in blue for $V_{sd,dot} = 0.9\,\text{mV}$,
and in red for $V_{sd,dot} = 1.5\,\text{mV}$. For both bias values, the correspond-
ingly colored parts of the background illustrate the detuning interval
$0 \leqslant \Delta_{23} \leqslant eV_{sd,dot}$.

Coming from negative detuning $\Delta_{23}$, the current $I_{dot}$ increases toward
$\Delta_{23} = 0$. For $V_{sd,dot} = 0.9\,\text{mV}$, the current hereby starts at $I_{dot} \approx 0$,
whereas for $V_{sd,dot} = 1.5\,\text{mV}$ the current is finite at negative detun-
ing due to overlap with a different triangular structure. Toward positive
detuning $\Delta_{23}$ the current then goes through a maximum for both bias
voltages and then decreases again, dropping to zero for large detuning.
However, in contrast to the DQD case described in section 4.1, the cur-
rent here does not show relatively smooth peaks, but both cuts show ad-
ditional substructures.

A very pronounced structure is given by the double peak around $\Delta_{23} =$
0 for the $V_{sd,dot} = 1.5\,\text{mV}$ case. The color plot in figure 4.17 (b) shows
almost vertical features around $\Delta_{23} = 0$, providing a strong indication for
a process strongly influenced by QD1. Additionally, the almost vertical
feature to the left of the cut line at $V_{Dg1} \approx -0.55\,\text{V}$ shows a bulge in
$V_{Dg1}$-direction at $V_{Dg3} \approx -0.51\,\text{V}$. This bulge indicates the presence of
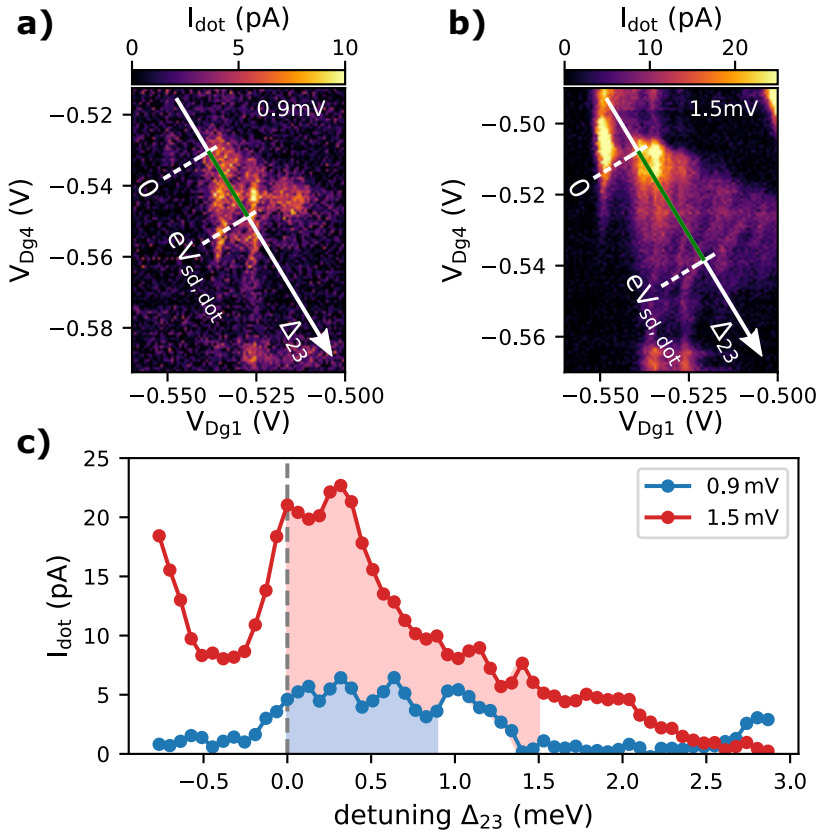
**Figure 4.17.:** Further zoom into the triangular shaped regions of finite current $I_{dot}$ for **(a)** $V_{sd,dot} = 0.9\,mV$ and **(b)** $V_{sd,dot} = 1.5\,mV$ in linear scale. **(c)** Current along the arrows in (a) and (b) as function of the detuning $\Delta_{23}$ between QD2 and QD3. The colored parts of the background indicate the intervals $0 \leqslant \Delta_{23} \leqslant eV_{sd,dot}$ for the two bias values. For both bias values, the finite current and hence the triangular features in the stability diagram clearly exceed $\Delta_{23} = eV_{sd,dot}$.

an additional QD4 charging line crossing this point. The dominant double peak structure is thus most likely a feature due to a QQD resonance, which would also be conductive for very small bias voltages. Also the smaller fluctuations to the right of the dominant double peak structure, as well as those observed over the full width of the peak for $V_{sd,dot} = 0.9\,\mathrm{mV}$ follow a systematic behavior in the two-dimensional gate space. Thus, the fluctuations are most likely not due to noise but originate from the arrangement of the energy levels in the QQD. However, although systematic behavior is observed, some of the features consist only of two to three datapoints, so that assigning the smaller features to specific resonances would be questionable, especially in the presence of capacitive coupling between the QDs and the possibility of excited states playing a role, as seen for the TQD under applied bias in section 4.2.

The smaller fluctuations as well as the $V_{sd,dot} = 1.5\,\mathrm{mV}$ cut line showing a double peak structure around $\Delta_{23} \approx 0$ are thus most likely explained by the presence of additional resonances with QD1 and QD4. Apart from the smaller fluctuations, the overall trend of the $V_{sd,dot} = 0.9\,\mathrm{mV}$ cut line shows a broad and flat peak structure as function of the detuning $\Delta_{23}$. For the $V_{sd,dot} = 1.5\,\mathrm{mV}$ case, the double peak structure around $\Delta_{23} \approx 0$ dominates the observed current. However, for larger detuning values $\Delta_{23} \gtrsim 1\,\mathrm{meV}$, i.e. far away from the double peak structure, the curve resembles the right half of a broad and flat peak structure. Similar peak structures were observed for the DQD under applied bias discussed in section 4.1, where the width of the peaks was given by $w \approx eV_{sd,dot}$. For the cut lines as function of detuning $\Delta_{23}$ in figure 4.17 (c), the colored parts of the background correspond to the detuning interval $0 \leqslant \Delta_{23} \leqslant eV_{sd,dot}$. The finite current and hence the triangular structures clearly exceed the detuning $\Delta_{23} = eV_{sd,dot}$ for both bias voltages.

For the data shown here, there are two possible explanations for this behavior. First, the lever arms of the plunger gates on the corresponding

QD $\alpha_{Dgi,i}$ have been determined via Coulomb diamond measurements of the individual quantum dots and the cross lever arms $\alpha_{Dgi,j}$ with $i \neq j$ were thereafter calculated from the slopes of the charging lines. In addition to the readout error for the charging energies of the single quantum dots and the determination of the slopes, both typically of the order of 10 %, the lever arms were determined for single quantum dots with a very different potential landscape compared to the QQD, so that larger deviations are possible. An indicator that such deviations play a role is found in the cut lines in figure 4.17 (c). For $V_{sd,dot} = 0.9 \, mV$, the full width at half maximum (FWHM) for the peak can be approximated to $w \approx 1.25 \, meV \approx 1.4 \, eV_{sd,dot}$. For the $V_{sd,dot} = 1.5 \, mV$ cut line, the same scaling would result in $w = 2.1 \, meV$. Based on the trend of the $V_{sd,dot} = 1.5 \, mV$ curve for larger detunings, i.e. far away from the dominant double peak structure, this seems a reasonable value for the FWHM.

In a more quantitative way, the width can be estimated by analyzing the detuning dependency of the $V_{sd,dot} = 1.5 \, mV$ in more detail. Figure 4.18 shows a slightly larger detuning window, including an additional peak in the negative detuning direction. With the current at both ends for the given detuning window dropping down to approximately zero, the shown curve can be treated as an isolated feature and no overlap with additional structures has to be considered.

The full curve of the current $I_{dot}$ as function of the detuning $\Delta_{23}$ is fitted by a sum of three Lorentzians, and an additional Gaussian. The three Lorentzians describe the triple peak structure for $\Delta_{23} \lesssim 1 \, meV$ originating from resonances with QD1 and QD4, the additional Gaussian describes the remaining background, which is attributed to the applied bias voltage. The resulting fit, shown in black, reproduces the data nicely. Additionally, the green curve shows separately the contribution of the three Lorentzians, the Gaussian contribution is shown in blue. The Gaussian describes a broad peak centered at a positive detuning value, similar
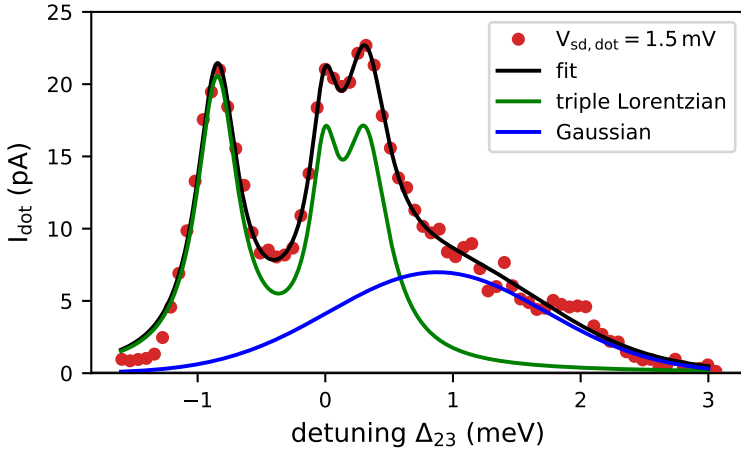
**Figure 4.18.:** Slightly larger range for the $V_{sd,dot} = 1.5\,\text{mV}$ cut (red dots) shown in figure 4.17 (c), including the left peak. The data is nicely fitted (black) by the sum of three Lorentzian and a Gaussian peak. The green line shows the Lorentzian contributions, and the blue line the Gaussian contribution. With $\sigma = 0.85\,\text{meV}$ for the Gaussian distribution, the FWHM becomes FWHM $\approx 2\,\text{meV}$, supporting the argumentation of a scaled detuning axis.

to the $V_{sd,dot} = 0.9\,\text{mV}$ case and the bias dependent current peaks observed for the DQD. With fit parameter $\sigma = 0.85\,\text{meV}$ for the Gaussian distribution, the FWHM becomes $w \approx 2\,\text{meV}$, very close to $1.4\,eV_{sd,dot}$, supporting the argumentation of a scaled detuning axis.

A second reason for the triangular structures exceeding the detuning $\Delta_{23} = eV_{sd,dot}$ are overlapping resonance features. The triangular structures observed in the more positive gate voltage regime, i.e. for stronger coupling of QD1 and QD4, are even larger compared to those analyzed here (compare figure 4.16 (a) and (b)). Additionally, the triangular structures at more positive voltages show a pronounced pattern of the almost vertical QD1 and the almost horizontal QD4 resonances. The larger extent of the triangular structures at more positive gate voltages is therefore

most likely due to the combination of strong coupling, leading to high currents also for the tails of the peaks, and overlap with different resonances with their individual bias dependent transport characteristics close to the resonances. The most accurate results can thus be obtained for the weak coupling regime.

Nevertheless, the size of the triangular structures of finite current in the stability diagram of a biased QQD show a linear dependence on the applied bias voltage $V_{sd,dot}$. With the width of the peaks in detuning direction being $w \approx eV_{sd,dot}$, this allows to directly determine the gate lever arms in the QQD configuration, instead of relying on the values determined from single QD measurements with their significantly different potential landscapes.

To summarize, this part discussed electronic transport through a serial QQD system. An introduction was given based on a stability diagram as function of the outer plunger gate voltages. In the current through the QQD, the two center QDs, which are only indirectly coupled to the electron reservoirs, showed a dominant behavior, so that a DQD typical honeycomb pattern of the two center QDs was observed. On top of this honeycomb pattern, modulations due to resonances with the outer QDs were observed. A QQD resonance was identified in the regime, where off-resonant transport is strongly suppressed. Even though the center QDs are dominant, the current in the resonance area was found to occur asymmetrically with respect to the QD2-QD3 charging lines. Bias dependent transport through the QQD was analyzed to investigate the influence on this symmetry. Close to zero bias voltage, the transport through the QQD was found to be strongly dependent on the coupling configuration and thus the states involved. Areas favoring positive current as well as areas favoring the opposite transport direction were observed. For larger bias voltages, triangular structures of finite current formed, originating from the QD2-QD3 resonances, similar to the structures observed for the bias dependent transport through the DQD. This leads to a clear asymmetry of

the transport with respect to the QD2-QD3 resonances. The dependency of the current on the detuning between QD2 and QD3 was analyzed for a well defined triangular structure with only small overlap to other current features. The extent of the triangular structures was found to increases with bias voltage but can be strongly modulated by the exact arrangement of the energy levels, including those of QD1 and QD4. The bias dependent extent of the observed triangular structures provides an opportunity to directly determine the gate lever arms in a system as complex as a QQD.

# 5

# Transport in Quantum Dot Arrays

A critical aspect for the implementation of semiconductor QDs for applications is the potential for scaling toward larger array sizes. As already seen in the last chapter, where transport through double, triple, and quadruple quantum dots was discussed, larger array sizes do not only come with more functionality, but the number of control parameters increases as well. At the same time, the internal energy level alignment becomes relevant, especially under availability of energy. This drastically increases the tuning complexity of larger arrays. Successful operation of QD arrays therefore requires efficient and scalable methods for tuning the device into the desired configuration while maintaining the high level of flexibility and tunability.

In the past few years, a variety of different approaches has already demonstrated remarkable progress in this direction. Computer automated tuning protocols have been implemented to tune a double quantum dot into the single-electron regime [134], to determine the initialization, manipulation and read-out points for a two-electron spin qubit [135], or to manipulate the interdot coupling without influencing the chemical potentials of the quantum dots [136]. The latter made use of so-called virtual gates, which are a linear combination of multiple physical gates, to compensate the capacitive cross-talk from the tunnel barrier gate to the energy levels of the quantum dots. The scheme of virtual gates has also been implemented to individually tune the tunnel couplings and the electron numbers of a triple quantum dot over a wide range [57]. Similarly, a

high level of control over the interdot couplings was achieved on a 2 x 2 quantum dot matrix [58].

This chapter focuses on a complementary approach to tune quantum dot arrays in a defined way. The approach is based on isolating the quantum dot array from the electron reservoirs. By isolating a quantum dot array from the electron reservoirs, the total number of electrons inside the array is fixed. However, the electrostatic environment is still tunable by the gate voltages, which allows to tune the energy level alignment. Even though current through the device is blocked in these isolated systems, electrons can still tunnel between different quantum dots inside the array. A sensitive charge detector [22, 65] allows to observe these transitions [137], which are a direct measure of the internal energy level alignment. Some of the potential of this isolation scheme has already been demonstrated. For example, coherent manipulation of two-electron spin states in an isolated double quantum dot at a sweet spot with respect to the charge detuning noise was shown [138], and significant improvement of the coherence time of a charge qubit was reported for an isolated double quantum dot on silicon basis [28]. In larger arrays, significant simplification of the stability diagram was shown for small electron numbers [139–141], and highly tunable co-tunneling between non-neighboring quantum dots was found [140, 141]. In a two-dimensional 3 x 3 quantum dot matrix, the isolation scheme was utilized to fix the number of electrons in the array and coherent control over the electron spins was demonstrated [142]. At the same time, the isolation naturally prevents reservoir induced limiting effects such as metastabilities [143].

In the following, experimental results on isolated double, triple, and quadruple quantum dot arrays are discussed. Capacitive model simulations are performed to complement the understanding of the interdot transitions in isolated arrays. Parts of this chapter are published in [140, 141].

## 5.1. Double Quantum Dot

A DQD provides an excellent system to introduce the fundamental effects of isolating a QD array due to its relatively low complexity compared to larger arrays. To isolate a QD array from the electron reservoirs, the tunneling rates between QDs and reservoirs have to become small compared to the measurement timescale. A direct consequence of this is, that the transport through the QD array is blocked and information about the system is only obtained from the charge detector signal.

A DQD charge stability diagram showing the transition from a DQD well coupled to the reservoirs to an isolated DQD is shown in figure 5.1. The coloration of the device image (top) illustrates the voltages applied to the gates. Gates, which are colored in gray, do not deplete the 2DEG, golden gates deplete the 2DEG and are kept at fixed voltages. Reddish colored gates are measurement parameters. The DQD consists of QD2 and QD3, the two outer tunnel barrier gate voltages $V_{Tg2}$ and $V_{Tg4}$ are the measurement parameters. This results in large changes of the coupling strength between the DQD and both reservoirs over the measurement range. The fixed gate voltages are $V_{Bg1} = V_{Bg2} = -0.55\,\text{V}$, $V_{Dg2} = V_{Dg3} = -0.5\,\text{V}$, and $V_{Tg3} = -0.6\,\text{V}$. The signal shown is the detector signal, which is given by the numerical derivative of the DC detector current in x-direction $dI_{qpc}/dV_{Tg2}$. White and red color hereby corresponds to decreasing negative potential in the vicinity of the detector QPC, for example due to an electron tunneling out of the DQD. Dark blue color is observed for increasing negative potential at the detector QPC.

Two different slopes of white/red charging lines are visible in the detector signal. Equivalent to the transport regime, discussed in 4.1, the slopes of the charging lines can be assigned to the two QDs. The charging lines with the larger slope belong to (dis-)charging of QD2, the charging lines with the smaller slope belong to (dis-)charging of QD3.
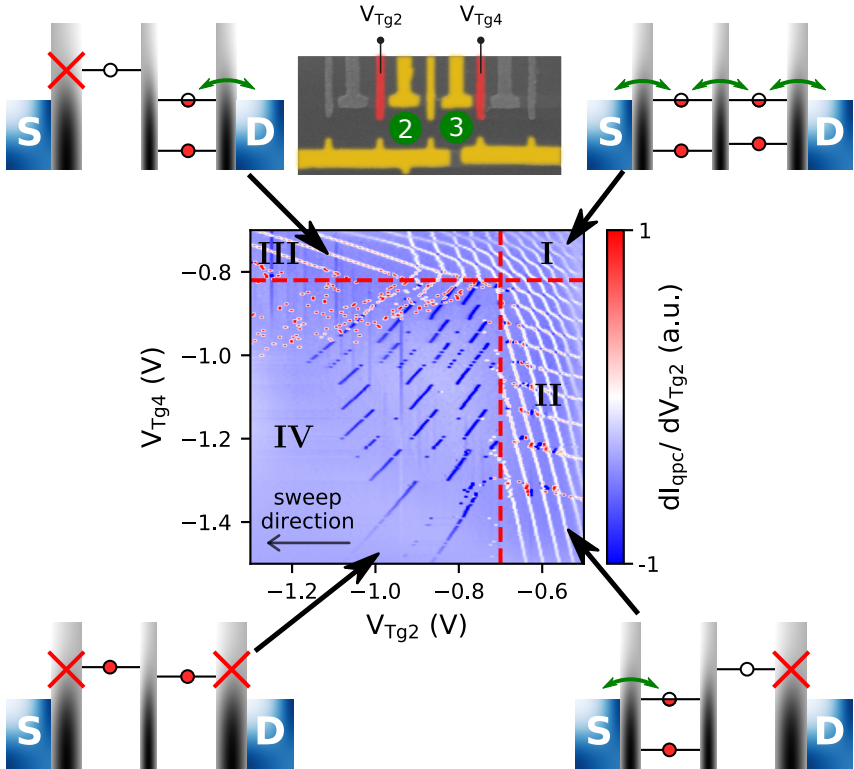
**Figure 5.1.:** Charge detector signal of a DQD stability diagram as a function of the tunnel barrier gate voltages $V_{Tg2}$ and $V_{Tg4}$. Red dashed lines indicate the voltages, where the respective tunnel barriers becomes isolating. The lines divide the stability diagram in three regimes of different coupling between the DQD and the electron reservoirs. Region I is well coupled to both reservoirs, regions II and III are coupled to only one reservoir, and in region IV the DQD is isolated from both reservoirs. Black arrows connect the four energy level diagrams to positions, where the tunnel barriers match the depicted situation. Red crosses indicate isolating tunnel barriers. The device image on top is colored to represent the measurement conditions. Reddish colored gates are measurement parameters, golden gates are on fixed voltages, gray gates do not deplete the 2DEG.

Referring to the coupling between the DQD and the reservoirs, the stability diagram can be divided into three qualitatively different regimes. For the most positive gate voltages $V_{Tg2} \gtrsim -0.7\,\text{V}$ (right of the vertical red dashed line) and $V_{Tg4} \gtrsim -0.82\,\text{V}$ (above the horizontal red dashed line) both tunneling barriers are transparent and the DQD is well coupled to both reservoirs. In this region I, electrons can tunnel into the DQD from both reservoirs and tunnel out of the DQD into both reservoirs, as depicted by the top right energy diagram. In consequence, current can flow through the DQD in this regime (see appendix A.4) and the charge detector signal nicely resolves the honeycomb pattern, the characteristic charging line pattern of a DQD [59]. In addition to shifting the energy levels of both QDs via the lever arms, which results in the honeycomb pattern, the voltages $V_{Tg2}$ and $V_{Tg4}$, applied to the tunnel barrier gates are control parameters for the coupling strength to the respective reservoir. More negative voltages correspond to larger tunnel barriers and therefore weaker coupling. Beginning in region I, and moving toward more negative voltage $V_{Tg4}$ therefore reduces the coupling strength to the right reservoir. At a certain threshold value $V_{Tg4} \approx -0.82\,\text{V}$, marked by the horizontal red dashed line in figure 5.1, the tunneling rate through the right barrier drops below the measurement speed of $28.6\,\text{Hz}$. Even more negative $V_{Tg4}$ further reduce this tunneling rate and the DQD effectively gets isolated from the right reservoir.

In this region II, where $V_{Tg4} < -0.82\,\text{V}$ and $V_{Tg2} \gtrsim -0.7\,\text{V}$, the DQD is well coupled to the left reservoir but isolated from the right reservoir, as depicted in the bottom right energy diagram. Nevertheless, the detector signal still shows the charging lines of both QDs in this region. Since the detector signal is only sensitive to potential changes, this means both QDs can still be discharged, even though QD3 is not directly coupled to a reservoir. In this region, the DQD typical honeycomb pattern is preserved in the presence of co-tunneling-mediated charge transitions, which allow electrons to tunnel between QD3 and the left reservoir through a virtual

energy state despite QD2 being in Coulomb-blockade [144]. Since these co-tunneling-mediated transitions occur more likely for stronger inter-dot coupling [59], co-tunneling is suppressed for weak interdot coupling. QD3 can then only be discharged in situations, where sequential tunneling via an unoccupied state of QD2 is energetically available, which leads to a hysteretic behavior of the charge states [145]. Since the suppression of co-tunneling changes the energetic conditions under which QD3 can be charged or discharged, the shape of the charging lines in the stability diagram changes as well. The two QD3 charging lines at the most negative $V_{Tg4}$ indeed appear differently compared to those at more positive $V_{Tg4}$. However, changes in neither $V_{Tg2}$ nor $V_{Tg4}$ are expected to have a large influence on the interdot coupling. Since these two charging lines correspond to the first and the second electron on QD3, the reason for the interdot coupling to be weaker is most likely due to the electron wavefunction being smaller for lower orbital shells [58], which effectively increases the tunnel barrier width.

In region III ($V_{Tg2} < -0.7\,\text{V}$, $V_{Tg4} \gtrsim -0.82\,\text{V}$), the situation is similar. Here, the DQD is well coupled to the right reservoir while being isolated from the left reservoir, as depicted by the top left energy diagram. Consequently, region III behaves similar to region II but with reversed roles of QD2 and QD3. The charging line at the most negative $V_{Tg2}$ corresponds to the first electron on QD2.

For tunnel barrier gate voltages $V_{Tg2} < -0.7\,\text{V}$ and $V_{Tg4} < -0.82\,\text{V}$, both tunnel barriers are isolating with respect to the measurement timescale. In this region IV, electrons are trapped inside the DQD [104, 137, 138] and the pattern observed in the detector signal changes drastically with respect to the pattern observed for a DQD coupled to at least one reservoir. Due to the isolation from both reservoirs, the total number of electrons in the DQD is fixed when entering this region and occupied energy levels are lifted above the Fermi level. The potential changes observed in the detector signal are therefore only due to charge recon-

figurations inside the DQD. The experiment was performed by sweeping $V_{Tg2}$ from more positive to more negative voltages, beginning at a point well coupled to the left reservoir for each value of $V_{Tg4}$. For this sweep direction, electrons are exclusively transferred from QD2 to QD3, thus closer to the detector QPC, which is located below QD3. In the detector signal, these transitions occur in dark blue color. By changing the voltage $V_{Tg4}$, the energy levels of both QDs are energetically shifted with respect to reservoir chemical potentials. However, the voltage $V_{Tg2} \approx -0.7\,\text{V}$, where the left barrier becomes isolating is first order insensitive to $V_{Tg4}$. Therefore the number of electrons trapped in the DQD changes in $V_{Tg4}$ direction.

A capacitive model including the trapping of electrons can now be set up to model the experimental DQD including the different coupling regimes. On the one hand, the implementation of such a model allows to review the given interpretation of a DQD in the transition to the isolation. On the other hand, by extending the model toward more QDs, the model provides a useful tool to complement the understanding of charge reconfigurations in isolated QD arrays. Similar to the experiment, the capacitive model uses QDs and two gates. Each QD is implemented as a set of energies with fixed energy distances as the energy levels. Each of the energy levels can either be occupied or unoccupied. In the model, virtual gate voltages $V_G$ are used to shift the energy levels of QDi via a lever arm $\alpha_{G,i}$, so that $\Delta E_i = -e\alpha_{G,i}\Delta V_G$ (see equation 2.13). As long as coupled to a reservoir, all energy levels below the Fermi level are occupied, energy levels above the Fermi level are unoccupied. A threshold voltage $V_{G,th}$ is introduced for both gates, which allows to transfer the system into the isolated configuration, if $V_G < V_{G,th}$ is fulfilled for both gates. Here, the total number of electrons in the array is fixed to the value when entering the isolated configuration, but electrons can be transferred between the QDs, if an unoccupied energy level of lower energy is present. The simulation yields the number of electrons in each QD, which can be used

to generate a signal similar to the experimental detector signal by linear combinations of these electron numbers. No tunneling rates or integration times feed into the simulation, all transitions are therefore abrupt.

A comparison between experimental and calculated stability diagrams is shown in figure 5.2. The experimental signal (a) is identical to the data already presented in figure 5.1. For the calculated stability diagram, the energy level alignment and the lever arm ratios have been extracted from the experimental data and adjusted to achieve good comparability with respect to the electron numbers. The simulated stability diagram is shown in figure 5.2 (b). Beginning from the lowest electron number, the implemented charging energies $E_{C2}$ for QD2 and $E_{C3}$ for QD3 are

$$E_{C2} = [2.25, 2.16, 1.76, 1.42, 1.50, 1.31, 1.31, ...] \, meV$$
$$E_{C3} = [3.17, 2.60, 2.02, 1.73, 1.44, 1.27, 1.27, ...] \, meV$$

with all following being $1.31 \, meV$ for $E_{C2}$ and $1.27 \, meV$ for $E_{C3}$. The lever arms $\alpha_{G,i}$ between the gates and both QDs used for this simulation are given in table 5.1. To account for the interdot capacitance, a mutual charging energy $\Delta_{2,3} = 100 \, \mu eV$ was implemented. the energy levels of QD2 are energetically lifted by $\Delta_{2,3}$ for each electron in QD3 and vice versa. Note, that a different set of parameters can yield an identical result, as long as all ratios remain constant.

|  | QD2 | QD3 |
|---|---|---|
| $\alpha_{Tg2}$ | 0.0405 | 0.0116 |
| $\alpha_{Tg4}$ | 0.0076 | 0.0341 |

**Table 5.1.:** Gate to dot lever arms used for the DQD simulation.

Comparing the experimental and the simulated stability diagram in figure 5.2 (a) and (b), reveals several differences and similarities. The purely classical simulation can naturally not reproduce tunnel coupling induced

effects such as the broadening of the charging and reconfiguration lines or the formation of bonding and anti-bonding states, which leads to the additional energy splitting found in region I. Additionally, the simulation allows all energy levels to be discharged in equilibrium as long as the system is not isolated, which in regions II and III leads to a behavior as if co-tunneling mediated transitions are present. However, concerning the general pattern, experiment and simulation are in good agreement, especially the charge reconfiguration pattern in the isolated region IV is nicely reproduced by the capacitive model simulation, showing that the underlying assumptions are valid. For comparison, figure 5.2 (c) shows a simulated stability diagram using identical parameters but with the isolation threshold values $V_{Tg2,th}$ and $V_{Tg4,th}$ chosen more negative, so that isolation is not reached within the given range. The simulation then yields the typical honeycomb pattern over the full range.

For the isolated situation, the number and distribution of electrons trapped in the DQD for each $V_{Tg4}$-value is a parameter exactly known for the simulation. From this information, the charge reconfiguration pattern in the isolated regime can be understood. The number of charge reconfigurations occurring in a single $V_{Tg2}$ line is equal to the number of electrons $N_2$ in QD2 at the isolation point. This is a consequence of the sweep direction. While sweeping $V_{Tg2}$ from more positive to more negative voltages, the energetic shift on the QD2 energy levels is larger than on the QD3 energy levels, due to $\alpha_{Tg2,2} > \alpha_{Tg2,3}$. Therefore, the occupied energy levels of QD2 are lifted faster than the unoccupied energy levels of QD3. At some point, the highest occupied energy level of QD2 comes into resonance with the lowest unoccupied energy level of QD3 and the electron can tunnel between QD2 and QD3. By sweeping $V_{Tg2}$ further negative, the QD3 energy level becomes lower in energy and the electron remains in QD3. This process then repeats until QD2 is empty, which opens up a possibility to exactly determine the number of electrons on a QD.
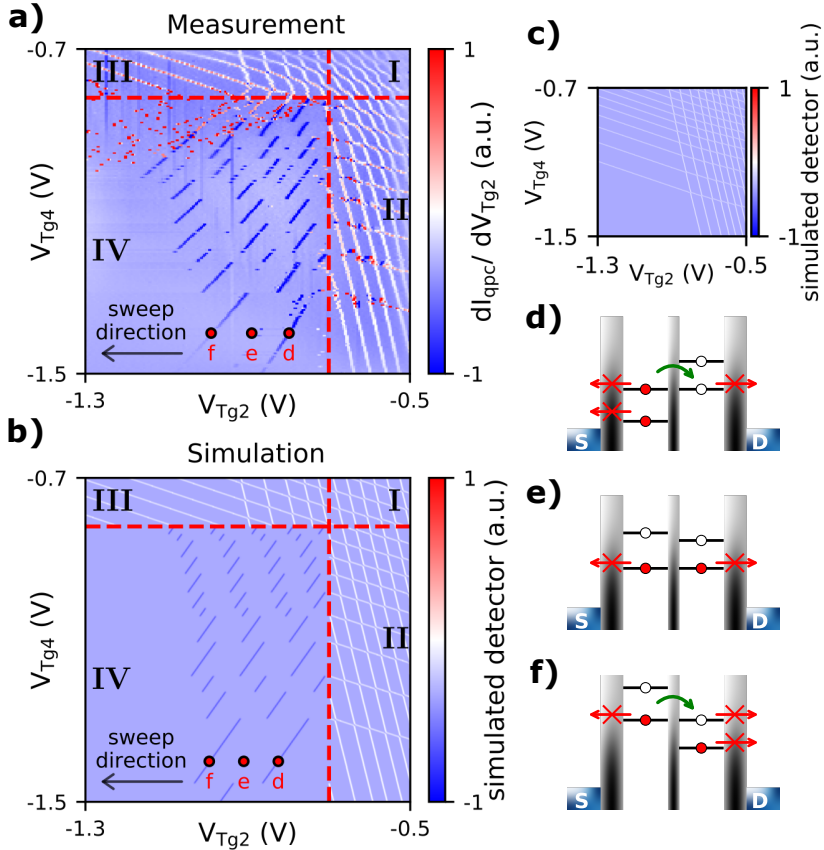
**Figure 5.2.: (a)** DQD stability diagram as a function of the tunnel barrier gate voltages $V_{Tg2}$ and $V_{Tg4}$, same data as in figure 5.1. Red dashed lines again indicate the isolation points of the tunnel barriers. **(b)** Corresponding capacitive model simulation with energy level alignment and lever arm ratios adjusted so that the electron numbers match the experiment. The reconfiguration pattern in the isolated region IV is nicely reproduced, especially for small electron numbers. **(c)** Simulated stability diagram using identical parameters except for the isolation threshold values. The simulation yields the typical honeycomb pattern, since isolation is not reached within the given range. **(d-f)** Energy level schemes for the points d, e, and f, marked in (a) and (b).

Compared to the spacing between two QD2 charging lines in the reservoir coupled regime, the spacing between two reconfiguration lines in the isolated regime is considerably larger. Two effects are contributing to this increase. First, in the regime well coupled to a reservoir, the gate voltage distance between the charging lines of QD2 in the reservoir coupled regime is determined by the charging energy $E_{C2}$ and the lever arm $\alpha_{Tg2,2}$. In the isolated regime, only the relative energetic shift between the QD2 and the QD3 energy levels is relevant, which is characterized by $\alpha_{Tg2,2} - \alpha_{Tg2,3}$. The second effect is illustrated in the three energy level diagrams figure 5.2 (d-f), which correspond to the three positions marked accordingly in 5.2 (a) and (b), where the electron configuration at the isolation point is $(N_2, N_3) = (2, 0)$. The energy diagram (d) shows the configuration at the transition $(2, 0) \rightarrow (1, 1)$ in the isolated regime. Changing $V_{Tg2}$, so that the relative energetic shift between QD2 and QD3 energy levels matches the charging energy of QD2 $\Delta\mu_{23} = -e(\alpha_{Tg2,2} - \alpha_{Tg2,3})\Delta V_{Tg2} = E_{C2}$ results in an internal energy level alignment as depicted in (e). Here, the lowest energy level of QD2 is in resonance with the lowest energy level of QD3. However, no transition occurs in the experimental and simulated stability diagrams, since both resonant levels are already occupied by an electron. Providing an additional relative energy shift of $\Delta\mu_{23} = E_{C3}$ then ends up in point (f), where the $(1, 1) \rightarrow (0, 2)$ transition occurs. The gate voltage difference between two reconfiguration lines is therefore given by

$$\Delta V_{Tg2} = -\frac{E_{C2} + E_{C3}}{e(\alpha_{Tg2,2} - \alpha_{Tg2,3})}.$$

This second effect also explains the general charge reconfiguration pattern observed in the isolated regime. The resonances, which are visible as transitions in the detector signal are determined by the electron configuration $(N_2, N_3)$ at the isolation point. For the measurement and simulation presented in figure 5.2 (a) and (b), $V_{Tg4}$ acts as a control parameter

for this electron configuration. With changing $V_{Tg4}$, the energy levels of both QDs are energetically shifted with respect to the isolation point. For every change in electron number or distribution, a different set of transitions becomes observable, where each reconfiguration line visible in the isolated regime corresponds to one specific transition between two charge states of the DQD.

This now opens up the possibility of preparing a DQD into a state with a defined number of electrons simply by entering the isolated regime in the desired configuration. Additionally, the interdot charge transitions observed in the isolated regime are energetically well separated from other charge states. For the reservoir coupled regime, the charge reconfiguration lines interconnect the triple points of the DQD resonances. As described in section 2.2, the energetic separation between the two triple points of a resonance is defined by the mutual charging energy $E_m$ due to the capacitive coupling and the additional splitting $2|\tilde{t}|$ due to the tunnel coupling. In similar devices, the total splitting is typically of the order $\Delta E = E_m + 2|\tilde{t}| \lesssim 0.2E_C$ [97, 146, 147], with $E_C$ being the charging energy of a single QD. Assuming a (for similar devices) relatively large charging energy of $E_C \approx 2\,\mathrm{meV}$, the maximum energetic distance to different charge configurations, in the center between the two triple points, is thus $\Delta E/2 \lesssim 0.1E_C = 200\,\mathrm{\mu eV}$. By using floating gates to increase the capacitive coupling between the two QDs, this can be approximately increased by a factor of two [148, 149]. Isolating and manipulating one of these transition lines thus requires very low temperatures ($k_B T_{1.5K} \approx 130\,\mathrm{\mu eV}$) and accurate tuning. In contrast, in the isolated regime, the energetic separation to the next transition is $\Delta E \approx 2E_C$, making the charge reconfiguration lines in the isolated regime very robust and efficiently tunable.

An efficient way of tuning the interdot coupling is given by the variation of the tunnel barrier gate voltage $V_{Tg3}$. Figure 5.3 (a) shows the charge detector signal $dI_{qpc}/dV_{Tg2}$ of the $(1,1) \Rightarrow (0,2)$ reconfigura-

tion line as function of $V_{Tg2}$ and the interdot tunnel barrier gate voltage $V_{Tg3}$, where again $V_{Tg2}$ was swept from more positive to more negative voltages. The right tunnel barrier gate voltage was fixed at $V_{Tg4} = -1.4\,\text{V}$, all other voltages are equal to figure 5.2 (a). The $V_{Tg3} = -0.6\,\text{V}$ line therefore corresponds to a small range around point (f). Due to the large difference in gate voltage range of $\Delta V_{Tg2} = 30\,\text{mV}$ compared to $\Delta V_{Tg3} = 150\,\text{mV}$, the two axes in 5.3 (a) are scaled differently for better visibility.

From more positive (top) to more negative (bottom) $V_{Tg3}$ the interdot tunnel barrier is enlarged, which decreases the interdot coupling. In the weak coupling regime, for the most negative $-0.6\,\text{V} \leqslant V_{Tg3} \leqslant -0.575\,\text{V}$, the reconfiguration line is not a single line, but is split into two transitions. With increasing the coupling strength these two lines merge into a single line at $V_{Tg3} \approx -0.565\,\text{V}$. Further increasing the tunnel barrier gate voltage further increases the interdot coupling, resulting in a broadening of the reconfiguration line, which is observed for $-0.55\,\text{V} \lesssim V_{Tg3} \lesssim -0.475\,\text{V}$. For even more positive $V_{Tg3} \gtrsim -0.45\,\text{V}$, the reconfiguration line vanishes. In this regime, the interdot tunnel barrier becomes too small to distinguish between QD2 and QD3 and both QDs merge into one large single QD.

By moving over the reconfiguration line, the amount of charge transferred from one QD to the other is always exactly one electron. This charge transfer leads to a step in the detector current $I_{qpc}$, where the width of this step is a function of the electron temperature $T_e$ and the interdot coupling. DiCarlo *et. al.* [150] set up a model for the charge sensor conductance of such a step. The model accounts for the sensor offset conductance, the gate voltage dependence of the sensor conductance and the excess charge on the QDs. Hensgens *et. al.* [57] expanded this model to first-order correct the back-effect of the excess charge on the charge sensor. The model can be used to fit the detector step, which allows to determine the tunnel coupling between the QDs. The blue dots in figure
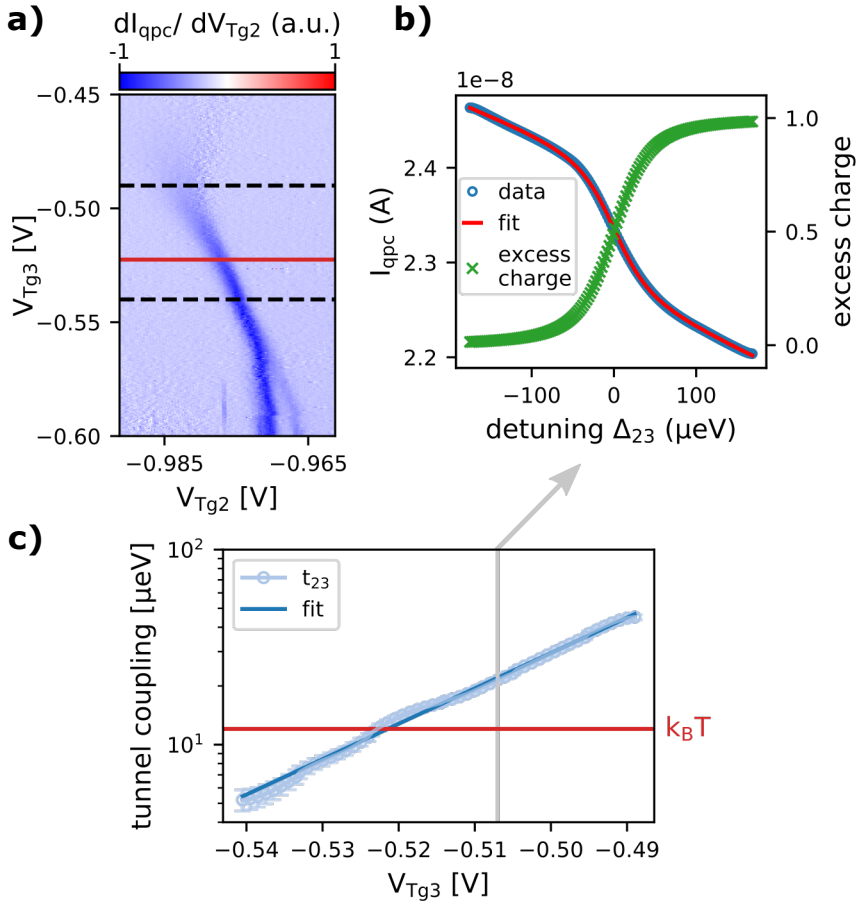
**Figure 5.3.: (a)** $(1, 1) \Rightarrow (0, 2)$ transition as function of the interdot tunnel barrier gate voltage $V_{Tg3}$. The interdot coupling strength and therefore the reconfiguration line width increases toward more positive $V_{Tg3}$. **(b)** Exemplary detector signal and fit to extract tunnel coupling $t_{23}$ and excess charge distribution. Negative detuning $\Delta_{23}$ corresponds to $\mu(1, 1) < \mu(0, 2)$. **(c)** Logarithmic plot of the interdot tunnel coupling strength as function of $V_{Tg3}$, extracted in the range between the horizontal black lines in (a).

5.3 (b) are an exemplarily curve at $V_{Tg3} = -0.507\,V$, which show such a step in the detector current as function of the detuning $\Delta_{23}$ between both QDs. Negative detuning corresponds to $\mu(1,1) < \mu(0,2)$, i.e. the electron being in QD2. The red line is a fit to the data according to ref. [57]. The fit allows to extract the excess charge in QD3

$$Q(\Delta_{23}) = \frac{1}{2}\left(1 + \frac{\Delta_{23}}{\Omega}\tanh\left(\frac{\Omega}{2k_B T_e}\right)\right), \qquad (5.1)$$

with $\Omega = \sqrt{\Delta_{23}^2 + 4t_{23}^2}$, which is a function of electron temperature $T_e$ and tunnel coupling $t_{23}$ and shown as green crosses in figure 5.3 (b). By using the same fitting routine in a regime, where the tunnel coupling is small, the electron temperature can be determined to $T_e \approx 140\,mK$. With the given electron temperature, it is then possible to determine the tunnel coupling.
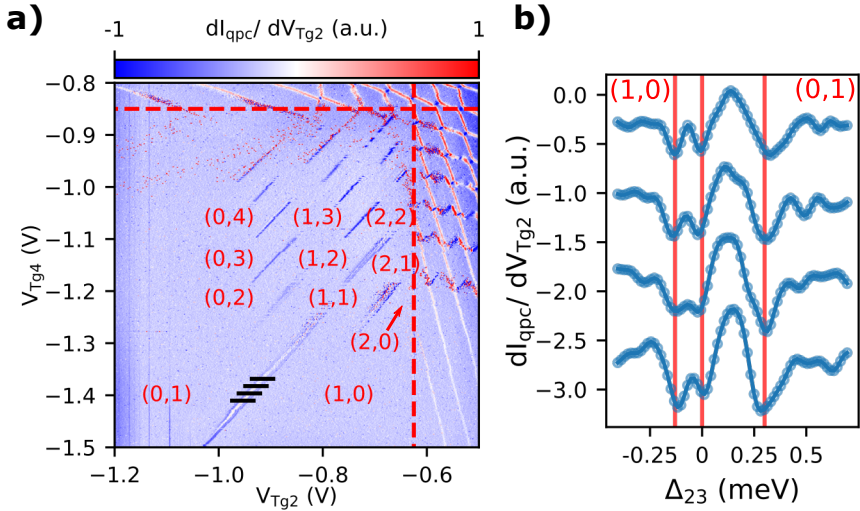
As function of the interdot tunnel barrier gate voltage $V_{Tg3}$, figure 5.3 (c) shows a logarithmic plot of the tunnel coupling obtained by fitting the step in $I_{qpc}$ within the horizontal black dashed lines in (a). The window $-0.54\,V \leqslant V_{Tg3} \leqslant -0.49\,V$ was chosen to ensure reasonable fits to the data. In this voltage range, the tunnel coupling strength $t_{23}$ between QD2 and QD3 ranges from $t_{23} \approx 5.5\,\mu eV$ for $V_{Tg3} = -0.54\,V$ to $t_{23} \approx 46\,\mu eV$ for $V_{Tg3} = -0.49\,V$. The red line in (c) marks the thermal energy $k_B T \approx 12\,\mu eV$. The red line in (a) marks the $V_{Tg3}$-value, where $t_{23} \approx k_B T$. The blue line in (c) provides an exponential fit to the tunnel coupling as function of the barrier gate voltage, which allows to calculate the change in tunnel coupling to an order of magnitude per $\Delta V_{Tg3} \approx 55\,meV$. Over the full range $\Delta V_{Tg3} = 150\,mV$ of panel (a) the tunnel coupling was therefore tuned over more than two orders of magnitude, while the whole stability diagram was measured with the two particular electrons which were trapped in the DQD when entering the isolation.

The exponential fit allows to estimate the tunnel coupling for $V_{Tg3} = -0.6\,V$, where the reconfiguration line does not appear as a single tran-

sition. By extrapolation, $t_{23} \approx 0.45\,\mu eV$ is obtained. This splitting was not observed in the original stability diagram in figure 5.1 and 5.2 (a), which can be explained by the low resolution of $\Delta_{Tg2} = 4\,mV$ with which the stability diagram was taken. A similar stability diagram but with both plunger gates $50\,mV$ more negative and a higher resolution of $\Delta V_{Tg2} = 0.7\,mV$ is shown in figure 5.4 (a). Due to the more negative plunger gate voltages, the energy levels of both QDs are lifted with respect to the isolation point, which results in differing electron numbers in the isolated regime. The stable charge configuration $(N_2, N_3)$ is given for up to two electrons per QD at the isolation point.

The given higher resolution allows to observe additional features in the stability diagram. The $(2,0) \rightarrow (1,1)$ and the upper part of the $(1,0) \rightarrow (0,1)$ transition are dominated by stochastic behavior. Here, the interdot coupling is very weak, resulting in tunneling times being comparable to the integration time $t_{int} = 20\,ms$ of the detector current. The charge detector therefore does not integrate over a large number of tunneling events in this regime, but resolves single events. This results in a bistable detector current close to the degeneracy lines.

When following the $(1,0) \rightarrow (0,1)$ reconfiguration line from the most positive voltages toward more negative voltages, this stochastic behavior vanishes. Even though $V_{Tg3}$ is kept constant, the interdot coupling increases toward more negative $V_{Tg2}$ and $V_{Tg4}$. Here, the tunnel barrier does not change, but the energy levels of both QDs are energetically lifted, which effectively reduces the tunnel barrier width. For $-1.3\,V \gtrsim V_{Tg4} \gtrsim -1.45\,V$, parallel substructures are observed in the $(1,0) \rightarrow (0,1)$ reconfiguration line. As function of the detuning, four line cuts along the black lines are shown in figure 5.4 (b). The cuts are vertically offset for better visibility. Due to the sign change in the voltage to energy conversion, the direction of the line cuts is inverted. The line cuts show a series of three dips, which are marked by the vertical red lines. The position of the center dip was chosen to $\Delta_{23} = 0$. The energy differ-

**Figure 5.4.: (a)** DQD stability diagram as a function of the tunnel barrier gate voltages $V_{Tg2}$ and $V_{Tg4}$. Red dashed lines indicate the voltages, where the respective tunnel barriers becomes isolating. The resolution of $\Delta V_{Tg2} = 0.7\,\mathrm{mV}$ allows to observe substructures in the reconfiguration lines. **(b)** Line cuts through the $(1,0) \rightarrow (0,1)$ transition along the black lines in (a). Due to the sign change in voltage to energy conversion, the direction of the line cuts is inverted. Curves are vertically offset for better visibility. The vertical red lines mark three dips occurring in the detector signal. The dips correspond to the average occupation being shifted more toward the right QD. The reference value $\Delta_{23} = 0$ for the detuning was chosen on the dip most likely corresponding to the ground state to transition.

ences between the left (l), center (c), and right (r) dip are $\Delta E_{lc} \approx 130\,\mu eV$, $\Delta E_{cr} \approx 300\,\mu eV$, and $\Delta E_{lr} \approx 430\,\mu eV$. Additionally, between the center and right dip, the detector signal increases to values larger than the background, so that this increase has to be considered as a peak (p) with $\Delta E_{cp} \approx 130\,\mu eV$. Comparing these energy differences to the excitation spectra of the single QDs, which are obtained via Coulomb diamonds, the first excited state of the first electron is of the order of $\Delta E_{cr} \approx 300\,\mu eV$ for both QDs.

The fact that multiple transitions are observed despite having only a single electron trapped in the DQD can be explained by the detector integration time $t_{int}$. For tunneling rates $\Gamma >> 1/t_{int}$, the detector signal does not observe single events, but averages over many back and forth tunneling events. From figure 5.3, the coupling strength was estimated to $t_{23} \approx 0.45\,\mu eV$ for the regime, where the reconfiguration line is split. Via $E = h\Gamma$, this converts into $\Gamma \approx 0.1\,GHz$. In this regime, the detector indeed integrates over many events. The detector signal then depends on the ratio $\Gamma_l/\Gamma_r$, where $\Gamma_l$ is the tunneling rate from the right to the left QD, $\Gamma_r$ is the tunneling rate from the left to the right QD. The only transitions, which are expected to occur in equilibrium are ground state to ground state transitions. However, the charge detector QPC was biased with $V_{qpc} = 0.5\,mV$ for this measurement. A biased QPC charge detector acts as a source of phonons with energies up to $E_{max} = |eV_{qpc}|$ [74, 75]. Plausible processes in the system are thus the ground state to ground state transition, inelastic tunneling, for example by absorbing a phonon, and exciting the electron followed by an excited state to ground state transition. The line cuts shown in figure 5.4 (b) show two small dips, followed by a peak and a larger dip. A dip hereby corresponds to the occupation probability being shifted more toward the right QD3, a peak shifts the occupation probability more toward the left QD2. As function of the detuning, the occupation probability is thus shifted toward the right QD3, back to the left QD2 and then toward the right QD3 again.

With the equal energy spacing $\Delta E_{lc} \approx \Delta E_{cp}$ the center dip is symmetrically enclosed by two features of opposite sign. Due to this symmetry, the center dip most likely corresponds to the ground state to ground state transition. Considering $\Delta_{23} = 0$ as the ground state resonance, the left dip and the peak are then due to inelastic tunneling at a detuning of $\pm 130\,\mu eV$. For negative detuning, where QD2 is energetically more favorable, inelastic tunneling results in an occupation increase of QD3 and thus a dip. Vice versa, inelastic tunneling at the same but positive detuning, where QD3 is energetically more favorable, results in an occupation increase of QD2 and thus a peak. Further increasing the detuning, more energy is needed for inelastic tunneling from QD3 to QD2. If this energy can not be provided, the system will remain in the ground state with the electron occupying QD3. The decrease of the inelastic tunneling rate then leads to the right dip in the detector signal.

For even more negative voltages $V_{Tg2}$ and $V_{Tg4}$, the coupling strength further increases. The parallel substructures occurring in the $(1, 0) \rightarrow (0, 1)$ transition merge into a single reconfiguration line. Excitation rates, for example due to QPC phonons, do not depend on the coupling strength between the two QDs, whereas the relaxation process might. Due to the time average of the detector signal, the charge detector shows the occupation probability. In a situation with an excitation rate large compared to the relaxation rate, the detector will show the excited configuration. Vice versa, for a relaxation rate large compared to the excitation rate, the detector response will mainly show the ground state configuration. In the low coupling regime, the relaxation process might be the bottleneck and excited configurations occur in the detector signal. Whereas for large coupling, the system relaxes to the equilibrium configuration fast, so that the ground state transition becomes dominant.

To summarize, this part introduced a DQD system isolated from the electron reservoirs. While current through the system is blocked in this situation, a charge detector is able to resolve electron transport inside

the isolated DQD, from one QD to the other. An introduction was given, showing the DQD typical honeycomb pattern and the transition into the isolated regime. The total number of electrons in the DQD is preserved in the isolated configuration and the observable charge reconfigurations depend on this number of electrons. A capacitance model was set up and the calculated stability diagrams nicely reproduced the observed charge reconfiguration pattern. With two electrons isolated in the DQD, the tunability of the reconfiguration resonances was discussed based on the $(1, 1) \leftrightarrow (0, 2)$ transition. As function of the center tunnel barrier gate, the tunnel coupling strength between the two QDs was determined. The coupling was shown to be tunable from merging the two QDs into a single larger QD to a regime, where excited states become observable due to the interdot tunneling becoming slow compared to excitation rates.

## 5.2. Triple Quantum Dot

With increasing the number of quantum dots in the array, the concept of isolating the array from the electron reservoir becomes even more relevant. A triple quantum dot coupled to electron reservoirs is characterized by a three-dimensional energy space [116, 124, 126], where each QD contributes its own energy scale. By isolating the TQD from the electron reservoirs only relative energies remain relevant, which reduces the number of independent energy scales to two. A stability diagram of a TQD (QD1, QD2, QD3) in the isolated regime is shown in figure 5.5 (a) as function of the two outer plunger gate voltages $V_{Dg1}$ and $V_{Dg3}$. Using the plunger gates as parameters allows to investigate a larger region in the energy space of the TQD, while the influence on the outer tunnel barriers is large enough to isolate the system. The constant gate voltages are $V_{Bg1} = V_{Bg1} = -0.55\,\mathrm{V}$, $V_{Tg1} = -0.675\,\mathrm{V}$, $V_{Tg2} = -0.35\,\mathrm{V}$, $V_{Tg3} = -0.5\,\mathrm{V}$, $V_{Tg4} = -0.7\,\mathrm{V}$, and $V_{Dg2} = -0.5\,\mathrm{V}$. The coloration of the inset again illustrates the device and the applied voltages.
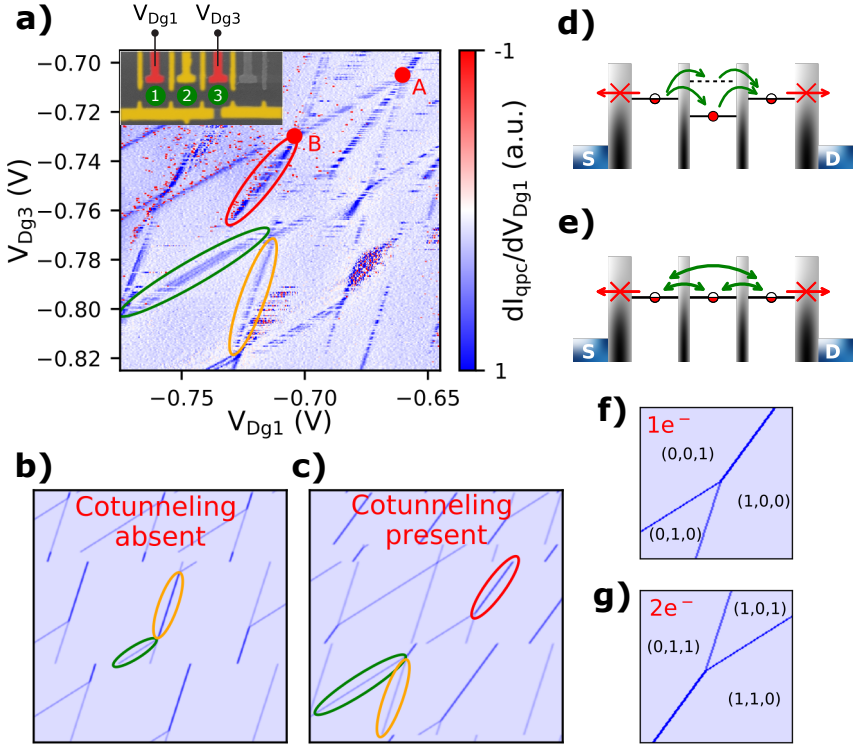
**Figure 5.5.: (a)** TQD stability diagram in the isolated regime as a function of the plunger gate voltages $V_{Dg1}$ and $V_{Dg3}$ with inset sample scheme. Three different slopes of charging lines are observed. Sequential transitions are marked in orange and green, a co-tunneling transition between QD1 and QD3 is marked in red. **(b)** Capacitive model simulation of an isolated TQD stability diagram excluding and **(c)** including transitions directly between QD1 and QD3. Transitions are marked equal to (a). **(d)** Energy diagram illustrating co-tunneling transitions between QD1 and QD3 via two different states of the center QD2. **(e)** Energy level diagram illustrating a TQD resonance in the isolated regime. **(f, g)** Zoom into two simulated resonances. The qualitatively different behavior allows the distinction between resonances with one resonant electron (f) and two resonant electrons (g). Points A and B in (a) mark two resonances similar to (f) and (g), respectively.

Similar to the DQD overview stability diagram in figure 5.2 (a), the TQD presented here was reset to a state well coupled to at least one reservoir at the beginning of each $V_{Dg1}$-line. The number of electrons trapped in the TQD is therefore constant in $V_{Dg1}$-direction but may change for different $V_{Dg3}$. The number and distribution of electrons at the isolation point again determines the transitions occurring during a single $V_{Dg1}$ sweep. Charge reconfiguration lines of three different slopes are observed in the isolated TQD stability diagram. One reconfiguration line of each slope is highlighted by an ellipse in figure 5.5 (a). The largest slope, marked in orange, corresponds to an electron being transferred from QD1 to QD2. A reconfiguration line of the smallest slope, corresponding to a transition from QD2 to QD3, is marked by the green ellipse. The occurrence of the intermediate slope, which is marked in red, can be understood by comparing two capacitive model simulations. A simulated TQD stability diagram in the isolated regime is shown in figure 5.5 (b). For this case, the model was set up to only allow nearest neighbor transitions. Only two different slopes of reconfiguration lines (orange, green) are observed in the simulation. Enabling direct transitions between the non-neighboring QD1 and QD3 in the model changes the outcome to what is shown in figure 5.5 (c). A third, intermediate slope emerges, which is consistent with the experimental observation. The origin of this intermediate slope of reconfiguration lines can therefore be found in direct transitions between QD1 and QD3 with QD2 being off-resonant. These transitions can be understood, when taking higher order tunneling, e.g., co-tunneling via virtual occupation of the center QD, into account [127, 128, 151], which is sketched in the energy diagram in figure 5.5 (d).

Whenever two charge reconfiguration lines meet in the isolated stability diagram, all three QDs are in resonance. At this resonances, three charge states are degenerate, as depicted in figure 5.5 (e). Comparable to a DQD coupled to electron reservoirs, two species of resonances are found in the stability diagram [61]. With zero referring to the back-

ground charge configuration, one possibility is given by a degeneracy between the $(1, 0, 0)$, $(0, 1, 0)$, and $(0, 0, 1)$ charge states, which is a TQD resonance occupied by one electron. The other possibility is a TQD resonance, occupied by two electrons, with degenerate charge states $(1, 1, 0)$, $(1, 0, 1)$, and $(0, 1, 1)$. In the stability diagram these two cases are distinguishable due to differences in the electrostatic environment. Two zooms into the simulated stability diagram figure 5.5 (c), where co-tunneling is present, are shown in figure 5.5 (f) and (g). In the first case (f), the resonance is occupied by one electron. When starting from the resonance and changing $V_{Dg1}$ and $V_{Dg3}$ so that the energetic shifts $\Delta E_1 = \Delta E_3$ ($\mu_{QD1} = \mu_{QD3}$ degeneracy line), the energetic shift of the center QD2 $\Delta E_2$ is generally not equal to $\Delta E_1$ and $\Delta E_3$. For the given lever arm configuration (cf. tabular 4.1) and along the $\mu_{QD1} = \mu_{QD3}$ degeneracy line, $|\Delta E_2| < |\Delta E_1| = |\Delta E_3|$. By going toward more negative voltages, i.e., increasing the energy, the $(0, 1, 0)$ state therefore becomes energetically most favorable. In a $V_{Dg1}$-sweep this results in the electron being shuttled sequentially from QD1 to QD2 to QD3, which is found in 5.5 (f) in every line below the resonance. When moving toward more positive voltages on the $\mu_{QD1} = \mu_{QD3}$ degeneracy line, the $(0, 1, 0)$ state is energetically least favorable. In a $V_{Dg1}$ sweep, this results in the electron being shuttled directly from QD1 to QD3 via co-tunneling, which is found in every line above the resonance.

The resonance shown in 5.5 (g) is occupied by two electrons with resonant charge states $(1, 1, 0)$, $(1, 0, 1)$, and $(0, 1, 1)$. From the energetic point of view, the situation is the same as for the single electron resonance, however, the additional electron always occupies the energetically most favorable energy level. Coming from the resonance and going toward more negative voltages along the $\mu_{QD1} = \mu_{QD3}$ degeneracy line, QD2 is therefore occupied by the additional electron. A co-tunneling transition from QD1 to QD3 is thus the energetically most favorable option for the transition from $(1, 1, 0)$ to $(0, 1, 1)$ in a $V_{Dg1}$-sweep. In the opposite

direction, where $\mu_{QD2}$ is higher in energy at the $\mu_{QD1} = \mu_{QD3}$ degeneracy line, two sequential transitions via the intermediate state $(1, 0, 1)$ are the energetically most favorable option for the transition from $(1, 1, 0)$ to $(0, 1, 1)$ in a $V_{Dg1}$-sweep. Depending on the transitions observed around the resonance, it is thus possible to distinguish between one-electron and two-electron resonances in an isolated TQD stability diagram. In figure 5.5 (a), a resonance occupied by one electron is marked by point A, point B marks a two-electron resonance. However, due to the electron number stochastically changing at the isolation point, the visible transitions differ from line to line, which leads to fragmented charge reconfiguration lines and thereby complicates the interpretation of the isolated stability diagram. This can be overcome by isolating the system in a more defined way.

### 5.2.1. Controlled Electron Loading

An important step toward efficient control over quantum dot arrays is the possibility to load the array with a defined number of electrons. The number of electrons inside an isolated quantum dot array is constant and the value is given by the number of electrons occupying the system at the transition point into the isolation. By controlling the number of electrons at the isolation point, it is therefore possible to define the number of electrons loaded into an isolated quantum dot array. Figure 5.6 illustrates one possible way to set up a control procedure, which allows to load and isolate a TQD with a defined number of electrons $N_{TQD}$.

An overview stability diagram of the TQD is presented in figure 5.6 (a) as function of both outer plunger gate voltages $V_{Dg1}$ and $V_{Dg3}$. The overview shows the transition from reservoir coupled TQD to the isolated TQD in $V_{Dg1}$-direction. Depending on the gate voltages, which are not used as measurement parameters, such an overview can include the charging lines of the first electron for QD2 and QD3. In the stability diagram, these two charging lines are highlighted by the black dashed lines,

where the smaller slope corresponds to the QD3 charging line, and the larger to QD2, respectively. Below these two charging lines both QD2 and QD3 are empty, $N_2 = N_3 = 0$. In this situation, the total number of electrons in the TQD equals the number of electrons in QD1, $N_{TQD} = N_1$.
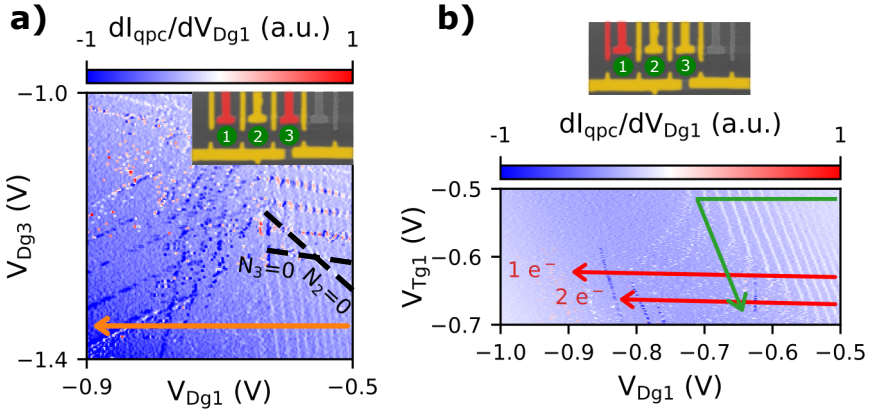


**Figure 5.6.: (a)** Overview stability diagram of a TQD as function of the outer plunger gate voltages $V_{Dg1}$ and $V_{Dg3}$. Dashed lines mark the charging lines of the first electron for QD2 and QD3. Below these lines, $N_2 = N_3 = 0$. **(b)** Sweep along the orange arrow in (a) as function of the tunnel barrier gate voltage $V_{Tg1}$. The energy levels of QD1 are shifted with respect to the isolation point, which allows to change the number of electrons in QD1 at the isolation point. This can be used to define the number of electrons trapped in the TQD, due to $N_{TQD} = N_1$. Following the upper red arrow, the most probable number of electrons loaded is $N_1 = 1$, the lower red arrow most likely loads $N_1 = 2$ electrons. Stochastic fluctuations can be reduced by implementing a more complex loading procedure, for example along the green arrow. The transition into the isolation is hereby achieved while the desired electron number is the equilibrium charge configuration.

By scanning a line along the orange arrow, where $N_2 = N_3 = 0$, QD1 can still be discharged until the isolation threshold is reached. The number of electrons isolated in the TQD therefore solely depends on the number of electrons on QD1 at the isolation point. This line can now be mea-

sured as function of $V_{Dg1}$ and $V_{Tg1}$, as shown in figure 5.6 (b). Since $V_{Tg1}$ has a larger influence on the tunnel barrier than $V_{Dg1}$, while $V_{Dg1}$ has a larger influence on the energy levels, a measurement as function of these two gate voltages tunes the energy levels of QD1 with respect to the isolation point. Up to the uncertainty given by the stochastic nature of the tunneling process, this allows to isolate a well defined number of electrons. Simply by fixing $V_{Tg1} = -0.63$ V (upper red arrow) and sweeping $V_{Dg1}$ equal to the measurement, it is most likely to have one electron in QD1 at the isolation point, which results in $N_{TQD} = N_1 + N_2 + N_3 = 1 + 0 + 0 = 1$ electron isolated in the TQD. By using the same sweep but with a different $V_{Tg1} = -0.67$ V (lower red arrow), the most probable number of electrons trapped can be changed to $N_{TQD} = N_1 = 2$.

However, due to the stochastic nature of tunneling, the error rate is quite large in this simple approach. One parameter, that influences the error rate is given by the measurement speed. The stability diagram in figure 5.6 (b) has been measured relatively slow, so that a voltage change of $\Delta V_{Dg1} = 0.1$ V took $t \approx 1.75$ s. At the same time, the influence of the plunger gate voltage on the tunnel barrier is not very large. This results in a slow transition into the isolation, and therefore a long time, in which electrons might tunnel out. A way to overcome this is by using rapid voltage pulses to transfer fast and deep into the isolated regime [139]. Another option is given by using a sequence depicted by the green arrow. QD1 is hereby loaded by the desired amount of electrons in a regime, where the tunneling rates are large (horizontal part). By implementing a virtual gate consisting of $V_{Tg1}$ and $V_{Dg1}$, the tunneling rate can now be reduced, while the energy levels are kept constant with respect to the source potential (sloped part, parallel to the QD1 charging lines). This allows to transfer deep into the isolated regime, with the desired electron number $N_1$ being the equilibrium charge state. Even though a real isolation can not be achieved, since tunneling is a stochastic process, the system is effectively isolated for $\Gamma << 1/t_{meas}$, where $t_{meas}$ is the time

of a complete measurement. Macroscopic timescales can be achieved, as already presented for the DQD, where figure 5.3 (a) was measured without leaving the isolated regime and with $t_{meas} \approx 1.5\,\text{h}$.

Once in the effective isolation, the tunability of the system is fully restored. All gates in the center of the device can be varied over large voltage ranges, which enables the tuning of the interdot tunnel couplings and the energy level alignment between the QDs. In this state of extremely wide tunnel barriers between the reservoirs and the QDs it is possible to use the individual, trapped electrons to obtain charge stability diagrams or to apply manipulation schemes. Additionally, the array can be investigated below the Fermi energy, since tunneling into the array is suppressed as well. The principle of the described controlled loading procedure is also scalable to larger array sizes. When all QDs except one, which is coupled to a reservoir, are empty, the number of electrons isolated in the array is defined by the number of electrons on this QD when entering the isolation.

### 5.2.2. Single Electron

A comparison between two different situations of a single electron isolated in a TQD is presented in figure 5.7. The two measurements in (a) and (b) correspond to two different coupling regimes of the TQD. A further difference is given by the isolation method. In (a) a simple and non-optimized loading procedure was repeated at the beginning of each line, whereas in (b) a loading procedure has been used to trap a single electron and the whole stability diagram was measured with this particular electron. Consequently, not every line in figure 5.7 (a) corresponds to a single electron trapped, but stochastically zero or two electrons were loaded. This leads to fragmentation of the charge reconfiguration lines, since different transitions are observed for two electrons in the TQD and no transitions happen for zero electrons. In contrast, figure 5.7 (b) does not show any fragmentation, due to the fact that the stability diagram was

measured with one particular electron, which was trapped in the TQD by using a loading procedure. The voltages equal for both measurements are $V_{Bg1} = V_{Bg2} = -0.6\,\mathrm{V}$, $V_{Tg1} = -0.85\,\mathrm{V}$, and $V_{Tg4} = -0.8\,\mathrm{V}$. The unequal voltages are given in table 5.2.

|  | $V_{Tg2}$ | $V_{Tg3}$ | $V_{Dg2}$ |
|---|---|---|---|
| (a) | 0.05 V | 0.15 V | −1.125 V |
| (b) | 0.125 V | 0.3 V | −0.85 V |

**Table 5.2.:** Gate voltages, which are unequal in figure 5.7 (a) and (b).

Panels (c) and (d) in figure 5.7 show two capacitive model simulations corresponding to the measurements in (a) and (b), respectively. Both simulations were performed with the same gate to dot lever arms, which are given in table 5.3. As there is only a single electron loaded into the TQD, only the lowest energy level of each QD can be occupied, making the implementation of charging energies redundant for the simulations. The electron can either occupy QD1, QD2 or QD3. This results in a significant simplification of the stability diagram with only three different charge states. The three charge states are interconnected by three different reconfiguration lines and are labeled in both simulations. The difference between both simulations is given by disabled (c) and enabled (d) long range transitions between both outer QDs.

|  | QD1 | QD2 | QD3 |
|---|---|---|---|
| $\alpha_{Dg1}$ | 0.105 | 0.410 | 0.010 |
| $\alpha_{Dg3}$ | 0.013 | 0.033 | 0.082 |

**Table 5.3.:** Gate to dot lever arms for the single electron TQD simulation.

As seen in table 5.2, both tunnel barrier gate voltages $V_{Tg2}$ and $V_{Tg3}$, and the plunger gate voltage in the center of the TQD are more positive for
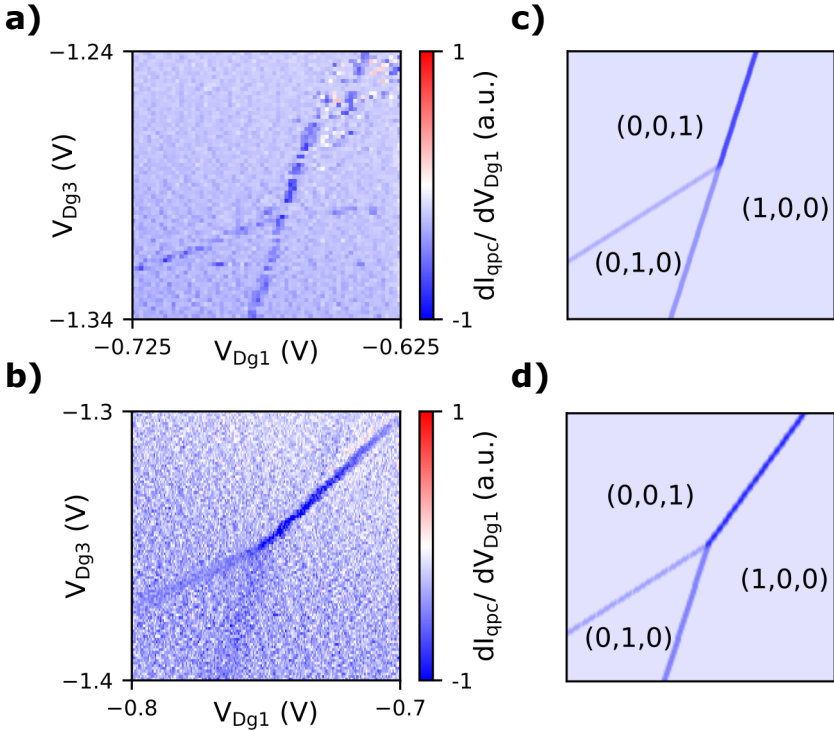
**Figure 5.7.:** Experimental stability diagram of a single electron isolated in a TQD in the weak **(a)** and strong **(b)** coupling regime. Qualitative differences are found for the $(1,0,0) \rightarrow (0,0,1)$ long range transition. In the weak coupling regime, this transitions is a two-step sequential process, whereas in the strong coupling regime the transition is co-tunneling mediated. Capacitive model simulations for a single electron in a TQD excluding **(c)** and including **(d)** long range transitions nicely reproduce the weak coupling and the strong coupling stability diagrams, respectively.

figure 5.7 (b). Especially the tunnel barrier gates hereby have a large influence on the interdot coupling. When comparing the reconfiguration lines of the sequential transitions $(1, 0, 0) \rightarrow (0, 1, 0)$ and $(0, 1, 0) \rightarrow (0, 0, 1)$, the more positive voltages in (b) result in significant broadening of the reconfiguration lines, which is consistent with the expected larger interdot coupling.

For the $(1, 0, 0) \rightarrow (0, 0, 1)$ reconfiguration line, which corresponds to a long range transition, the difference in interdot coupling leads to qualitatively different behavior. The weak coupling case in figure 5.7 (a) is nicely reproduced by the simulation (c), where only sequential transitions are permitted. Here, the electron transfer from QD1 to QD3 is only possible, if an energy level of QD2 is energetically available as an intermediate state. This condition is met at the $(1, 0, 0) - (0, 1, 0)$ degeneracy line. In both experiment (a) and simulation (c), the long range transition from QD1 to QD3 (above the resonance) occurs at this QD1 - QD2 degeneracy, which leads to a continuation of the $(1, 0, 0) \rightarrow (0, 1, 0)$ sequential reconfiguration line. However, the color of the reconfiguration line changes toward darker blue, which corresponds to more negative potential in the vicinity of the charge detector. This implies, the electron is indeed transferred from QD1 to QD3. The $(1, 0, 0) \rightarrow (0, 0, 1)$ long range transition in the weak coupling regime in figure 5.7 (a) can therefore be ascribed to a two-step sequential process. The electron tunnels from QD1 to QD2 as soon as an energy level of QD2 becomes energetically available for sequential transport, followed by an inelastic tunneling process from QD2 to QD3.

In the strong coupling regime in figure 5.7 (b), three different slopes of charge reconfiguration lines are observed. This regime is nicely reproduced by the capacitive model simulation where long range transitions between QD1 and QD3 are permitted (d). Since the underlying process for the sequential reconfiguration lines does not change compared to the weak coupling regime, the major difference is here given by the broaden-

ing of the reconfiguration lines due to the larger interdot coupling. The long range $(1, 0, 0) \rightarrow (0, 0, 1)$ reconfiguration line however shows qualitatively different behavior in terms of a different slope, which means the underlying process depends on different energetic conditions. Here, the long range transition is observed at the $(1, 0, 0) - (0, 0, 1)$ degeneracy line, with the lowest energy level of QD2 being off resonant and higher in energy than those of QD1 and QD3. The $(1, 0, 0) \rightarrow (0, 0, 1)$ long range transition in the strong coupling regime in figure 5.7 (b) can therefore be ascribed to a co-tunneling transition via virtual occupation of the center QD2, which leads to an effective tunnel coupling between the non-neighboring QD1 and QD3 [128].

The efficient tunability of the individual tunnel couplings inside the TQD here allows to switch co-tunneling on and off within the measurement timescale. This effectively enables a switching of long range interaction in quantum dot arrays and can be seen as an important step toward controlled long distance correlations, which are important ingredients for quantum computation and simulation.

### 5.2.3. Two Electrons

By slightly modifying the loading procedure, two electrons can be loaded into the isolated TQD array. The tunnel barrier gate voltage $V_{Tg1}$ shifts the isolation point with respect to the QD1 energy levels. More negative $V_{Tg1}$ result in the isolation point being reached for more positive $V_{Dg1}$. Compared to the single electron case presented before, a larger number of trapped electrons can therefore be achieved by simply changing $V_{Tg1}$ toward more negative voltages without changing anything else in the loading procedure.

An experimental and a simulated stability diagram for two electrons isolated in a TQD is shown in figure 5.8 (a) and (b). The experimental stability diagram was probed with two particular electrons, which were loaded into the TQD in a preceding loading procedure. The simulation
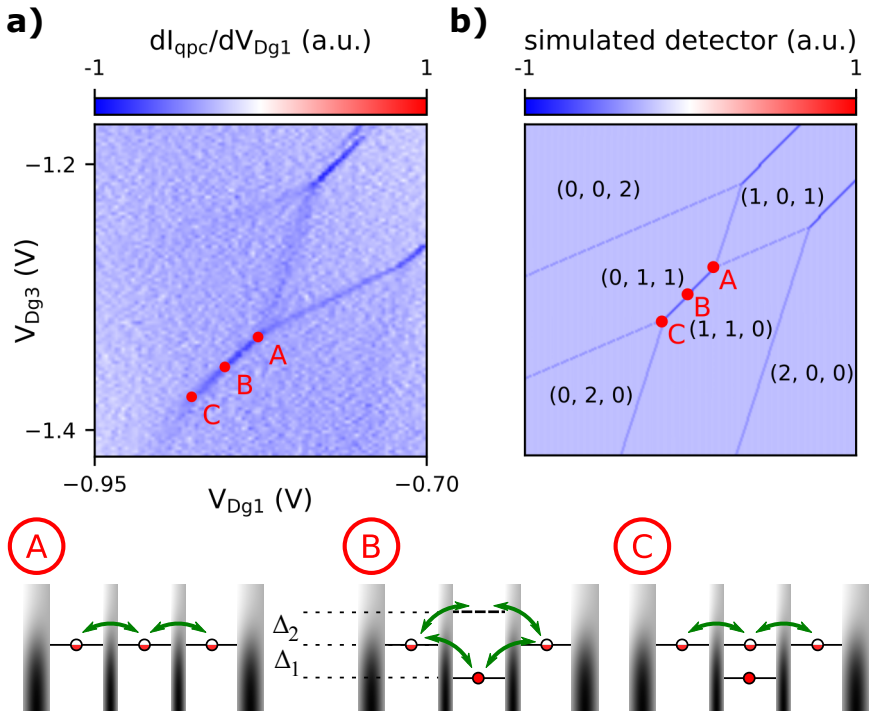
**Figure 5.8.: (a)** Experimental and **(b)** simulated stability diagram of a two-electron isolated TQD. All possible charge configurations $(N_1, N_2, N_3)$ and transitions for a two-electron TQD are visible in the simulation. The experimental stability diagram was probed with two particular electrons and shows a similar pattern, but with low contrast of the sequential reconfiguration lines due to the coupling induced broadening. A, B, and C provide schematic energy diagrams for the three positions marked in (a) and (b). Point A marks the $(1, 1, 0) - (1, 0, 1) - (0, 1, 1)$ resonance, where both electrons tunnel resonantly between the three QDs. Point C marks the $(1, 1, 0) - (0, 2, 0) - (0, 1, 1)$ resonance, where one electron tunnels resonantly between the three QDs, while the second electron remains in the center QD2. Both resonances are connected by the $(1, 1, 0) - (0, 1, 1)$ co-tunneling reconfiguration line. At point B, centered between both resonances, both outer QDs are resonant, while the occupied and the lowest unoccupied energy level of QD2 being equally detuned.

was performed with all gate to dot lever arms except $\alpha_{Dg3,3}$ equal to the single electron TQD simulation in figure 5.7 (d). Here, $\alpha_{Dg3,3} = \alpha_{Dg1,1} = 0.105$ was chosen to achieve a better agreement between the experimental and the simulated co-tunneling reconfiguration line slope. The charging energies implemented in the simulation are given by $E_{C1} = 3.1\,\text{meV}$, $E_{C2} = 2.8\,\text{meV}$, and $E_{C3} = 3.1\,\text{meV}$. The constant gate voltages for the experimental stability diagram are $V_{Bg1} = V_{Bg2} = -0.6\,\text{V}$, $V_{Tg1} = -0.85\,\text{V}$, $V_{Tg} = 0.15\,\text{V}$, $V_{Tg3} = 0.275\,\text{V}$, $V_{Tg4} = -0.8\,\text{V}$, and $V_{Dg2} = -0.85\,\text{V}$. The gate voltages in the center of the device are similar to the strong coupling regime of the single electron TQD presented before, where co-tunneling was present.

Two electrons in a TQD result in six possible charge configurations. In the simulated stability diagram figure 5.8 (b), all six charge configurations are visible and labeled $(N_1, N_2, N_3)$ and all transitions possible in this system are observed. Both sequential transitions QD1 $\rightarrow$ QD2 and QD2 $\rightarrow$ QD3, as well as the co-tunneling transition QD1 $\rightarrow$ QD3 occur three times in the stability diagram. The resonant states hereby differ due to the remaining electron, which can occupy either of the three QDs. All charge states and transitions are as well found in the experimental stability diagram shown in figure 5.8 (a). However, the sequential reconfiguration lines show significant broadening due to the strong interdot coupling, which results in low contrast in the stability diagram. Especially toward the most negative $V_{Dg1}$ and $V_{Dg3}$, where the energy levels are located at higher energies, which effectively decreases the tunnel barrier width, the sequential reconfiguration lines are only vaguely visible.

In both, the experimental and the simulated stability diagram, three specific situations A, B, and C are marked on the $(1, 1, 0) \rightarrow (0, 1, 1)$ co-tunneling reconfiguration line. The three energy level schemes in figure 5.8 depict the energetic situation for these three points. Point A marks a TQD resonance with the resonant states $(1, 1, 0), (1, 0, 1), (0, 1, 1)$. Here,

both electrons can tunnel resonantly between the three QDs. A second TQD resonance is marked by point C, where the resonant states are given by $(1, 1, 0), (0, 2, 0), (0, 1, 1)$. Only one electron tunnels resonantly between the three QDs, while the other electron occupies the lowest energy level of the center QD2. While both resonances involve only the lowest energy level of both QD1 and QD3, the resonant energy level of QD2 is the lowest energy level for resonance A, but the second energy level for resonance C. When moving from resonance A to C, the energy levels of the center QD2 are therefore exactly shifted by the charging energy $E_{C2}$ with respect to the resonant states of QD1 and QD3. Between these two resonances and on the co-tunneling reconfiguration line, the two outer QDs are resonant with the center QD2 being off-resonant. Point B, found in the center between both resonances, hereby marks a special situation, where the detuning $\Delta_1$ of the occupied energy level of QD2 and the detuning $\Delta_2$ of the lowest unoccupied energy level of QD2 with respect to the resonant states of QD1 and QD3 are equal.

The pattern observed in the stability diagram of this serial TQD array is found to be very similar to that of a two electron isolated TQD in a triangular configuration [123]. The presence of co-tunneling leads to an effective tunnel coupling between both outer QDs in a serial TQD array, which leads to a configuration, where each QD is tunnel coupled to both others, similar to a triangular configuration. The co-tunneling coupling strength $t_{co}$ is hereby a function of the nearest neighbor interdot couplings, and of the detuning of the relevant energy levels [128]

$$t_{co} = \frac{t_{12} t_{23}}{\Delta_1} + \frac{t_{12}' t_{23}'}{\Delta_2},$$
(5.2)

where $t_{12}$ ($t_{23}$) is the coupling strength between QD1 (QD3) and the occupied energy level of QD2. The couplings to the unoccupied states are given by $t_{12}'$ and $t_{23}'$. $\Delta_1$ and $\Delta_2$ are the detunings of the respective QD2

energy level with respect to the resonant states of QD1 and QD3. Equation 5.2 is valid, as long as the detuning $\Delta_{13}$ between the energy levels of the outer QDs is small compared to the detuning of the center QD2 $\Delta_{13} << \Delta_{1/2}$, i.e. invalid close to the TQD resonance, where the detuning of the center QD goes to zero and resonant tunneling between the three QDs occurs.

When moving from resonance A to resonance C, the energy levels of QD2, and therefore the detuning values $\Delta_1$ and $\Delta_2$, are shifted by the charging energy $E_{C2} = 2.8\,meV$. The effective tunnel coupling strength $t_{co}$ between the outer QDs via virtual states of QD2 is therefore expected to decrease when moving from point A, where $\Delta_1 = E_{C2}$ and $\Delta_2 = 0$, to B, where $\Delta_1 = \Delta_2 = E_{C2}/2$. Going further to point C results in $\Delta_1 = 0$ and $\Delta_2 = E_{C2}$. Since $t_{co}$ is an effective tunnel coupling, the coupling strength is expected to induce a broadening of the co-tunneling reconfiguration line. An analysis of the width of such a co-tunneling reconfiguration line is shown in figure 5.9. Panel (a) shows a stability diagram of the $(1,1,0) - (0,1,1)$ co-tunneling transition, where the points A, B, and C are marked as in figure 5.8. The horizontal dashed lines mark the region, in which the analysis is performed. The interval is chosen between the two resonances but not including them, to avoid the influence of the TQD resonance on the width of the reconfiguration line.

Due to the low resolution and a high level of noise in the experimental data, fitting the reconfiguration line to extract the tunnel coupling, as performed for the DQD in section 5.1, was not possible. To extract information about the trend of the co-tunneling coupling, the detector signal $dI_{qpc}/dV_{Dg1}$ was smoothed using a Gaussian filter and afterwards fitted by a Gaussian. The width of this Gaussian is overestimated due to the filtering and should not be interpreted quantitatively. Figure 5.9 (b) exemplarily shows the absolute value of the filtered detector signal $|dI_{qpc}/dV_{Dg1}|$ and the corresponding Gaussian fit at $V_{Dg3} = -1.225\,V$. The full width half maximum (FWHM) of such a fit is now a parame-
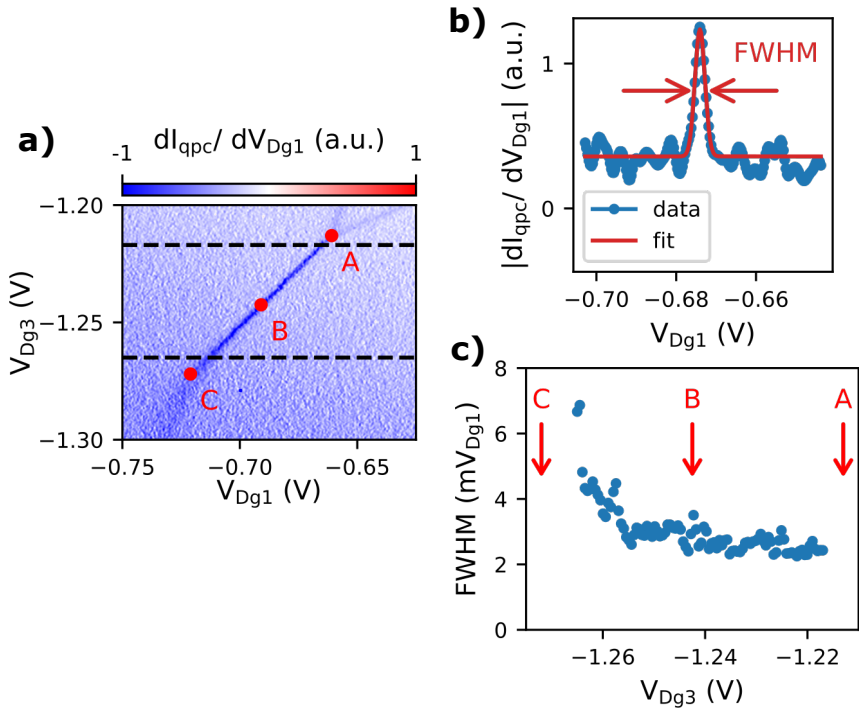
**Figure 5.9.: (a)** Stability diagram of a two-electron isolated TQD around the $(1,1,0) - (0,1,1)$ co-tunneling reconfiguration line. Points A, B, and C are marked as in figure 5.8. **(b)** Exemplary curve of the filtered detector signal $|\mathrm{dI}_{qpc}/\mathrm{dV}_{Dg1}|$ of the $(1,1,0) - (0,1,1)$ co-tunneling charge reconfiguration (blue). Gaussian fitting (red) allows to extract the FWHM, which depends on the co-tunneling coupling $t_{co}$ between QD1 and QD3. **(c)** FWHM of Gaussian fits to the $(1,1,0)-(0,1,1)$ co-tunneling reconfiguration line. Fitting was done for $V_{Dg3}$ values between the dashed lines in (a). Within this $V_{Dg3}$ interval, the detuning of the center QD2 is varied over almost the charging energy $E_{C2}$. The FWHM of the co-tunneling reconfiguration line increases for the most negative $V_{Dg3}$ (close to C), which indicates an increasing co-tunneling coupling. No increase in the reconfiguration line width is found toward the most positive $V_{Dg3}$ (close to A), which can be explained by competing effects due to the changes in both $V_{Dg1}$ and $V_{Dg3}$.

ter depending on the broadening of the reconfiguration line, which in turn depends on the co-tunneling coupling strength $t_{co}$. Figure 5.9 (c) shows the FWHM in $mV_{Dg1}$ of the Gaussian fits to each line between the horizontal dashed lines in (a) as function of $V_{Dg3}$, which is a measure for the detuning values $\Delta_1$ and $\Delta_2$. The positions A, B, and C are marked by the red arrows. Point B, where $\Delta_1 = \Delta_2 = E_{C2}/2$, is located at $V_{Dg3} = -1.242$ V.

For the most positive voltages $V_{Dg3}$ the situation is close to the $(1, 1, 0) - (1, 0, 1) - (0, 1, 1)$ resonance (A), the most negative voltages are close to the $(1, 1, 0) - (0, 2, 0) - (0, 1, 1)$ resonance (C). Both detunings $\Delta_1$ and $\Delta_2$ are therefore changed over almost the charging energy $E_{C2}$. From equation 5.2, the resulting co-tunneling coupling strength $t_{co}$ is expected to have a minimum around point B, where $\Delta_1 = \Delta_2$, and an increasing behavior toward the two TQD resonances, where one of the detunings becomes small. Experimentally, a clear increase of the co-tunneling reconfiguration line width and therefore the co-tunneling coupling strength $t_{co}$ is observed for the most negative voltage $V_{Dg3}$, i.e. for decreasing $\Delta_2$. For the most positive $V_{Dg3}$ however, where $\Delta_1$ becomes small, no increasing tendency of the reconfiguration line width is found.

This behavior can be explained by competing effects, which occur as a result of changing the gate voltages $V_{Dg1}$ and $V_{Dg3}$ along the co-tunneling reconfiguration line. On the one hand, there is finite crosstalk from plunger gate voltages to the tunnel barriers. More negative $V_{Dg1}$ decreases the coupling between QD1 and QD2, more negative $V_{Dg3}$ decreases the coupling between QD2 and QD3. This effect however decreases both $t_{12}$ and $t_{23}$, and therefore $t_{co}$, toward more negative voltages, whereas the trend observed in figure 5.9 (c) shows increasing coupling toward more negative voltages. On the other hand, the energy levels of all three QDs are energetically lifted with increasingly negative gate voltages. This effectively decreases the tunnel barrier widths, which therefore increases both interdot couplings $t_{12}$ and $t_{23}$, and therefore $t_{co}$. The

$\Delta V_{Dg1} \approx 50\,\text{mV}$ gate voltage difference between points A and C hereby corresponds to an energy shift of $\Delta\mu \approx 3.5\,\text{meV}$ of the energy levels of QD1. The trend of the co-tunneling reconfiguration line width indicates the latter mechanism being dominant, which is supported by the appearance of the sequential reconfiguration lines in the stability diagram in figure 5.9 (a). The broadening of the sequential reconfiguration lines below resonance C is considerably larger than the broadening of those above resonance A, which corresponds to larger interdot couplings $t_{12}$ and $t_{23}$ for more negative $V_{Dg1}$ and $V_{Dg3}$. This is also in agreement with the DQD case, where the energy level lifting was as well found to be the dominant effect in the discussion of figure 5.4 (a).

The influence of these competing effects prevents to resolve a behavior as expected for the co-tunneling coupling strength $t_{co}$ as function of the energy level detunings in the given configuration. Nevertheless, the width of the co-tunneling reconfiguration line is found to increase toward the $(1, 1, 0) - (0, 2, 0) - (0, 1, 1)$ resonance. This shows, that the co-tunneling coupling, which is an effective tunnel coupling between non-neighboring QDs, is a tunable parameter in this system. The efficient tunability of the interdot tunnel couplings via the tunnel barrier gates, which was discussed for the DQD in figure 5.3, could provide a way to overcome the influence of the competing effects. By implementing a virtual gate, where the tunnel barrier gates are coupled to the plunger gates, more negative tunnel barrier gate voltages can be used to compensate for the effect of lifting the energy levels.

Overall, this leads to a highly tunable long range coupling in an isolated TQD system. According to equation 5.2, the co-tunneling coupling strength $t_{co}$ is a function of the interdot couplings and of the energy level detunings of the center QD. Both interdot couplings can be efficiently tuned via the tunnel barrier gate voltages, and additionally by energetically shifting the resonant energy levels, which influences the effective the tunnel barrier widths. The detuning of the center QD2 can be varied

over the full range of the charging energy $E_{C2}$. Due to this high level of tunability of the long range coupling between non-neighboring QDs, the isolated regime provides a versatile platform for example for photon assisted co-tunneling experiments or the investigation of dark states [152–154].

In summary, this part discussed the charge reconfiguration inside an isolated serial triple quantum dot system. Three different slopes of reconfiguration lines are present in the stability diagram of an isolated triple quantum dot. By comparison to calculated stability diagrams based on a capacitance model, these were attributed to two sequential transitions between neighboring QDs and an additional long-range transition directly between the non-neighboring outer QDs. The arrangement of the sequential and the long-range transition close to a resonance between all three QDs allows to distinguish between electron-like resonances with a single electron tunneling between the three resonant states and hole-like resonances, where two electrons tunnel between the resonant states. A loading procedure was implemented and used to load the TQD with a fixed number of electrons before isolating from the reservoirs. Stability diagrams for a single electron isolated in the TQD were discussed and the ability to suppress the long-range tunneling by decreasing the coupling between the QDs was demonstrated. For two electrons isolated in the TQD, the full energy space with all six possible charge configurations was measured and compared to model calculations. With all charge states and transitions known, a highly tunable long-range transition $(1, 1, 0) \leftrightarrow (0, 1, 1)$ could be identified, providing a candidate for the investigation of interference effects in co-tunneling via two different virtual paths under full control over the detunings and tunnel couplings.

## 5.3. Quadruple Quantum Dot

With negative voltages applied to all gates of the device, a QQD is formed. As an extension of the TQD, the QQD naturally inherits the functionality of the smaller QD arrays. Similar to the DQD and TQD, the QQD can be brought into the isolated configuration by applying highly negative voltages to the outermost gates of the device. For an isolated TQD, three different transitions are possible. Two sequential tunneling transitions (QD1 $\rightarrow$ QD2) and (QD2 $\rightarrow$ QD3), as well as a co-tunneling transition (QD1 $\rightarrow$ QD3). With including the fourth QD, another sequential transition (QD3 $\rightarrow$ QD4) and an additional co-tunneling transition (QD2 $\rightarrow$ QD4) are expected to occur, since these transitions are equivalent to the transitions already observed for the TQD.

In addition, there is another plausible option in a serial QQD device, a transition directly between the outer QDs (QD1 $\rightarrow$ QD4) via two intermediate QDs. In the context of metrological junction charge pump experiments [91, 155, 156], co-tunneling rates and higher order co-tunneling rates for more than one intermediate tunnel junction were calculated [157–159] and found to be a limiting factor for the accuracy of these devices. In terms of the QQD, this implies that higher order co-tunneling transitions via more than one intermediate QD might occur, despite the long distance.

A stability diagram of an isolated QQD as function of the outer plunger gate voltages $V_{Dg1}$ and $V_{Dg4}$ is shown in figure 5.10 (a). A corresponding capacitive model simulation is given in figure 5.10 (b). The experimental stability diagram was obtained by sweeping $V_{Dg1}$ from more positive to more negative voltages. At the beginning of each $V_{Dg4}$-line, the system was reset to a state well coupled to the left reservoir, so that the number of electrons trapped in the QQD can change in $V_{Dg4}$-direction. The constant center gate voltages are $V_{Bg1} = V_{Bg2} = -0.4\,\text{V}$, the tunnel barrier gate voltages are $V_{Tg1} = -0.45\,\text{V}$, $V_{Tg2} = -0.2\,\text{V}$, $V_{Tg3} = -0.1\,\text{V}$, $V_{Tg4} =$

$-0.4\,$V, and $V_{Tg5} = -0.45\,$V, and the two constant plunger gate voltages are $V_{Dg2} = V_{Dg3} = -0.375\,$V. Based on this gate voltage configuration, the electron numbers in the QQD array can be estimated. Comparing the applied voltages with another measurements of the same cooldown of the device, in particular with figure 4.2, the electron numbers for the two center QDs can be estimated to around $N_2 \approx N_3 \approx 10$. The slightly more negative $V_{Dg1}$ compared to $V_{Dg2}$ and $V_{Dg3}$ suggests N1 < N2, N3. Similarly the voltages defining QD4 are more negative than those defining the other QDs, so that $N_4 < N1 < N2 \approx N3$ can be estimated.

The capacitive model simulation, shown in figure 5.10 (b), was obtained using the gate to dot lever arms given in table 5.4. The implemented charging energies range between $1.4\,\text{meV} \leqslant E_{C1} \leqslant 3.3\,\text{meV}$, $1.5\,\text{meV} \leqslant E_{C2} \leqslant 2.8\,\text{meV}$, $2.3\,\text{meV} \leqslant E_{C3} \leqslant 2.6\,\text{meV}$, and $1.7\,\text{meV} \leqslant E_{C4} \leqslant 2.4\,\text{meV}$.

|  | QD1 | QD2 | QD3 | QD4 |
|---|---|---|---|---|
| $\alpha_{Dg1}$ | 0.085 | 0.036 | 0.012 | 0.007 |
| $\alpha_{Dg4}$ | 0.007 | 0.012 | 0.032 | 0.081 |

**Table 5.4.:** Gate to dot lever arms for the QQD simulation.

Similar to the DQD and TQD case, resetting the system to a state well coupled to the left reservoir leads to a fragmented appearance of the experimental reconfiguration lines due to stochastic fluctuations of the charge configuration at the isolation point. Comparing the DQD, TQD, and QQD, these fragmentation become a more and more dominant effect with an increasing number of QDs. For the QQD case, the observable transitions in the isolated configuration are determined by the configuration $(N_1, N_2, N_3, N_4)$ at the isolation point. The fluctuations increase with an increasing number of QDs, since the number of electrons on each QD may fluctuate due to the stochastic nature of tunneling. Additionally, the system is only well coupled to the left reservoir at the beginning of each
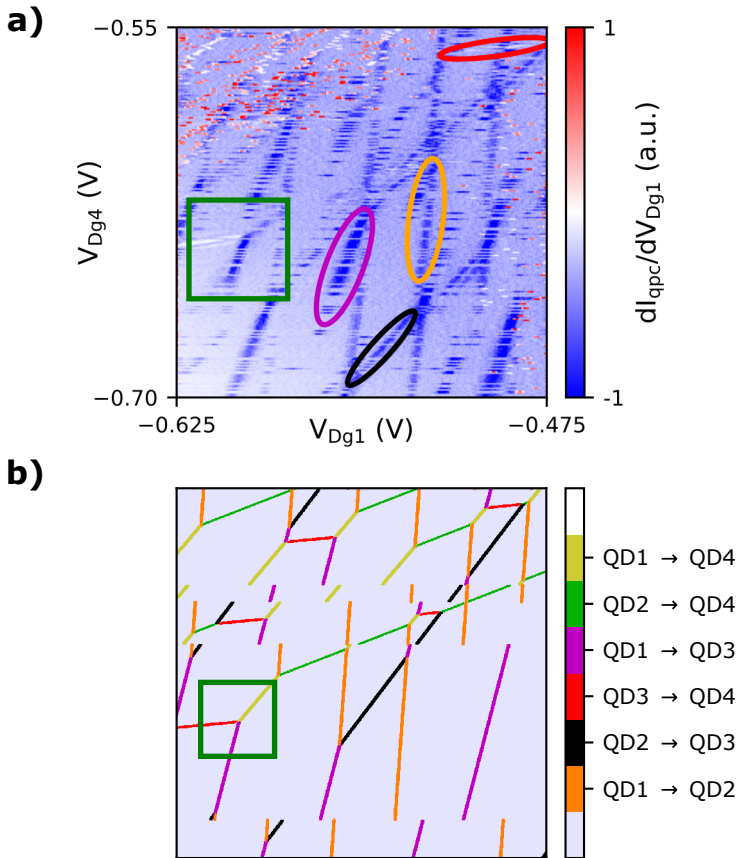
**Figure 5.10.: (a)** Experimental and **(b)** simulated stability diagram of an isolated QQD in the many electron regime. The six possible transitions are color coded in the simulation. Four of these transitions can be clearly identified in the experimental data, where one of each transition is marked by an ellipse with colors according to the simulation. The green boxes in (a) and (b) highlight a situation similar to a single electron TQD resonance.

line, while being isolated from the righ reservoir. Consequently, QD2, QD3, and QD4 are only indirectly coupled to the reservoir. The coupling hereby decreases with increasing distance from the reservoir. Decreasing coupling corresponds to decreasing tunneling rates, which eventually results in metastable states, even before the isolation point is reached. The electron configuration at the isolation point therefore depends on the lifetimes of the metastable states and the measurement frequency.

In contrast to the DQD and TQD case, not only dark blue, but also white reconfiguration lines are found in the experimental stability diagram. The dark blue reconfiguration lines correspond to increasing negative potential in the vicinity of the detector, i.e., electrons tunneling toward the detector. In contrast, white and red color correspond to negative potential being removed from the vicinity of the detector. Since the detector is located below QD3, the white reconfiguration lines can be attributed to the (QD3 → QD4) sequential transition. The noisy part in the upper left part of the experimental stability diagram stems from electrons tunneling out of the QQD into the right reservoir.

All six types of transitions are found in the simulated stability diagram in figure 5.10 (b). The transitions are color coded for clarity. The three sequential transitions (QD1 → QD2), (QD2 → QD3), and (QD3 → QD4) are colored in orange, black, and red, respectively. The co-tunneling transition (QD1 → QD3), which was already observed for the isolated TQD, is colored in magenta. Green reconfiguration lines correspond to the equivalent (QD2 → QD4) co-tunneling transition. The higher order co-tunneling transitions directly between the outer QDs (QD1 → QD4) is marked in yellow.

Comparing the simulated and the experimental stability diagram allows to clearly identify four of the six transitions in the experiment. All three sequential transitions are present in the experimental stability diagram, where one of each transition is marked by an ellipse, colored according to the simulation. Additionally, the co-tunneling transition (QD1

$\rightarrow$ QD3), which was already present in the TQD, can be identified in the experimental data. However, the (QD2 $\rightarrow$ QD4) co-tunneling transition, even though it is equivalent, can not be clearly identified. A reason for this transition not to be observed can be found in the device design. The detector used for the measurements is located below QD3, which means QD2 and QD4 are located at a similar distance from the detector. Due to this symmetric arrangement with respect to the detector, the potential of an electron being in QD2 or QD4 is similar at the detector, which leads to a vanishing detector signal. Even if (QD2 $\rightarrow$ QD4) co-tunneling transitions are present in the experimental stability diagram, it is therefore not expected to observe these transitions in the detector signal.

The remaining transition is the special case for the QQD, the higher order co-tunneling transition directly between the outer QDs (QD1 $\rightarrow$ QD4). For symmetry reasons, the slope of the reconfiguration lines corresponding to these transitions is expected to be similar to the (QD2 $\rightarrow$ QD3) sequential reconfiguration lines (marked in black). Additionally, due to the long distance and the two intermediate QDs, the coupling between QD1 and QD4 is expected to be much smaller than the coupling between the neighboring QD2 and QD3. The sequential transitions are therefore expected to be dominant. It is therefore not possible to assign one of the reconfiguration lines in the experimental stability diagram in figure 5.10 (a) to the (QD1 $\rightarrow$ QD4) higher order co-tunneling transition without any doubt.

However, by comparing the simulated and the experimental stability diagram, an energetic situation is found, where the (QD1 $\rightarrow$ QD4) transition is energetically favorable. The green boxes in figure 5.10 (a) and (b) highlight the region, where this configuration is found. Zooms into these green boxes are shown in figure 5.11.

The reconfiguration line pattern shown in the experimental (a) and simulated (b) stability diagram is similar to that of a TQD resonance charged with one electron, which was already discussed in section 5.2. The transi-

**a)**



**b)**
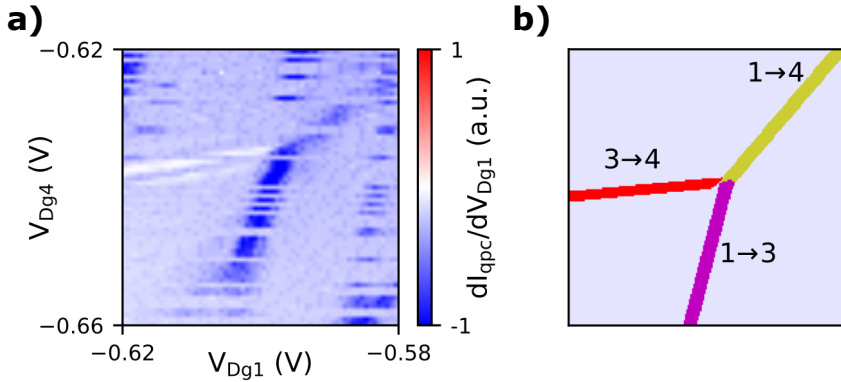
**Figure 5.11.:** Zoom into the **(a)** experimental and **(b)** simulated stability diagram of figure 5.10. The reconfiguration line pattern is similar to a singly charged TQD resonance. The three resonant QDs are QD1, QD3, and QD4, which results in the energetically favorable transition above the resonance being the higher order co-tunneling transition directly between QD1 and QD4.

tion found on the left side of the resonance corresponds to the sequential (QD3 → QD4) transition, which is colored in red in the simulation. In the experimental stability diagram, this reconfiguration lines appears in white due to an electron being transferred away from the detector. The reconfiguration line below the resonance, magenta in the simulation, dark blue in the experimental data, can be attributed to the (QD1 → QD3) co-tunneling transition. Since both reconfiguration lines coincide with the degeneracy between an energy level of each involved QD, the respective energy levels of all three QDs are degenerate at the position, where the two reconfiguration lines meet. The TQD resonance pattern is therefore defined by a resonance of QD1, QD3, and QD4.

The third reconfiguration line defining this TQD resonance pattern is located in the upper right. The slope of this reconfiguration line is close to diagonal. Due to symmetry reasons, only two of the possible transitions in a QQD system are expected to exhibit a reconfiguration line slope close

to diagonal as function of $V_{Dg1}$ and $V_{Dg3}$. The two options are given by either the sequential (QD2 $\rightarrow$ QD3) transition or the higher order co-tunneling (QD1 $\rightarrow$ QD4) transition directly between both outer QDs. The resonance is defined by QD1, QD3, and QD4, without including QD2. As seen in the simulated case in figure 5.11 (b), the transition is therefore not expected to involve QD2, but being a transition directly between the outer QDs (QD1 $\rightarrow$ QD4). The TQD resonance pattern in figure 5.11 (a) can therefore be seen as experimental evidence of a higher order co-tunneling charge reconfiguration inside this QQD device.

Implementing a controlled loading procedure, as described for the TQD in 5.2.1, to load the QQD with a well defined number of electrons would be a way to confirm this observation and additionally provides the possibility to investigate these higher order co-tunneling transitions in more detail. A controlled electron number hereby provides multiple benefits.
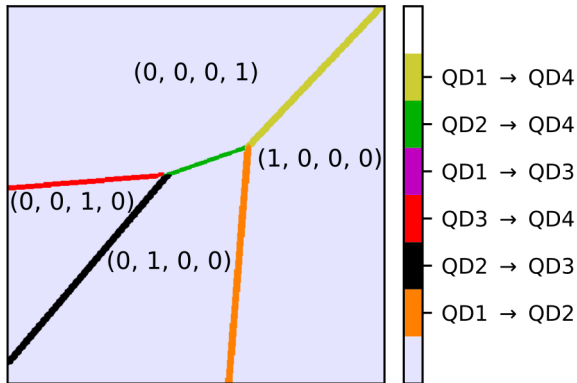


**Figure 5.12.:** Capacitive model calculation of the stability diagram of a single electron isolated in a quadruple quantum dot with all long-range transitions allowed. The drastic simplification in comparison with the many electron regime provides a suitable basis for the investigation of co-tunneling and higher order co-tunneling under well controlled conditions.

A simulated stability diagram for a single electron isolated in a QQD

is exemplarily shown in figure 5.12. Similar to the TQD, the stability diagram of a QQD significantly simplifies when only a single electron is loaded into the system. Only four different charge configurations are possible in this configuration, one for each QD the electron can be located in. The four charge configurations are given by $(1, 0, 0, 0)$, $(0, 1, 0, 0)$, $(0, 0, 1, 0)$, and $(0, 0, 0, 1)$, and the total number of transitions is reduced to the transitions between these four charge states. At the same time, the loading procedure eliminates the stochastic fluctuations of the number of electrons isolated in the QQD, which in turn eliminates the fragmentation of the charge reconfiguration lines and therefore simplifies the assignment of observed transitions.

These simplifications might provide the possibility to clearly assign all transitions in a QQD stability diagram in the isolated configuration, including higher order co-tunneling transitions directly between both outer QDs. At this point, the high level of control over the tunnel couplings and the internal energy level alignment in the isolated configuration provides a versatile platform for further investigations of these long range transitions, which are already known to be a limiting factor for the accuracy of junction charge pumps. Similarly, the accuracy of other QD array devices, for example QD qubit arrays, might also be negatively affected by these long range transitions. On the other hand, a long range coupling also provides an opportunity in terms of implementing long range interactions in QD array devices.

In a situation, where all transitions can be clearly assigned, the isolated QQD system provides a versatile platform for further investigations on long range transitions. The high level of control over the energy level alignment, which comes as a consequence of isolating the system, allows to tune the device into configurations, where long range transitions are energetically favorable and the detuning of the energy levels of the intermediate QDs can be adjusted. At the same time, the high level of control over the interdot couplings provides an additional way to increase or de-

crease the virtual coupling between the non-neighboring QDs. This high level of tunability combined with a known number of electrons enables the investigation of long range transitions under well defined conditions. Increasing the number of trapped electrons to two or more and using the single electron case as a reference might provide a way to identify interaction effects or for example interference effects between different virtual paths of higher order tunneling.

To summarize, this part presented a serial quadruple quantum dot in the isolated configuration. In the many electron regime, all three sequential transitions could be identified, as well as the long-range transition already present in the TQD. The second possible and equivalent next-nearest neighbor long-range transition can not be resolved due to the symmetric alignment of the respective QDs with respect to the charge detector. However, a resonance between three of the four QDs was identified, where the surrounding reconfiguration pattern strongly suggests the presence of a higher order co-tunneling transition directly between QD1 and QD4 via two intermediate QDs. A capacitance model simulation was used to show the drastic simplification of the reconfiguration pattern, when only a single electron is isolated in the QQD. The single electron QQD would therefore provide a suitable basis for the investigation of these higher order co-tunneling transitions under controlled conditions.

# 6

# Time-Resolved Electron Tunneling

The previous chapter discussed the charge reconfiguration behavior and the tunability of isolated quantum dot arrays based on charge stability diagrams. The focus of this chapter lies on an isolated double quantum dot system and the statistical analysis of time-resolved tunneling between the two quantum dots. The first part will introduce the time-resolved charge detection and the statistical analysis, followed by a detailed analysis of the tunneling statistics for different electron numbers isolated in the double quantum dot.

## 6.1. Time-Resolved Charge Detection

The detection of individual tunneling events in or through quantum dots in a time-resolved manner is a way to acquire information about dynamic properties of the quantum dot system, for example the tunneling rates into or out of a quantum dot. To resolve individual tunneling events in the charge detector signal, the time resolution of the measured detector current $I_{qpc}$ has to be large compared to the time between two tunneling events. All time-resolved data discussed in this chapter was acquired using the ADwin-Pro II real-time controller with a sampling rate of $400\,\text{kHz}$. In addition, each tunneling event has to create an observable change in the detector current $I_{qpc}$. In order to achieve a low noise floor and therefore

a high sensitivity, the QPC drain was connected to a low capacitance line ($\sim 30\,\mathrm{pF}$) and a low-noise $\mathrm{FEMTO}$ LCA-100K-50M current amplifier. All time-resolved measurements were performed in an Oxford Instruments Teslatron cryostat with variable temperature insert (VTI) at $\mathsf{T} \approx 1.5\,\mathrm{K}$.
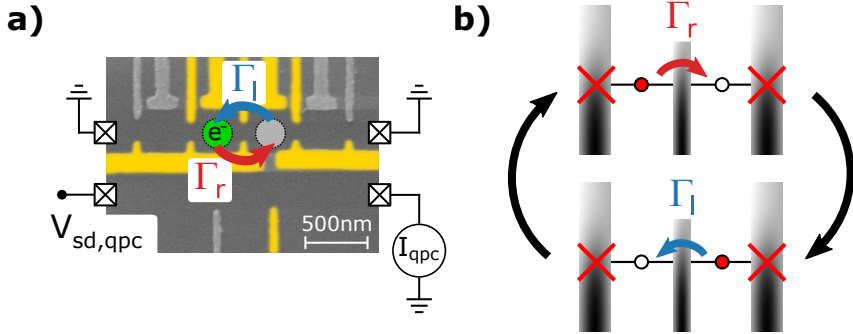


**Figure 6.1.: (a)** SEM image of the device. A double quantum dot and a QPC charge detector are formed by applying negative potentials to the golden colored gates while keeping the gray gates grounded. By isolating the double quantum dot from the electron reservoirs, the total number of electrons trapped inside the double quantum dot is fixed. In the proximity of a reconfiguration line, the electrons can however still tunnel back and forth between the two quantum dots with tunneling rates $\Gamma_r$ from QD2 to QD3 (left to right) and $\Gamma_l$ from QD3 to QD2 (right to left). The back and forth tunneling can be tracked by monitoring the detector current $I_{qpc}$ as function of time. **(b)** Simplified energy level schematic of an isolated double quantum dot. Whenever an occupied level of one quantum dot is resonant with an unoccupied level of the other quantum dot, back and forth tunneling between the two quantum dots becomes possible.

A first important step for the time-resolved analysis of electron tunneling events lies in the definition of an appropriate operation point for the device, where the requirements for the time resolution and the detector sensitivity are met. Additionally, the tunneling rates should be large enough so that a large number of events, required for statistical analysis, can be detected within a reasonable time frame. As indicated in figure

6.1 (a), the system of choice here is a double quantum dot, formed by the gates colored in gold in the SEM image. The double quantum dot is then initialized by using a loading procedure similar to the one discussed in section 5.2.1 to load a specific number of electrons into the double quantum dot and then isolate it from the electron reservoirs. In this configuration, tunneling events can only occur between the two quantum dots. The tunneling rates $\Gamma_r$ from QD2 to QD3 (left to right) and $\Gamma_l$ from QD3 to QD2 (right to left) then depend on the barrier between the two QDs and the alignment of the energy levels.

For tunneling to occur, there has to be an occupied state in one of the QDs with an energetically accessible empty state in the other QD, exactly the condition for the occurrence of reconfiguration lines in the stability diagram, as discussed in section 5.1. Figure 6.1 (b) shows two energy level schematics for such a resonance. After each tunneling event in one direction the prerequisites for tunneling into the other direction are met, leading to a cycle of back and forth tunneling between the two QDs. Even though these tunneling events do not change the total number of electrons in the DQD, there is a potential change at the charge detector due to the right QD3 being located closer to the charge detector than the left QD2, allowing to differentiate between the two charge states.

For a single electron loaded into the DQD and in the vicinity of the $(1, 0) \leftrightarrow (0, 1)$ resonance, a short window of a detector current trace $I_{qpc}$ as function of time is shown in figure 6.2 (a). Whenever the electron tunnels from the left QD2 to the right QD3, the electron moves closer to the detector channel, thereby increasing the negative potential and thus decreasing $I_{qpc}$. As the electron tunnels back into QD2, this effect is reversed and $I_{qpc}$ returns to the original value. This cycle repeats multiple times within the shown time window, where each jump in $I_{qpc}$ represents a single tunneling event.

The histogram of the full $3\,\text{min}$ time trace of $I_{qpc}$ in figure 6.2 (b) shows two distinct peaks. The higher current peak corresponds to the
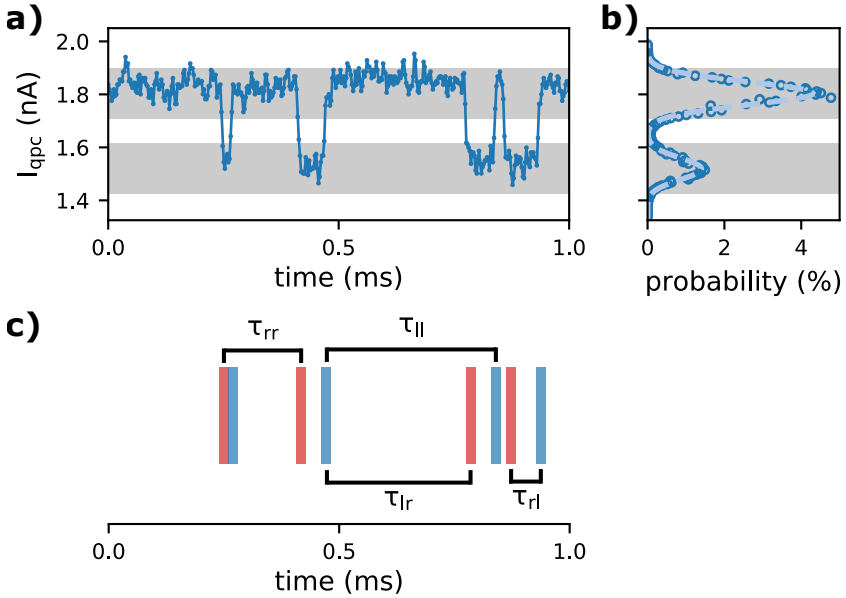
**Figure 6.2.:** **(a)** Short window of a detector current $I_{qpc}$ time trace with a single electron isolated in a DQD and close to the degeneracy of the $(N_2, N_3) = (1, 0)$ and $(N_2, N_3) = (0, 1)$ charge states. A series of abrupt jumps is observed as function of time. Whenever the electron tunnels to the right quantum dot, and thus closer to the detector, the current decreases. As the electron tunnels back into the left quantum dot, the current returns to the original level. **(b)** The histogram of $I_{qpc}$ is used to define a current interval for each charge states, as indicated by the gray bars. **(c)** Transitions extracted from the time trace (a), by assigning each datapoint to one of the two charge states. Red bars represent tunneling events from the left to the right quantum dot ($(1, 0) \rightarrow (0, 1)$), whereas blue bars show the timing of right to left ($(0, 1) \rightarrow (1, 0)$) tunneling events. The residence times $\tau_{lr}$ and $\tau_{rl}$, as well as the return times $\tau_{ll}$ and $\tau_{rr}$ can be extracted from the time sequence of the tunneling events.

$(1, 0)$ charge state of the DQD, the lower one to the $(0, 1)$ state, respectively. Experimentally, these two states are not perfectly sharp, but each level is given by a broadened distribution due to the noise floor of the detector. In typical measurement setups and in the absence of additional intrinsic noise sources, as for example given by charge traps in the vicinity of the QPC, this noise band is dominated by the noise band of the current amplifier [160, 161].

A first statement about the tunneling rates can already be made based on the histogram. The difference in height of the two peaks in the histogram means that the system is more often found in the $(1, 0)$ state (large peak) and less often in the $(0, 1)$ state (small peak). The operation point is therefore not exactly at the resonance condition but in a regime, where $\Gamma_l > \Gamma_r$. Detailed information about the individual rates is however not accessible from only the histogram but can be obtained from statistical analysis of all detected tunneling events.

To perform statistical analysis on the tunneling dynamics of such a two level system, the measured current has to be assigned to either one of the two charge states, so that the timing of transitions between the two states can be determined. Here, this assignment was done using a post processing algorithm based on defining a current interval for each of the charge states. Each point inside one of the intervals was assigned to the corresponding state, while values lying outside of both intervals are assigned to the last known state. The time of a detected transition is therefore the time, when the first datapoint lies in the interval of the new state. The accuracy of this type of detection algorithm depends on the signal to noise ratio, given by the peak separation compared to the peak width for the peaks in the histogram. For ideal situations with well separated peaks, large current intervals can be chosen for each state without detecting statistically relevant numbers of false events due to the noise floor. For less ideal systems with more overlap between the two peaks, it can be beneficial to choose smaller intervals for the states or average over several

datapoints in order to reduce the probability for detecting noise induced false events. Both methods however come at the cost of bandwidth, thus increasing the probability of missing fast events. For the statistical analysis, the highest impact of both detection errors, the detection of false events, as well as missing fast events is on short timescales.

The gray bars in figure 6.2 (a) and (b) represent the intervals used for the detection algorithm, and (c) shows the detected tunneling events using these intervals and averaging the time trace over three points. Red bars mark detected tunneling events from left to right, and blue bars tunneling events from right to left, respectively. The obtained sequence of tunneling events is now used to determine the time intervals annotated in figure 6.2 (c). The two time intervals $\tau_{lr}$ (blue to red; tunneling left - right) and $\tau_{rl}$ (red to blue; tunneling right - left) between consecutive tunneling events will be called residence times, since they represent the time the electron resides in the left ($\tau_{lr}$) and right ($\tau_{rl}$) quantum dot, respectively. Additionally, the time intervals between consecutive tunneling events of the same direction $\tau_{ll}$ (blue to blue; tunneling left - left) and $\tau_{rr}$ (red to red; tunneling right - right) are determined. The latter two time intervals represent the time it takes the system to fulfil one tunnel cycle and return to the original condition. In literature in the context of single electron tunneling, these times are often called waiting times [162–164]. However, the term waiting times is rather generic and would also be a reasonable choice for the times introduced as residence times. To avoid confusion, the times $\tau_{ll}$ and $\tau_{rr}$ will therefore be referred to as return times.

## 6.2. Single Electron in a Double Quantum Dot

The case of a single electron isolated in a DQD provides a two state system, where the electron can either be located in the left or in the right quantum dot. In a time-resolved charge detector signal, this results in a two-level system, very similar to the case electron transport through a

single quantum dot, where the two levels are defined by the presence or absence of an additional electron in the quantum dot [86, 99, 165]. While this allows to use identical methods, the physical meaning of the resulting quantities can differ from the single quantum dot case.

With extracting all residence times $\tau_{lr}$ and $\tau_{rl}$ from a time trace, the individual tunneling rates can be calculated [87, 160, 166]

$$\Gamma_l = \frac{1}{\langle \tau_{rl} \rangle} \quad , \quad \Gamma_r = \frac{1}{\langle \tau_{lr} \rangle}, \tag{6.1}$$

where $\langle \tau_{lr} \rangle$ and $\langle \tau_{rl} \rangle$ are the average values of the extracted residence times.

For the time trace shown in figure 6.2 (a), the tunneling rates become $\Gamma_l = 8.7\,\text{kHz}$ and $\Gamma_r = 2.8\,\text{kHz}$, calculated from approximately $75\,000$ detected tunneling events for each direction. Thus, $\Gamma_l \approx 3\Gamma_r$, in good agreement with the detector current histogram in figure 6.2 (b), where the peak height of the higher current peak is approximately three times the peak height of the lower current peak.

The approach of using equation 6.1 to determine the tunneling rates is based on the assumption that the probability to observe a residence time $\tau$ is given by a single stochastic process with a characteristic rate $\Gamma$. The probability distribution $\rho(\tau)$ of the residence times in this case follows an exponential decay with only a single exponent [166, 167]

$$\rho(\tau_{rl}) = \Gamma_l e^{-\Gamma_l \tau_{rl}}, \tag{6.2}$$

$$\rho(\tau_{lr}) = \Gamma_r e^{-\Gamma_r \tau_{lr}}. \tag{6.3}$$

The distribution of the residence times $\tau_{lr}$ and $\tau_{rl}$ extracted from the experiment, as shown in logarithmic scale in figure 6.3 (a), can be used to validate this assumption and to obtain information about deviations. Both distributions clearly follow a single exponential decay. The solid lines are fits according to equations 6.2 and 6.3 with tunneling rates $\Gamma_l = 9.0\,\text{kHz}$
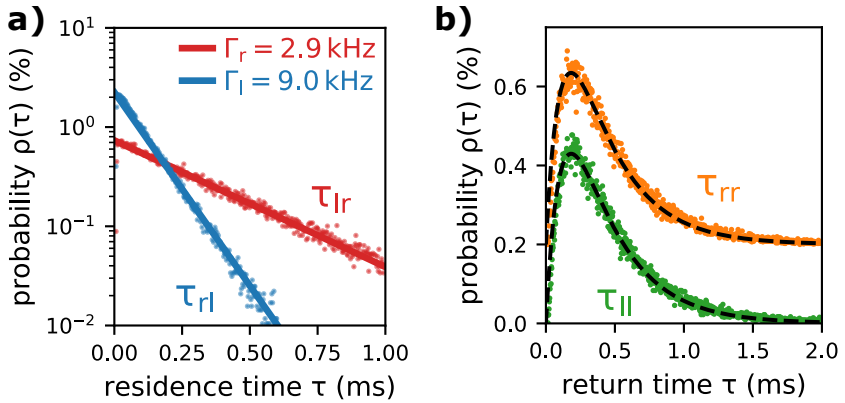
**Figure 6.3.: (a)** Probability distribution of the residence times $\rho(\tau_{lr})$ (red) and $\rho(\tau_{rl})$ (blue) of a $3\,\mathrm{min}$ detector time trace containing approximately $150\,000$ events in total. The solid lines are fits using equations 6.2 - 6.3 with tunneling rates $\Gamma_l = 9.0\,\mathrm{kHz}$ and $\Gamma_r = 2.9\,\mathrm{kHz}$. **(b)** Probability distribution of the return times $\rho(\tau_{ll})$ (green) and $\rho(\tau_{rr})$ (orange, offset for clarity). The dashed lines are are based on equation 6.4 with tunneling rates determined from (a).

and $\Gamma_r = 2.9\,\text{kHz}$. Both rates are slightly larger than the values determined via the inverse average residence times (equation 6.1). These deviations most likely originate from the finite detector bandwidth $\Gamma_{det}$ [168]. Due to the finite bandwidth, the detector signal does not follow changes in the DQD state instantly. The faster consecutive tunneling events occur, the more likely the charge detector signal does not change its state before the DQD returns to the original state. As a result, the number of events missed by the detection algorithm unavoidably increases toward shorter times. Additionally, missing an event merges residence times into a single but longer detected time, resulting in an overestimation of longer times $\tau$. These two effects result in an overall underestimation of the extracted tunneling rates.

Increasing the detector bandwidth reduces the number of missed events, however, at the same time increases the measurement noise, which in turn increases the number of false events detected by the algorithm. To achieve a consistent analysis for the single electron data, the here used detection algorithm sacrifices parts of the bandwidth for filtering the noisy data, which in return allows to use the same algorithm for all measured time traces.

While the residence time distributions $\rho(\tau_{lr})$ and $\rho(\tau_{rl})$ are valuable to obtain information about the individual tunneling rates, the return time distributions $\rho(\tau_{ll})$ and $\rho(\tau_{rr})$, as shown in figure 6.3 (b), contain information about the total two-level system. Both distributions start at zero, since no two electrons can tunnel at the same time, run through a maximum, followed by an exponential decay on longer times. Interestingly, the dashed lines, which are based on the theoretical distributions for electrons tunneling through a single quantum dot [162, 169]

$$\rho(\tau_{ll}) = \rho(\tau_{rr}) = \frac{\Gamma_l \Gamma_r}{\Gamma_l - \Gamma_r}\left(e^{-\Gamma_r \tau} - e^{-\Gamma_l \tau}\right) \qquad (6.4)$$

but with substituting the tunneling rates into and out of the quantum

dot with the already determined rates for tunneling to the left QD2 $\Gamma_l = 9.1\,\text{kHz}$ and to the right QD3 $\Gamma_r = 2.9\,\text{kHz}$, respectively, nicely describe the observed distributions. Due to the distributions being equal, $\rho(\tau_{rr})$ (orange) was offset for clarity in figure 6.3 (b). For equal tunneling rates $\Gamma_l = \Gamma_r = \Gamma$, equation 6.4 simplifies to $\rho(\tau) = \Gamma^2 \tau e^{-\Gamma\tau}$ [162].

Even though a lot of similarities can be found, when comparing the here observed distribution with those of single particle sources, such as single photon emitters [170, 171] or single electron emitters [164], the here presented system does not act as a single particle emitter. In contrast to single particle sources, the single electron in the isolated double quantum dot is only ringing back and forth and is never emitted into one of the reservoirs. At the same time, also the interpretation of the short time behavior is slightly different compared to electrons tunneling through a single quantum dot. For the single quantum dot case, Coulomb blockade prevents double occupation of the quantum dot, so that no two tunneling events of the same type can occur simultaneously. For the isolated double quantum dot loaded with a single electron however, the absence of simultaneous tunneling events in the same direction is not due to Coulomb blockade but directly results from the absence of other electrons. With only one electron inside the DQD, the electron has to tunnel back before tunneling in the same direction can occur again.

In a double quantum dot system, the two main contributions to the interdot tunneling are the tunnel coupling strength and the detuning of the energy levels. A detailed discussion about the tunability of the tunnel coupling strength in an isolated DQD by changing the interdot tunnel barrier gate voltage $V_{Tg3}$ was already given based on the analysis of stability diagrams in section 5.1. The direct method of analyzing the time-resolved tunneling is now used to analyze the effect of the detuning between the energy levels.

The tunnel barrier gate voltage $V_{Tg2}$ was hereby used as a control parameter for the detuning of the DQD. For the DQD consisting of QD2

and QD3, this gate is closer to QD2 than to QD3, leading to a difference in lever arms and therefore to a different effect on the energy levels of the two QDs for a fixed voltage difference. A loading procedure was used to initialize the system each time before recording the time-resolved data. Since the loading procedure is not fully deterministic but involves tunneling, this leads to an uncertainty in the electron number. Additionally, the system is not ideally isolated but only separated from the reservoirs by very large tunneling barriers. However, even though the rates are small compared to the measurement times, every once in a while an electron might tunnel out of the DQD during the data acquisition. An additional electron tunneling into the DQD is even less likely, since the QDs are operated with their lowest energy level well above the chemical potentials of the source and drain reservoirs. Both scenarios, zero or two electrons in the DQD, will change the interdot tunneling characteristics. Zero electrons trivially prevents tunneling events, therefore no transitions will be observable. Interestingly, also the two electron case prevents tunneling in the region close to the $(1,0) \leftrightarrow (0,1)$ transition. Due to Coulomb blockade, the ground state becomes $(1,1)$ and no empty states are energetically accessible to tunnel into. Only by providing energy of the order of the single QD charging energy ($\gtrsim 3\,\mathrm{meV}$ for the 2nd electron), this blockade could be overcome. To reliably obtain data for the single electron in a DQD scenario, a set of three time trace of $3\,\mathrm{min}$ length was taken for each gate voltage value. Each of the three time traces was individually initialized before recording the data.

For voltages $-0.7\,\mathrm{V} \geqslant V_{\mathrm{Tg2}} \geqslant -0.76\,\mathrm{V}$ figure 6.4 (a) shows the tunneling rates $\Gamma_{\mathrm{l}}$ (blue) and $\Gamma_{\mathrm{r}}$ (red). The rates were determined via equation 6.1. The filled circles are the average tunneling rates, whereas crosses correspond to the values obtained from the individual $3\,\mathrm{min}$ time traces. For the most positive voltages, the DQD is almost exclusively in the $(1,0)$-state, for the most negative voltages, the DQD is almost exclusively in the $(0,1)$-state. In the intermediate regime $-0.72\,\mathrm{V} \gtrsim V_{\mathrm{Tg2}} \gtrsim -0.74\,\mathrm{V}$,
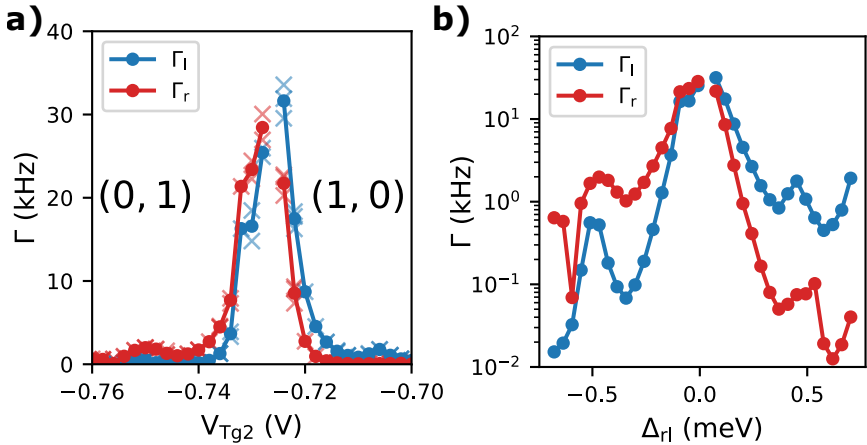
**Figure 6.4.: (a)** Tunneling rates $\Gamma_l$ and $\Gamma_r$ of a single electron tunneling back and forth inside an isolated DQD as function of the gate voltage $V_{Tg2}$. The gate voltage shifts the energy levels of the QDs relative to each other. Since the tunnel coupling is the same for both directions, the tunneling rates only depend on the detuning of the energy levels. Both rates thus increase and decrease symmetrically when crossing the resonance, resulting in two strongly overlapping peaks. The small offset between the peaks resembles one level being energetically more favorable, except for the exact resonance condition in the center of the peak. Due to the tunneling rates being of the order of the detector bandwidth, the tunneling rates in the center could not be determined. **(b)** Same as in (a) but in logarithmic scale with the gate voltage converted into energy via the detailed balance condition.

a peak is observed for both rates. The value for $V_{Tg2} = -0.726\,\text{V}$ is missing. For this voltage, the tunneling rates are too close to the detector bandwidth, so that the two levels can not be distinguished in the detector current histogram. Thus, the detection algorithm could not be applied.

The overall behavior of the tunneling rates as function of $V_{Tg2}$ is in strong contrast to the behavior observed for a single quantum dot. Tunneling into and out of a single quantum dot probes the occupied and unoccupied states of the electron reservoirs, respectively, and thus typically resolves the Fermi distributions in the reservoirs [56, 86, 87, 172]. In contrast, the single electron in the coupled DQD forms a bonding and an antibonding state and the transition rates are defined by the interdot tunnel coupling strength $t_{23}$ and the energy level detuning $\Delta_{23}$. Within the small range of gate voltage $V_{Tg2}$ shown in figure 6.4 (a) the tunnel coupling strength can safely be assumed to be constant. In addition, a rough estimate of $t_{23}$ can be given by estimating the tunneling rates at zero detuning. Assuming a tunneling rate of $\Gamma = 100\,\text{kHz}$ the coupling strength becomes $t_{23} = h\Gamma \approx 0.4\,\text{neV}$. In contrast, the stepsize $\Delta V_{Tg2} = 2\,\text{mV}$ between the datapoints results in a detuning of $\Delta_{23} = \alpha e \Delta V_{Tg2} \approx 60\,\mu\text{eV}$. The dominant contribution in the gate voltage dependence is thus the detuning between the energy levels. The fact that the detuning is a relative quantity between the energy levels already explains the similar behavior of the rates $\Gamma_l$ and $\Gamma_r$ as function of the voltage, with both rates showing a similar peak around the resonance condition. In contrast, probing the Fermi distribution of a reservoir with a single quantum dot leads to an opposite behavior of the rates as function of gate voltage. The tunneling rate into the quantum dot is proportional to the occupied states in the reservoirs, whereas the tunneling rate out of the quantum dot is proportional to the unoccupied states, so that when one rate increases, the other rate decreases.

For a single electron isolated in the DQD, the ratio of two rates $\Gamma_l$ and $\Gamma_r$ directly resembles the ratio of the occupation probabilities of the two

QDs. This ratio of the occupation probabilities is the Boltzmann factor, so that

$$\frac{p_l}{p_r} = \frac{\Gamma_l}{\Gamma_r} = \exp\left(\frac{\epsilon_r - \epsilon_l}{k_B T}\right) = \exp\left(\frac{\Delta_{rl}}{k_B T}\right), \qquad (6.5)$$

where $p_{l(r)}$ is the probability to find the electron in the left (right) QD, $\epsilon_{l(r)}$ is the energy of the left (right) level, $k_B$ is the Boltzmann constant, $T$ is the temperature, and $\Delta_{rl}$ is the energy detuning between the two levels.

With the given temperature $T = 1.5\,\mathrm{K}$ and the experimentally determined rates $\Gamma_l$ and $\Gamma_r$ in the regime around the resonance, equation 6.5 can be used to convert the gate voltage into energy detuning $\Delta_{rl}$.

For the gate voltage range $-0.72\,\mathrm{V} \gtrsim V_{Tg2} \gtrsim -0.74\,\mathrm{V}$, the detuning $\Delta_{rl} = \log(\frac{\Gamma_l}{\Gamma_r})k_B T$ changes linearly and fitting yields a lever arm of $V_{Tg2}$ on the detuning $\Delta_{rl}$ of $\alpha_{Tg2,\Delta_{rl}} = 0.021$. Using this lever arm, figure 6.4 (b) shows the rates $\Gamma_l$ and $\Gamma_r$ in logarithmic scale as function of the detuning $\Delta_{rl}$. The mirror symmetry of the central peak around $\Delta_{rl} = 0$ nicely underlines the relative quantity $\Delta_{rl}$ to be the main tuning parameter for the two rates.

In addition to the main peak around $\Delta_{rl} = 0$, there are two smaller peaks found close to $\Delta_{rl} \approx \pm 0.5\,\mathrm{mV}$. Similar to the central peak, the two peaks are again observed in both rates, again indicating a mechanism that is based on the detuning. The energetic detuning $|\Delta_{rl}| \approx 0.5\,\mathrm{meV}$ is hereby of the expected order of the level spacing of the individual QDs, so that the side peaks could be due to transitions involving excited states.

In general, there are two possibilities how excited state transitions become observable. The first being a direct excitation of the electron inside the QD, leading to a finite population of the excited state. As long as the electron resides in the excited state, the excited state interacts with all available states of the other QD. The second possibility inversely relies on finite tunneling rates between the detuned QDs, for example due to inelastic tunneling or thermal occupation. As long as the electron resides

in the energetically unfavorable QD, excited states of the energetically favorable QD can be tunneled into.

Due to the charge detector bias of $V_{sd,qpc} = 0.5\,\text{mV}$, a finite population of the excited state via phonon excitation, as well as inelastic tunneling between the QDs is plausible. However, for the given temperature $T = 1.5\,\text{K}$ and detuning $\Delta_{rl} = 0.5\,\text{mV}$, the thermal occupation of the higher energy state, given by the Boltzmann factor, is $\frac{p_{high}}{p_{low}} \approx 2\,\%$, so that the origin of the side peaks cannot be clearly determined. With measuring the tunneling rates of the side peaks as function of the QPC bias voltage, the contribution of phonons emitted by the QPC could be determined. Temperature dependent measurements on the other hand directly affect the thermal occupation. Even though such measurements have not been performed, the presence of the side peak is a clear indicator for finite occupation of non-equilibrium charge configurations in the system. For a stability diagram of the isolated DQD, as discussed in section 5.1, the charge detector signal resolves the average occupation of the QDs, so that the here observed side peaks confirm the origin of the substructures in the charge reconfiguration lines in the low coupling regime being due to finite population of excited charge configurations.

## 6.3. Two Electrons in a Double Quantum Dot

With using a slightly different loading procedure, two electrons can be loaded into the isolated DQD. With an additional electron present in the system, interaction between the electrons can become relevant. In the following, the two-electron tunneling dynamics will be analyzed using time-resolved charge detection close to the degeneracy between the $(2, 0)$ and the $(1, 1)$ charge states. Figure 6.5 (a) and (b) each show a $50\,\text{ms}$ time intervals of the detector current $I_{qpc}$ for two different values of $V_{Tg2}$. Converting the gate voltage difference into a detuning difference, via the lever arm $\alpha_{Tg2,\Delta_{rl}} = 0.021$ determined for the single electron, the situ-

ation shown in (a) is $\Delta_{rl} \approx 25 \, \mu eV$ further away from the $(2,0)$ - $(1,1)$ degeneracy. An absolute detuning can not be provided, since the tunneling rates at the resonance again exceed the detector bandwidth, and thus can not be determined.
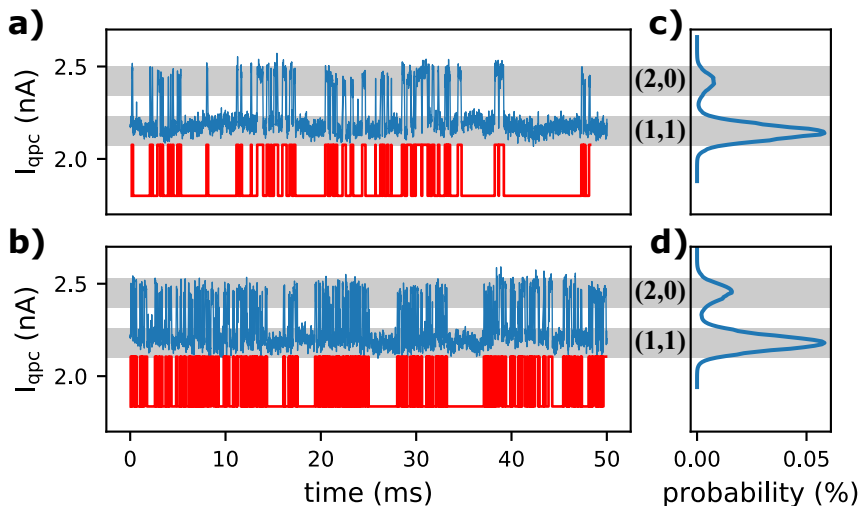


**Figure 6.5.: (a, b)** Time-resolved charge detector current $I_{qpc}$ for two situations close to the $(2,0)$ - $(1,1)$ degeneracy. The detuning between the two QDs is reduced by $\Delta_{rl} \approx 25 \, \mu eV$ from (a) to (b), leading to larger tunneling rates for (b). Clustering of the tunneling events occurs, and longer intervals without events can occur when the system is in the $(1,1)$-state. The digitized signal is shown in red, offset for clarity. **(c, d)** Detector current histograms corresponding to (a) and (b), respectively. Both show two peaks, corresponding to two charge states of the DQD. The lower current state corresponds to the $(1,1)$ configuration, the higher current to the $(2,0)$ configuration, respectively.

The two panels (c) and (d) in figure 6.5 show the detector current $I_{qpc}$ histograms corresponding to (a) and (b), respectively, over the entire $3 \, min$ time traces. Both show clearly a two-level system, so that a detection algorithm very similar to the single electron case is applicable. The lower current state, corresponding to more negative potential at the

charge detector, can be assigned to the $(1, 1)$ state, since the detector is located below the right QD. A digitized version of the two time traces obtained by the detection algorithm is shown in (a) and (b) in red. The detected tunneling events well reproduce the switching between the two states.

Many tunneling events are present in the two time intervals shown in figure 6.5 (a) and (b). However, with considerably more events and thus larger tunneling rates in (b), where the actual resonance condition is energetically closer. For both cases, but much more noticeable for the larger tunneling rates, there are several long time intervals without any events separating clusters of fast back and forth tunneling, an indication for competing processes acting on different timescales being relevant in the system.

Information about the underlying rates can be obtained from the residence times, which are the time intervals between successive events. In case of two competing rates, using equation 6.1 to determine the tunneling rates via the inverse of the average residence times is not valid anymore. However, information about the rates can still be obtained via the residence time distribution $\rho(\tau)$. Figure 6.6 shows the experimentally obtained probability distribution of the residence times $\rho(\tau_{lr})$ in red and $\rho(\tau_{rl})$ in blue for the two situations shown before. Panels (a) and (b) again correspond to more and less detuned from the $(2, 0)$-$(1, 1)$ degeneracy, respectively. The residence time $\tau_{lr}$ corresponds to tunneling from the left QD to the right QD, i.e. to transitions $(2, 0) \rightarrow (1, 1)$. Vice versa, $\tau_{rl}$ corresponds to tunneling from the right QD to the left QD, i.e. to transitions $(1, 1) \rightarrow (2, 0)$.

For the two detuning configurations, the residence time distributions are quite similar. However, the distributions for the two tunneling directions are significantly different. For tunneling to the right, both distributions $\rho(\tau_{lr})$ are straight lines in the logarithmic scale, the same as observed in the single electron case, showing that the process is deter-
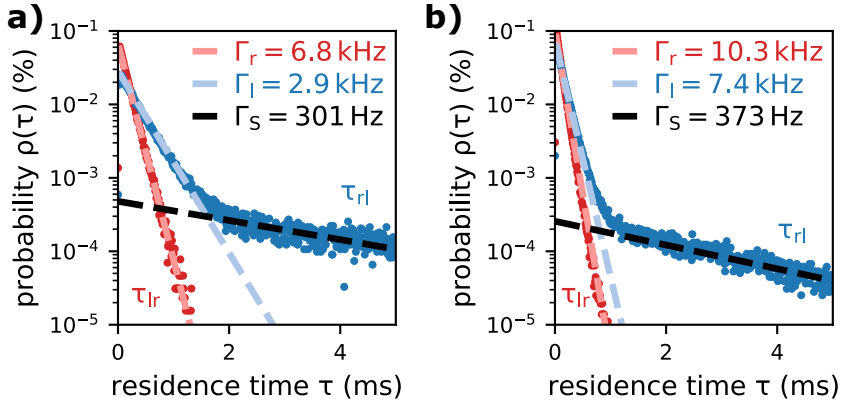
**Figure 6.6.:** Probability distribution of the residence times $\tau_{lr}$ (red) for tunneling to the right QD and $\tau_{rl}$ (blue) for tunneling into the left QD for **(a)** further away from and **(b)** closer to the degeneracy between the $(2, 0)$ and $(1, 1)$ charge states. The tunneling times $\tau_{rl}$ from the $(1, 1)$ into the $(2, 0)$ state indicate the presence of two competing rates. The rates are fit individually with fits provided by the dashed lines. Due to spin-flips, the two-electron DQD can be spin blocked in the $(1, 1)$ configuration. The slow rates $\Gamma_S$ are the rate with which the blockade is lifted, i.e the spin-flip rates in the system.

mined by a single rate parameter. By fitting the distribution using equation 6.3, the underlying tunneling rates from left to right are determined to $\Gamma_r = 6.8\,\text{kHz}$ and $\Gamma_r = 10.3\,\text{kHz}$, the corresponding fits are given by the orange dashed lines in figure 6.6 (a) and (b).

In contrast, the distributions $\rho(\tau_{rl})$ for tunneling to the left do not show straight lines but start with a large slope at short times $\tau$ decreasing toward longer times $\tau$. However, for both the shortest times as well as the longest times, $\rho(\tau_{rl})$ is well described by a straight line. Only for intermediate times, i.e. in the regime, where the two straight lines would intersect, a significant curvature is found. Both, the short times as well as the long times thus follow an exponential decay with a single exponent. By separating the two regimes and fitting them individually, the two corresponding rates can be determined. For the two configurations discussed here, the fast rates are given by $\Gamma_l = 2.9\,\text{kHz}$ and $\Gamma_l = 7.4\,\text{kHz}$, the corresponding fits are given by the blue dashed lines. The same procedure for the slower rates yields $\Gamma_S = 301\,\text{Hz}$ and $\Gamma_S = 373\,\text{Hz}$ with fits given by the black dashed lines.

The fact that two regimes exist, each following an individual rate dependence, shows clearly, that these are competing processes. For independent processes starting from the same level, fast events of one process prevent the occurrence of slow processes of the other, so that the individual dependencies mask each other and combine into a single but faster rate dependence of the events.

For the here presented case, the tunneling from the $(2, 0)$ into the $(1, 1)$ state is determined by a single rate, the tunneling rate $\Gamma_r$. For tunneling from the $(1, 1)$ into the $(2, 0)$ state, two competing processes are present, a fast process with rate $\Gamma_l$ and a slow process with rate $\Gamma_S$. This can be understood by taking the spin blockade in quantum dots and spin flips into account [173]. With two electrons occupying the left quantum dot, the right quantum dot is empty and tunneling is always possible, leading to a single rate $\Gamma_r$ observed for tunneling from the left QD to the right

QD. However, in the $(1, 1)$ configuration, spin conserving tunneling into the ground state is only possible if the two spins are aligned anti-parallel. In case a spin flip occurs, either due to spin flip tunneling or due to a spin flip in the $(1, 1)$ configuration, tunneling back into the into the $(2, 0)$ ground state is spin blocked. As long as the triplet state is energetically not accessible for tunneling, tunneling back into the $(2, 0)$ state is blocked until another spin flip occurs. The slow rates $\Gamma_S$, which are blocking the faster events, are thus the spin flip rates of the system.

## 6.4. Three Electrons in a Double Quantum Dot

This part will discuss time-resolved charge detection with three electrons trapped inside an isolated double quantum dot and around the degeneracy of the $(3, 0)$ and $(2, 1)$ charge states. A naive expectation for this system is sketched in figure 6.7 (a). In an energetic situation close to the $(3, 0)$ and $(2, 1)$ degeneracy, two electrons are expected to always remain in the left QD. The box containing the up and down arrow depicts these two electrons occupying the two spin configurations of the lowest energy level of the QD. The third electron is then unpaired on the next energy level, and in resonance with the lowest level of the right quantum dot. Since the lowest energy level of the left QD is much lower in energy, these electrons are not expected to tunnel.

In such an idealized situation, looking at a time resolved charge detector signal, the behavior would be very similar to the one observed for the single electron case, since only one of the three electrons in the DQD has an energetically accessible state to tunnel into. Surprisingly, the histogram of a $500\,\text{s}$ long time-resolved measurement of the charge detector current $I_{qpc}$, as shown in figure 6.7 (b), reveals a much more complex level structure with multiple peaks. The purple dotted line is a 50 times magnification of the blue curve. In total, there are eight different peaks (L0 - L7) with different weightings found in the histogram, correspond-
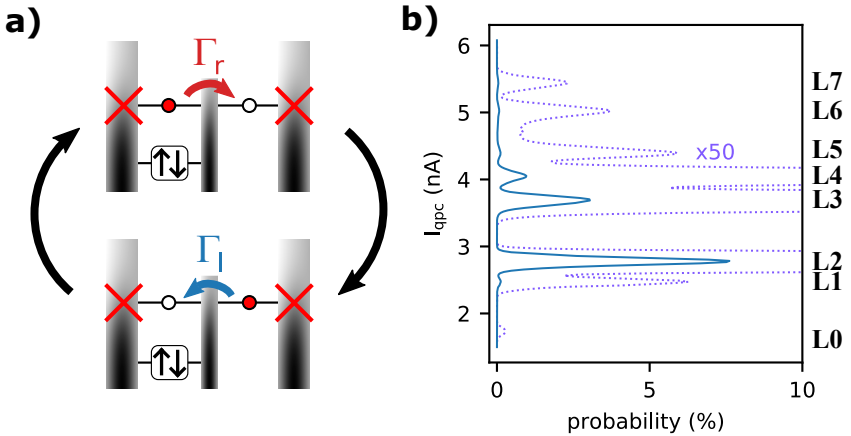
**Figure 6.7.: (a)** Energy level schematic of the expected configuration of an isolated DQD loaded with three electrons at the $(3,0)$-$(2,1)$ degeneracy. Two electrons with opposite spins, indicated by the arrows, populate the lowest energy level of the left QD. The third electron can tunnel back and forth between a higher state of the left QD and the ground state of the right QD. **(b)** Histogram of a time-resolved detector current measurement close to the $(3,0)$-$(2,1)$ degeneracy (blue). The purple dotted line is a 50x magnification of the histogram. A total of eight peaks are observed in the histogram, corresponding to eight different charge configurations seen by the charge detector. Due to the presence of more than two charge distributions, the transition behavior clearly deviates from the simple model shown in (a).

ing to eight different potential distributions seen by the charge detector, in clear contrast to the naive expectation of a two level system. A smaller detector current $I_{qpc}$ hereby correspond to a more negative potential at the detector, i.e. electrons being closer to the detector, which is located below the right QD3.

Even though the observed histogram is not only a two level system, a post-processing algorithm very similar to the single electron case can be used to digitize that data. A current interval is assigned to each of the peaks and each measured current value inside one of the intervals is assigned to the respective level. Points lying in none of the intervals are assigned to the last known state. The algorithm yields the level and the timing of each transition out of this level, the values necessary for a full reconstruction of the time trace. Due to considerable overlap between some of the neighboring peaks, a combination of averaging and small level intervals has been used to minimize the detection of noise induced false events but at the cost of increasing the probability to miss fast events.

A $\Delta t = 1\,$s time window of a detector current time trace at reference time $t_0 = 0$ is shown in blue in figure 6.8 (a). The reference time $t_0 = 0$ is set at the beginning of a time-resolved measurement, directly after initializing the system by loading three electrons, transferring the DQD into the isolated configuration, and moving to the $(3, 0)$-$(2, 1)$ degeneracy line. The corresponding digitized signal obtained from the detection algorithm is shown in red (offset for clarity). Similar to the single electron case, switching events between different states are observed in the time-resolved detector current. However, the current does not switch back and forth between two states, but between multiple levels, as already indicated by the number of peaks observed in the current histogram. Nevertheless, the digitized signal obtained by the detection algorithm shows a good agreement with the measured time trace.

The $1\,$s time window shown in figure 6.8 (b) is part of the same time trace as shown in (a), but starting at time $t_0 = 10\,$s. As before, the cur-
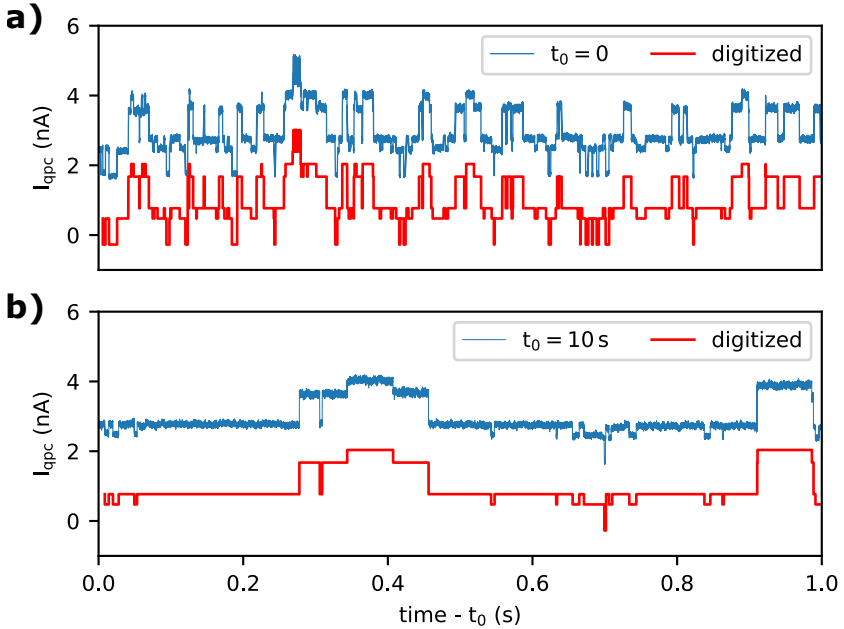
**Figure 6.8.: (a)** $\Delta t = 1\,\text{s}$ time window of a detector current time trace (blue) at time $t_0 = 0$, directly after the initialization of the DQD by loading three electrons, isolating the DQD from the reservoirs, and moving to the $(3,0) - (2,1)$ degeneracy. A post processing detection algorithm was used to assign the current values to a total of eight different levels and thereby determine the time intervals $\tau$ the system resides in each level. The digitized version of the time trace is shown in red and shows a good agreement with the experimental data. **(b)** Same as in (a) but for $t_0 = 10\,\text{s}$ after starting the data acquisition. The number of transitions observed for the same time interval of $\Delta t = 1$ s is drastically lower, an indication for the occurrence of relaxation in the system.

rent jumps between different levels and the digitized signal nicely reproduces the measured signal. However, the time intervals between successive events are larger and thus the number of events in the same time interval is smaller. Since tunneling events are distributed statistically for a fixed tunneling rate, this observation could be due to statistical extreme values for the given time windows. However, there is an initialization process happening before the time $t_0 = 0$ (a) but not before $t_0 = 10\,\text{s}$ (b), so that the initial conditions are not identical, and the possibility of time dependent switching rates $\Gamma_{ij}(t)$ between level $i$ and level $j$ has to be taken into account.

In the latter case, the absolute time dependence of the system parameters has to be taken into account for the statistical analysis. Single quantum dots with time-dependent tunneling rates have been discussed under periodic manipulation of the tunneling rates in [99, 164, 174], and based on the real-time analysis of short time intervals, a stabilization of the single electron tunneling process was achieved by manipulating the tunneling rates in a closed-loop feedback control [99, 165, 175]. In a similar way, the time dependency of the here presented system will in the following be characterized by analyzing and comparing short time intervals of the full time traces.

To achieve a better basis for the statistical analysis, the time-resolved measurement was repeated three times under the same conditions, each time beginning with an initialization procedure and thereafter measuring the detector current $I_{qpc}$ for $500\,\text{s}$. As a first step, the time traces are divided into intervals of $\Delta t = 5\,\text{s}$ and the total occupation time of each state within each time interval is calculated. For the levels L1 - L4, the occupation times are shown in figure 6.9 as function of time $t_0$ after starting the time-resolved measurement. The remaining levels L0, L5, L6, and L7 are not shown, since their combined total occupation sums up to less than 5%.

Colored dots are the occupation values for the individual time traces,
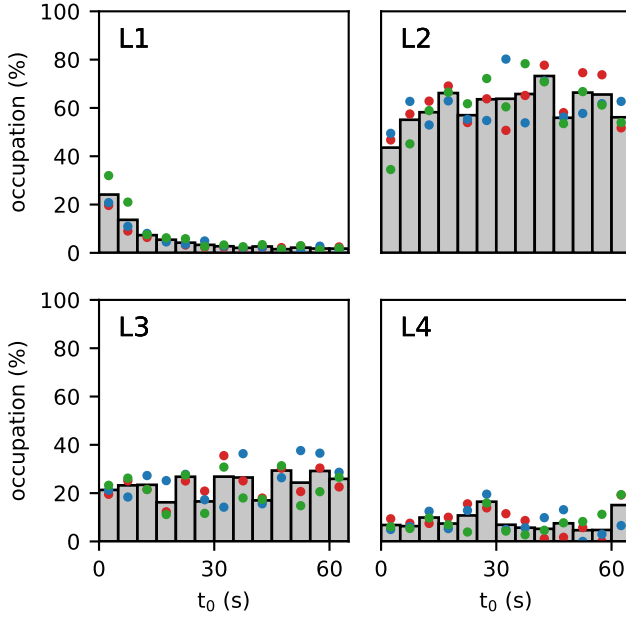
**Figure 6.9.:** Occupation probability of the levels L1 - L4 evaluated for time intervals of $\Delta t = 5\,$s and shown as function of time distance $t_0$ to the beginning of the measurements directly after the initialization procedure. The colored dots correspond to three individual time traces measured under the same conditions. The grey bars are an average over the individual time traces. The occupation probability of L1 decays with increasing $t_0$, whereas the occupation of L2 increases for approximately the same amount, indicating an excitation process driving the transition from L2 to L1 that relaxes over time. The occupation probability of both levels L3 and L4 stays approximately constant as function of $t_0$.

the gray bars are the average over the individual time traces, the errorbars show the standard deviation. Although the values of the individual traces scatter due to the small data basis for each datapoint, there is a clear tendency observable for all four levels. Averaging over the three time traces results in a more or less smooth behavior of the occupation for all levels. While the occupation of the levels L3 and L4 are approximately independent of the absolute time, level L1 is occupied about $21.0\% \pm 5.1\%$ of the time at the beginning of the time-resolved measurement ($t_0 = 0$), which decreases to less than 5% until $t_0 = 30$ s. The opposite trend is observed for L2, where the occupation at $t_0 = 0$ is $44.5\% \pm 2.2\%$ and increases to above 60% until $t_0 = 30$ s. The sum of the occupation of the two levels L1 and L2 is thus approximately constant. This indicates the presence of a decaying excitation process driving the transition from L2 to L1.

Such an excitation could be a reason for a time dependence of the transitions between L1 and L2. However, the two parts of the time trace in figure 6.8 show many and fast events between all levels at the beginning of the time-resolved measurement ($t_0 = 0$) compared to the much less and slower transitions at $t_0 = 10$ s. This behavior rather implies a time dependency of the overall system than only of an individual transition.

This time dependence however becomes clearly observable in the switching characteristics. For the two transitions L2 $\rightarrow$ L3 and L2 $\rightarrow$ L1, figure 6.10 (a) shows the inverse of the mean residence times $1/ < \tau_{23} >$ and $1/ < \tau_{21} >$ as function of time $t_0$ after starting the time-resolved measurement. The residence time $\tau_{ij}$ hereby is the time interval between entering the state L$i$ and leaving into state L$j$. The dots show the values obtained from the individual time traces, the lines are the average over the three traces. Each datapoint is evaluated over a time interval $\Delta t = 5$ s and assigned to the value $t_0$ centered in the interval.

For the smallest value $t_0 = 2.5$ s the two rates are of the order of $\Gamma = 100$ Hz, sharply dropping with increasing time, and with both curves following the same baseline. The latter is an effect of the shared initial
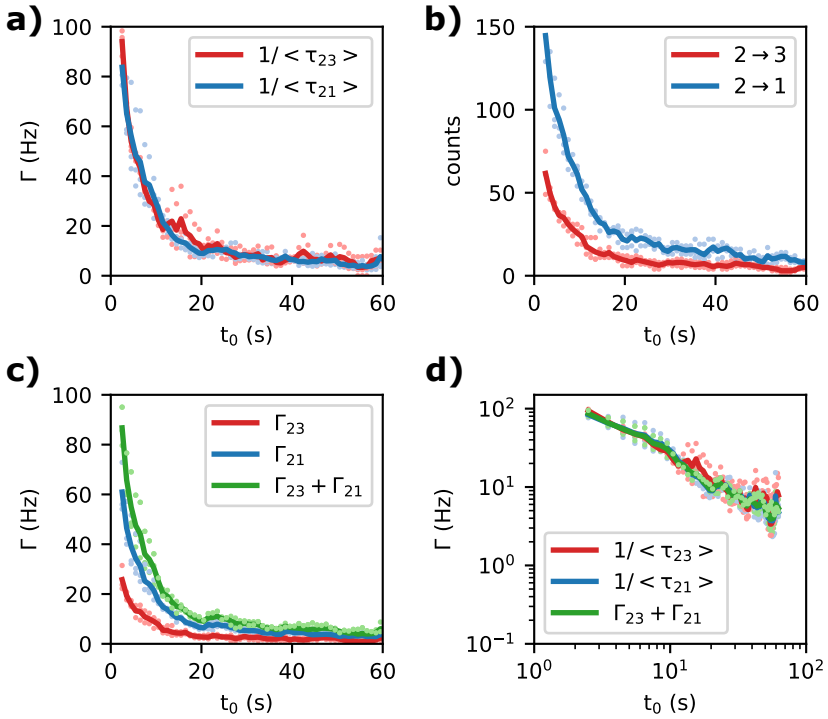
**Figure 6.10.:** Determination of the time dependent switching rates from L2 to the neighboring L1 and L3 as function of the time distance $t_0$ to the beginning of the time-resolved measurements by analyzing time windows of $\Delta t = 5$ s. **(a)** Switching rates $1/<\tau_{23}>$ from L2 to L3 and $1/<\tau_{21}>$ from L2 to L1 calculated from the average residence times. Due to the shared initial state the residence times for the two possible switching directions follow the same statistics and thus the same time dependency. **(b)** In contrast number of events for the two possible transitions differs. **(c)** The switching rates of the individual processes are given by the observed transitions (counts) per time spent in the initial state L2. **(d)** The rates shown in (a) and additionally the sum of the individual switching rates $\Gamma_{23} + \Gamma_{12}$ (green) in log-log scale. The sum of the individual rates determines the statistics for the observed residence times. The approximately linear behavior with slope $-1$ implies a $t_0^{-1}$ dependency for the tunneling rates.

state L2. Observing an event $\tau_{23}$ requires that no event into L1 has occurred before. Thus, every observed residence time $\tau_{23}$ prevents the observation of a longer residence time $\tau_{21}$, and vice versa. The waiting times $\tau_{23}$ and $\tau_{21}$ are thus not independent, but follow a shared distribution. This also directly implies that the rates $1/<\tau_{23}>$ and $1/<\tau_{21}>$ are not equal to the individual switching rates $\Gamma_{23}$ and $\Gamma_{21}$.

In contrast, for the number of transitions observed within the same time intervals, shown in figure 6.10 (b), the result differs for the two transitions. The dots again are the values obtained from the individual time traces, the lines are averaged over the traces. Again, both transitions show a strong $t_0$ dependency with a high number of counts per time interval $\Delta t = 5\,\mathrm{s}$ at small $t_0$, and them dropping fast with more distance to the start of the time-resolved measurement. The number of events is, however, greater for the L2 → L1 transition compared to the L2 → L3 transition. The state L2 thus favors switching into L1, implying that $\Gamma_{21} > \Gamma_{23}$. The ratio of the counts hereby equals the ratio of the individual switching rates.

The switching rates define the number of switching events expected per second. Thus, they can be estimated by dividing the number of transitions observed within a time interval $\Delta t$ by the total time spent in the initial state L2 during the same time interval. The number of transitions has to be compared to the lifetime of the state rather than to the total time interval, since the respective transitions can only occur while the system is in state L2. The individual switching rates $\Gamma_{23}$ (red) and $\Gamma_{21}$ (blue) calculated this way are shown in figure 6.10 (c). In addition, the green curve shows the sum of the two switching rates $\Gamma_{23} + \Gamma_{21}$, which can be seen as the decay rate of L2. This decay rate defines the two rates obtained from the observed residence times $<\tau_{ij}>$ in (a). The fact that the occupation of L2 is not constant over time but increases for small $t_0$, as shown earlier in figure 6.9, does not affect the qualitative behavior of the switching rates $\Gamma_{23}$ and $\Gamma_{21}$ compared to the number of counts, but only results in a

slightly smaller slope observed at small $t_0$.

Figure 6.10 (d) shows the same data as in (a) but in log-log scale and additionally the sum of the individual switching rates $\Gamma_{23} + \Gamma_{21}$ is shown in green. The similarity between the three curves clearly underlines that the residence time statistics is determined by the sum of the two switching rates. Additionally, the approximately linear behavior in the log-log plot indicates a power law dependence of the rates as function of $t_0$ with $\Gamma \propto t_0^{-1}$.

The discussed procedure of calculating the individual switching rates via the number of observed transitions divided by the lifetime of the state can now be used to also determine other switching rates of the system. However, for some of the individual transitions, the lifetimes of the initial state as well as the number of events is small or even zero for most of the $\Delta t = 5\,\mathrm{s}$ time windows, so that this procedure for determining the tunneling rates as function of $t_0$ is not applicable. For the six transitions providing a suitable data basis, these switching rates are shown as dots in figure 6.11 in (a) linear scale and (b) log-log scale.

Additionally, for each rate except $\Gamma_{12}$, which does not show a clear time dependency, the data was fit using the empirical formula

$$\Gamma(t_0) = c + \frac{1}{at_0 + b} \tag{6.6}$$

with fitting parameters $a$, $b$, and $c$. The corresponding fits are shown as black dashed lines in figure 6.11 and describe the observed time dependency of the switching rates reasonably well, clearly underlining the presence of a $1/t_0$ decay in the system. The obtained fitting parameters $a_{ij}$, $b_{ij}$, and $c_{ij}$ for transitions $Li \rightarrow Lj$ are given in table 6.1. The parameter $a$ hereby scales the timescale of the decay, parameter $b$ prevents divergence at $t_0 = 0$, and parameter $c$ can be interpreted as the equilibrium switching rate, since $\lim\limits_{t_0 \to \infty} \Gamma_{ij}(t_0) = c$.

Interestingly, the fits yield $c_{ij} = 0$ for all switching rates except $\Gamma_{43}$,
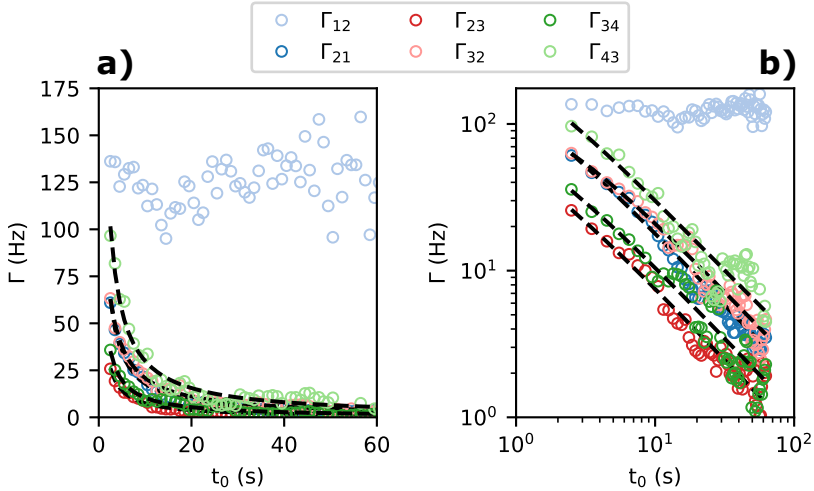
**Figure 6.11.:** Switching rates $\Gamma_{ij}$ as function of $t_0$ for transitions from L$i$ to L$j$ in **(a)** linear scale and **(b)** log-log scale. The lowest level L0 and the higher levels L5-L7, are only rarely occupied, so that the transitions involving these levels are not evaluated due to a lack of information for most of the times $t_0$. All transition rates, except $\Gamma_{12}$ show a pronounced time dependency with larger rates close to the beginning of the measurement at $t_0 = 0$. The black dashed lines are fits to each switching rate individually via $\Gamma(t) = c + \frac{1}{at+b}$. The good agreement between data and fits clearly underlines a $1/t$ time dependency. The rate $\Gamma_{12}$ on the other hand does not show a clear time dependency. In combination with $\Gamma_{21}$ decreasing over time, this explains the correlation between the occupation times of L1 and L2.

where, however, the fitting error is greater than $c_{43}$. One the one hand, the vanishing $c_{ij}$ could be an artifact due to the small data basis for large $t_0$, where the number of events within a time interval $\Delta t = 5$ s becomes small for all transitions. On the other hand, from the electrostatics point of view switching is only expected to occur between two charge states, $(3, 0)$ and $(2, 1)$. It is thus plausible, that most of the transitions are observed only due to excitation during the initialization procedure and disappear on longer timescales due to relaxation of the system.

|  | $a_{ij}$ | $b_{ij}$ (s) | $c_{ij}$ (Hz) |
|---|---|---|---|
| $\Gamma 21$ | $5.34 \cdot 10^{-3}$ | $2.55 \cdot 10^{-3}$ | $0$ |
| $\Gamma 23$ | $12.67 \cdot 10^{-3}$ | $6.64 \cdot 10^{-3}$ | $0$ |
| $\Gamma 32$ | $4.26 \cdot 10^{-3}$ | $5.23 \cdot 10^{-3}$ | $0$ |
| $\Gamma 34$ | $8.99 \cdot 10^{-3}$ | $5.91 \cdot 10^{-3}$ | $0$ |
| $\Gamma 43$ | $3.17 \cdot 10^{-3}$ | $1.93 \cdot 10^{-3}$ | $276 \cdot 10^{-3}$ |

**Table 6.1.:** Fit parameters a, b, and c obtained for fitting $\Gamma_{ij}(t) = c + \frac{1}{at+b}$.

For the other two parameters $a_{ij}$ and $b_{ij}$ the values fluctuate between the individual rates but are of the same order of magnitude with $a_{max}/a_{min} \approx 4$ and $b_{max}/b_{min} \approx 3.5$. Hereby, $a_{max} = a_{23}$ and $a_{min} = a_{43}$. As can be seen in figure 6.11, these are the two transitions with the overall smallest transition rate $\Gamma_{23}$ (red circles) and the overall highest transition rate $\Gamma_{43}$ (light green circles). This provides an indication on a dependency between the scaling parameter $a_{ij}$ and the observed switching rates $\Gamma_{ij}$.

Normalizing the rates determined from the time traces on the value obtained for the first time interval $0 \leqslant t_0 \leqslant 5$ s (datapoint at $t_0 = 2.5$ s), the time dependencies of the individual rates become similar. Figure 6.12 shows the normalized rates $\Gamma/\Gamma_0$ with $\Gamma_0 = \Gamma_{|t_0=2.5\,s}$ in (a) normal scale and (b) log-log scale. Except for $\Gamma_{12}$, which does not show a significant time dependence, all other normalized rates collapse onto a single curve.

For larger times $t_0$ the fluctuations hereby increase due to the number of events per time interval becoming small. Apart from the fluctuations, all normalized rates show an almost identical behavior as function of $t_0$.
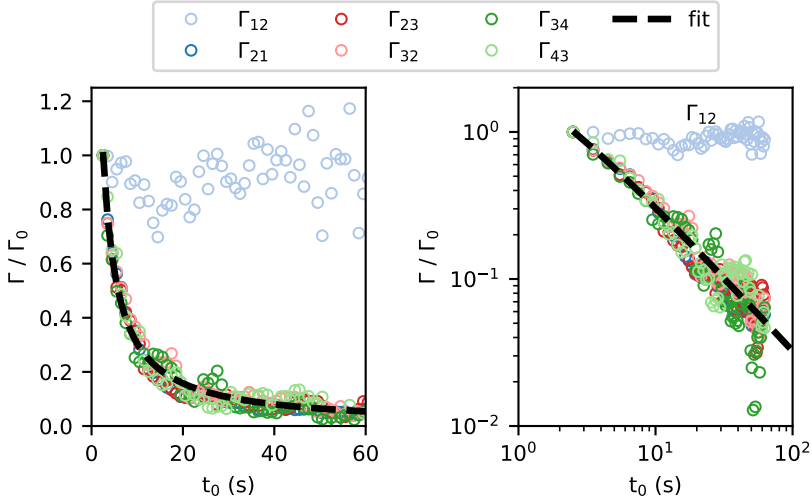


**Figure 6.12.:** Tunneling rates $\Gamma_{ij}$ relative to the value at $t_0 = 2.5\,\text{s}$. All rates except $\Gamma_{12}$ show a $1/t$ time dependency and collapse on a single curve. A global fit to all rates except $\Gamma_{12}$ via $\Gamma(t) = c + \frac{1}{at+b}$ yields parameters $a = 0.306\,\text{Hz}$, $b = 0.228$, and $c = 0$.

The collapse of all time dependent rates on a single curve allows to fit the rates globally instead of individually. The global fit via equation 6.6 hereby yields $a = 0.306\,\text{Hz}$, $b = 0.222$, and $c \approx 0$. The values $a$ and $b$ obtained from the global fit after the normalization are large compared to the ones for the individual rates. However, using the parameters $a_{ij}$ and $b_{ij}$ obtained by fitting the rates individually (table 6.1) and multiplying them by the normalization coefficient $\Gamma_{0,ij}$ of the respective transitions shows $a \approx a_{ij}\Gamma_{0,ij}$ and $b \approx b_{ij}\Gamma_{0,ij}$. Hereby, $a_{ij}\Gamma_{0,ij} = 0.310\,\text{Hz} \pm 0.021$ and $b_{ij}\Gamma_{0,ij} = 0.211 \pm 0.062$ (mean $\pm$ standard deviation).

Over all, the normalized rates can be described by the same $1/t_0$ de-

cay, an indication for a single shared relaxation parameter in the system. Unfortunately, the origin of this $1/t_0$ decay cannot be conclusively determined at this point. However, the shared relaxation parameter implies a likewise shared excitation parameter. Combined with the $1/t_0$ decay, this points toward a two-dimensional diffusion process. With (isotropic) diffusion coefficient $D$ and concentration $U$, the two-dimensional diffusion equation is given by

$$\frac{\partial^2 U}{\partial x^2} + \frac{\partial^2 U}{\partial y^2} = \frac{1}{D}\frac{\partial U}{\partial t}. \tag{6.7}$$

For an instantaneous point source, i.e., a concentration $U$, instantaneously released at time $t = 0$ at location $r = \sqrt{x^2 + y^2} = 0$, a solution for equation 6.7 is given by [176]

$$U = \frac{M}{4\pi Dt}\exp\left(\frac{-r^2}{4Dt}\right), \tag{6.8}$$

where $M$ is the total amount of diffusing substance. At the position of the point source $r = 0$, equation 6.8 simplifies to

$$U = \frac{M}{4\pi Dt} \propto \frac{1}{t}, \tag{6.9}$$

resulting in a $1/t$ dependency.

A candidate for a local source of non-equilibrium leading to diffusion would be Joule heating at the QPC due to the QPC current being larger during the initialization. The power $P = V_{sd,qpc} \cdot I_{qpc} \approx 0.5\,\mathrm{mV} \cdot 10\,\mathrm{nA} = 5\,\mathrm{pW}$ dissipated near the QPC during the initialization is approximately three times the power dissipated during the measurement. This can be considered as a heat source that is regulated down at the beginning of the time-resolved measurement so that a cooling process takes place. Indeed, for low temperatures, the heat capacitance of a 2DEG becomes very small [177], and a QPC operated at $P \approx 1.25\,\mathrm{pA}$ has

already been used for heating a 2DEG [178], however, at temperatures even smaller than the $T \approx 1.5\,\mathrm{K}$ present here.

Another possibility is a local excitation due to the gate voltage ramp used for the initialization. The gate voltage change was $\Delta V_{Tg2} \approx 0.5\,\mathrm{V}$ at a rate of $0.3\,\mathrm{V/s}$. The gate is located on the surface of the sample, while the 2DEG is located approximately $110\,\mathrm{nm}$ below the surface. In-between, there is the Si-$\delta$-doping layer, located $70\,\mathrm{nm}$ below the surface, consisting of positively charged donor atoms. Changing the gate voltage could locally modify the charge distribution, for example by injecting electrons due to gate leakage, which can then accumulate at the doping layer. This local non-equilibrium would then equilibrate via diffusion.

In any case, the $1/t_0$ dependency was only observed for the three electron system but not for the single or two electron case, where very similar initialization procedures were used. At the same time, also the number of charge configurations observed for the three electron case exceeds the number of possible distributions of the electrons inside the DQD. Even if taking large excitation energies into account and thereby allowing all possible configurations with three electrons, instead of only the $(3,0)$ and $(2,1)$ configurations, which are close to degenerate, only the four charge states $(3,0)$, $(2,1)$, $(1,2)$, and $(0,3)$ exist. However, there were eight levels present in the charge detector signal histogram, corresponding to eight different charge configurations.

Nevertheless, both scenarios could be the reason for the observed time dependency, since the three electron configuration qualitatively differs from the single and two electron case. While the first two electrons occupy the two spin configurations of the ground state of a quantum dot and thus have an s-type wave function, the third electron has to occupy the next higher level with a p-type wave function. In contrast to the s-type wave function, a p-type wave function is not centered in the QD and the position of the wave function maxima becomes sensitive to the shape and symmetry of the QD. The exact shape of the potential forming the

here discussed QDs is not known. However, due to the system being a DQD there is some initial asymmetry present. In the presence of fluctuations or deformations of the potential landscape, for example due to charge fluctuations in trap states near the QD, the shape and symmetry of the QD can change as function of time. Changing the shape of the QD can then effectively displace the charge within the quantum dot, which could change the potential at the QPC. For a p-type wave function, the length over which charges can be displaced is hereby significantly larger than for the s-type wave function, which is centered in the QD.

In summary, this chapter presented time-resolved single electron tunneling measurements on a single, two, and three electrons isolated in a double quantum dot. For the single electron case, a two-level system was observed, so that statistical analysis similar to a single quantum dot coupled to reservoirs was applicable. After an introduction into the processing of the time-resolved charge detector signal, the residence time and return time distributions were evaluated and the tunneling rates back and forth between the two QDs could be determined. A gate voltage was used to change the detuning between the QDs, showing a symmetric behavior of the two tunneling rates with both rates increasing toward smaller detunings. This symmetric behavior is a clear indicator for the relative quantity of the energetic detuning between the QDs being the tuning parameter for the rates. From the gate voltage dependence, the detailed balance approach allows to calculate the lever arms for a known temperature or vice versa.

With two electrons isolated in the DQD, similar switching between two charge states was observed. The waiting time distributions showed a single rate dependency for the $(2, 0) \rightarrow (1, 1)$ transition, and two competing rate dependencies for the $(1, 1) \rightarrow (2, 0)$ transition. For the latter transition, tunneling becomes spin-blocked after a spin-flip occurs, so that a second spin-flip is needed to lift the blockade. The tunneling rates and the spin-flip rate was extracted from the residence time distribution.

For three electrons isolated in the DQD close to the degeneracy of the $(3, 0)$ and $(2, 1)$ configurations, eight different charge states were observed in the time-resolved charge detector signal. Additionally, a significant time-dependency of the switching rates was observed. After introducing the procedure to extract the switching rates in a multi-level system, small time intervals were analyzed as function of the time $t_0$ after starting the time-resolved charge detection. A $1/t_0$ dependency was found for most of the switching rates. By normalizing the switching rates to their initial value $\Gamma_0$ at $t_0 = 0$, all time-dependent rates collapsed on a single curve, a clear signature of a shared relaxation process. The $1/t_0$ dependency hereby indicates a relaxation process based on a two-dimensional diffusion process.

# 7
# Summary

This thesis covers experimental approaches to characterize and control the electronic properties of quantum dot arrays. Arrays consisting of two to four tunnel coupled quantum dots were investigated using transport spectroscopy and successfully transferred into a configuration isolated from the electron reservoirs, where the number of electrons inside the quantum dot array is fixed. In the isolated configuration, a simplification of the parameter space and a high level of tunability of the interdot transitions, including long-range transitions between non-neighboring quantum dots, was demonstrated. The findings contribute to enabling and simplifying the tuning of coupled quantum dot systems for applications in quantum technologies.

The device used was based on a two-dimensional electron gas (2DEG) formed in a GaAs/AlGaAs heterostructure. Lithographically defined Ohmic contacts allowed to perform electronic transport measurements. A total of 13 gate electrodes on the surface of the heterostructure were used to electrostatically form and control the quantum dot arrays inside the 2DEG. The energy levels of the quantum dots, as well as the tunnel barriers, and thus the coupling parameters, were controlled by voltages applied to the gate electrodes. A quantum point contact (QPC), capacitively coupled to the quantum dots, was used as a charge detector. Tuning the QPC into the transition regime between two conductance plateaus, the QPC conductance becomes very sensitive to changes in the potential landscape. This high sensitivity was utilized to detect charging events

into and out of the quantum dot arrays, and to observe charge reconfigurations inside the arrays. Three different sizes of serially coupled quantum dot arrays were analyzed, the double quantum dot (DQD), triple quantum dot (TQD), and the quadruple quantum dot (QQD) array.

A combination of electronic transport measurements and charge detection was used to introduce the basic transport phenomena through the different array sizes and to extract electrostatic properties. For small bias voltages, the stability diagram of a DQD was introduced, the energetic extent of a TQD resonance in its three-dimensional energy space was determined, and a QQD resonance could be identified. For larger bias voltages, the characteristic bias triangles emerged in the DQD stability diagrams, showing finite current up to a detuning between the quantum dots equal to the energy window opened up by the applied bias voltage. Similar bias dependent structures, originating from resonances between two of the quantum dots, were analyzed for the TQD and showed additional substructures under asymmetric coupling conditions. Excited state resonances were identified as the origin of the substructures enabling excited states spectroscopy. Bias triangles originating from resonances between two center quantum dots were analyzed for the QQD. In the weak coupling regime, the linear dependence between detuning and applied bias could be confirmed, providing a characterization method directly in the QQD configuration instead of relying on single quantum dot characterizations with their strongly differing potential landscapes.

For all array sizes, a strong dependency of the transport characteristics on the coupling parameters was observed. In the weak coupling regime, transport through the quantum dot arrays was only observed close to resonances between all quantum dots. With increasing the coupling, finite current through the arrays also emerged for situations, where only one of the quantum dots was in resonance with the electron reservoirs. Finite current through serially coupled quantum dots with one or more of the quantum dots in Coulomb blockade shows that long-range tunneling

with an energetically detuned quantum dot in between is experimentally accessible in these systems. For the DQD system, this long-range tunneling was shown to depend in a non-monotonic way on the number of electrons in the off-resonant quantum dot, fitting well to changes in the coupling originating from a two-dimensional electronic shell structure.

By isolating the quantum dot arrays from the electron reservoirs, a framework was realized that allowed for a detailed analysis of the inter-dot transitions. While transport through the array is blocked in such isolated systems, the charge detector allows tracking of electrons transferred within the array. Complemented by capacitance model simulations, the example of the DQD was used to introduce the transfer to the isolated configuration and the arising pattern of charge reconfiguration lines. With two electrons isolated in the DQD, a high level of control over the inter-dot couplings was demonstrated, from a fully delocalized electron down to interdot tunneling rates of only a few Hz. For the isolated TQD, charge reconfiguration lines corresponding to three different interdot tunneling transitions have been found. The reconfiguration line pattern was only reproduced in the capacitance model simulations by allowing long-range transitions directly between the non-neighboring quantum dots. It was shown experimentally that the number of electrons loaded into the array before isolation can be controlled. With a single electron isolated in the TQD, it was successfully demonstrated that long-range transfer can be suppressed by reducing the interdot coupling. The ability to control the strength of the long-range coupling between the non-neighboring quantum dots was demonstrated with two electrons isolated in the TQD. Signatures indicating the experimental presence of long-range transitions across two intermediate quantum dots have been found for the isolated QQD array.

The tunneling dynamics inside an isolated quantum dot array were analyzed on the basis of a DQD by detecting tunneling events in a time-resolved manner. With a single electron isolated in the DQD, back and

forth tunneling between the two quantum dots could be detected over timescales of minutes and the time intervals between the tunneling events were analyzed statistically. The tunneling rates were controllable by the detuning between the quantum dots. For two electrons isolated in the DQD, two competing rates were observed due to spin-flips leaving the system in spin blockade and the spin-flip rate could be determined. A qualitatively different switching behavior was observed for three electrons loaded into the DQD. Multiple charge states were detected by the charge sensor and time dependent switching rates were observed and analyzed. The rates showed a decreasing behavior with temporal distance from the loading procedure, fitting to an excitation during the loading procedure and relaxation based on a two-dimensional diffusion process.

Overall, the operation of quantum dot arrays in the regime isolated from the electron reservoirs has been shown to be beneficial. Decoupling from the electron reservoirs simplifies the energy space of the array and increases the energy distance between different charge states while providing a high degree of tunability over the interdot tunneling, including long-range tunneling between non-neighboring quantum dots.

# A

# Appendix

## Complementary Data

### Double Quantum Dot
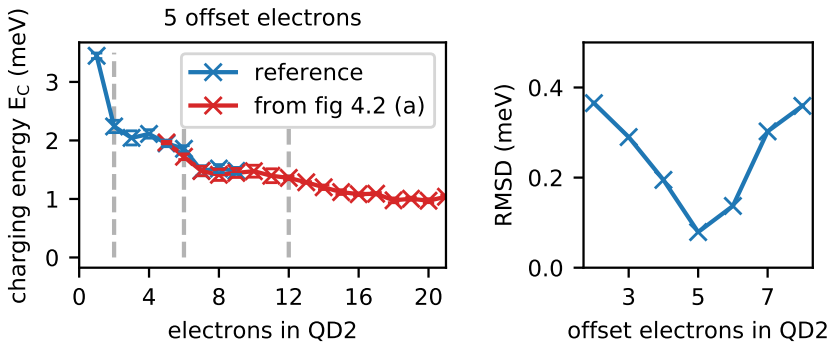


**Figure A.1.:** (a) Evolution of the charging energies for reference data (blue) and data from fig 4.2(a) (red) with an offset of five electrons in QD2. (b) RMSD for different offset electrons in QD2. The clear minimum at five offset electrons determines the number of electrons in QD2.

## Triple Quantum Dot
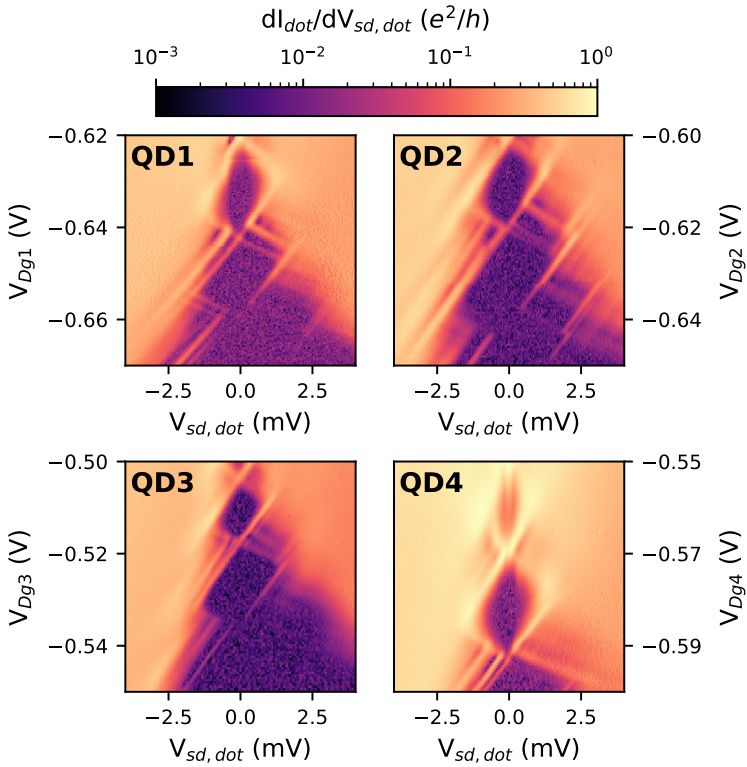


**Figure A.2.:** Coulomb diamond measurements of the four single quantum dots, used to extract the charging energies $E_C$ and gate voltage distances $\Delta V_{gate}$ to calculate the lever arm $\alpha_{gate}$.
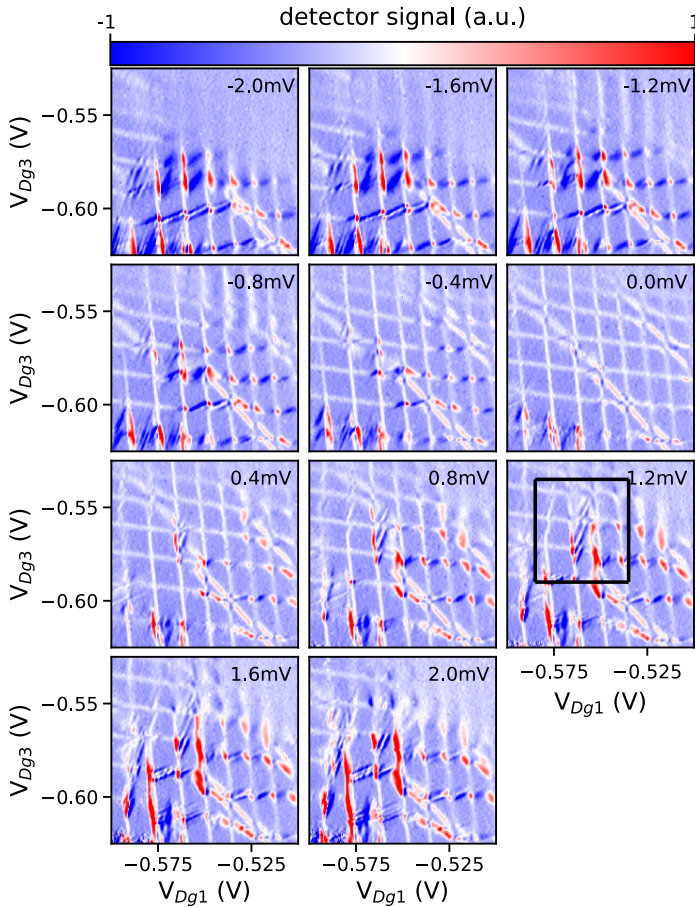
**Figure A.3.:** Detector signals corresponding to figure 4.9. A typical stability diagram is obtained for $V_{sd,dot} = 0\,V$. With increasing $|V_{sd,dot}|$, the appearance of the charging lines changes and charge reconfiguration (dark blue) and charging events involving more than one electron (red) become increasingly dominant.

## Isolated Double Quantum Dot
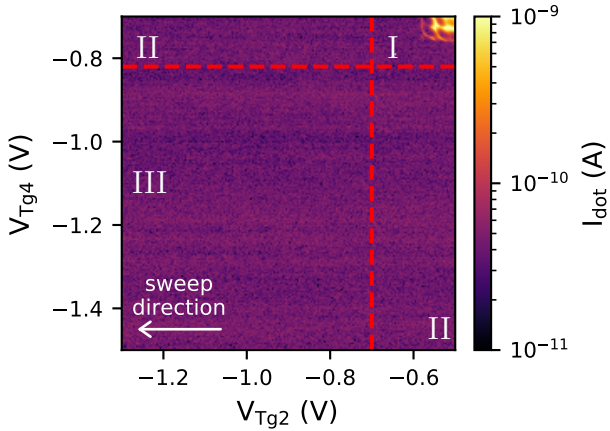


**Figure A.4.:** Current $I_{dot}$ corresponding to figure 5.1 for the same voltage range and with the same annotations for the different coupling regions. Current through the DQD is only found in region I, where the DQD is well coupled to both reservoirs. The bending of the charging lines and their visibility also away from the triple points is the typical behavior of a strongly coupled DQD.

# Bibliography

1. M. Fricke *et al.* Shell structure and electron-electron interaction in self-assembled InAs quantum dots. *Europhysics Letters* **36,** 197 (1996).

2. M. Bruchez Jr *et al.* Semiconductor nanocrystals as fluorescent biological labels. *Science* **281,** 2013–2016 (1998).

3. S. Baskoutas & A. F. Terzis. Size-dependent band gap of colloidal quantum dots. *Journal of Applied Physics* **99** (2006).

4. U. Banin *et al.* Identification of atomic-like electronic states in indium arsenide nanocrystal quantum dots. *Nature* **400,** 542–544 (1999).

5. L. P. Kouwenhoven, D. Austing & S. Tarucha. Few-electron quantum dots. *Reports on Progress in Physics* **64,** 701 (2001).

6. A. Schliwa, M. Winkelnkemper & D. Bimberg. Impact of size, shape, and composition on piezoelectric effects and electronic properties of In (Ga) As/ Ga As quantum dots. *Physical Review B* **76,** 205324 (2007).

7. M. A. Kastner. The single-electron transistor. *Reviews of Modern Physics* **64,** 849 (1992).

8. S. A. Empedocles & M. G. Bawendi. Quantum-confined stark effect in single CdSe nanocrystallite quantum dots. *Science* **278,** 2114–2117 (1997).

9. R. Ashoori *et al.* N-electron ground state energies of a quantum dot in magnetic field. *Physical Review Letters* **71,** 613 (1993).

10. S. Tarucha *et al.* Shell filling and spin effects in a few electron quantum dot. *Physical Review Letters* **77,** 3613 (1996).

11. F. Guffarth *et al.* Strain engineering of self-organized InAs quantum dots. *Physical Review B* **64,** 085305 (2001).

12. K. Jöns *et al.* Dependence of the redshifted and blueshifted photo-luminescence spectra of single In x Ga 1- x As/GaAs quantum dots on the applied uniaxial stress. *Physical Review Letters* **107,** 217402 (2011).

13. A. J. Nozik. Quantum dot solar cells. *Physica E: Low-dimensional Systems and Nanostructures* **14,** 115–120 (2002).

14. E. H. Sargent. Colloidal quantum dot solar cells. *Nature Photonics* **6,** 133–135 (2012).

15. P. Michler *et al.* A quantum dot single-photon turnstile device. *Science* **290,** 2282–2285 (2000).

16. P. Senellart, G. Solomon & A. White. High-performance semiconductor quantum-dot single-photon sources. *Nature Nanotechnology* **12,** 1026–1039 (2017).

17. R. M. Stevenson *et al.* A semiconductor source of triggered entangled photon pairs. *Nature* **439,** 179–182 (2006).

18. N. Akopian *et al.* Entangled photon pairs from semiconductor quantum dots. *Physical Review Letters* **96,** 130501 (2006).

19. S. Giblin *et al.* Towards a quantum representation of the ampere using single electron pumps. *Nature Communications* **3,** 930 (2012).

20. F. Stein *et al.* Validation of a quantized-current source with 0.2 ppm uncertainty. *Applied Physics Letters* **107** (2015).

21. P. Lafarge *et al.* Direct observation of macroscopic charge quantization. *Zeitschrift für Physik B Condensed Matter* **85,** 327–332 (1991).

22. F. Hofmann *et al.* Single electron switching in a parallel quantum dot. *Physical Review B* **51,** 13872 (1995).

23. J. R. Petta *et al.* Coherent manipulation of coupled electron spins in semiconductor quantum dots. *Science* **309,** 2180–2184 (2005).

24. K. Nowack *et al.* Single-shot correlations and two-qubit gate of solid-state spins. *Science* **333,** 1269–1272 (2011).

25. K. Takeda *et al.* A fault-tolerant addressable spin qubit in a natural silicon quantum dot. *Science Advances* **2,** e1600694 (2016).

26. J. M. Nichol *et al.* High-fidelity entangling gate for double-quantum-dot spin qubits. *npj Quantum Information* **3,** 3 (2017).

27. T. Hayashi *et al.* Coherent manipulation of electronic states in a double quantum dot. *Physical Review Letters* **91,** 226804 (2003).

28. J. Gorman, D. Hasko & D. Williams. Charge-qubit operation of an isolated double quantum dot. *Physical Review Letters* **95,** 090502 (2005).

29. K. Petersson *et al.* Quantum coherence in a one-electron semiconductor charge qubit. *Physical Review Letters* **105,** 246804 (2010).

30. G. Cao *et al.* Ultrafast universal quantum control of a quantum-dot charge qubit using Landau–Zener–Stückelberg interference. *Nature Communications* **4,** 1401 (2013).

31. D. Kim *et al.* Microwave-driven coherent operation of a semiconductor quantum dot charge qubit. *Nature Nanotechnology* **10,** 243–247 (2015).

32. D. Kim *et al.* High-fidelity resonant gating of a silicon-based quantum dot hybrid qubit. *npj Quantum Information* **1,** 15004 (2015).

33. G. Cao *et al.* Tunable hybrid qubit in a GaAs double quantum dot. *Physical Review Letters* **116,** 086801 (2016).

34. M. A. Kastner. Artificial atoms. *Physics Today* **46,** 24–31 (1993).

35. R. Ashoori. Electrons in artificial atoms. *Nature* **379,** 413–419 (1996).

36.  L. Kouwenhoven & C. Marcus. Quantum dots. *Physics World* **11,** 35 (1998).

37.  B. Roche *et al.* Detection of a large valley-orbit splitting in silicon with two-donor spectroscopy. *Physical Review Letters* **108,** 206812 (2012).

38.  B. Weber *et al.* Spin blockade and exchange in Coulomb-confined silicon double quantum dots. *Nature Nanotechnology* **9,** 430–435 (2014).

39.  B. Van Wees *et al.* Quantized conductance of magnetoelectric sub-bands in ballistic point contacts. *Physical Review B* **38,** 3625 (1988).

40.  R. J. Haug, J. M. Hong & K. Y. Lee. Electron transport through one quantum dot and through a string of quantum dots. *Surface Science* **263,** 415–418 (1992).

41.  J. Weis *et al.* Competing channels in single-electron tunneling through a quantum dot. *Physical Review Letters* **71,** 4019 (1993).

42.  T. Ihn. *Semiconductor Nanostructures: Quantum States and Electronic Transport* 1st ED (Oxford University Press, 2010).

43.  L. P. Kouwenhoven *et al.* Electron transport in quantum dots. *Mesoscopic Electron Transport,* 105–214 (1997).

44.  D. S. Duncan *et al.* Direct measurement of the destruction of charge quantization in a single-electron box. *Applied Physics Letters* **74,** 1045–1047 (1999).

45.  H. Grabert, M. Devoret & M. Kastner. *Single Charge Tunneling: Coulomb Blockade Phenomena in Nanostructures* 1st (American Institute of Physics, 1993).

46.  D. Davidović & M. Tinkham. Spectroscopy, interactions, and level splittings in Au nanoparticles. *Physical Review Letters* **83,** 1644 (1999).

47.  L. P. Kouwenhoven *et al.* Single electron charging effects in semiconductor quantum dots. *Zeitschrift für Physik B Condensed Matter* **85,** 367–373 (1991).

48.  A. Kumar, S. E. Laux & F. Stern. Electron states in a GaAs quantum dot in a magnetic field. *Physical Review B* **42,** 5166 (1990).

49.  V. Fock. Bemerkung zur Quantelung des harmonischen Oszillators im Magnetfeld. *Zeitschrift für Physik* **47,** 446–448 (1928).

50.  C. G. Darwin. *The diamagnetism of the free electron* in *Mathematical Proceedings of the Cambridge Philosophical Society* **27** (1931), 86–90.

51.  R. Hanson *et al.* Spins in few-electron quantum dots. *Reviews of Modern Physics* **79,** 1217 (2007).

52.  D. Averin & K. Likharev. Coulomb blockade of single-electron tunneling, and coherent oscillations in small tunnel junctions. *Journal of Low Temperature Physics* **62,** 345–373 (1986).

53.  U. Meirav, M. Kastner & S. Wind. Single-electron charging and periodic conductance resonances in GaAs nanostructures. *Physical Review Letters* **65,** 771 (1990).

54.  C. W. Beenakker. Theory of Coulomb-blockade oscillations in the conductance of a quantum dot. *Physical Review B* **44,** 1646 (1991).

55.  E. Foxman *et al.* Effects of quantum levels on transport through a Coulomb island. *Physical Review B* **47,** 10020 (1993).

56.  A. Hofmann *et al.* Measuring the degeneracy of discrete energy levels using a GaAs/AlGaAs quantum dot. *Physical Review Letters* **117,** 206803 (2016).

57.  T. Hensgens *et al.* Quantum simulation of a Fermi–Hubbard model using a semiconductor quantum dot array. *Nature* **548,** 70–73 (2017).

58. U. Mukhopadhyay *et al.* A 2 × 2 quantum dot array with controllable inter-dot tunnel couplings. *Applied Physics Letters* **112,** 183505 (2018).

59. W. G. Van der Wiel *et al.* Electron transport through double quantum dots. *Reviews of Modern Physics* **75,** 1 (2002).

60. A. C. Johnson. *Charge sensing and spin dynamics in gallium arsenide quantum dots* PhD thesis (Harvard University, Cambridge, Massachusetts, 2005).

61. R. H. Blick *et al.* Single-electron tunneling through a double quantum dot: The artificial molecule. *Physical Review B* **53,** 7899 (1996).

62. C. Barthel *et al.* Fast sensing of double-dot charge arrangement and spin state with a radio-frequency sensor quantum dot. *Physical Review B* **81,** 161308 (2010).

63. M. Delbecq *et al.* Full control of quadruple quantum dot circuit charge states in the single electron regime. *Applied Physics Letters* **104,** 183111 (2014).

64. A. Noiri *et al.* Radio-frequency-detected fast charge sensing in undoped silicon quantum dots. *Nano Letters* **20,** 947–952 (2020).

65. M. Field *et al.* Measurements of Coulomb blockade with a noninvasive voltage probe. *Physical Review Letters* **70,** 1311 (1993).

66. J. Elzerman *et al.* Few-electron quantum dot circuit with integrated charge read out. *Physical Review B* **67,** 161308 (2003).

67. J. Petta *et al.* Manipulation of a single charge in a double quantum dot. *Physical Review Letters* **93,** 186802 (2004).

68. M. H. Devoret, D. Esteve & C. Urbina. Single-electron transfer in metallic nanostructures. *Nature* **360,** 547–553 (1992).

69. R. Schoelkopf *et al.* The radio-frequency single-electron transistor (RF-SET): A fast and ultrasensitive electrometer. *Science* **280,** 1238–1242 (1998).

70. A. Cleland *et al.* Very low noise photodetector based on the single electron transistor. *Applied Physics Letters* **61,** 2820–2822 (1992).

71. M. Yoo *et al.* Scanning single-electron transistor microscopy: Imaging individual charges. *Science* **276,** 579–582 (1997).

72. A. N. Cleland & M. L. Roukes. A nanometre-scale mechanical electrometer. *Nature* **392,** 160–162 (1998).

73. U. Gasser *et al.* Phonon-mediated back-action of a charge readout on a double quantum dot. *Nanotechnology* **21,** 274003 (2010).

74. D. Harbusch *et al.* Phonon-mediated versus coulombic backaction in quantum dot circuits. *Physical Review Letters* **104,** 196801 (2010).

75. G. Granger *et al.* Quantum interference and phonon-mediated back-action in lateral quantum-dot circuits. *Nature Physics* **8,** 522–527 (2012).

76. C. Beenakker & H. van Houten. *Quantum transport in semiconductor nanostructures* in *Solid State Physics* 1–228 (Elsevier, 1991).

77. B. J. van Wees *et al.* Quantum ballistic and adiabatic electron transport studied with quantum point contacts. *Physical Review B* **43,** 12431 (1991).

78. J. Krans *et al.* The signature of conductance quantization in metallic point contacts. *Nature* **375,** 767–769 (1995).

79. T. Ando. Quantum point contacts in magnetic fields. *Physical Review B* **44,** 8017 (1991).

80. M. Büttiker. Quantized transmission of a saddle-point constriction. *Physical Review B* **41,** 7906 (1990).

81. A. Szafer & A. D. Stone. Theory of quantum conduction through a constriction. *Physical Review Letters* **62,** 300 (1989).

82. L. Kouwenhoven *et al.* Nonlinear conductance of quantum point contacts. *Physical Review B* **39,** 8040 (1989).

83. C. Rössler *et al.* Transport properties of clean quantum point contacts. *New Journal of Physics* **13,** 113006 (2011).

84. K. Thomas *et al.* Possible spin polarization in a one-dimensional electron gas. *Physical Review Letters* **77,** 135 (1996).

85. F. Bauer *et al.* Microscopic origin of the '0.7-anomaly'in quantum point contacts. *Nature* **501,** 73–78 (2013).

86. W. Lu *et al.* Real-time detection of electron tunnelling in a quantum dot. *Nature* **423,** 422–425 (2003).

87. R. Schleser *et al.* Time-resolved detection of individual electrons in a quantum dot. *Applied Physics Letters* **85,** 2005–2007 (2004).

88. L. Vandersypen *et al.* Real-time detection of single-electron tunneling using a quantum point contact. *Applied Physics Letters* **85,** 4394–4396 (2004).

89. J. Elzerman *et al.* Single-shot read-out of an individual electron spin in a quantum dot. *Nature* **430,** 431–435 (2004).

90. A. Morello *et al.* Single-shot readout of an electron spin in silicon. *Nature* **467,** 687–691 (2010).

91. M. W. Keller *et al.* Accuracy of electron counting using a 7-junction electron pump. *Applied Physics Letters* **69,** 1804–1806 (1996).

92. L. Fricke *et al.* Self-referenced single-electron quantized current source. *Physical Review Letters* **112,** 226803 (2014).

93. H. Störmer *et al.* Two-dimensional electron gas at a semiconductor-semiconductor interface. *Solid State Communications* **29,** 705–709 (1979).

94. M. J. Manfra. Molecular beam epitaxy of ultra-high-quality AlGaAs/GaAs heterostructures: Enabling physics in low-dimensional electronic systems. *Annu. Rev. Condens. Matter Phys.* **5,** 347–373 (2014).

95. B. Joyce. Molecular beam epitaxy. *Reports on Progress in Physics* **48,** 1637 (1985).

96. J. R. Arthur. Molecular beam epitaxy. *Surface Science* **500,** 189–217 (2002).

97. J. C. Bayer. *Herstellung und Charakterisierung von Mehrfachquantenpunkten* MA thesis (Leibniz Universität Hannover, 2014).

98. F. Pobell. *Matter and Methods at Low Temperatures* 3rd ED (Springer, 2007).

99. T. Wagner. *Kontrolle zeitaufgelöster Einzelelektronen-Tunnelprozesse in einem Quantenpunkt* PhD thesis (Leibniz Universität Hannover, Hannover, Germany, 2017).

100. M. C. Rogge *et al.* Coupling symmetry of quantum dot states. *Physical Review B* **72,** 233402 (2005).

101. D. Goldhaber-Gordon *et al.* Kondo effect in a single-electron transistor. *Nature* **391,** 156–159 (1998).

102. S. M. Cronenwett, T. H. Oosterkamp & L. P. Kouwenhoven. A tunable Kondo effect in quantum dots. *Science* **281,** 540–544 (1998).

103. G. Bazan *et al.* Charge detector realization for AlGaAs/GaAs quantum-dot cellular automata. *Journal of Vacuum Science & Technology B: Microelectronics and Nanometer Structures Processing, Measurement, and Phenomena* **14,** 4046–4050 (1996).

104. A. Johnson *et al.* Charge sensing of excited states in an isolated double quantum dot. *Physical Review B* **71,** 115333 (2005).

105. L. Hofstetter *et al.* Cooper pair splitter realized in a two-quantum-dot Y-junction. *Nature* **461,** 960–963 (2009).

106. R. Deacon *et al.* Cooper pair splitting in parallel quantum dot Josephson junctions. *Nature Communications* **6,** 7446 (2015).

107. P. Trocha & J. Barnaś. Large enhancement of thermoelectric effects in a double quantum dot system due to interference and Coulomb correlation phenomena. *Physical Review B* **85,** 085408 (2012).

108. M. A. Sierra *et al.* Interactions and thermoelectric effects in a parallel-coupled double quantum dot. *Physical Review B* **93,** 235452 (2016).

109. S. Juergens *et al.* Thermoelectric performance of a driven double quantum dot. *Physical Review B* **87,** 245423 (2013).

110. Y. Liu *et al.* A high-efficiency double quantum dot heat engine. *Applied Physics Letters* **103,** 093901 (2013).

111. J. Weis *et al.* Single-electron tunnelling transistor as a current rectifier with potential-controlled current polarity. *Semiconductor Science and Technology* **10,** 877 (1995).

112. M. Stopa. Rectifying behavior in Coulomb blockades: charging rectifiers. *Physical Review Letters* **88,** 146802 (2002).

113. A. Vidan *et al.* Triple quantum dot charging rectifier. *Applied Physics Letters* **85,** 3602–3604 (2004).

114. C. S. Lent *et al.* Quantum cellular automata. *Nanotechnology* **4,** 49 (1993).

115. L. Gaudreau *et al.* Stability diagram of a few-electron triple dot. *Physical Review Letters* **97,** 036807 (2006).

116. M. C. Rogge & R. J. Haug. The three dimensionality of triple quantum dot stability diagrams. *New Journal of Physics* **11,** 113037 (2009).

117. D. P. DiVincenzo *et al.* Universal quantum computation with the exchange interaction. *Nature* **408,** 339–342 (2000).

118. A. D. Greentree *et al.* Coherent electronic transfer in quantum dot systems using adiabatic passage. *Physical Review B* **70,** 235317 (2004).

119. L. Gaudreau *et al.* Coherent control of three-spin states in a triple quantum dot. *Nature Physics* **8,** 54–58 (2012).

120. M. Seo *et al.* Charge frustration in a triangular triple quantum dot. *Physical Review Letters* **110,** 046803 (2013).

121. M. Kotzian *et al.* Channel blockade in a two-path triple-quantum-dot system. *Physical Review B* **94,** 035442 (2016).

122. A. Noiri *et al.* A triangular triple quantum dot with tunable tunnel couplings. *Semiconductor Science and Technology* **32,** 084004 (2017).

123. H. Flentje *et al.* Coherent long-distance displacement of individual electron spins. *Nature Communications* **8,** 501 (2017).

124. D. Schröer *et al.* Electrostatically defined serial triple quantum dot charged with few electrons. *Physical Review B* **76,** 075306 (2007).

125. M. C. Rogge & R. J. Haug. Two-path transport measurements on a triple quantum dot. *Physical Review B* **77,** 193306 (2008).

126. G. Granger *et al.* Three-dimensional transport diagram of a triple quantum dot. *Physical Review B* **82,** 075304 (2010).

127. M. Busl *et al.* Bipolar spin blockade and coherent state superpositions in a triple quantum dot. *Nature Nanotechnology* **8,** 261–265 (2013).

128. F. R. Braakman *et al.* Long-distance coherent coupling in a quantum dot array. *Nature Nanotechnology* **8,** 432–437 (2013).

129. D. Taubert *et al.* Determination of energy scales in few-electron double quantum dots. *Review of Scientific Instruments* **82,** 123905 (2011).

130. O. Dani *et al.* Temperature-dependent broadening of coherent current peaks in InAs double quantum dots. *Communications Physics* **5,** 292 (2022).

131.   M. D. Shulman *et al.* Demonstration of entanglement of electrostatically coupled singlet-triplet qubits. *Science* **336,** 202–205 (2012).

132.   Y. P. Kandel *et al.* Coherent spin-state transfer via Heisenberg exchange. *Nature* **573,** 553–557 (2019).

133.   R. Thalineau *et al.* A few-electron quadruple quantum dot in a closed loop. *Applied Physics Letters* **101,** 103102 (2012).

134.   T. A. Baart *et al.* Computer-automated tuning of semiconductor double quantum dots into the single-electron regime. *Applied Physics Letters* **108,** 213104 (2016).

135.   T. Botzem *et al.* Tuning methods for semiconductor spin qubits. *Physical Review Applied* **10,** 054026 (2018).

136.   C. Van Diepen *et al.* Automated tuning of inter-dot tunnel coupling in double quantum dots. *Applied Physics Letters* **113,** 033101 (2018).

137.   A. Rushforth *et al.* Noninvasive detection of the evolution of the charge states of a double dot system. *Physical Review B* **69,** 113309 (2004).

138.   B. Bertrand *et al.* Quantum manipulation of two-electron spin states in isolated double quantum dots. *Physical Review Letters* **115,** 096801 (2015).

139.   H. Flentje *et al.* A linear triple quantum dot system in isolated configuration. *Applied Physics Letters* **110,** 233101 (2017).

140.   J. C. Bayer *et al.* Charge reconfiguration in arrays of quantum dots. *Physical Review B* **96,** 235305 (2017).

141.   J. C. Bayer *et al.* Charge reconfiguration in isolated quantum dot arrays. *Annalen der Physik* **531,** 1800393 (2019).

142.   P.-A. Mortemousque *et al.* Coherent control of individual electron spins in a two-dimensional quantum dot array. *Nature Nanotechnology* **16,** 296–301 (2021).

143. D. Biesinger *et al.* Intrinsic metastabilities in the charge configuration of a double quantum dot. *Physical Review Letters* **115,** 106804 (2015).

144. L. Geerligs, D. Averin & J. Mooij. Observation of macroscopic quantum tunneling through the Coulomb energy barrier. *Physical Review Letters* **65,** 3037 (1990).

145. C. Yang *et al.* Charge state hysteresis in semiconductor quantum dots. *Applied Physics Letters* **105,** 183505 (2014).

146. C. Livermore *et al.* The Coulomb blockade in coupled quantum dots. *Science* **274,** 1332–1335 (1996).

147. D. McClure *et al.* Tunable noise cross correlations in a double quantum dot. *Physical Review Letters* **98,** 056801 (2007).

148. I. Chan *et al.* Capacitively coupled quantum dots as a single-electron switch. *Physica E: Low-dimensional Systems and Nanostructures* **17,** 584–588 (2003).

149. A. Hübel *et al.* Two laterally arranged quantum dot systems with strong capacitive interdot coupling. *Applied Physics Letters* **91,** 102101 (2007).

150. L. DiCarlo *et al.* Differential charge sensing and charge delocalization in a tunable double quantum dot. *Physical Review Letters* **92,** 226801 (2004).

151. R. Sánchez *et al.* Long-range spin transfer in triple quantum dots. *Physical Review Letters* **112,** 176803 (2014).

152. R. Sánchez, F. Gallego-Marcos & G. Platero. Superexchange blockade in triple quantum dots. *Physical Review B* **89,** 161402 (2014).

153. F. Gallego-Marcos, R. Sánchez & G. Platero. Photon assisted long-range tunneling. *Journal of Applied Physics* **117,** 112808 (2015).

154. P. Stano *et al.* Fast long-distance control of spin qubits by photon-assisted cotunneling. *Physical Review B* **92,** 075302 (2015).

155.   J. M. Martinis, M. Nahum & H. D. Jensen. Metrological accuracy of the electron pump. *Physical Review Letters* **72,** 904 (1994).

156.   M. W. Keller *et al.* A capacitance standard based on counting electrons. *Science* **285,** 1706–1709 (1999).

157.   H. D. Jensen & J. M. Martinis. Accuracy of the electron pump. *Physical Review B* **46,** 13407 (1992).

158.   V. Mel'nikov. Cotunneling rate in a series array of tunnel junctions. *Physics Letters A* **176,** 267–269 (1993).

159.   P. Lafarge & D. Esteve. Nondivergent calculation of unwanted high-order tunneling rates in single-electron devices. *Physical Review B* **48,** 14309 (1993).

160.   S. Gustavsson. *Time-resolved single-electron detection in semiconductor nanostructures* PhD thesis (ETH Zurich, Zurich, Switzerland, 2008).

161.   C. Fricke. *Der Quantenpunktkontakt als Ladungsdetektor in der Transportspektroskopie* PhD thesis (Leibniz Universität Hannover, Hannover, Germany, 2009).

162.   T. Brandes. Waiting times and noise in single particle transport. *Annalen der Physik* **520,** 477–496 (2008).

163.   M. Albert, C. Flindt & M. Büttiker. Distributions of waiting times of dynamic single-electron emitters. *Physical Review Letters* **107,** 086805 (2011).

164.   F. Brange *et al.* Controlled emission time statistics of a dynamic single-electron transistor. *Science Advances* **7,** eabe0793 (2021).

165.   T. Wagner *et al.* Optimal single-electron feedback control. *Physica Status Solidi (b)* **254,** 1600701 (2017).

166.   S. Gustavsson *et al.* Counting statistics of single electron transport in a quantum dot. *Physical Review Letters* **96,** 076605 (2006).

167. C. Fricke *et al.* Bimodal counting statistics in single-electron tunneling through a quantum dot. *Physical Review B* **76,** 155307 (2007).

168. O. Naaman & J. Aumentado. Poisson transition rates from time-domain measurements with a finite bandwidth. *Physical Review Letters* **96,** 100201 (2006).

169. J. H. Davies *et al.* Classical theory for shot noise in resonant tunneling. *Physical Review B* **46,** 9620 (1992).

170. B. Lounis & W. E. Moerner. Single photons on demand from a single molecule at room temperature. *Nature* **407,** 491–493 (2000).

171. H. Barros *et al.* Deterministic single-photon source from a single ion. *New Journal of Physics* **11,** 103004 (2009).

172. S. Gustavsson *et al.* Electron counting in quantum dots. *Surface Science Reports* **64,** 191–232 (2009).

173. V. F. Maisi *et al.* Spin-orbit coupling at the level of a single electron. *Physical Review Letters* **116,** 136803 (2016).

174. T. Wagner *et al.* Quantum stochastic resonance in an ac-driven single-electron quantum dot. *Nature Physics* **15,** 330–334 (2019).

175. T. Wagner *et al.* Strong suppression of shot noise in a feedback-controlled single-electron transistor. *Nature Nanotechnology* **12,** 218–222 (2017).

176. J. Crank. *The Mathematics of Diffusion* 2nd ED (Oxford University Press, 1979).

177. J. Wang *et al.* Heat capacity of the two-dimensional electron gas in GaAs/Al x Ga 1- x As multiple-quantum-well structures. *Physical Review B* **38,** 6174 (1988).

178. N. Hartman *et al.* Direct entropy measurement in a mesoscopic quantum system. *Nature Physics* **14,** 1083–1086 (2018).

# Lebenslauf

| | |
|---|---|
| **Name:** | M. Sc. Johannes Bayer |
| **Geburtstag:** | 10. März 1988 |
| **Geburtsort:** | Karlsruhe |

**seit 2015**   Vorbereitung der Dissertation am
Institut für Festkörperphysik der
Leibniz Universität Hannover,
bei Prof. Dr. Rolf Haug

**2011 - 2014**   Studium der Physik (Master)
Leibniz Universität Hannover,
Masterarbeit:
"Herstellung und Charakterisierung
von Mehrfachquantenpunkten"

**2007 - 2011**   Studium der Physik (Bachelor)
Leibniz Universität Hannover,
Bachelorarbeit:
"Herstellung und Charakterisierung
von Quantenpunktkontakten"

**2004 - 2007**   Edith-Stein-Gymnasium, Bretten

**1998 - 2004**   Salzach-Gymnasium, Maulbronn

# Publications

Parts of this thesis are published:

- **Charge reconfiguration in isolated quantum dot arrays**,
  J. C. Bayer, T. Wagner, E. P. Rugeramigabo & R. J. Haug
  *Annalen der Physik* **531**, 235305 (2019)

- **Charge reconfiguration in arrays of quantum dots**,
  J. C. Bayer, T. Wagner, E. P. Rugeramigabo & R. J. Haug
  *Physical Review B* **96**, 235305 (2017)

Further publications:

- **Direct measurement of spin-flip rates in single-electron tunneling**, O. Dani, R. Hussein, J. C. Bayer, K. Pierz, S. Kohler & R. J. Haug, *submitted*
  arXiv:2310.11259 [cond-mat.mes-hall] (2023)

- **Temperature-dependent broadening of coherent current peaks in InAs double quantum dots**, O. Dani, R. Hussein, J. C. Bayer, S. Kohler & R. J. Haug, *Communication Physics* **5**, 292 (2022)

- **Towards 28 %-efficient Si single-junction solar cells with better passivating POLO junctions and photonic crystals**, R. Peibst, M. Rienäcker, Y. Larionova, N. Folchert, F. Haase, C. Hollemann, S. Wolter, J. Krügener, P. Bayerl, J. C. Bayer, M. Dzinnik, R. J. Haug & R. Brendel, *Solar Energy Materials and Solar Cells* **238**, 111560 (2022)

- **Contacting a single nanometer-sized pinhole in the interfacial oxide of a poly-silicon on oxide (POLO) solar cell junction**, P. Bayerl, N. Folchert, J. C. Bayer, M. Dzinnik, C. Hollemann, R. Brendel, R. Peibst & R. J. Haug, *Progress in Photovoltaics: Research and Applications* **29**, 936-942 (2021)

- **Controlled emission time statistics of a dynamic single-electron transistor**, F. Brange, A. Schmidt, J. C. Bayer, T. Wagner, C. Flindt & R. J. Haug, *Science Aadvances* **7**, eabe0793 (2021)

- **Spectral properties of stochastic resonance in quantum transport**, R. Hussein, S. Kohler, J. C. Bayer, T. Wagner & R. J. Haug, *Physical Review Letters* **125**, 206801 (2020)

- **Quantum stochastic resonance in an a.c.-driven single-electron quantum dot**, T. Wagner, P. Talkner, J. C. Bayer, E. P. Rugeramigabo, P. Hänggi & R. J. Haug, *Nature Physics* **15**, 330-334 (2019)

- **Optimal single-electron feedback control**, T. Wagner, J. C. Bayer, E. P. Rugeramigabo & R. J. Haug, *Physica Status Solidi B* **254**, 1600701 (2017)

- **Strong suppression of shot-noise in a feedback controlled single-electron transistor**, T. Wagner, P. Strasberg, J. C. Bayer, E. P. Rugeramigabo, T. Brandes & R. J. Haug, *Nature Nanotechnology* **12**, 218–222 (2017)